

Development of a new compact  
three-foil plunger device  
and  
Lifetime measurements using the  
Recoil Distance Doppler-shift method



**Inaugural-Dissertation**

zur  
Erlangung des Doktorgrades  
der Mathematisch-Naturwissenschaftlichen Fakultät  
der Universität zu Köln

vorgelegt von:

**Marcel Beckers**  
aus Mönchengladbach

Köln 2023

**Berichterstatter:**  
**(Gutachter)**

Prof. Dr. Alfred Dewald  
Prof. Dr. Andreas Zilges  
Prof. Dr. Alexandra Gade

**Tag der letzten Prüfung:**

24. April 2023

## Abstract

This thesis presents the development of a new compact differential three-foil plunger (Cologne Compact Differential Plunger - CoCoDiff) for the measurement of lifetimes of excited states in nuclei with the Recoil Distance Doppler-shift (RDDS) method as well as auxiliary techniques and methods to aid the usage of this new plunger and of other plunger devices. The new plunger apparatus has been commissioned in an experiment on level lifetimes in  $^{50}\text{Cr}$  which was carried out at the Cologne FN tandem accelerator. There, lifetimes of the first  $2^+$  and  $4^+$  states have been measured with good precision which match with literature values and shell-model calculations. To enhance the precision of plunger experiments that need absolute foil separations, a new method to measure these has been developed, using an optical sensor. This method has been tested using an experiment on known level lifetimes in  $^{181}\text{Ta}$  also conducted in Cologne.

Furthermore, an RDDS experiment on level lifetimes in  $^{144}\text{Ce}$  was carried out, which is a candidate for octupole deformation. Lifetimes of the first  $2^+$ ,  $4^+$ ,  $6^+$  and  $3^-$  states have been measured with good precision, the latter three for the first time. From these lifetimes,  $B(E2)$  and  $B(E1)$  transition strengths could be determined that give further proof for possible octupole deformation. Additionally, the lifetime of the  $3^-$  state is important for a possible future Coulomb excitation measurement in search of the yet unobserved  $3^- \rightarrow 0^+$  transition.

Lastly, level lifetimes of the first  $2^+$  and  $4^+$  states in  $^{60}\text{Ni}$  have been measured using the RDDS method. They shed light into a prior confusing situation of contradicting literature values that allowed for no clear physical interpretation of the onset of collectivity of Ni isotopes regarding the tentative  $N=40$  sub-shell closure.

# Contents

<b>1</b>	<b>Introduction</b>	<b>1</b>
1.1	Lifetime measurements using the Recoil Distance Doppler-shift (RDDS) method .	2
1.1.1	The RDDS method . . . . .	3
1.1.2	The Differential Decay Curve Method (DDCM) . . . . .	4
1.1.3	The Differential Plunger Method . . . . .	6
1.1.4	Absolute foil separations . . . . .	8
1.1.5	Doppler-shift attenuation effects in RDDS measurements . . . . .	9
1.2	The Plunger apparatus . . . . .	11
1.2.1	Compact Plunger designs . . . . .	12
1.3	The experiments at the Cologne FN tandem accelerator . . . . .	15
1.4	Theoretical approaches relevant for this thesis . . . . .	19
1.4.1	The nuclear shell model . . . . .	19
1.4.2	Octupole collectivity in nuclei . . . . .	22
<b>2</b>	<b>Overview of the publications and contributions by the author</b>	<b>28</b>
<b>3</b>	<b>Publication I:</b>	
	<b>Development of the multi-purpose Cologne Compact Differential Plunger (CoCoDiff) for the measurement of nuclear level lifetimes with the Recoil Distance Doppler-shift method</b>	<b>31</b>
<b>4</b>	<b>Publication II:</b>	
	<b>Revisiting the measurement of absolute foil-separation fo RDDS measurements and introduction of an optical measurement method</b>	<b>43</b>
<b>5</b>	<b>Publication III:</b>	
	<b>Lifetime measurement of excited states in <math>^{144}\text{Ce}</math>: Enhanced E1 strengths in a candidate for octupole deformation</b>	<b>52</b>
<b>6</b>	<b>Publication IV:</b>	
	<b>Lifetime measurement of the <math>2_1^+</math>, <math>4_1^+</math> states in semi-magic <math>^{60}\text{Ni}</math></b>	<b>64</b>
<b>7</b>	<b>Summary and Outlook</b>	<b>74</b>
7.1	Development of the CoCoDiff plunger . . . . .	74
7.1.1	Further developments of plunger devices and plunger software package . .	75
7.1.2	Work in progress and future developments . . . . .	78
7.2	Optical plunger foil distance measurement method . . . . .	79
7.3	Lifetime measurement in $^{144}\text{Ce}$ . . . . .	80
7.4	Lifetime measurement in $^{60}\text{Ni}$ . . . . .	81
	<b>References</b>	<b>82</b>
	<b>Appendix</b>	<b>94</b>
	Manual for the Cologne Plunger Software Package and the Set-Up of a Compact Plunger measurement . . . . .	94
	<b>Erklärung zur Dissertation</b>	<b>115</b>

# 1 Introduction

Lifetimes of excited states in nuclei, together with their excitation energies, are among the most important experimental observables in nuclear structure physics. They allow the determination of transition strengths between excited nuclear states, which in turn give insight into the structure of the nucleus itself. Level lifetimes in nuclei span over a wide range, from nuclear isomers with lifetimes in the range of many years<sup>1</sup> to very short lifetimes in the range of femtoseconds, depending on the character of the excitation and structure of the nucleus. Therefore, many different techniques exist to obtain lifetimes from these different regions [2]. One of these is the Recoil Distance Doppler-shift (RDDS) method, which covers the range from about one to several hundreds of picoseconds, depending on the experimental circumstances. The RDDS method makes use of the so-called plunger apparatus, a sophisticated device which allows the measurement to be conducted with a very high precision. In the last decades, several of these devices have been built specifically for different laboratories and experimental conditions. Many of these plungers followed the design of the Cologne Coincidence Plunger [3], which will be described in detail later. Some examples of such plungers are described in Refs. [4, 5]. In the more recent years, however, the progress in the manufacturing of highly precise piezo motors (a key component of all plunger devices) that allowed for a massive reduction of the motor sizes, has opened the possibility for new, very compact plunger designs. These have the advantage that they can fit inside compact particle detector arrays like MICROBALL [6], enabling new possibilities for specialized plunger measurements. At the same time the advent of next-generation research facilities like the Facility for Rare Isotope Beams (FRIB)<sup>2</sup> and the Facility for Antiproton and Ion Research (FAIR) will lead to novel possibilities for nuclear structure research. However, beam time at these facilities will be extremely valuable and obtaining it will be a highly competitive process, even more than it is already for the existing state-of-the-art facilities. Since RDDS measurements require fairly long beam times to be successful, this restriction is especially valid. Therefore, decreasing the amount of required beam time can become of great value. One possibility to achieve such a reduction of beam time is the use of the differential plunger method, which utilizes a three-foil plunger device [7].

One main objective of this thesis is therefore the combination of the new possibilities of very compact plunger designs and the differential plunger method to design, construct and commission a novel compact three-foil plunger device which can be employed at different experimental facilities. One part of this thesis reports on the development of this new plunger as well as on the derivation of an adjustment to the established Differential Decay Curve Method (DDCM) for the usage with three-foil plungers. The new plunger device has been tested in a commissioning experiment, measuring lifetimes of excited states in  $^{50}\text{Cr}$ .

Additionally, this thesis is also focused on developing auxiliary methods and techniques which can improve RDDS measurements with the new device as well as with other plunger devices. For this, a new method to obtain absolute foil separations in plungers with higher precision than

---

<sup>1</sup>The longest living isomer known today is  $^{180m}\text{Ta}$ , a  $9^-$  state with a half-life of  $>7.1 \cdot 10^{15}$  years [1]

<sup>2</sup>FRIB officially started operating in 2022.

previously achievable will be presented. Absolute foil distances are needed for certain use cases of the differential plunger method as well as in conventional RDDS measurements with two-foil plungers that do not use the DDCM. The new method to obtain absolute distances has been compared to the standard capacitance method as well as to a distance measurement with known lifetimes in an experiment on  $^{181}\text{Ta}$ .

Another focus was laid on the handling of Doppler-Shift Attenuation (DSA) effects in RDDS measurements with the simulation toolkit PTBG4 that has been developed by T. Braunroth [8]. To benchmark the usage of this toolkit for DSA effects with real data, an RDDS experiment on  $^{60}\text{Ni}$  was utilized, a semi-magic nucleus close to the proposed neutron sub-shell closure at  $N=40$ , where the experimental situation prior to this experiment yielded a partly contradictory message regarding the onset of deformation in the Ni isotopes towards (proposed) mid-shell. DSA effects are expected to play a role for the lifetime of the first  $2^+$  state in this nucleus.

Apart from these developments in the design of plunger devices and auxiliary techniques, another lifetime measurement using the RDDS method has been carried out during the course of this thesis at the Cologne FN Tandem accelerator. The investigation of level lifetimes in  $^{144}\text{Ce}$  explores further the octupole deformation in neutron-rich lanthanide nuclei, a topic that has been of great interest in the nuclear physics community over the past decades (see, e.g., [9]).

In the following introduction, an overview of the RDDS method with a special focus on the differential plunger method will be given. The significance of absolute foil distances for plunger measurements will be introduced. Furthermore, the design of the Cologne Coincidence Plunger will be presented as well as the possibilities of and requirements for a new compact plunger design. Afterwards, the different reaction types that have been used for the experiments conducted during the work for this thesis will be briefly reviewed with a special focus on their characteristics that are important for plunger measurements. Lastly, a short introduction into the theoretical frameworks that are important for the description of the results from the different lifetime studies will be given.

## 1.1 Lifetime measurements using the Recoil Distance Doppler-shift (RDDS) method

The measurement of nuclear level lifetimes allows to probe properties of the strong force between nucleons. They are directly related to the transition matrix elements between different states in nuclei, which makes them ideal to test predictions of sophisticated theories about nuclear structure like the shell-model and different collective models. The level lifetime is directly connected with the transition strength between two states. For example, for a pure E2 transition between two states, the reduced transition strength can, following the derivations in [10, 11], be calculated from the lifetime  $\tau$  via

$$B(E2) = \frac{2(5!)^2}{24\pi} \frac{\alpha_{br}}{1 + \alpha_{IC}} \left( \frac{\hbar c}{E_\gamma} \right)^5 \frac{\hbar}{\tau} \quad (1)$$

where  $\alpha_{br}$  is the branching ratio and  $\alpha_{IC}$  the ratio for internal conversion.

The Recoil Distance Doppler-shift method (RDDS) is used to extract lifetimes of excited nuclear states. For a detailed review on this method see Ref. [3]. In the following, only a brief overview

of the method itself and of the principles of the analysis of such measurements will be given.

### 1.1.1 The RDDS method

The RDDS method exploits the fact, that  $\gamma$  radiation emitted from a decaying state while the nucleus is in motion with velocity  $v$  gets detected with a Doppler-shifted energy:

$$E_{\gamma,sh} = E_{\gamma} \frac{\sqrt{1 - \beta^2}}{1 - \beta \cos(\theta)}, \quad (2)$$

where  $E_{\gamma,sh}$  is the Doppler-shifted energy of the  $\gamma$ -ray from the decay,  $\beta = \frac{v}{c}$  and  $\theta$  is the angle between the motion vector of the recoil and the detector [3].

To obtain a level lifetime, a plunger apparatus is used. This consists of two (or more, see below) foils, a target and one (several) degrader foil(s). The nuclei created in the target get knocked out and travel towards the degrader foil. Excited states in these nuclei can either decay in-flight or after the nuclei have been stopped or slowed-down in the degrader foil, changing the observed  $\gamma$ -energy according to the Doppler-effect. Different foil separations lead to different flight times  $t$  and therefore give information about the time behavior of the decay, represented in the decay curve:

$$R(t) = \frac{I_{us}}{I_{us} + I_{sh}} \quad (3)$$

where  $I_{us}$  and  $I_{sh}$  are the intensities of the peaks observed at the unshifted and Doppler-shifted energies, respectively [3]. A schematic representation of the method is shown in Fig. 1.

For an isolated excited state with no feeding, the decay curve is described by an exponential function of the form

$$R(t) = N(0)e^{-\frac{t}{\tau}} \quad (4)$$

with  $N(0)=1$  because Eq. 3 is normalized with respect to the total amount of decays. To extract the lifetime from RDDS data, one has to fit the decay curve of the state of interest to the data points from the different foil separations. In the general case, however, a level is not populated directly but through multiple feeding paths. This is especially true if the respective nucleus has been created in a fusion-evaporation reaction, where nuclei are populated in highly excited states<sup>3</sup>. In such cases the decay is described by the general set of differential equations

$$\dot{n}_i(t) = -\lambda_i n_i(t) + \sum_k b_{ki} \lambda_k n_k(t) \quad (5)$$

where  $n_i(t)$  describes the population of level  $i$  at time  $t$ ,  $i$  is the state of interest,  $k$  are the feeding states,  $\lambda$  is the respective decay constant and  $b_{ki}$  are the branching ratios between states  $k$  and  $i$  [3]. If solved for a certain decay scheme, one obtains the Bateman equations of the decay, from which the decay curve  $R(t)$  can be derived [12]. For the lifetime analysis this means that it is necessary to know precisely the feeding pattern of a state, including the lifetimes of the

---

<sup>3</sup>see chapter 1.3

feeders, as well as the initial population of all feeding states. In all cases, for an analysis using the Bateman equations, absolute foil separations are needed to obtain the flight times.

If the analytical decay curve is used, a comfortable way to perform the lifetime analysis is the use of Monte-Carlo type (MC) simulations [13]. MC methods are used to obtain a probability distribution of a dependent variable when the probabilities of all independent variables are known but no closed formula is available (or the closed formula is too demanding to obtain or solve analytically). In the process of determining lifetimes with the Bateman equations, they are used to incorporate all types of uncertainties to give a well-defined uncertainty for the resulting lifetime value. This is especially useful because the uncertainties (and their types of distributions, e.g. linear, Gaussian etc.) of the input parameters, like feeding lifetimes, branching ratios and absolute foil distance, are generally well known. At the same time, the calculation of their influence on the resulting lifetime may be analytically demanding, especially since some uncertainties might be correlated. In a Monte-Carlo type simulation, each input variable is treated independently and is varied within its uncertainty range using its probability distribution. This way, in each simulation step a random value (within and depending on the respective probability distribution) is assigned to every input variable and a lifetime value is calculated using these values. A large number of steps yields a probability distribution of lifetime values from which in turn the uncertainty of the lifetime (e.g. by using the  $\sigma$  intervals) can be calculated. An example of a resulting probability distribution of a lifetime analysis is shown in Fig. 2. Another advantage of using Monte-Carlo type simulations is that also unknown quantities like unobserved feeding can easily be incorporated, if a measure of its probability (e.g. observation limits, lifetimes in neighboring nuclei) can be found. This technique has been used in the analysis of  $^{144}\text{Ce}$  to obtain realistic uncertainties for cases where unobserved feeding might be possible (see chapter 5).

### 1.1.2 The Differential Decay Curve Method (DDCM)

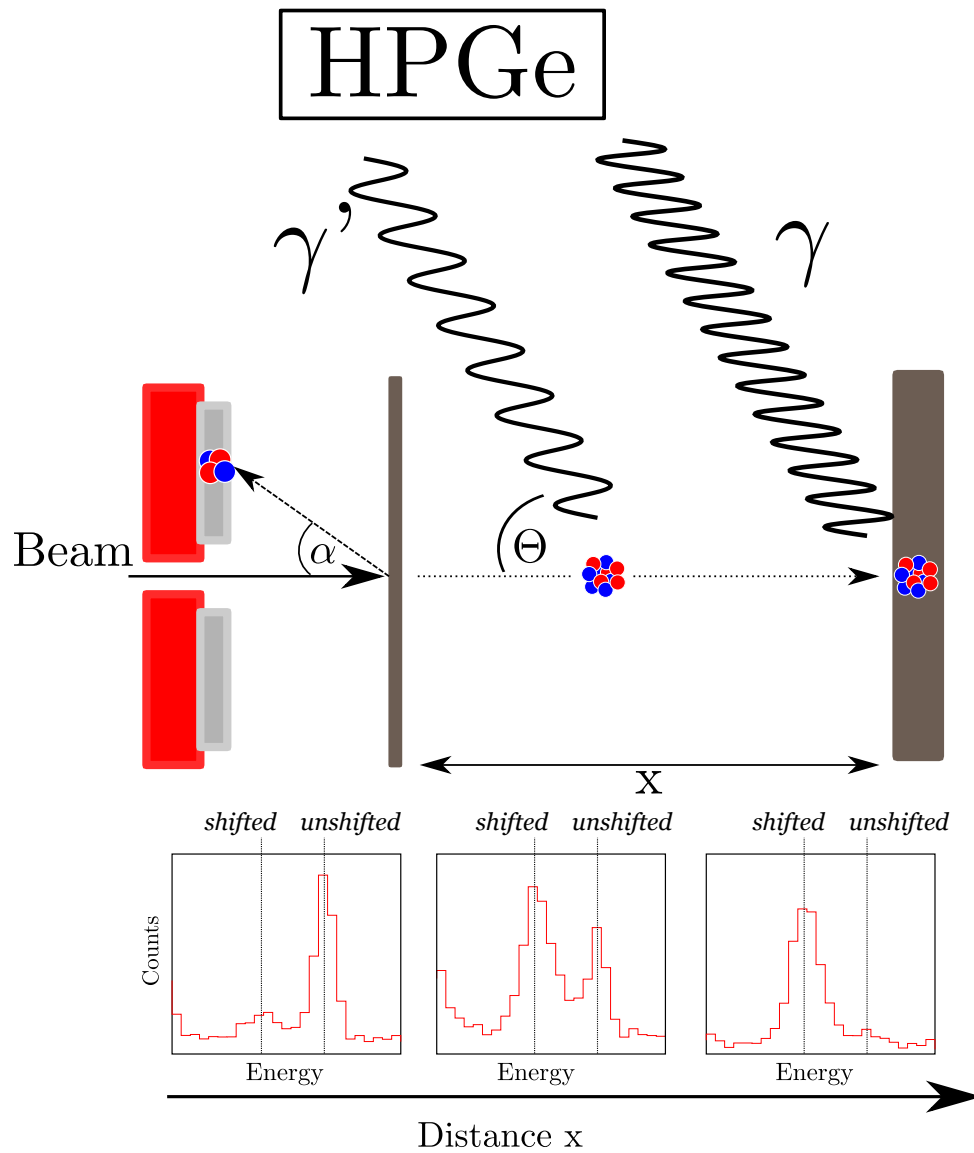
An alternative to the analytical decay curve analysis is the use of the Differential Decay Curve Method (DDCM). The derivation of this method shall not be repeated here. Instead, the reader is referred to Refs. [15, 3]. The DDCM states that the lifetime of a state is given by

$$\tau_i(x) = \frac{-R_i(x) + \sum_k b_{ki} \alpha_{ki} R_k(x)}{\frac{d}{dt} R_i(x)} \cdot \frac{1}{v} \quad (6)$$

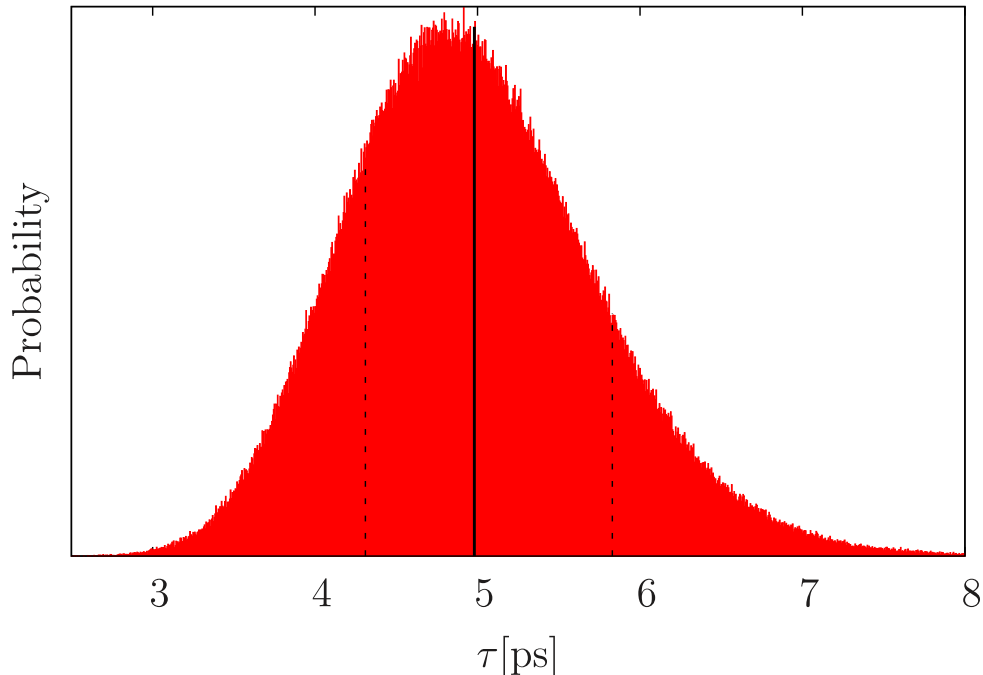
where  $R_i(x)$ ,  $R_k(x)$  are the decay curves of the state of interest  $i$  and the  $k$  direct feeding states.  $\alpha_{ki}$  denotes a factor of proportionality for the difference in detection efficiency for different  $\gamma$  energies and differences in angular distributions and  $b_{ki}$  represents the branching ratio [3]. The DDCM offers some advantages over the analytical decay curve approach, among them are the possibility to detect certain systematic error types and the need for relative distances instead of absolute distances, which can be obtained with a much higher precision.

If it is possible to use  $\gamma - \gamma$  coincidences and to set a gate on the shifted component of a direct





**Figure 1:** Schematic representation of a plunger measurement. In this case an additional particle detector upstream of the target is shown, which is used to detect back-scattered reaction partners. See chapter 1.3 for more details.



**Figure 2:** Example of the result of a Monte-Carlo type simulation being used for the lifetime analysis. The lifetime was chosen to be the first moment of the probability distribution (solid line) and the uncertainties are the  $\sigma$  intervals to both sides thereof (dashed lines). The example stems from the analysis of  $^{144}\text{Ce}$ . Details regarding the analysis are given in chapter 5. Figure adapted from Ref. [14].

feeding transition of the state of interest Eq. 6 simplifies further to

$$\tau_i(x) = \frac{I_{us}}{v \frac{d}{dx} I_{sh}}, \quad (7)$$

where  $I_{us}$  is the intensity of the unsifted component and  $I_{sh}$  is the intensity of the Doppler-shifted component [3]. This adds the advantage that no feeding assumptions have to be taken into account, reducing the general systematic uncertainty of all types of RDDS measurements significantly.

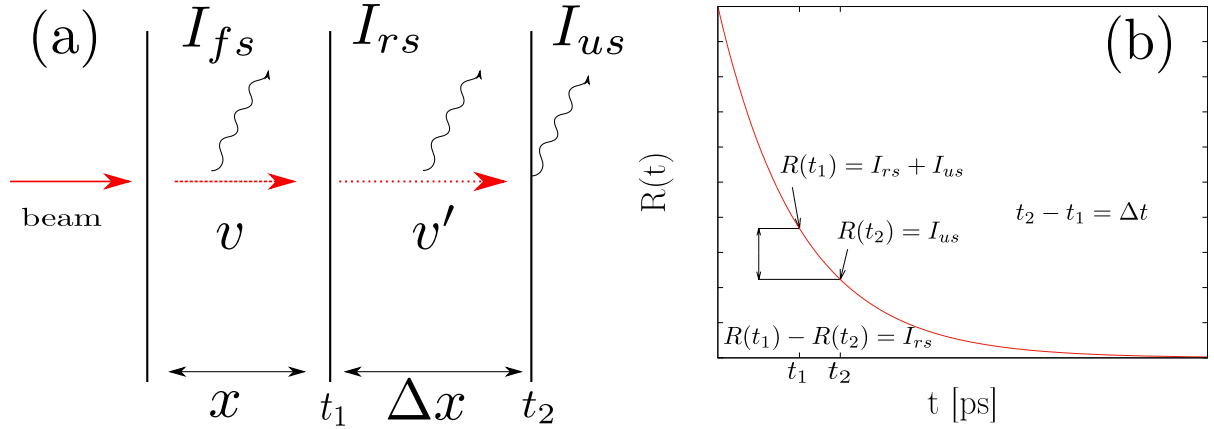
In this work, the DDCM is mostly used for the lifetime analysis of excited states in  $^{144}\text{Ce}$  in the  $\gamma$ -single version due to a lack of statistics which prevents the use of  $\gamma - \gamma$  coincidences. The lifetimes of excited states in  $^{60}\text{Ni}$  have been analyzed with the  $\gamma - \gamma$  coincidence version of the DDCM.

### 1.1.3 The Differential Plunger Method

Introduced by Dewald *et al.* [7] the Differential Plunger Method (DPM) is a further development of the DDCM. While the DDCM is a very successful and well-established method, it still suffers from some drawbacks, the most consequential one is the need for extensive beam times. According to Eqs. 6, the derivative of decay curve  $R(t)$  is needed for the calculation of the lifetime. Since the decay curve of the state is not known beforehand, this means it has to be sampled by measuring the shifted and unshifted components of the level's decay radiation at different

target-stopper distances to be able to obtain the derivative of this function.

The DPM is meant to overcome this restriction. In principle, it enables the user to extract



**Figure 3:** Schematic depiction of a three-foil plunger (a) and exemplary decay curve with the experimentally observable quantities (b). Figure adapted from Ref. [16].

lifetimes from one single distance configuration by directly measuring the derivative of the decay curve. To do so, a three-foil plunger apparatus is needed. In this apparatus, a degrader at a separation  $x$  after the target foil is used to slow down the recoiling nuclei with velocity  $v$ , so that they travel the last distance  $\Delta x$  to the stopper with a reduced velocity  $v'$  (see Fig 3(a)). This yields three different peaks in the corresponding  $\gamma$ -spectrum, originating from decays happening between target and first degrader (fully-shifted intensity  $I_{fs}$ ) between first degrader and stopper (reduced-shifted intensity  $I_{rs}$ ) and in the stopper (unshifted intensity  $I_{us}$ ). Transferred to absolute flight times, these peaks relate to different positions on the decay curve of the level of interest. As can be seen in Fig. 3(b),  $-I_{rs} = R(t_2) - R(t_1)$ , where  $t_1$  ( $t_2$ ) is the time when the recoil leaves (enters) the first degrader foil (stopper foil)<sup>4</sup> By dividing it by the time difference  $\Delta t = t_2 - t_1$  between the recoil leaving the first degrader and reaching the stopper one obtains the differential quotient

$$\frac{\Delta R}{\Delta t} = \frac{R(t_2) - R(t_1)}{t_2 - t_1} = \frac{-I_{rs}}{\Delta t} = \frac{-I_{rs} \cdot v'}{\Delta x} \quad (8)$$

which describes the slope of the secant between  $R(t_1)$  and  $R(t_2)$ . If one requires  $\Delta x$  to be very small (technically  $\lim \Delta x \rightarrow 0$ ), then Eq. 8 describes  $\frac{dR(t_2)}{dt}$ . Using the DDCM as given in Eq. 7 and the fact that  $I_{us}$  describes  $R(t_2)$  one gets the standard DPM formula [7]

$$\tau_i = \frac{I_{us} \Delta x}{I_{rs} v'}. \quad (9)$$

The requirement of very small  $\Delta x$  naturally opposes the practical requirements for a measurement, since it leads to a very small intensity of the reduced-shifted peak which lies beyond the observation limit. Therefore, for a precise measurement a certain minimum distance, at which  $I_{rs}$  has a high enough peak-to-background ratio, is needed. On the other hand, of course, the

<sup>4</sup>Note: In this section,  $R(t)$  means the non-normalized decay curve, following the notation of chapter 3.

larger  $I_{rs}$  gets, the less valid the approximation made in Eq. 9 becomes. To solve this problem, a correction factor to treat deviations of Eq. 8 from  $\frac{dR(t_2)}{dt}$  when  $\Delta x$  is not negligible was proposed by Iwasaki *et al.* [5] and used for example by Giles *et al.* for a lifetime analysis [17]. This factor is derived from the ratio of Eq. 8 and the analytical derivative of  $R(t_2)$ , obtained by assuming that  $R(t) = N_0 \cdot \exp(-t/\tau)$  and therefore reads

$$C(\tau, \Delta t) = \frac{\exp(\Delta t/\tau) - 1}{\Delta t/\tau}. \quad (10)$$

A corrected lifetime could then be obtained via [5]

$$\tau_{corr} = C(\tau, \Delta t) \cdot \frac{I_{us}}{I_{rs}} \frac{\Delta x}{v'}. \quad (11)$$

However, as explained above, this derivation assumes the decay function  $R(t)$  to be a simple exponential. This, again, is not applicable to general cases, where, because of complicated feeding patterns, the decay function can become much more complicated and, as has to be stressed, is generally not known beforehand in detail. Therefore, the DPM is only applicable to certain cases, where the lifetimes are long enough to be able to choose  $\Delta x$  sufficiently large or where the feeding pattern is extremely simple and the correction factor can be used.

Apart from the DPM, a three-foil plunger can also be used to measure at two distances at the same time and therefore reduce the time needed for an experiment. This is especially advantageous if lifetimes of different magnitudes are targeted in one experiment. Formulas to obtain lifetimes this way using the DDCM and  $\gamma$ - $\gamma$  coincidences have been derived in the course of this thesis and are given in chapter 3.

#### 1.1.4 Absolute foil separations

To determine the time-of-flight of the recoils between the target and the degrader foil(s), the absolute foil separations are needed. These are not trivial to measure because the absolute zero point is unknown. The electrical contact point of the foils, which is often used as a zero point for the relative distances, differs in most cases from the absolute zero point where both foils are completely in contact with each other [3]. One possible reason for this are microscopic spikes in the foils that cause electrical contact early.

The need for absolute distances vanishes when the DDCM is used for the analysis, because only relative distances are needed there. However, in some cases it is preferable to perform the analysis with the Bateman equations, e.g. if only a low number of distances have been measured or if there are few distances in the region of sensitivity. Absolute distances are also needed, if the data are analyzed with the help of simulations and in certain cases of the DPM as explained in chapter 3. In most modern plunger experiments the capacitance method is utilized to obtain absolute distances [18]. However, as will be shown in detail in chapter 4, this method suffers from certain drawbacks and lacks in precision. Therefore, a new method to measure absolute plunger distances directly has been developed in this thesis and will be presented in chapter 4.

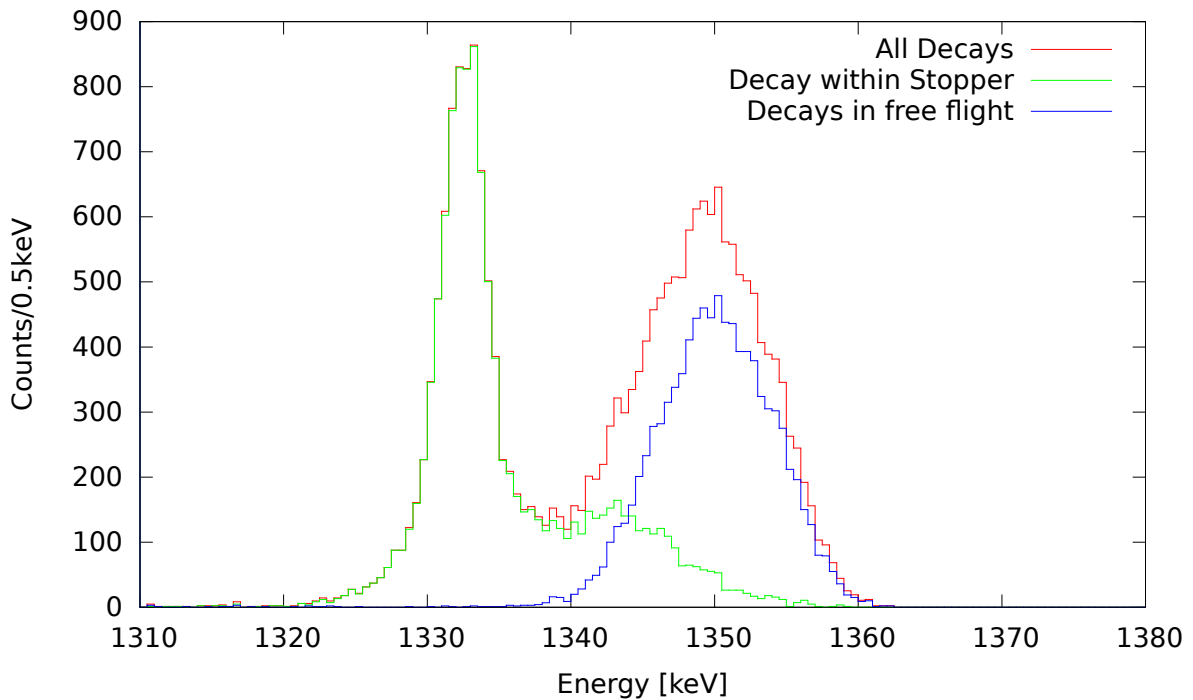
This new method allows for a reduction of uncertainties in lifetime measurements where absolute distances are needed.

### 1.1.5 Doppler-shift attenuation effects in RDDS measurements

If very short lifetimes are measured using the RDDS method, Doppler-shift attenuation (DSA) effects have to be taken into account [3]. Since the slowing-down of the recoiling nuclei in the stopper foil is not instantaneous, a finite stopping time exists where the recoils already entered the stopper foil but are still in motion.  $\gamma$ -rays from decays happening during the slowing-down phase will therefore be observed with a (reduced) Doppler-shift in the detector, leading to non-Gaussian peak forms where the unshifted peak receives a tail in the direction of the Doppler-shifted peak. If Gaussian fits are still used for the analysis, the decays during the slowing-down effects are partly counted towards the shifted peak, even if the recoils already penetrated the stopper foil. Furthermore, if  $\gamma$ - $\gamma$  coincidences and a gate on the flight component of a feeding transition are used, recoils that have already entered the stopper but have not slowed down completely can contaminate the gate. For lifetimes which are long compared to the stopping time, this effect is negligible because the number of decays happening during the slowing-down process is small. If, however, the stopping time is comparable to the lifetime that shall be measured, the DSA effect highly influences the obtained lifetime. A simulated spectrum where the DSA effect on the lineshapes of the peaks is visualized is shown in Fig. 4. A more detailed description of the DSA effect on RDDS measurements is given in Ref. [3] and references therein.

One possibility to analyze lifetimes obscured by the DSA effect is the use of simulations that reproduce the experimental circumstances. Spectra, produced by this type of simulations can then be compared to the experimentally obtained ones to extract the lifetime of the state of interest. The main issue regarding the correct simulation of the DSA effect is the knowledge about the correct stopping powers. The stopping power consists of nuclear and electronic stopping powers and has not been measured with the necessary precision for all combination of nuclei. Therefore, different (semi-)empiric formulas exist that calculate or extrapolate these stopping powers from measured ones (see, e.g., Ref. [19]). Depending on which formulas are used and how well the stopping powers are known, this might be the main source of uncertainty for such kinds of simulations.

One possibility to conduct DSA corrections with is the Geant4-based [20, 21, 22] simulation toolkit PTBG4 [8]. This simulation is fine-tuned to the Cologne plunger spectrometer to precisely simulate the experimental conditions, including the type and position of the detectors as well as their efficiency and resolution. The PTBG4 toolkit accepts the types and thicknesses of plunger foils, their separation, the reaction, the level scheme and the lifetimes of all simulated levels as input parameters. The reaction process itself is simulated, which includes the resulting velocity of the recoiling nuclei which is calculated from the initial transmission of kinetic energy from the reaction and the energy loss within the target foil. The stopping powers are taken from the SRIM database [23]. While the PTBG4 toolkit is very capable of producing realistic spectra for many types of reactions with this approach, one major drawback exists: If the calculated velocity



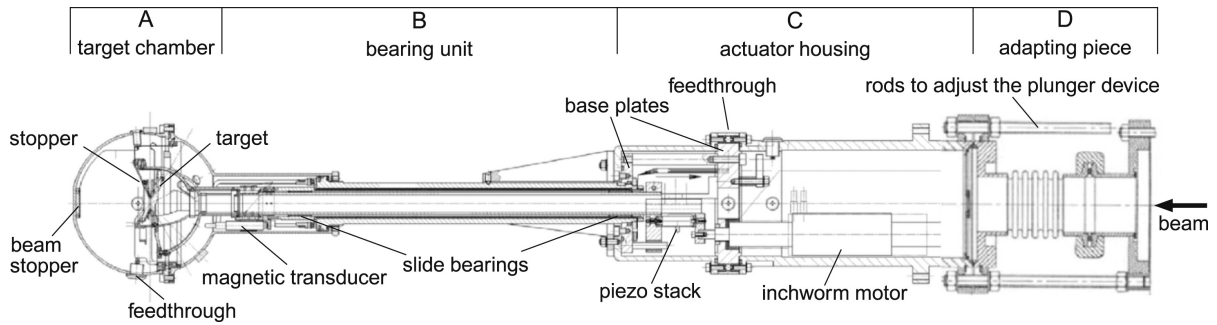
**Figure 4:** Visualization of the influence of DSA effects on the lineshape of the unshifted and the shifted peak in a RDDS measurement. The spectrum was obtained using the PTBG4 simulation toolkit [8] to simulate the decay of the  $2^+$  state from the lifetime measurement on  $^{60}\text{Ni}$  described in chapter 6.

from the simulation does not match the experimentally observed velocity there is no direct way to fine-tune the simulation to the experiment.

The prerequisite for using PTBG4 (or any simulation) to analyze the lifetime of a state is to fix the feeding of this state. Since it is likely that the feeding pattern including all lifetimes and branching ratios is not entirely known, it is necessary and convenient to use effective lifetimes of the states feeding into the state of interest. These will include all lifetimes of higher-lying states branching into the feeding state. If  $\gamma$ - $\gamma$  coincidences can be used for the experimental data to fix the feeding path, one effective lifetime of the direct or indirect feeder of the selected cascade is sufficient to describe the feeding of the state of interest. For singles data, however, effective lifetimes of all feeders together with their initial populations and branching ratios into the state of interest have to be determined.

As a good case to benchmark the PTBG4 simulation toolkit, a measurement on  $^{60}\text{Ni}$  conducted in Cologne was chosen. The  $2_1^+$  state in this nucleus exhibits several features that make it a valuable test case for the usage of the simulation: The lifetime of the state is known from several past experiments <sup>5</sup> to be very short ( $\approx 1\text{ps}$ ) and is therefore very likely heavily influenced by DSA effects. Moreover, the  $2_1^+ \rightarrow 0_1^+$  transition has a high energy of 1332 keV. This, together with a relatively large recoil velocity of the  $^{60}\text{Ni}$  nuclei of about 2% $c$ , leads to a large Doppler-shift

<sup>5</sup>Some of these lifetime measurements disagree with each other, as is explained in detail in chapter 6. However, a recent Coulomb excitation measurement that gives a very precise  $B(E2)(0_1^+ \rightarrow 2_1^+)$  value also measured transition strengths in neighboring nuclei and shows very good agreement to literature values in these nuclei [24]. It can therefore be used as a trustworthy comparison.



**Figure 5:** Model of the Cologne Coincidence plunger. The target chamber (A), where target and stopper foil are located, is separated from the motor via a large bearing unit (B). Picture taken from Ref. [3].

and therefore to a good separation of the shifted and the unshifted peak. Thus, the effect of the Doppler-shift attenuation should be clearly visible in the  $\gamma$ -ray spectrum. The analysis of  $^{60}\text{Ni}$  will be presented in chapter 6, where also the results of the simulation with the PTBG4 toolkit are shown.

## 1.2 The Plunger apparatus

The apparatus needed for RDDS experiments, the plunger, is used to position the foils precisely at different separations and to keep these separations constant during a measurement. For the setting of the foil distances, most modern plungers use piezo motors, which can obtain reliable step widths in the range of a hundred nanometers. The process of keeping the distance constant is handled by a feedback system. It is needed to account for slow changes of the foil surfaces in the beam, e.g. due to thermal effects. Modern-day plungers use the capacitance method for this task, as first presented by Alexander and Bell [18]. Briefly summarized, an electric signal is fed to one plunger foil. The two plunger foils together will then act as a plate capacitor and thus a voltage is induced in the second foil. The amplitude of this induced voltage depends on the distance between both foils following the capacitance of a plate capacitor:

$$C_{plate} \propto \frac{A}{d} \quad (12)$$

where  $A$  is the area of the plates and  $d$  is the distance between the plates. By measuring changes in the capacitance via the induced voltage, a feedback system is able to detect changes in the distance between the foils. For this feedback system and other complementary tasks around setting up and running a plunger measurement, sophisticated control software is needed. The capacitance method can also be used to obtain absolute distances. A comprehensive overview about this method will be given in chapter 4.

For the required distance adjustments for the feedback system, many plunger designs rely on an additional piezo stack. However, it can also be viable to use the piezo motor for this task as well.

The design of the Cologne Coincidence Plunger [3], which has been used for the lifetime measurements on  $^{144}\text{Ce}$  and  $^{60}\text{Ni}$  that will be presented in this thesis, is shown in Fig. 5. The most

prominent design feature of this plunger is the separation of the target chamber from the actuator housing (motor, piezo stack) via a large bearing unit. This ensures a minimum of material in the chamber itself and therefore minimizes the unwanted absorption of  $\gamma$ -rays. Additionally, the  $\gamma$ -ray detector can be positioned very closely because the chamber is small, thus further increasing the efficiency. Other features include an additional piezo stack which is used for the feedback system while the motor is solely used for changing the distances and an inductive probe in the target chamber to measure relative distances independently of the built-in sensor of the motor.

### 1.2.1 Compact Plunger designs

To perform the required tasks, a plunger apparatus relies heavily on very precise step motors to be able to set foil separations in the micrometer range. In the last years, much smaller motors of this kind have become commercially available. Especially, very small linear stages offer advantages for the design of plunger devices. In existing plunger designs like the Cologne Coincidence Plunger the motor is placed upstream of the actual plunger foils and is connected to them via a very precise bearing unit as described above. The modern linear stages, however, are self-guided and small enough to be placed directly inside of the reaction chamber. Therefore, the movable foil holders can be mounted directly on top of them. Plungers based on this design can thus be of a very compact size, opening up the possibility to place them inside of surrounding particle detector arrays like Microball [6] or JYtube<sup>6</sup>. The first compact plunger of this type built in Cologne was the GALILEO plunger [26], built for the Ge-detector array of the same name at the Laboratori Nazionali di Legnaro (LNL). Next to the advantages already mentioned, this new design also significantly simplifies the manufacturing of new plungers. Furthermore, the handling of the plunger during the preparation of an experiment becomes easier, because tasks like mounting and aligning the foils can be done at tabletop due to the much simpler process of removing the plunger from the beam line.

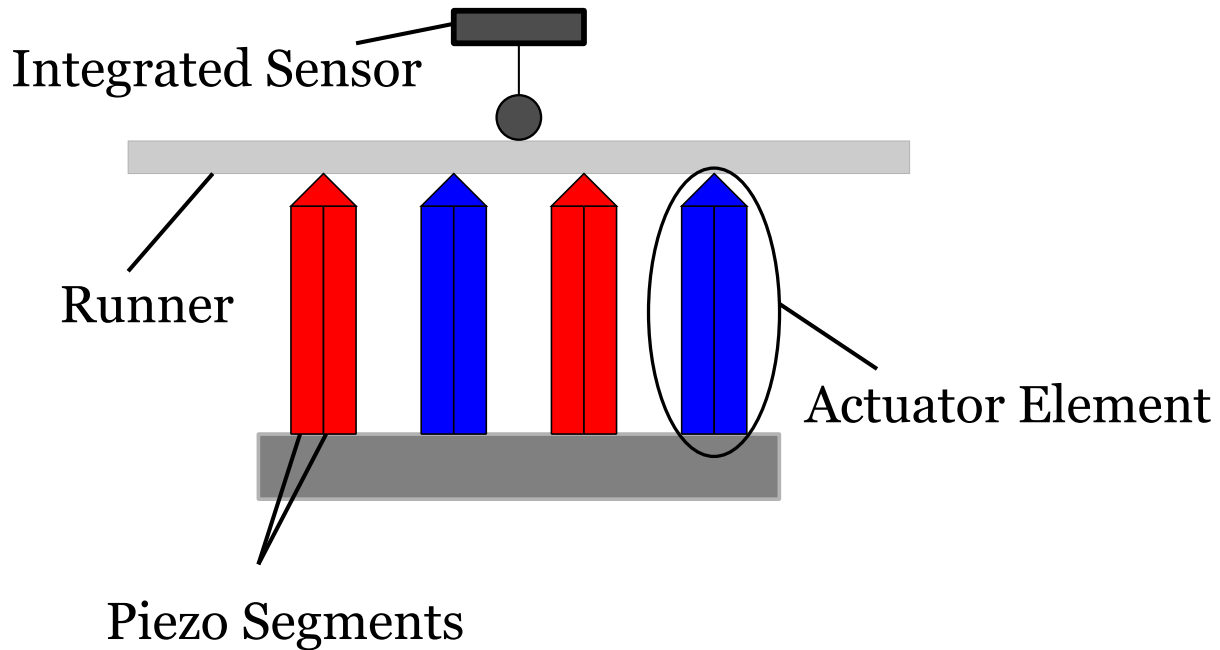
Since no additional piezo stack for the feedback is installed in the compact plunger design, the precision and the smallest possible step width of the piezo motor are of especially high importance. For setting the desired distances, a step width and precision of about  $0.5\text{-}1\mu\text{m}$  is sufficient. However, if it is desired to keep the distance constant within a precision range of  $\delta x < 0.5\mu\text{m}$ , which is easily achievable with the capacitance method at small distances, the smallest possible step size has to be at least  $< \delta x/2$  to ensure that corrective moves within the range are possible. To understand the challenges caused by this requirement, in the following a short overview of the functionality of the type of piezo motors by the company *Physik Instrumente*(PI) that are used in the plungers designed in Cologne will be given.

The PI piezo motor uses so-called NEXACT<sup>®</sup> modules to perform movements with down to about hundred nanometer step widths [28]. They consist of multiple actuators which belong to two groups. Each actuator is built up by two separate piezo segments (see Fig. 6). To move the runner, a walk-like movement is performed: By applying different voltages to each of the two

---

<sup>6</sup>A further development based on the older UoYTube detector [25]



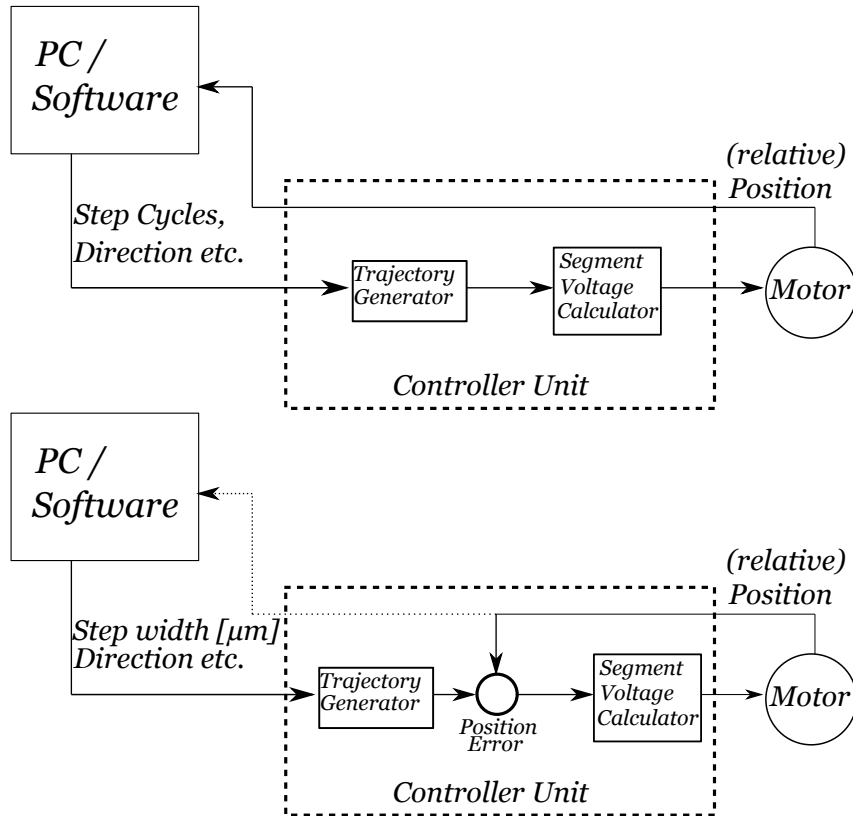


**Figure 6:** Model of a NEXACT<sup>®</sup> module from a PI piezo motor. The actuator elements belong to two distinct groups, marked here in red and blue. The mode shown here is the locked position where the runner is held in place by all actuator elements. For details about the movement process see text. Figure adapted and redrawn from [27].

piezo segments in an actuator, it will bend either to the left or to the right, taking the runner along. Afterwards, both elements will receive voltages that trigger a compression of the crystals, causing a loss of contact between actuator and runner. In this contact-less state, the actuator can then bend in the opposite direction, extend again to reestablish contact and bend in the direction of the movement again. Repeating this process, the runner is moved step-by-step to the desired position. To accelerate the movement, two groups of actuators are used that can work with a matching phase shift making the movement nearly constant. If the desired position is reached, all actuators will extend and hold the runner in place. The movement range of such a motor is in principle only limited by the length of the runner.

There are two modes to operate the motor: Open-loop and closed-loop operation (see Fig. 7). In the first, the desired movement is given in step cycles. The motor controller calculates the corresponding voltages that will be given to the piezo elements and give back the new (relative) position of the runner after the movement. A step cycle, however, does not imply the same travel distance each time. This will depend on several factors, like the load and the position of the runner and also on effects like abrasion during the lifetime of the motor. In closed-loop operation, on the other hand, the dimensions of the movement are given in physical units, e.g. in  $\mu\text{m}$ . The firmware of the motor controller will then automatically carry out the needed amount of step cycles in a feedback loop with the integrated sensor. In the motor type used for the newly developed compact plungers, for this an optical sensor with a resolution of 4nm is built into the motor housing.

For a compact plunger, where the motor drives the feedback system, it is, due to the mentioned



**Figure 7:** Representation of the open-loop (top) and closed-loop (bottom) operation modes. Simplified and redrawn from Ref. [28].

disadvantages of the open-loop mode, favorable to use the closed-loop mode for the motor control. Since a physical step width can be chosen, it will be easy to adjust the feedback step width to a sufficiently small value to run the feedback system with a very high precision, while the same task proves more difficult with the open-loop operation, because the step width will not necessarily be constant over the course of the experiment and at different distances.

The existing plunger control software for the Cologne Coincidence Plunger is built upon the usage of the open-loop operation mode, since the requirements on the precision are lower due to the additional piezo stack that is used for the feedback system. However, the same software has until now also been used for the compact GALILEO plunger. In practice, this has led to situations during several experiments with the GALILEO plunger, where the precision of the feedback system had to be decreased even if a higher precision would have been possible with the capacitance method. For the compact differential (three-foil) plunger that was constructed during this thesis, it was therefore desirable to create a new control software as well that utilizes the closed-loop approach to drastically increase the reliability and precision of the feedback system. The design and commissioning of this new plunger as well as the new software will be described in chapter 3.

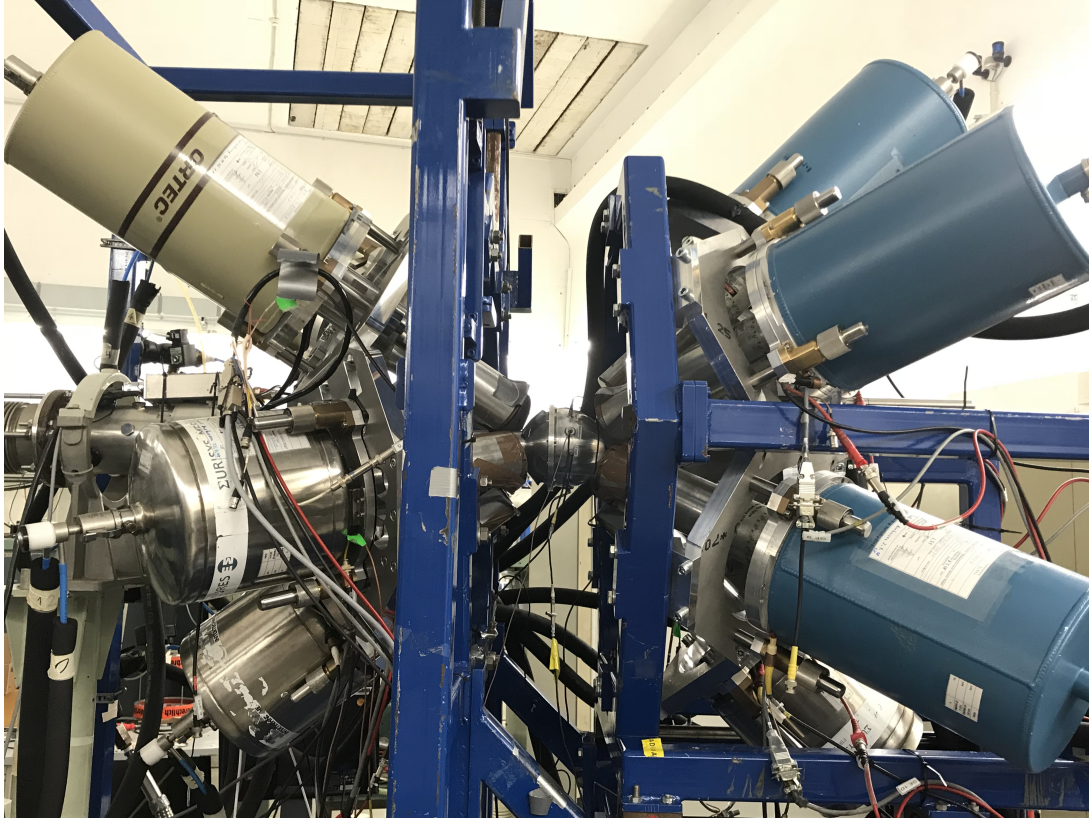


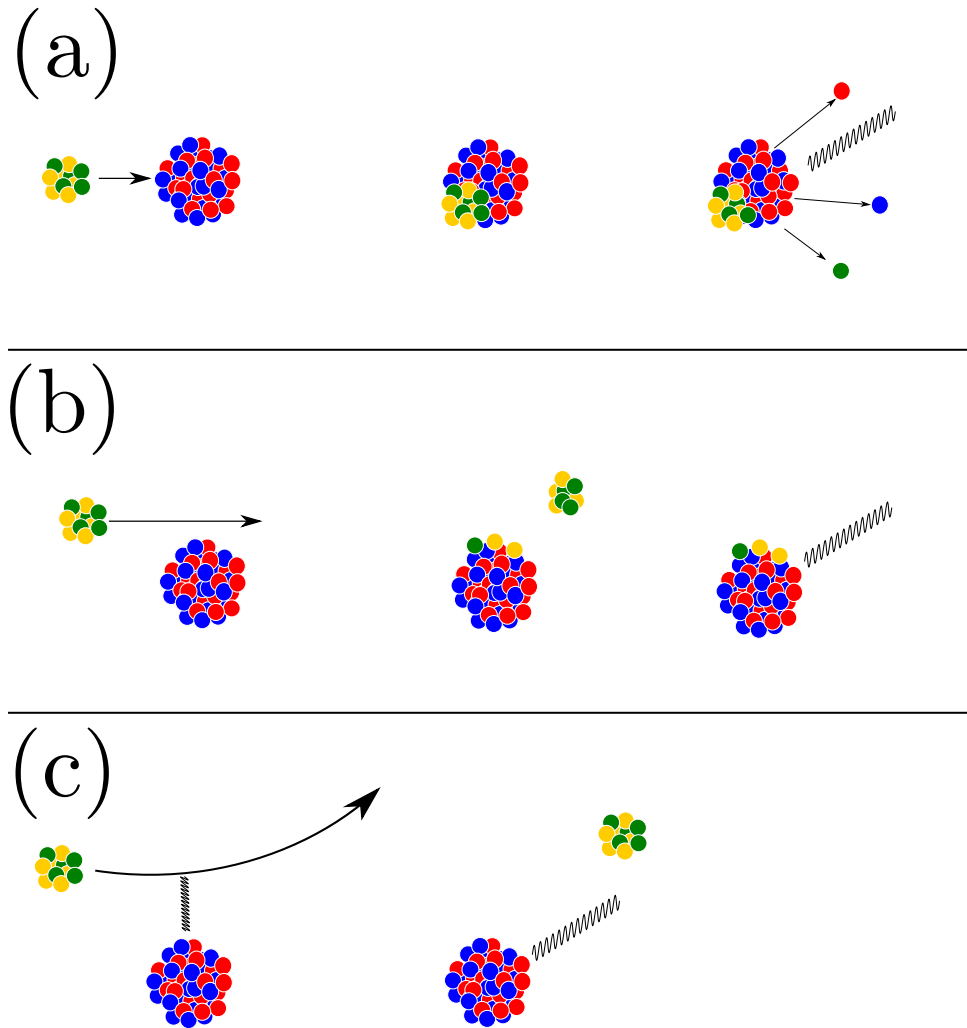
Figure 8: The Cologne plunger spectrometer with the Cologne Coincidence Plunger mounted inside.

### 1.3 The experiments at the Cologne FN tandem accelerator

The experiments reported on in this thesis have been carried out at the FN Tandem accelerator facility at the University of Cologne. There, stable ions can be accelerated with a terminal voltage of up to 10 MV to deliver very well focused beams with high intensity to the experimental stations.

For experiments using the RDDS method, the Cologne plunger spectrometer is used. It comprises two hemispheres consisting of 5 and 6 High-Purity Germanium (HPGe) detectors for the upstream and downstream hemispheres, respectively. The detectors are placed in two rings at  $142^\circ$  and  $45^\circ$  with respect to the beam axis. An additional single detector can be added at  $0^\circ$  if needed. Extreme angles are chosen to offer large Doppler shifts. The lifetime measurements on  $^{144}\text{Ce}$  and  $^{60}\text{Ni}$  presented in this thesis employed the Cologne Coincidence Plunger, which has been described in chapter 1.2. A picture of the plunger spectrometer with the Cologne Coincidence Plunger mounted inside is shown in Fig. 8. For the commissioning experiment of the new three-foil plunger, which also took place at the Cologne plunger spectrometer, a dedicated target chamber has been built to fit within the geometry of the spectrometer.

The experiments conducted in the frame of this thesis use different types of nuclear reactions to populate the nuclei of interest. In the following, a brief overview about these reactions will be given, with special focus on their specialties regarding RDDS measurements. A schematic overview of the different reaction types is shown in Fig. 9.



**Figure 9:** Schematic drawing of different reaction types: (a) Fusion-evaporation reaction. (b) Transfer reaction (stripping). (c) Coulomb excitation. The nuclei depicted in yellow and green represent the beam while the nuclei depicted in red and blue represent the target.

### Fusion-evaporation reaction experiments

Fusion-evaporation reactions are two-step processes, where projectile and target first fuse to a highly-excited compound nucleus which in turn evaporates light particles like single nucleons or, e.g., alpha-particles. A certain compound nucleus can decay via multiple different evaporation channels where each has a certain statistical probability based on the excitation energy and the available phase space [29]. During the fusion process, a large energy and angular momentum transfer occurs, leaving the compound nucleus with both high excitation energy and high angular momentum. Since the evaporated light particles carry away only little angular momentum, the resulting nucleus remains in a high-spin state and cascades down to the ground state via consecutive  $\gamma$ -ray transitions [30]. For  $\gamma$ -ray spectroscopy this consequently means that it is possible to observe a large number of transitions from excited states up to high spins and energies in a given nucleus by using fusion-evaporation reactions. At the same time, in even-even nuclei many transitions tend to lead to the ground state band (gsb) when they reach lower spins, often obscur-

ing low-lying non-yrast or non-gsb states. For lifetime measurements with the RDDS method, this property of fusion-evaporation reactions can also be problematic, because a large number of decays occurring before the transition of interest increases the feeding time and enhances the probability that long-lived feeding is present. Due to the possibility of very complex feeding patterns, the feeding of a state can be extremely hard to describe in a  $\gamma$ -singles experiment. However, the reaction cross sections of the experiments conducted using fusion-evaporation reactions at the FN Tandem accelerator in Cologne are typically large enough to enable the use of  $\gamma$ - $\gamma$  coincidences with energy gates on feeding transitions of the level of interest, where no feeding assumptions are needed if the DDCM is used for the analysis.

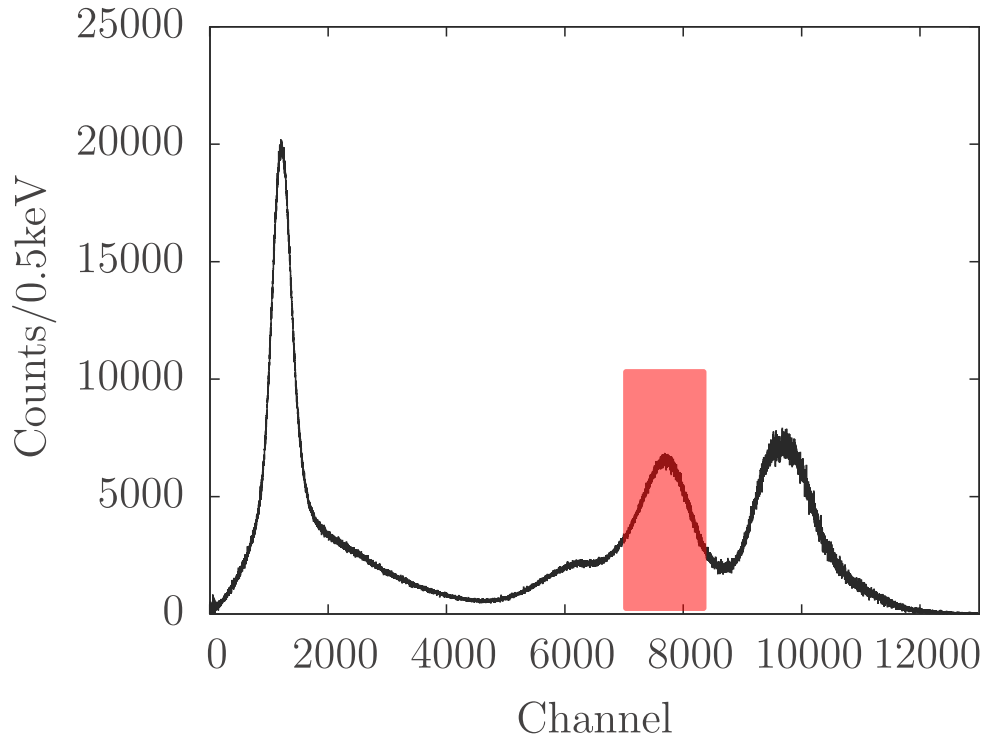
### **(Two-neutron) transfer reaction experiments**

In transfer reactions, the beam particles can either transfer nucleons to the target nucleus (stripping reaction) or gain nucleons from the target (pick-up reaction) [30]. In contrast to fusion-evaporation reactions, in transfer reactions only low amounts of energy and angular momentum are transferred to the resulting nucleus. This means that mostly low-energy, low-spin states get populated, leading to a  $\gamma$ -ray spectrum with comparably few transitions. Typically, the population of states decreases rapidly with increasing energy and spin. For RDDS measurements, this can help to circumvent problems with delayed feeding or high-lying isomers, which would render a measurement impossible if being populated. At the same time, transfer reactions are also better suited to study low-lying off-yrast states. For plunger measurements using the Cologne set-up, transfer reactions are normally conducted at beam energies slightly below the Coulomb barrier to avoid the opening of fusion-evaporation reaction channels, which can have much higher cross sections than the transfer channels and can therefore cause significant dead time in the  $\gamma$ -ray detectors and possibly lead to a high random background.

For the experiment to study lifetimes in  $^{144}\text{Ce}$ , a two-neutron transfer (stripping) reaction was used. A suitable reaction for many 2n transfer cases is ( $^{18}\text{O}, ^{16}\text{O}$ ), which was also utilized in this measurement.

For experiments using transfer reactions, an additional detector upstream of the target consisting of 6 solar cells is used in the Cologne plunger set-up to detect back-scattered reaction partners, e.g.  $^{16}\text{O}$  in the above mentioned reaction (see Fig. 1). This detection allows to set gates on this specific reaction which cleans the spectra significantly and at the same time fixes the kinematics of the reaction and only allows for fast recoils traveling in the direction of the stopper. However, it is not possible to distinguish between different isotopes (in this case  $^{16}\text{O}$  and  $^{18}\text{O}$ ) in the energy spectra of the solar cells which causes contaminations from Coulomb excitation reactions, where the beam particles are back-scattered into the solar cells. A typical solar cell spectrum from a reaction at the Cologne FN Tandem accelerator is shown in Fig.10.

The transfer reactions performed in Cologne (2n or  $\alpha$  transfer) mostly have cross sections of  $\lesssim 10$  mbarn. With the current set-up, it is therefore in most cases not possible to analyze particle- $\gamma$ - $\gamma$  gated spectra, where a gate is set on the back-scattered particle as well as on a certain  $\gamma$ -ray energy. Thus, contributions from feeding can not be excluded with gates on shifted feeder com-



**Figure 10:** Spectrum of backscattered particles from the reaction  $^{142}\text{Ce}(^{18}\text{O},^{16}\text{O})^{144}\text{Ce}$  detected with solar cells. A gate on  $^{16}\text{O}$  and  $^{18}\text{O}$  backscattered from the target is shown, which would return spectra containing  $^{144}\text{Ce}$  (2-n transfer) and  $^{142}\text{Ce}$  (Coulomb excitation). For details on this spectrum see chapter 5.

ponents and have to be considered in the analysis. However, due to the discussed restrictions on the number of excited states these feeding considerations are much easier than for comparable fusion-evaporation reactions.

### Coulomb excitation reaction experiments

During a Coulomb scattering process, where two nuclei interact via their respective Coulomb potentials, it is possible that not only the motion of the reaction partners changes but also some of the kinetic energy is converted into internal excitation energy of one or both reaction partners [29]. This process is called Coulomb excitation (CoulEx). Typically, CoulEx is used to measure transition strengths of low-lying (often off-yrast) states directly, by measuring their CoulEx cross section [31]. However, using CoulEx reactions for RDDS measurements has also significant advantages, e.g. if low-lying off-yrast states are targeted and no absolute  $\gamma$ -ray efficiencies or beam intensities are known, which are needed for a direct measurement via CoulEx. Another advantage is that one can make use of the large CoulEx cross sections, which is especially valuable for experiments with radioactive beams. In addition, for RDDS CoulEx measurements it is possible to conduct experiments very close or even above the Coulomb barrier to further increase the cross section [32].

For CoulEx RDDS measurements, the reaction kinematics have to be fixed in a similar way as for transfer reactions, to ensure that the recoiling excited nuclei have a sufficient velocity. Therefore,

typically particle detectors, like the above mentioned solar cell array, are used to detect the back-scattered projectile under extreme backward angles. Again, similar to the transfer reaction case, this also helps to significantly clean up the spectra from unwanted other reaction channels.

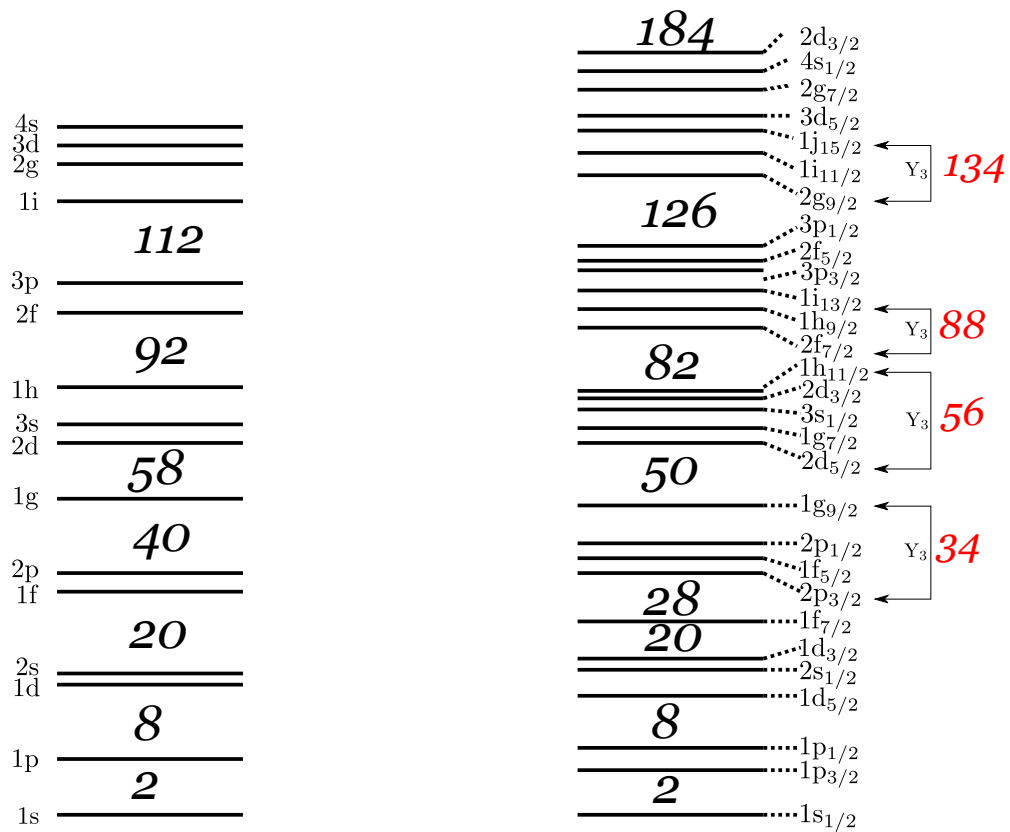
## 1.4 Theoretical approaches relevant for this thesis

### 1.4.1 The nuclear shell model

In this work, calculations performed on the basis of the nuclear shell model (NSM) are used to compare to the experimental findings for  $^{144}\text{Ce}$  and  $^{60}\text{Ni}$  and interpret these results. The respective physics cases of these nuclei are discussed in the corresponding chapters 5 and 6. Here, only a brief overview of the shell model will be given. For an extensive review of the shell model in general and the calculations needed to obtain predictions from it the reader is referred to Ref. [33].

The nuclear shell model is up to now one of the greatest gateways to understanding the structure of nuclei across the nuclear chart. A shell model, previously used to very successfully describe the structure of atoms in the quantum-mechanical framework, was first suggested to be applied to nuclei in the early 1930's. The motivation was to describe the observed large differences in stability, experimentally observed by the difference of neutron and/or proton separation energy, between neighboring nuclei [34]. The shell model is based on the suggestion that due to the Pauli principle the nucleons can move freely (without collisions with other nucleons) within the boundaries of the nucleus and the assumption that the interaction between all nucleons can be averaged to a central potential. This idea leads to the rise of discrete energy levels for neutrons and protons, the shells. These shells can be filled with a certain number of nucleons (again governed by the Pauli principle). Closed shells will then lead to especially stable nuclei compared to their neighbors with single nucleons or holes outside of the closed shell [34]. However, the first potentials applied for the calculation of the shell spacings failed to reproduce the experimentally observed, so-called "magic numbers" (2,8,20,28,50,82,126) for proton or neutron number, where nuclei appeared to be especially stable. Maria Goeppert-Mayer showed the existence of several of these magic numbers in her article "On Closed Shells in Nuclei" in 1948 [35]. Shortly after, Goeppert-Mayer [36] as well as Haxel, Jensen and Suess [37] independently found the solution to this problem by adding a spin-orbit coupling term to the potential. This term leads to a splitting of previously degenerate levels and therefore to a regrouping which is now in line with the magic numbers. From there onward, the shell model, while being constantly developed further, became very successful in describing and predicting nuclear structure in several regions of the nuclear chart. While many collective models emerged over time (first by A. Bohr and B. Mottelson [38], [39]), they still have to be compatible to the microscopic description of the shell model to be considered valid.

A simplified Hamiltonian for spherical nucleons in a self-created potential consisting only of



**Figure 11:** Energy levels of the shell model with an Woods-Saxon potential (left) and added spin-orbit term (right) with the resulting magic numbers. Additionally, octupole couplings between shells are shown in red. Fig. adopted from Refs. [34, 40].



2-body interactions can be given by

$$H = T + V = \sum_{i=1}^A \frac{\mathbf{p}_i^2}{2m_i} + \sum_{i>k=1}^A V_{ik}(\mathbf{r}_i - \mathbf{r}_k) \quad (13)$$

where  $V$  is the nucleon-nucleon potential [34]. Since this potential consists of 3-A position coordinates it is hard to solve for anything but the lightest nuclei. The shell-model approach of instead choosing a central potential can be included in the Hamiltonian to give

$$H = \sum_{i=1}^A \left[ \frac{\mathbf{p}_i^2}{2m_i} + U_i(\mathbf{r}) \right] + \sum_{i>k=1}^A V_{ik}(\mathbf{r}_i - \mathbf{r}_k) - \sum_{i=1}^A U_i(\mathbf{r}) \equiv H_0 + H_{residual} \quad (14)$$

where  $U_i(\mathbf{r})$  is a 1-body potential, which is chosen in a way that it combines the effects of all 2-body interactions [34].

A realistic potential is the Woods-Saxon potential [41], which is an intermediate form of the infinite well and the harmonic oscillator potential [42] with an additional spin-orbit term as explained above:

$$U(r) = \frac{-U_0}{1 + e^{\frac{r-R}{a}}} + U_{ls}(\ell \cdot \mathbf{s}) \quad (15)$$

where  $\ell$  is the orbital angular momentum and  $\mathbf{s}$  the spin.

Eq. 14 in combination with Eq. 15 is able to not only reproduce the magic numbers (see Fig. 11) but also to predict the structure of nuclei with only one particle outside of closed shells (or one hole), while treating  $H_{residual}$  only as a small perturbation. This so-called independent particle model [33], however, becomes rapidly less valid when one moves away from the magic numbers. For nuclei with multiple nucleons outside closed shells (or multiple holes),  $H_{residual}$  has to include the interactions between all these nucleons. Using the M-scheme, where the shells define a basis of Slater determinants, the solution of the Schrödinger equation to obtain the eigensolutions for the wave functions comes down to the diagonalization of matrices of the type  $\langle \Phi_l | H | \Phi_l' \rangle$  [33]. With multiple nucleons participating in the interaction process, the dimensions of these matrices quickly become extraordinary large and while their diagonalization is, in principle, a simple process it becomes extremely demanding on calculation power. In classical shell-model calculations, truncated model spaces are therefore used together with effective interactions derived from perturbation theory [43]. The model spaces normally include an inert core, typically a doubly-magic nucleus, which is assumed to not participate in the interactions. This approach has been employed in the calculations that are used later in this thesis to compare to experimental results. For example, for the calculations on  $^{50}\text{Cr}$  and  $^{60}\text{Ni}$ , doubly-magic  $^{40}\text{Ca}$  has been used as an inert core. Multiple (effective) interactions exist, which provide good results for different regions of the nuclear chart. For the  $pf$  shell, e.g., where  $^{50}\text{Cr}$  and  $^{60}\text{Ni}$  are situated, one of the standard interactions is GXPF1 [44], which is an empirical model based on the microscopic calculations by Hjorth-Jensen and the Bonn-C potential [45]. It uses two-body interaction matrix elements and was fitted to experimental data from 87 nuclei in the  $pf$  shell region [46]. Revised versions based on GXPF1 are GXPF1A [46] and

the slightly modified version GXPF1B [47]. Another interaction typically used for  $pf$  shell nuclei is KB3G [48]. In this thesis, shell model calculations done with these interactions are used to compare to experimental results from the nuclei  $^{60}\text{Ni}$  and  $^{50}\text{Cr}$ . An example of an interaction that can be used for heavier nuclei is the N3LOP effective interaction [49] which is a modification of the N3LO interaction derived from Chiral effective field theory potentials [50]. Calculations with this interaction yield good results for the region of neutron-rich lanthanides, where doubly-magic  $^{132}\text{Sn}$  is used as a closed core, and have therefore been used to compare to experimental results from the measurement of lifetimes in  $^{144}\text{Ce}$ .

Another approach that became viable with advances in computing power was the non-perturbative No Core Shell Model (NCSM) where, in principle, all nucleons are treated as active [51] and calculations are therefore done *ab initio*. Problems with phenomena like excitations of nuclei from the core can thus be avoided and unlike for perturbative approaches there are no difficulties related to the question of convergence.

A further approach that can also be combined with the NCSM is the Monte-Carlo shell model (MCSM), a stochastic approach to solve the Schrödinger equation faster [52]. A more recent extension for heavier nuclei is the Quasi-Particle Vacua shell model [53].

### 1.4.2 Octupole collectivity in nuclei

Octupole collectivity was already discussed in the nuclear structure community in the 1950's [54, 55]. In the framework of the shell model, octupole correlations are linked to a coupling between single-particle states with  $\Delta j = \Delta \ell = 3$  and are therefore strongest where such states exist in (energetic) proximity close to the fermi surface. This happens at nucleon numbers slightly above closed shells at the neutron/proton numbers 34,56,88 and 134, which are therefore sometimes called "octupole magic numbers"(see Fig. 11) [40]. In the last decades, compelling evidence for octupole collectivity close to these numbers could be gathered experimentally in different regions of the nuclear chart (see e.g. Refs. [9, 56, 57]). This led to an increased interest in this kind of deformation and made it to one of several "hot topics" in nuclear physics over the recent years.

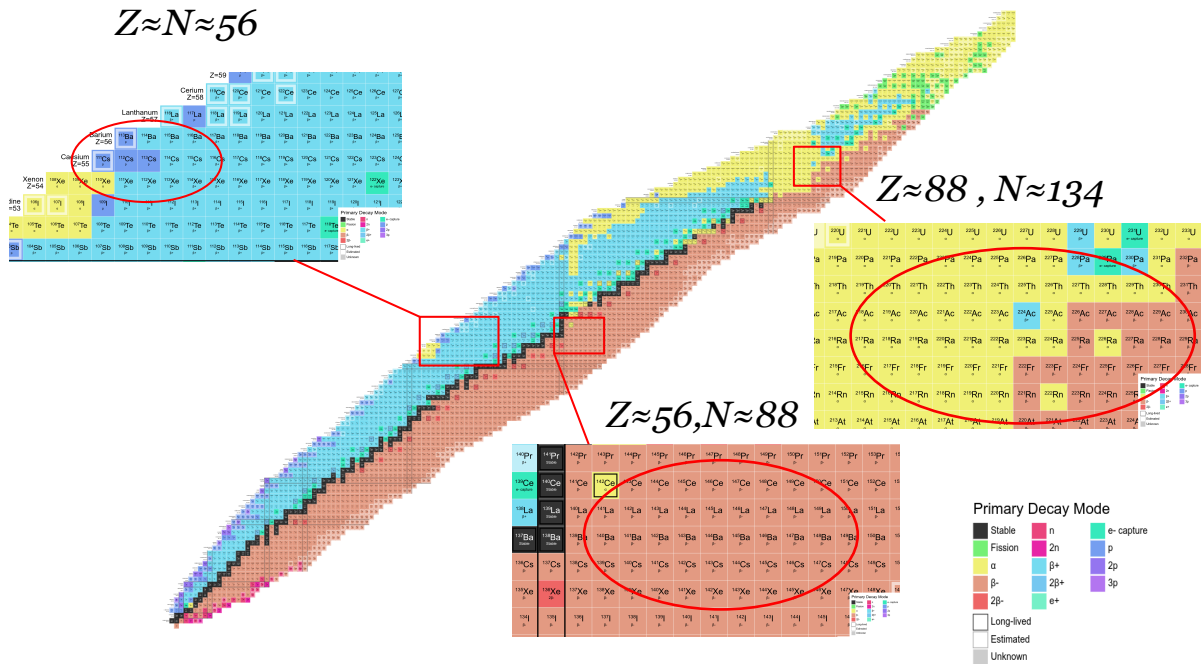
In general, octupole collectivity is linked to reflection-asymmetric forms of nuclei (so-called "pear shapes"). The following discussion will touch the theory of octupole deformation only slightly and will mostly be limited to even-even nuclei. For a more detailed review of this topic the reader is referred to Ref. [40] and references therein.

The surface or radius of a nucleus can be visualized in terms of spherical harmonic expansions  $Y$  [59]:

$$R(\theta, \Phi) = R_0 \left[ 1 + \sum_{\lambda, \mu} \alpha_{\lambda, \mu} Y_{\lambda}^{\mu}(\theta, \Phi) \right] \quad (16)$$

where  $R_0$  is the radius of the sphere representing the volume of the nucleus and  $\alpha_{\lambda, \mu}$  are the expansion coefficients. For axial symmetric bodies all coefficients with  $\mu \neq 0$  vanish. For deformed nuclei one can then define the deformation parameter

$$\beta_{\lambda} = \alpha_{\lambda 0} \quad \text{for } \lambda = 2, 3, 4, \dots \quad (17)$$



**Figure 12:** Some of the regions predicted by the octupole magic numbers where prominent experimental evidence for octupole deformation has been found. Figure created with graphics from [58].

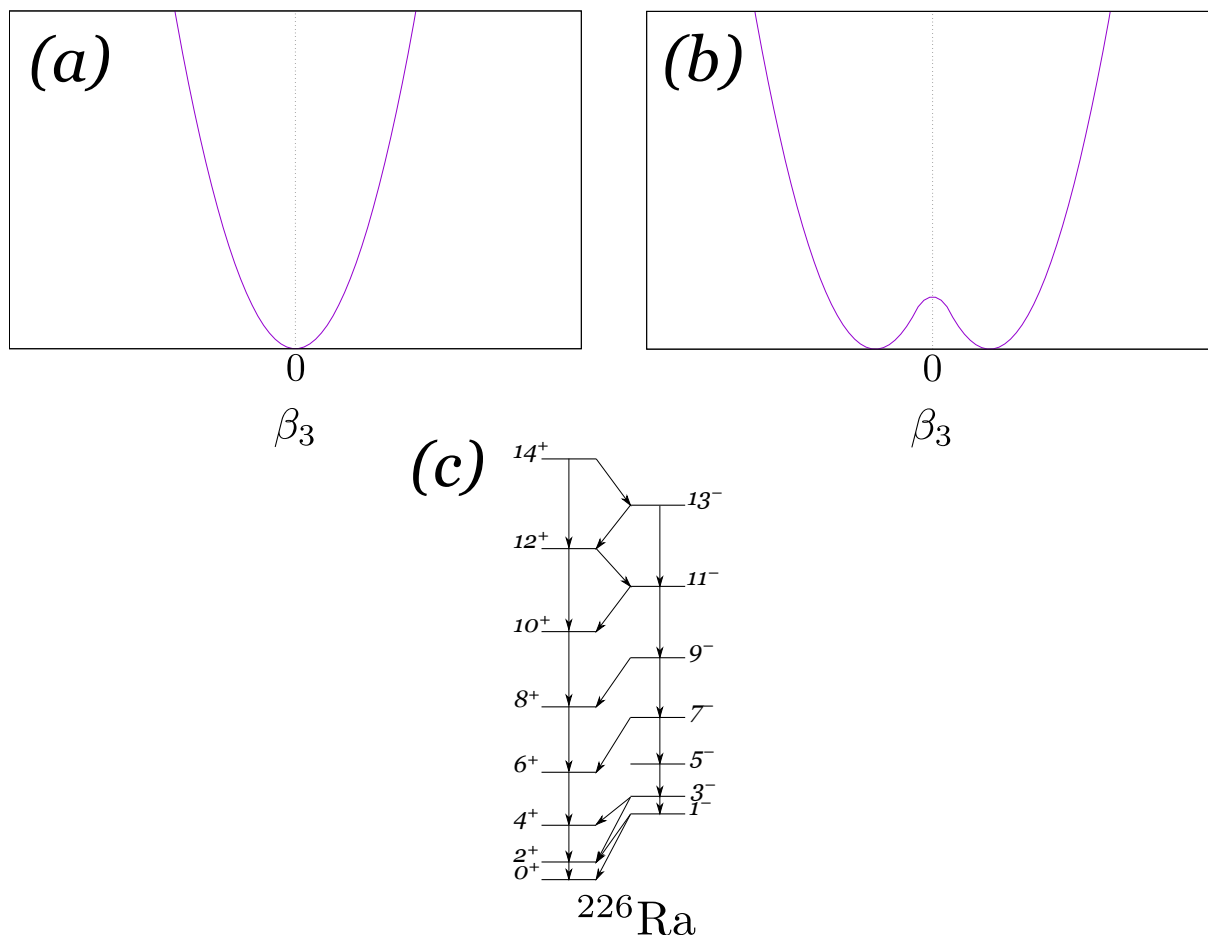
where  $\lambda=2$  represents quadrupole deformation,  $\lambda=3$  octupole deformation and so on [40].

In the collective framework, there are two basic possibilities for octupole collectivity in nuclei: On the one hand, octupole unstable nuclei, where the ground state is reflection symmetric but vibrations around a symmetric form at the octupole deformation parameter  $\beta_3=0$  can occur. In this case, the vibrational phonon with  $L=3\hbar$  can couple to the rotational angular momentum of the quadrupole deformed nucleus to create the typical level scheme of such nuclei. On the other hand, for nuclei with permanent octupole deformation  $\beta_3 \neq 0$  at the potential minimum. Potential energies with respect to  $\beta_3$  for both cases are shown in Fig. 13.

It can be shown, but is behind the scope of this thesis, that in both cases, low-lying negative-parity bands are the consequence [40]. In even-even nuclei, these typically form a molecule-like inter-spacing structure with the positive parity yrast band. A text-book example of a nucleus exhibiting these features is  $^{226}\text{Ra}$ , of which a level scheme is shown in Fig. 13. The precise structure can be used to obtain information about whether a nucleus exhibits a permanent octupole deformation or is an octupole vibrator. Following Refs. [40, 59], in the case of a permanent deformation, the angular momentum component that is aligned to the rotational axis of a positive and negative parity state ( $i_x^+$ ,  $i_x^-$ ) at the same rotational frequency  $\omega$  should be equal. An easy way to visualize this is by plotting

$$R(I) = \omega^-(I)/\omega^+(I) = 2 \frac{E(I+1)^- - E(I-1)^-}{E(I+2)^+ - E(I-2)^+} \quad \text{for even I,} \quad (18)$$

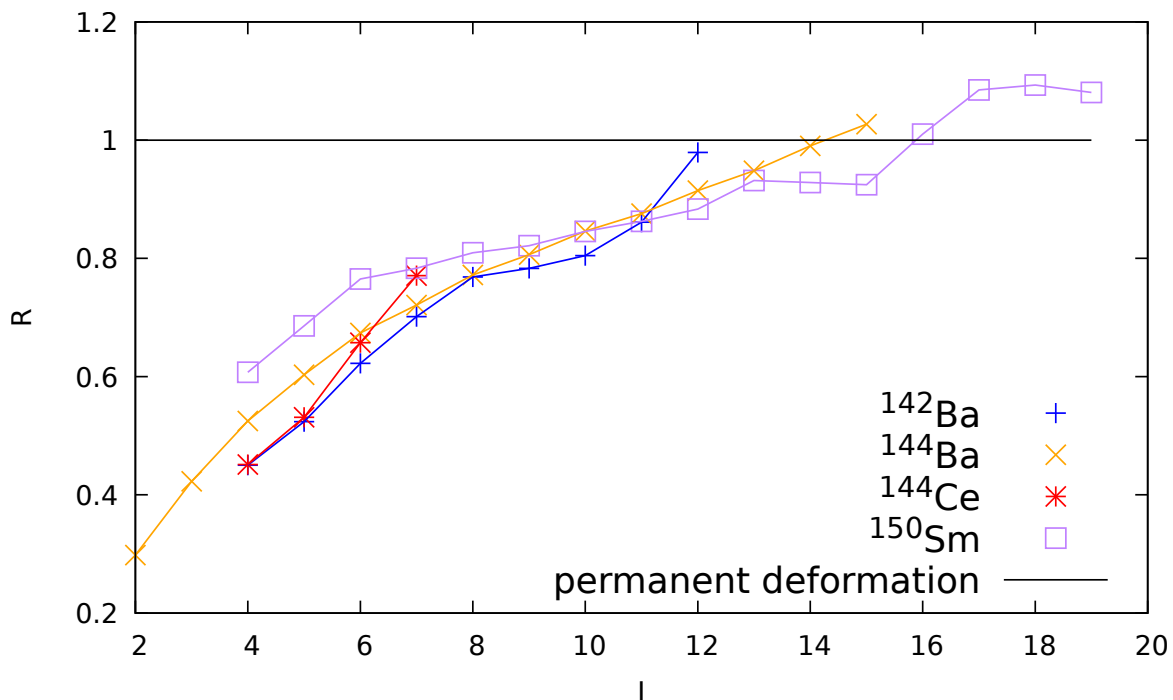
$$R(I) = \omega^-(I)/\omega^+(I) = 0.5 \frac{E(I+2)^- - E(I-2)^-}{E(I+1)^+ - E(I-1)^+} \quad \text{for odd I,} \quad (19)$$



**Figure 13:** (a) and (b) show examples for nuclear potentials as functions of the octupole deformation parameter  $\beta_3$  for a reflection symmetric nucleus where octupole vibrations are possible (a) and a nucleus with a stable octupole deformation (b). The stability of the deformation depends on the height of the potential barrier around  $\beta_3=0$ . Figure adapted and redrawn from Ref. [40]. (c) shows parts of the level scheme of  $^{226}\text{Ra}$ , which exhibits the typical characteristics of an octupole correlated nucleus: A low-lying negative-parity band interleaved with the positive-parity yrast band. The interleaving behavior continues at least up to the  $28^+$  state. Level energies and transitions taken from Ref. [60].

where  $R(I)$  should become  $\approx 1$  for stable octupole deformation [61]. However, no definitive evidence can be gathered from this.

Examples of different nuclei in the lanthanide region around  $N \approx 88$ ,  $Z \approx 56$  are shown in Fig. 14. It can be seen that e.g. for  $^{150}\text{Sm}$  the  $R$  value suggests a change from a reflection-symmetric form with octupole vibrations to stable octupole deformation at higher excitation energies around  $I \approx 16\hbar$ . For some of the nuclei shown there, e.g.  $^{144}\text{Ce}$ , information about the energy of higher spin states is missing, so no indication can be provided if a stable deformation is reached at some point.



**Figure 14:** Plot of  $R(I)$  for different nuclei in the lanthanide region around  $N=88$ .  $^{144}\text{Ba}$  reaches the characteristic value for stable octupole deformation at  $I=14\hbar$  and  $^{150}\text{Sm}$  at  $I=16\hbar$ . Excitation energies taken from Refs. [62],[63],[64],[65].

The most direct way to quantify octupole correlations in nuclei experimentally is the observation of octupole transitions with  $\Delta J=3$  and the measurement of the associated  $E3$  transition strengths. However, while being enhanced compared to non-octupole deformed nuclei, these transitions can still be largely suppressed in comparison to  $E2/E1$  transitions when decays are measured. Therefore, most direct measurements of  $E3$  transitions stem from Coulomb excitation experiments, often with radioactive beams, employing high-efficiency  $\gamma$ -ray spectrometers. The developments in the production of high-intensity radioactive ion beams at large-scale nuclear physics facilities are therefore one of the main reasons for the growing number of evidence for octupole deformation over the last decades (see, e.g., [56]).

Other important observables are the  $E1$  transition strengths between positive and negative-parity

bands. These dipole transitions correspond to the nuclear dipole moment

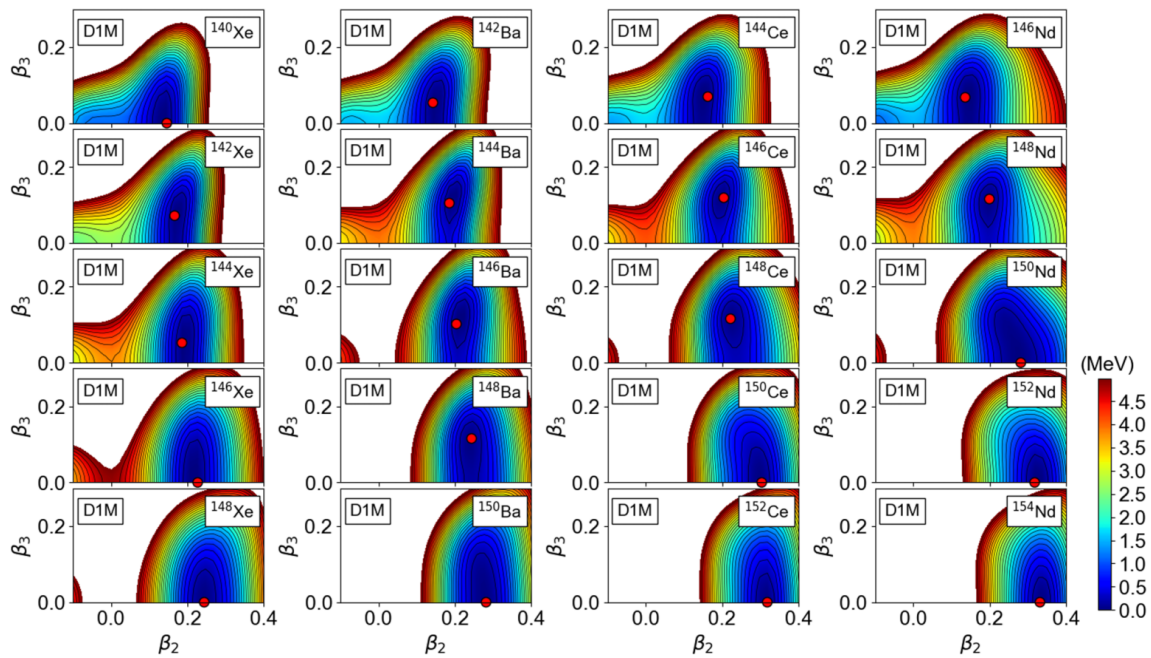
$$D_0^2 = \frac{4\pi}{3} B(E1) \frac{1}{\langle I_i 010 | I_f 0 \rangle^2} \quad (20)$$

where  $\langle I_i 010 | I_f 0 \rangle$  is the respective Clebsch-Gordan coefficient. Dipole moments are typically enhanced in reflection asymmetric nuclei, because the center-of-mass and center-of-charge can become separated [66].

Another very relevant topic, which is closely related to static octupole deformation, is the search for permanent atomic electric dipole moments (EDMs) [67]. The existence of such permanent EDMs in atoms would prove the violation of the basic symmetries T (time) and P (parity) and therefore, due to the CPT theorem, also a violation of CP. Although there are possibilities of CP violation in the standard model, this new kind of "flavor-diagonal" CP violation would be an evidence for beyond-standard-model physics [9]. In fact, this CP violation is required to explain the fact that there are more baryons than anti-baryons in the universe ("Sakharovs recipe" [68]).

Odd-A octupole-deformed nuclei have enlarged Schiff moments, which are the lowest observable moments in nuclei [69]. The Schiff moment, in turn, constitutes a large amount of the atomic EDM. Therefore, odd-A nuclei with stable octupole deformation are very good candidates for the first measurement of permanent EDMs and therefore the establishment of experimental limits for CP violation [67]. For more details about the theory and impact of EDMs the reader is referred to Ref. [70].

There are several regions formed by the "octupole magic numbers", where octupole correlations are expected and where experimental evidence could be gathered. Perhaps most prominent is the region of neutron-deficient actinides, i.e. the region around Ra, Rn and Th nuclei at  $A \approx 224$ . Here, the most textbook-like energy spectra for octupole deformed nuclei have been measured as well as some of the largest E3 transition strengths (see e.g. Refs. [60, 56, 71]). Another region is the one of neutron-deficient nuclei around  $^{112}\text{Ba}$ , where large E3 transition strengths have also been measured e.g. for  $^{114}\text{Xe}$  [57].



**Figure 15:** Potential energy surfaces for nuclei in the  $Z \approx 56$ ,  $N \approx 88$  region calculated with the Gogny-D1M EDF. Figure taken from Ref. [72].

The nucleus  $^{144}\text{Ce}$ , which has been investigated in this thesis, is part of the region around  $Z \approx 56$ ,  $N \approx 88$ , which consists of neutron-rich lanthanide nuclei. This region also includes several examples of nuclei where octupole deformation has been measured directly. The Ba chain around  $^{144,146}\text{Ba}$  is perhaps best known and shows some of the strongest octupole deformations yet measured [9, 73]. But also nuclei in the surrounding Xe, Nd and Ce chains show octupole characteristics, like the typical band structure. In a very recent theoretical study, potential energy surfaces (PES), calculated using the Gogny-D1M EDF [74], predict stable octupole deformation or softness in the octupole degree for many of these nuclei (see Fig. 15) [72]. One of these nuclei is  $^{144}_{58}\text{Ce}_{86}$ . Here the PES predicts already a minimum with  $\beta_3 \neq 0$  but with a general softness in the  $\beta_3$  regime.  $^{144,146}\text{Ba}$  and  $^{146}\text{Ce}$  are examples where a rigid deformation with  $\beta_3 \neq 0$  is predicted. A lifetime measurement of excited states in  $^{144}\text{Ce}$  is therefore very promising to gain insight into the onset of octupole deformation in this region.

## 2 Overview of the publications and contributions by the author

### Publication I:

#### Development of the multi-purpose Cologne Compact Differential Plunger (CoCoDiff) for the measurement of nuclear level lifetimes with the Recoil Distance Doppler-shift method

This paper reports on the development of a new compact three-foil plunger. It also presents the derivation of the application of the DDCM to data obtained in a three-foil plunger measurement and reports on a commissioning experiment with the new device, where lifetimes of excited states in  $^{50}\text{Cr}$  have been measured.

It is published in Nuclear Instruments and Methods in Physics Research A [16].

- M. Beckers wrote and tested the new software for the plunger.
- M. Beckers planned the commissioning experiment.
- M. Beckers set up the commissioning experiment with C. Fransen.
- M. Beckers performed the experiment.
- M. Beckers sorted the data.
- M. Beckers performed the lifetime analysis.
- M. Beckers wrote the paper.

### Publication II:

#### Revisiting the measurement of absolute foil-separation for RDDS measurements and introduction of an optical measurement method

This paper presents a new method to obtain absolute foil separations in plunger devices and demonstrates its precision by comparing it to the established method of determining these separations with the help of precisely known lifetimes in plunger measurements. It also presents a detailed overview of the most commonly used capacity method and its challenges and limitations. The new method helps increasing the precision of certain measurements with the new CoCoDiff plunger and other plunger devices.

The paper is published in Nuclear Instruments and Methods in Physics Research A [75].

- M. Beckers had the idea for the set-up and realized it in collaboration with S. Thiel and the mechanics workshop.
- M. Beckers performed the experiments with the sensor.
- M. Beckers set up the experiment on  $^{181}\text{Ta}$  with C. Fransen.



- M. Beckers participated in the experiment.
- L. Kornweibel sorted the data with help of M. Beckers, F. von Spee und C. Fransen.
- M. Beckers performed the analysis to obtain absolute distances.
- M. Beckers wrote the paper.

**Publication III:**

**Lifetime measurement of excited states in  $^{144}\text{Ce}$ : Enhanced E1 strengths in a candidate for octupole deformation**

This paper reports on a lifetime measurement in  $^{144}\text{Ce}$  using the RDDS method. A total of 4 level lifetimes as well as one effective lifetime could be measured. It also discusses the impact of the newly measured values, especially regarding the question if  $^{144}\text{Ce}$  exhibits properties of octupole deformation.

It is published in Physical Review C [14].

- C. Müller-Gatermann planned the experiment.
- M. Beckers participated in the experiment.
- M. Beckers sorted the data with help of C. Müller-Gatermann.
- M. Beckers performed the lifetime analysis.
- M. Beckers interpreted the results.
- M. Beckers wrote the paper.

**Publication IV:**

**Lifetime measurement of the  $2_1^+$ ,  $4_1^+$  states in semi-magic  $^{60}\text{Ni}$**

This paper presents results of a measurement of lifetimes in  $^{60}\text{Ni}$  with the RDDS method and discusses the impact of the measurement on the properties of the nucleus. This measurement was also utilized as a test case for the analysis of lifetimes influenced by the DSA effect using the simulation toolkit PTBG4.

It is published in The European Physical Journal A [76].

- K. Arnsward and C. Müller-Gatermann planned the experiment.
- M. Beckers participated in the experiment.
- M. Beckers sorted the data.

- M. Beckers performed the lifetime analysis.
- M. Beckers performed the simulations for the DSAM correction.
- M. Beckers interpreted the results.
- M. Beckers wrote the paper.

### **3 Publication I:**

**Development of the multi-purpose Cologne Compact Differential Plunger (CoCoDiff) for the measurement of nuclear level lifetimes with the Recoil Distance Doppler-shift method**





Contents lists available at ScienceDirect

## Nuclear Inst. and Methods in Physics Research, A

journal homepage: [www.elsevier.com/locate/nima](http://www.elsevier.com/locate/nima)

# Development of the multi-purpose Cologne Compact Differential Plunger (CoCoDiff) for the measurement of nuclear level lifetimes with the Recoil Distance Doppler-shift method

M. Beckers<sup>a,\*</sup>, A. Dewald<sup>a</sup>, C. Fransen<sup>a</sup>, K. Arnsward<sup>a</sup>, C. Müller-Gatermann<sup>b</sup>, F. von Spee<sup>a</sup><sup>a</sup> Institut für Kernphysik der Universität zu Köln, Zùlpicher Str. 77, D-50937 Köln, Germany<sup>b</sup> Argonne National Lab, Physics Division, 9700 S. Cass Av., Lemont, IL 60439, USA

## ARTICLE INFO

## Keywords:

Nuclear level lifetime measurement  
 Recoil-Distance Doppler-shift  
 Plunger  
 Nuclear structure  
 Differential plunger method  
 Differential decay curve method

## ABSTRACT

A new 3-foil plunger device, the Cologne Compact Differential (CoCoDiff) plunger has been built and commissioned. Due to its compact size, it can be used together with many different spectrometers and auxiliary detectors. As a commissioning experiment, level lifetimes of the  $2_1^+$  and the  $4_1^+$  excited states of  $^{50}\text{Cr}$  have been measured, using the Differential Decay Curve method (DDCM). A derivation is given on how this method can be applied to a differential plunger measurement, in order to measure distances for lifetimes from two different regions of sensitivity at the same time. The commissioning experiment took place at the Cologne FN tandem accelerator, using the reaction  $^{24}\text{Mg}(^{32}\text{S},4p2n)^{50}\text{Cr}$ . Lifetimes, deduced from this measurement, agree well with literature values from earlier measurements.

## 1. Introduction

Recoil-distance Doppler-shift (RDDS) based measurements are a widely used method to obtain level lifetimes of excited nuclear states experimentally. Transition strengths, derived from nuclear level lifetimes provide a versatile insight into nuclear structure. The differential decay curve method (DDCM) [1] provides versatile means to analyze data obtained by such measurements without the need to include any assumptions about non-observed feeding, if  $\gamma$ - $\gamma$  coincidence measurements are possible and a gate from above on a Doppler-shifted component of a feeding  $\gamma$ -ray transition is used. To conduct a RDDS measurement a plunger apparatus is used to vary the target-to-stopper-foil separation while the  $\gamma$  rays emitted of the decaying nuclear states are detected with a surrounding detector array. While the DDCM can be used in measurements with down to only three different distances, it is common to measure at a larger amount in order to decrease the uncertainties by providing more data points for the fit of the decay curve. If several level lifetimes, that differ in the order of magnitude, are targeted in one experiment, the need for significantly extensive beam times arises. In this case, a different set of distances has to be measured for every level lifetime, due to the difference in the region of sensitivity. Since recent experiments move further away from the valley of stability to more exotic regions, where the yields are low, beam times at large ion-beam facilities have to be used as efficient as possible. At this point, a variant of the standard plunger device, the differential or three-foil plunger, can significantly decrease the amount

of beam time needed to successfully conduct a RDDS measurement. On the one hand, it can be used to measure two distances simultaneously while on the other hand, it is also possible, under certain requirements, to use the differential plunger method to obtain lifetimes from a single set of distances. However, measuring with a three-foil plunger can also have possible downsides, the main one might be adding additional lines to a spectrum. In certain cases, where the line density is very high, this might complicate the analysis by making it more difficult to exclude contaminants. Therefore, the three-foil plunger technique does not aim to replace the two-foil plunger technique, but to offer additional versatility for cases, where its usage is preferable. In the recent years, some three-foil plunger devices have successfully been built and used, such as the Triple Plunger for Exotic Beams (TRIPLEX) [2].

In this paper, a new, multi-purpose plunger, the Cologne Compact Differential Plunger (CoCoDiff) is presented. This plunger is specifically designed to be as compact as possible, while still maintaining all requirements for precision. Furthermore a first successful experiment with the new device is presented, where level lifetimes in  $^{50}\text{Cr}$  have been (re-)measured as a proof of principle.

## 2. Design of the new plunger apparatus

The CoCoDiff plunger was designed under the following guidelines: The overall design philosophy was, to build the plunger as compact as possible to limit the amount of material shielding the detector

\* Corresponding author.

E-mail address: [mbeckers@ikp.uni-koeln.de](mailto:mbeckers@ikp.uni-koeln.de) (M. Beckers).

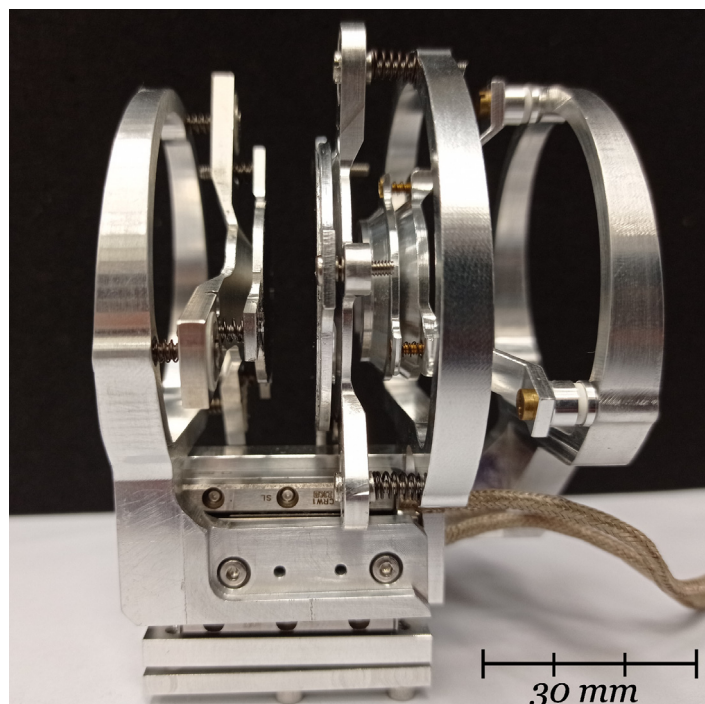


Fig. 1. The complete CoCoDiff plunger. From left to right the target, first degrader and second degrader are visible.

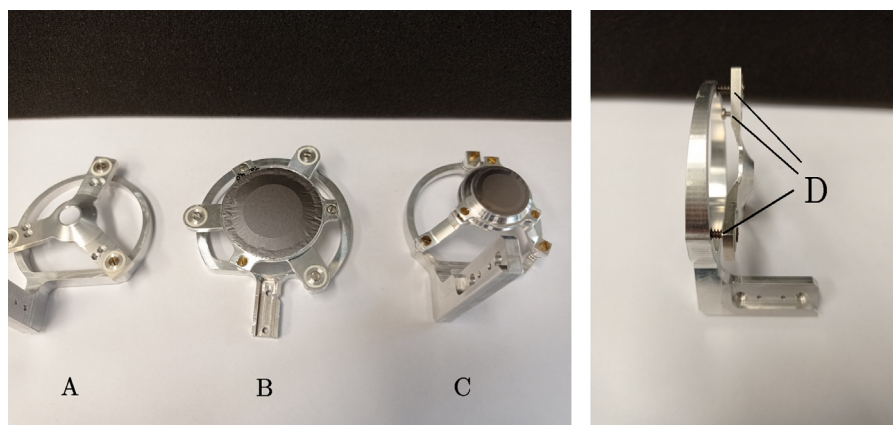


Fig. 2. Left: Cones for mounting the target (A), the first degrader (B) and the second degrader (C) foils on their respective holding structures. In the two later cases foils are stretched over the cones. (A) and (C) can be mounted on the linear stages while (B) is fixed between the other two. Right: Target cone viewed from the side, mounted on its holding structure on three equidistant points using springs and screws (D). These are used for the alignment process.

from the  $\gamma$ -rays. At the same time the small design should enable the plunger to be used in very different spectrometers, as well as together with a variety of auxiliary detectors. The complete plunger is shown in Fig. 1. Presently the plunger was tested at the Cologne Plunger Spectrometer. It is also compatible to the holding structure of the GALILEO Plunger [3] at the Istituto Nazionale di Fisica Nucleare Laboratori Nazionali di Legnaro (INFN-LNL), Italy. Further adapters and modifications are planned for the use together with the VAMOS++ spectrometer [4] at the Grand Accelérateur National d'Ions Lourds (GANIL) laboratory in France and the PRISMA spectrometer [5] also at INFN-LNL.

As the name suggests the new plunger comprises three foils: Target, first degrader and second degrader or stopper (from now on just called second degrader, even if it effectively stops the recoiling nuclei). All three of these need to have a plane surface and to be aligned in parallel to each other to ensure uniform distances between them. Therefore, at first the foils are stretched over cones using screws and springs (visible in Fig. 1, stretched foils shown in Fig. 2). The alignment procedure

can be done outside of the reaction chamber while the plunger is fixed to a support block, which eases the process. The alignment of the stretched foils is also done with adjustable springs and screws that are used to connect the cones to their respective holding structure at three equidistant points (see Fig. 2 D). The procedure is the following: First, the target and the second degrader foils are mounted. The second degrader cone is the only one that is fixed statically on its holding structure. The target foil is then optically aligned in parallel to the second degrader foil by moving these foils close together. After this, the first degrader is mounted, facing the target foil, and aligned in parallel to the target. During these steps, the alignment can also be checked using a distance calibration, where the induced voltage is measured against the foil separation. If the foils are well aligned, the resulting curve should become nearly linear for small distances.

For this process, as well as for measuring small distances in an experiment, it has to be possible to bring both the target and the second degrader in close contact with the first degrader foil. This is realized by constructing the first degrader foil much larger than the other two, so

that it is possible to fit the second degrader cone inside the cone of the first degrader. Additionally, the cone of the second degrader is very steep to ensure that only the stretched surfaces come into contact (see Fig. 2).

The target and the second degrader are directly fixed to two very compact precise motors (linear stage Q-521 from the company *Physik Instrumente* [6]), using holding structures with the least possible amount of material while still ensuring the needed stability. As the linear stages are placed directly below the foils, they shadow mostly only detectors at about 90° angle with respect to the beam axis, which are irrelevant for RDDS experiments. The position control and readout is solely achieved with the two linear stages.

It is possible to optionally mount particle detectors at the CoCoDiff plunger (solar cells or small silicon detectors) at a backward angle close to the target, which can be used to detect back-scattered reaction products if needed. A dedicated target chamber has been designed to use the CoCoDiff plunger at the Cologne FN Tandem accelerator and the Cologne Plunger Spectrometer.

Additionally, it is possible to mount a very precise optical distance sensor (KEYENCE CL-3000/L015 [7]), to the support block which can be used to precisely determine the absolute distances between the foils. The sensor and the measurement of absolute distances is explained in detail in [8]. Initially, the sensor is aligned to the center of the second degrader foil (or to the beam spot, if visible). After it has been fixed, the distance between the sensor and the second degrader foil is measured with very high precision. To account for surface roughness, the sensor measures an area of 300  $\mu\text{m}^2$  simultaneously. Therefore, the measured absolute distances are average distances for all recoils. Then, the second degrader foil is removed and the distance between sensor and first degrader foil is measured. The same goes for the target foil. Finally, for the second and first degrader foil, which are measured from the downstream facing side, the foil thicknesses have to be subtracted from the measurement. If the foil thicknesses are not known with the needed precision, they can be measured for example with a Rutherford backscattering spectroscopy (RBS) experiment. Another possibility is to use two of the above mentioned sensors, which can then be used to measure the thickness directly with very high precision. With this process it is possible to obtain the absolute foil separations with an uncertainty of 0.5–1  $\mu\text{m}$  after the measurement, while the commonly used capacitance method can introduce uncertainties up to about 5–10  $\mu\text{m}$  [8]. Since the knowledge of absolute distances is crucial for the use of a three-foil plunger in certain cases (see below) as well as for RDDS measurements where the DDCM cannot be used for the analysis, this improvement has a direct effect on the deduced lifetimes in these cases.

### 3. Development of the Cologne Plunger Software Package (CPSP)

The software package developed in Cologne (Plunger Feedback Control for Linux — PFCL) or adaptations of the same are used for several plunger devices around the world. It can be used to perform distance calibrations, adjust the distances in the plunger and keep them constant during an experiment with a feedback system in the case of for example thermal effects. This is done by applying an electric signal to one foil with a pulse generator and measuring the induced voltage at the other foil. This voltage depends on the capacitance between the foils which is, if stray capacitances are neglected, inversely proportional to the distance. In the case of a three-foil plunger, the signal has to be applied to the first degrader foil, which makes it possible to measure the induced signal at both the target and the second degrader foil individually. Details on this capacitance method can be found in Refs. [9,10]. As mentioned in Ref. [3], the software has been moved to Microsoft Windows® recently, in order to avoid problems with state-of-the-art versions of drivers from the company National Instruments used for the plunger control, which do not support Linux. For the CoCoDiff plunger, some parts of the software package have

been further adapted, to pay respect to the new type of motor that is used and the general design of the plunger. In older versions of the software, an “open-loop” approach was used to control the motor, where a certain voltage is applied to the motor via the software and the change in the distance is measured (for example with an additional distance probe). The new version uses a “closed-loop” approach, where the software directly gives the desired movement step in physical units and the motor controller’s firmware internally manages the applied voltage accordingly by using the included optical position measurement from the motor. This allows for overall more precise motion. This approach is also advantageous in case the motor suffers from abrasion or other negative effects during its lifetime. In this case, it could be seen for other motor types in the past, that while the same voltage was applied to the motor, the step width changed over time. The “closed-loop” approach should prevent this behavior. This also applies for effects caused by different behavior of the motor in air and in vacuum, respectively.

For the CoCoDiff plunger, the motor is used for the distance changes as well as for the feedback system. The later is further improved by the “closed-loop” approach, because it makes smaller movement steps possible. This makes the feedback of the new plunger as precise as older plunger devices like the Cologne Coincidence Plunger, which uses an additional piezo crystal stack for the feedback system [9].

Additionally, some minor functionalities and tools have been added to the package, for example software to include the above-mentioned optical sensor into the environment to automatically conduct the measurement of the absolute distances. Other features improve the fail-safety of the feedback system, for example by including a movement limiter that prevents the motor from damaging the foils if the measured voltage signal breaks down.

### 4. Lifetime measurement in $^{50}\text{Cr}$

As a first commissioning experiment, the new plunger was used at the FN Tandem accelerator of the University of Cologne to (re-)measure the lifetimes of the excited  $2_1^+$  and  $4_1^+$  states in  $^{50}\text{Cr}$ . The lifetime of the  $2_1^+$  state has been measured with good precision before (e.g.  $\tau_{2_1^+} = 13.3(6)\text{ps}$  [11],  $\tau_{2_1^+} = 13.0(4)\text{ps}$  [12],  $\tau_{2_1^+} = 13.2(4)\text{ps}$  [13]), so it provides a good testing case for the performance of the new device. In the case of the  $4_1^+$  state, disagreeing lifetime values from different measurements exist ( $\tau_{4_1^+} = 4.9(7)\text{ps}$  [11] and  $\tau_{4_1^+} = 2.5(7)\text{ps}$  [14]), which further motivates the new measurement, to help making a decision between contradicting values.

The nucleus of interest is populated by the fusion-evaporation reaction  $^{24}\text{Mg}(^{32}\text{S},4p2n)^{50}\text{Cr}$  with a beam energy of 100 MeV and an areal density of the self-supporting  $^{24}\text{Mg}$  target of  $0.6 \frac{\text{mg}}{\text{cm}^2}$ . The recoiling nuclei leave the target foil with an average velocity of  $\beta=v/c=3.9(1)\%$ . A first degrader consisting of Tantalum with an areal density of  $4.4 \frac{\text{mg}}{\text{cm}^2}$  decreased the average velocity to  $\beta=1.5(1)\%$ . The second degrader (stopper) also consisted of tantalum with an areal density of  $6.5 \frac{\text{mg}}{\text{cm}^2}$ , and stopped the recoiling nuclei. With this setup it is possible to obtain a difference in energy due to the Doppler shift, that is large enough to observe three distinct peaks in the  $\gamma$ -ray-energy spectra in the High Purity Germanium Detectors with relative efficiencies between 55% and 90%, that are arranged in two rings at 142.3° (5 detectors) and 45° (6 detectors) with respect to the beam axis, respectively. During the experiment a total of 9 different sets of distances has been measured, which leads to 18 different flight times in total. The distances range from 17  $\mu\text{m}$  to 750  $\mu\text{m}$  between the target and the first degrader and from 40  $\mu\text{m}$  to 335  $\mu\text{m}$  between the first and the second degrader. The distances have been chosen to match the region of sensitivity for measuring the lifetimes of the  $2_1^+$  and the  $4_1^+$  states in  $^{50}\text{Cr}$ . The main focus for the choice of distances was the analysis with the Differential Decay Curve Method (DDCM).

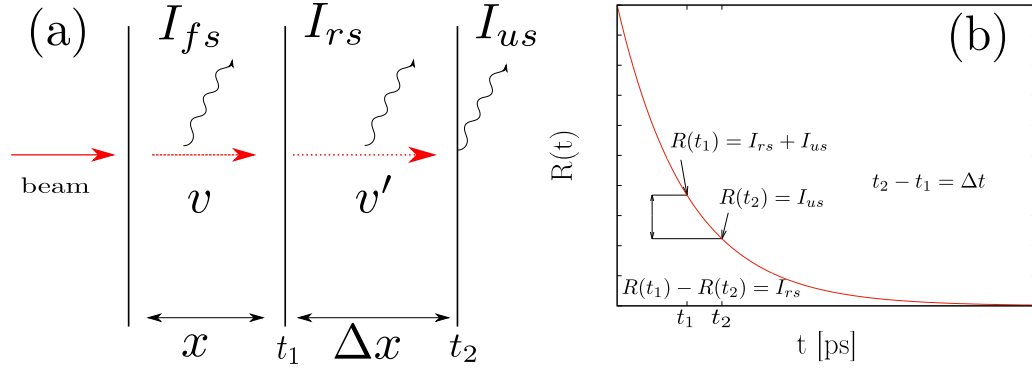


Fig. 3. (a) Schematic drawing of a three-foil plunger with relevant experimental quantities. (b) An example of a decay curve, where the experimentally available quantities are marked. The times  $t_1$  and  $t_2$  are the flight times where the recoil leaves the first degrader foil and enters the stopper foil, respectively.

#### 4.1. DDCM with a three-foil plunger and the differential plunger method

The DDCM [1,15] is a well-established way to analyze RDDS measurements. According to the DDCM, the level lifetime of an excited state can be obtained with the equation

$$\tau_i(x) = \frac{-R_i(x) + \sum_k b_{ki} \alpha_{ki} R_k(x)}{\frac{d}{dx} R_i(x)} \cdot \frac{1}{v} \quad (1)$$

where  $i$  is the state of interest,  $k$  are the states feeding  $i$  and  $R(x)$  is the decay curve of the respective state.  $b_{ki}$  are the branching ratios and  $\alpha_{ki}$  take into account the different detection efficiencies and angular correlations. The DDCM is especially useful for  $\gamma$ - $\gamma$  coincidence measurements. It can be shown, that for the case of a gate on the flight component of a direct feeder Eq. (1) simplifies to

$$\tau_i(x) = \frac{I_{(sh,us)}}{\frac{d}{dx} I_{(sh,sh)}} \cdot \frac{1}{v} \quad (2)$$

where  $I_{(sh,us)}$  and  $I_{(sh,sh)}$  are the intensities of the observed unshifted and shifted components coincident to the shifted component of the direct feeder, respectively.

Eq. (2), however, is not directly applicable for the case of a differential three-foil plunger. In this case, there are not two but three components:  $I_{us}$ ,  $I_{fs}$ ,  $I_{rs}$ , where the latter two are the fully and the reduced shifted component, respectively. The reduced shifted component originates from decays happening between the first and the second degrader (see Fig. 3(a)). One set of plunger distances  $x$  and  $\Delta x$  therefore provides two points on the non-normalized decay curve of a certain state:

$$R(t_1) = I_{us} + I_{rs} \quad R(t_2) = I_{us} \quad (3)$$

where  $t_1$  is the time by which the recoiling nucleus enters the first degrader ( $\frac{x}{v}$ ) and  $t_2$  the time it enters the second degrader ( $\frac{x}{v} + \frac{\Delta x}{v}$ ) (see Fig. 3(b)).

To again obtain a simplified formula for the DDCM to use with  $\gamma$ - $\gamma$  coincidences, both points have to be taken into account separately. For this treatment the same notation as in Ref. [9] will be used, where  $\{Y, X\}$  denotes the coincident intensities between the populating transition  $Y$  and the depopulating transition  $X$  of a state and  $X_m^n$  are the transitions occurring in the time interval between  $t_m$  and  $t_n$  with  $t_n > t_m$ . In the case of a three-foil plunger one gets

$$\begin{aligned} \{Y, X\} = \{Y_0^\infty, X_0^\infty\} = & \{Y_0^{t_1}, X_0^{t_1}\} + \{Y_0^{t_2}, X_0^{t_2}\} + \{Y_0^\infty, X_0^\infty\} \\ & + \{Y_{t_1}^{t_2}, X_{t_1}^{t_2}\} + \{Y_{t_1}^{t_2}, X_{t_1}^\infty\} \\ & + \{Y_{t_2}^\infty, X_{t_1}^{t_1}\} + \{Y_{t_2}^\infty, X_{t_1}^{t_2}\} + \{Y_{t_2}^\infty, X_{t_2}^\infty\}. \end{aligned} \quad (4)$$

The order in time gives

$$\{Y_{t_1}^{t_2}, X_0^{t_1}\} = \{Y_{t_2}^\infty, X_0^{t_1}\} = \{Y_{t_2}^\infty, X_{t_1}^{t_2}\} = 0. \quad (5)$$

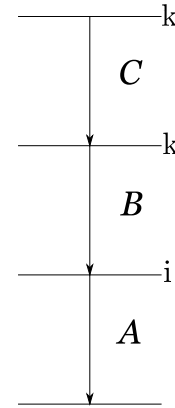


Fig. 4. Cascade of decays.

Therefore Eq. (4) can be rewritten as

$$\{Y_0^\infty, X_0^\infty\} = \{Y_0^{t_1}, X_0^{t_1}\} + \{Y_0^{t_2}, X_{t_1}^{t_2}\} + \{Y_0^\infty, X_{t_2}^\infty\}. \quad (6)$$

Since  $\{Y_0^\infty, X_0^\infty\}$  is time-independent Eq. (6) gives the relation

$$\frac{d}{dt} (\{Y_0^{t_1}, X_0^{t_1}\} + \{Y_0^{t_2}, X_{t_1}^{t_2}\} + \{Y_0^\infty, X_{t_2}^\infty\}) = 0 \quad (7)$$

This can be rewritten as

$$\frac{d}{dt} \{Y_0^\infty, X_{t_1}^\infty\} = -\frac{d}{dt} \{Y_0^{t_1}, X_0^{t_1}\} \quad (8)$$

where the left side is equal to the time derivative of the non-normalized decay curve at time  $t_1$  for decays via transition  $X$  in coincidence with transition  $Y$  and therefore equal to the denominator of Eq. (1) for  $t_1$ ,  $\frac{d}{dt} R_i(t_1)$ .

Equivalently, for  $t_2$  Eq. (7) can be rewritten as

$$\frac{d}{dt} R_i(t_2) = \frac{d}{dt} \{Y_0^\infty, X_{t_2}^\infty\} = -\frac{d}{dt} \{Y_0^{t_2}, X_{t_1}^{t_2}\} \quad (9)$$

For the numerator of Eq. (1) we need to distinguish two cases for a cascade as displayed in Fig. 4, a gate on a direct feeder (B) and on an indirect feeder (C), respectively. For the first case ( $Y = B, X = A$ ), we obtain analog to the argument for the direct gate in the classical DDCM from Ref. [9] in the above notation:

$$\begin{aligned} -R_i(t_1) + b_{ki} \alpha_{ki} R_k(t_1) = & \\ -\{B_0^\infty, A_{t_2}^\infty\} - \{B_0^\infty, A_{t_1}^{t_2}\} + \{B_{t_2}^\infty, A_0^\infty\} + \{B_{t_1}^{t_2}, A_0^\infty\} \end{aligned} \quad (10)$$

which simplifies to

$$-\{B_0^{t_1}, A_{t_1}^\infty\} = -I_{(fs,rs+us)}^A \quad (11)$$

The same calculation for  $t_2$  gives

$$-R_i(t_2) + b_{ki} \alpha_{ki} R_k(t_2) = -\{B_0^{t_2}, A_{t_2}^\infty\} = I_{(fs+rs,us)}^A \quad (12)$$



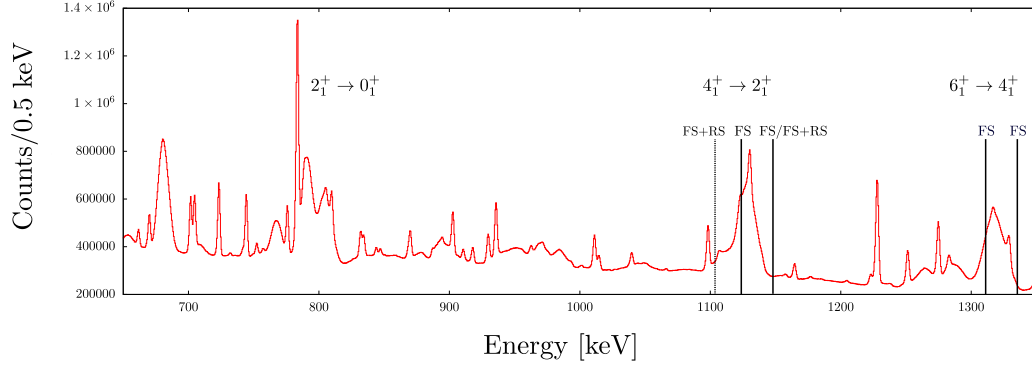


Fig. 5. Projection of the coincidence matrix obtained with detectors under forward angle, where the transitions of interest are marked. The gates, which have been used to obtain the spectra for the analysis, are indicated by lines. The solid lines mark the limits for the gates on the respective fully-shifted component while the dashed line marks the lower energy limit for the gate on the reduced-shifted and the fully-shifted component. See text for details.

Finally we obtain for the case of a gate on a direct feeder replacing the time-dependent notation with the respective transition component

$$\tau_i(t_1) = \frac{\{B_{f_s}, A_{rs+us}\}}{\frac{d}{dt}\{B_{f_s}, A_{f_s}\}} \quad \tau_i(t_2) = \frac{\{B_{f_s+rs}, A_{us}\}}{\frac{d}{dt}\{B_{f_s+rs}, A_{f_s+rs}\}} \quad (13)$$

where  $t_1 = x/v$  and  $t_2 = x/v + \Delta x/v'$ .

For the gate on an indirect feeder ( $Y = C, X = A$ ) we obtain in an analog way

$$\tau_i(t_1) = \frac{\{C_{f_s+rs}, A_{rs+us}\} - b_{ki}\alpha_{ki}\{C_{f_s+rs}, B_{rs+us}\}}{\frac{d}{dt}\{C_{f_s}, A_{f_s}\}} \quad (14)$$

$$\tau_i(t_2) = \frac{\{C_{f_s+rs}, A_{us}\} - b_{ki}\alpha_{ki}\{C_{f_s+rs}, B_{us}\}}{\frac{d}{dt}\{C_{f_s+rs}, A_{f_s+rs}\}}$$

With these formulas, a coincidence DDCM analysis can be carried out using both flight times obtained from the distance  $x$  and the distance  $x + \Delta x$  as separate sample points. This is especially useful if lifetimes from two different orders of magnitude need to be measured, as in fact two separate coincidence RDDS measurements are carried out simultaneously that can both be analyzed individually by the DDCM. As such, distances from two different regions of sensitivity can be measured at once. It is also possible to combine the distances from both sets (“ $t_1$ ” and “ $t_2$ ”) if both are within the region of sensitivity of the lifetime that is being measured, to double the amount of distances that can be used for the fit of the decay curve. In this case, however, it is important to note, that the distances used here have to be absolute distances, because the offsets between relative and absolute distances are different for the distances from the target to the first degrader and from the first degrader to the second degrader.

#### 4.2. The differential plunger method

Introduced in [1], the Differential Plunger Method (DPM) is a further development of the DDCM. It makes use of the fact that, in principle, with a three-foil plunger it is possible to measure the decay curve of a state  $R_i(t)$  and its derivative directly with one set of distances. For the case of a gate on a direct feeder the lifetime is obtained via

$$\tau_i = \frac{I_{(f_s+rs,us)} \Delta x}{I_{(f_s+rs,rs)} v'} \quad (15)$$

For this equation to hold,  $\frac{\Delta x}{v'} = \Delta t$  has to be small in comparison to  $\tau_i$ . For short lifetimes, that leads to the problem that the intensity of the reduced-shifted peak would become too small to be determined with good precision. For these cases where this is not possible, a correction factor has been introduced in [2], which uses the analytical derivative

of an exponential decay curve to correct for deviations between  $I_{rs}$  and  $\frac{dR_i(t)}{dt}$ :

$$C(\tau, \Delta t) = \frac{\exp(\Delta t/\tau) - 1}{\Delta t/\tau} \quad (16)$$

A corrected lifetime could then be obtained via

$$\tau_{corr} = C(\tau, \Delta t) \cdot \frac{I_s \Delta x}{I_r v'} \quad (17)$$

However, this correction factor is restricted to special cases, where the decay curve of the analyzed state can be treated as a “pure” exponential function, i.e. no feeding patterns have to be taken into account.

Due to these restrictions, the DPM is not used in the analysis presented here. However, if the prerequisites of the DPM are fulfilled, it is extremely useful to limit the amount of beam time needed to successfully conduct a RDDS lifetime measurement.

#### 4.3. Data analysis

The data were analyzed using  $\gamma$ - $\gamma$  coincidences and the DDCM with Eqs. (13), (14) as derived above. Therefore, gates have been set on feeding transitions in the projection of the coincidence matrix. Fig. 5 shows this projection and the limits of the gates which have been used to obtain the spectra for the analysis. As can be seen in this figure, the line density in this energy region is high, due to many competing fusion evaporation channels. A careful investigation of the possible contaminants in the gates showed, however, that they do not influence the analysis, because there are no coincident transitions in the same energy region as the analyzed transitions. A resulting  $\gamma$ -ray spectrum of the  $2_1^+ \rightarrow 0_1^+$  transition with a gate on the reduced-shifted and the fully-shifted components of the feeding  $4_1^+ \rightarrow 2_1^+$  transition, observed with the detectors under forward angle, is shown in Fig. 6 for three different distances. The same is shown for the  $4_1^+ \rightarrow 2_1^+$  transition in Fig. 7, this time with a gate on the fully-shifted component of the direct feeder only and detected by the detectors under backward angle.

For the analysis, intensities of the components are obtained as indicated above, by adding up the respective intensities obtained from the gated spectra depending on which distance set ( $x$  or  $x + \Delta x$ , respectively) is used. The distances  $\Delta x$  are re-normalized to the initial velocity  $v$ , by multiplying them by the factor  $\frac{v}{v'}$ . This is needed, because for the calculation of the lifetimes only one velocity is assumed during the complete flight time. The intensities obtained from the different distance sets have been normalized with respect to deviations in the beam intensity and total measurement time. For this task, a gate was set on all components of the lowest transition (“gate from below”) and the intensities of all components of higher lying transitions were obtained. By comparing these intensities for every distance set, normalization

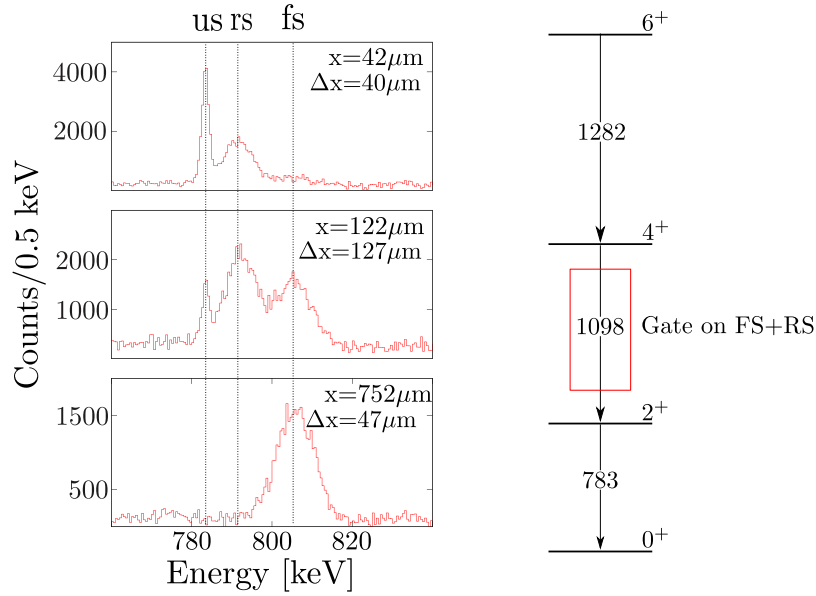


Fig. 6. Examples of spectra from the analysis of the  $2_1^+$  state’s lifetime analysis, all detected with forward angle detectors with a gate on the fully-shifted and the reduced-shifted components of the direct feeding transition. Markers show the positions of the unshifted, the reduced-shifted and the fully-shifted peaks, respectively.

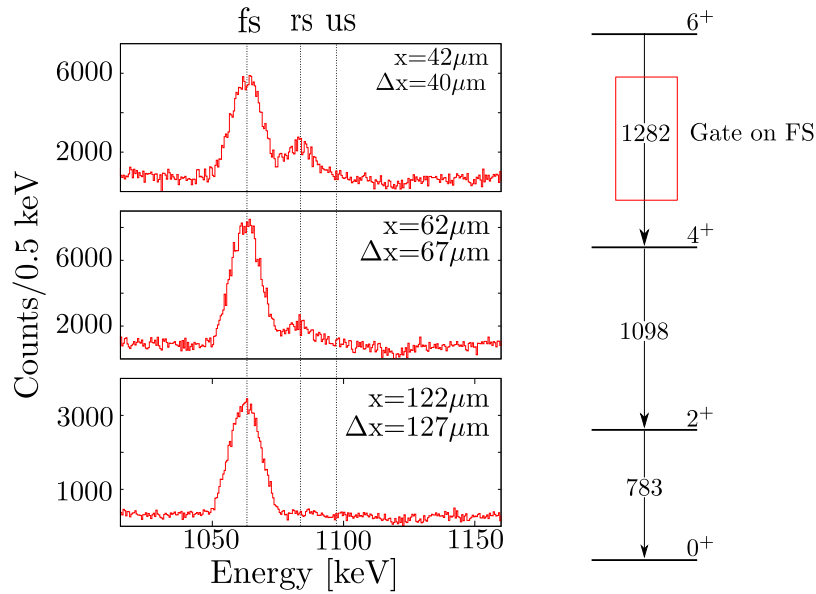


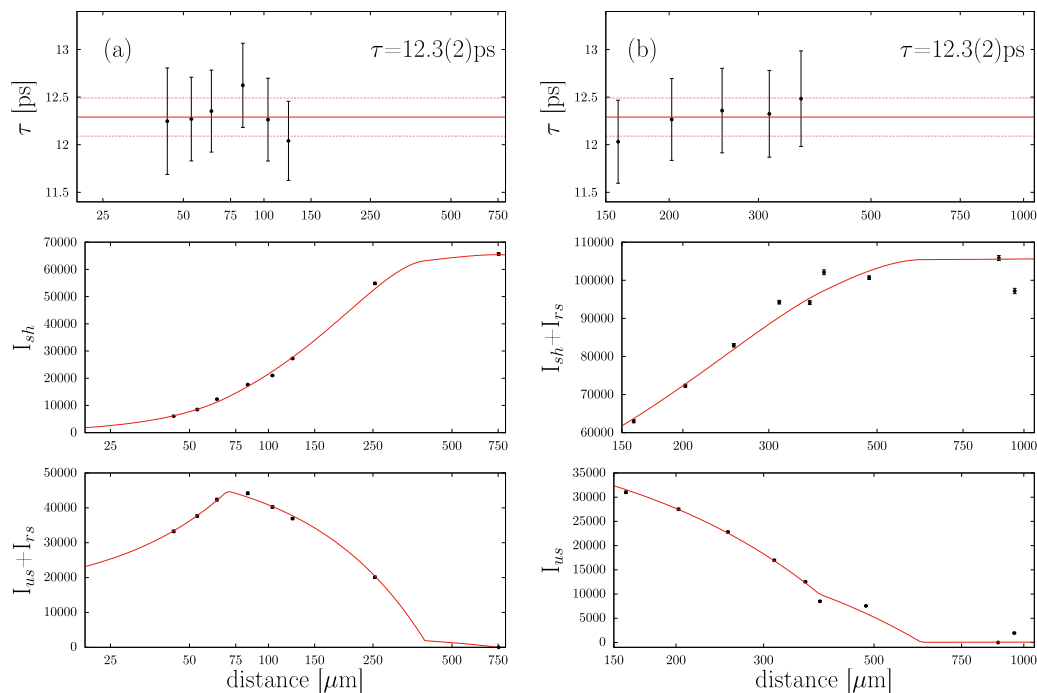
Fig. 7. Examples of spectra from the analysis of the  $4_1^+$  state’s lifetime analysis, all detected with backward angle detectors with a gate on the fully-shifted component of the direct feeding transition. Markers show the positions of the unshifted, the reduced-shifted and the fully-shifted peaks, respectively. Note, that due to the detection under backward angles the energies are shifted to the lower energy side.

factors can be calculated, since the combined intensity of all peaks does not depend on the distance.

For the analysis of the lifetimes of the  $2_1^+$  and  $4_1^+$  states, direct gates on the respective feeding transition are used. The fact that the peaks are not completely separated in the spectrum makes it impossible to gate for example on the complete fully-shifted component without getting contaminations of the reduced-shifted one and vice versa. This poses no problem for the usage of direct gates, because one can set partly gates to avoid contaminations. For the case of indirect gates, however,

Eq. (14) requires that a ratio of intensities, obtained from different gating conditions, is used. This is only possible, if the gates can be set on the complete peaks and all coincident events are included. If the same gating condition is used for all intensities, as it is done in the case of a direct gate, missing events due to partly gates cancel out in the ratio. Therefore, only direct gates are used in the analysis.

For the  $2_1^+$  state, both parts of the decay curve could be used while for the  $4_1^+$  state, due to its shorter lifetime, only the distances  $x$  are within the region of sensitivity. In the following, the terminology “ $t_1$ ”



**Fig. 8.**  $\tau$  curves of the  $2_1^+$  state together with the shifted and unshifted intensities as functions of the target-to-stopper distances normalized to the average velocity  $v$  for the distances  $x$  (a) and  $x + \Delta x$  (b). The intensities for both figures are from the same ring–ring combination (“forward–forward”). The error bars of the intensities are smaller than the symbol size and therefore not visible here. The lifetime values given in the upper panels are the results for the respective ring combination only and the uncertainties given are the statistical uncertainties only. For the final lifetimes of the states all ring combinations have been used and additional systematic uncertainties have been included.

and “ $t_2$ ” part will be used, to indicate the decay curves derived from the distances  $x$  and  $x + \Delta x$ , respectively, referring to the flight times in Fig. 3.

Examples of decay curves and  $\tau$ -plots are shown in Figs. 8 and 9. Note that the values shown there, are the results for the respective detector ring–ring combination only, while the final results take into account all usable detector combinations. It is clearly visible in the case of the  $2_1^+$  analysis, that the two distance sets sample different parts of the decay curve and result in the same lifetime value.

The final results of the lifetime analysis are shown in Table 1 in comparison to literature values. These have been obtained by using the weighted mean of all used ring combinations. The uncertainties of the single values include the statistical uncertainties (as shown for the cases in Figs. 8, 9) as well as additional systematic uncertainties.

#### 4.4. Discussion of the results

As can be seen in Table 1, the lifetime of the  $2_1^+$  state obtained from this work is slightly shorter but overall agrees well with the literature values. The lifetime value for the  $4_1^+$  state deviates from the one obtained by Giles et al. [11] but agrees with other previous measurements.

The lifetimes can be used to obtain electromagnetic transition strengths, which are shown in Table 2. For comparison results of different shell-model calculations are also given in Table 2. These have been obtained with the NuShellX@MSU code [16]. The KB3G [17] and GXPF1 A [18] interactions have been used in a model space containing the  $f_{7/2}$ ,  $p_{3/2}$ ,  $p_{1/2}$  and  $f_{5/2}$  orbitals with a  $^{40}\text{Ca}$  core. Two sets of effective charges have been used for the calculations, the first consisting of the standard values  $e_\pi=1.5e$ ,  $e_\nu=0.5e$  and the second consisting of  $e_\pi=1.31e$ ,  $e_\nu=0.46e$ , which have been derived by Dufour and Zuker [19]. For the  $2_1^+$  state the GXPF1 A and the KB3G interactions reproduce the newly measured value very well with

**Table 1**

Lifetimes of excited states in  $^{50}\text{Cr}$  from this work in comparison to literature values.

State	Lifetime [ps]	Origin	Method
$2_1^+$	12.2(4)	this work	
$2_1^+$	13.3(6)	Giles et al. [11]	RDDS
$2_1^+$	13.0(4)	Arnsward et al. [12]	RDDS
$2_1^+$	13.2(4)	Ernst et al. [13]	CoulEx
$4_1^+$	2.4(3)	this work	
$4_1^+$	4.9(7)	Giles et al. [11]	RDDS
$4_1^+$	2.5(7)	Brandolini et al. [14]	DSAM
$4_1^+$	3.2(7)	Ernst et al. [13]	CoulEx

**Table 2**

Electromagnetic transition strengths calculated from the level lifetimes derived from the above analysis together with shell-model predictions.

Transition	B(E2) [ $e^2\text{fm}^4$ ]				
	Experiment	GXPF1A <sup>a</sup>	KB3G <sup>a</sup>	GXPF1A <sup>b</sup>	KB3G <sup>b</sup>
$2_1^+ \rightarrow 0^+$	227(8)	218	218	171	171
$4_1^+ \rightarrow 2_1^+$	213(30)	308	310	241	243

<sup>a</sup>Effective charges  $e_\pi=1.5e$ ,  $e_\nu=0.5e$ .

<sup>b</sup>Effective charges  $e_\pi=1.31e$ ,  $e_\nu=0.46e$ .

the first set of effective charges. With the second set, the calculations underestimate the B(E2) value. In the case of the  $4_1^+$  state, the new, shorter value for the lifetime leads to a transition strength that matches the general trend of the shell-model predictions much better than the previously measured longer lifetime value. Here, the second set of effective charges reproduces the newfound value while the first set overestimates it.

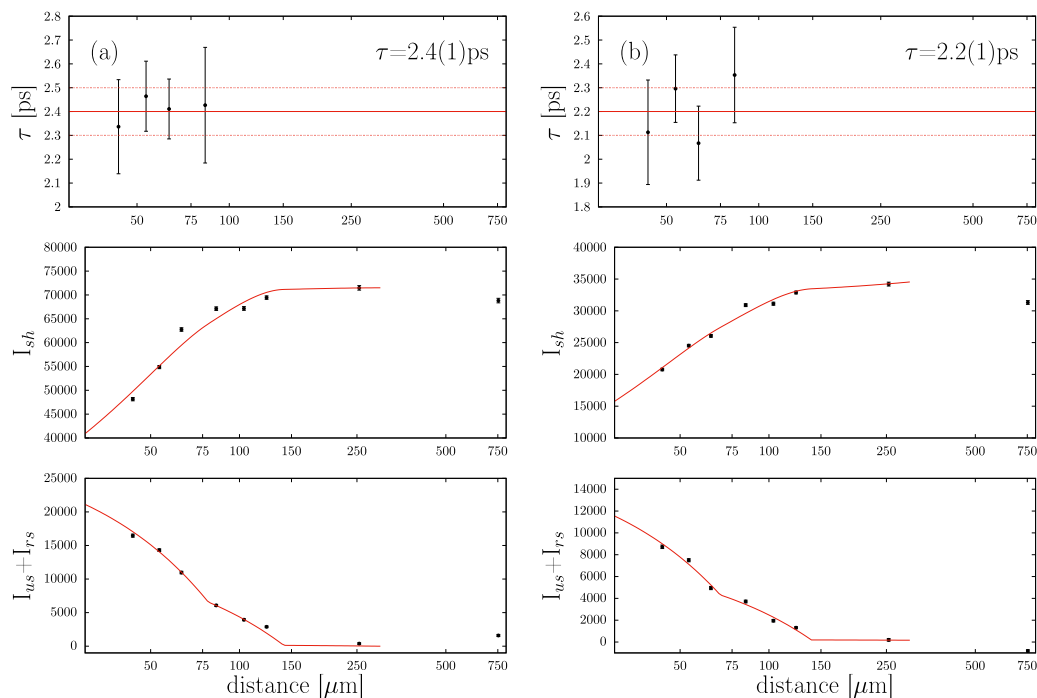


Fig. 9.  $\tau$  curves of the  $4^+$  state together with the shifted and unshifted intensities for the detector ring combinations ‘forward-forward’ (a) and ‘backward-backward’ (b). Only the distances  $x$  are used. For the uncertainties of the intensities and the given lifetime values the same as specified in the caption of Fig. 8 applies.

## 5. Conclusion

A new, portable, multi-purpose three-foil plunger device has been built and successfully used for the first time. The lifetimes obtained in the commissioning experiment agree well with most recent literature values. The advantages of a three-foil plunger have been demonstrated, by measuring two parts of the decay curves of the  $2^+$  and  $4^+$  states simultaneously. Furthermore a method has been described, to make use of that fact using the Differential Decay Curve Method in  $\gamma$ - $\gamma$  coincidence and has been shown to give reliable results.

The plunger can thus be reported to be operational and can be used in the future for further experiments at different laboratories.

## Declaration of competing interest

The authors declare that they have no known competing financial interests or personal relationships that could have appeared to influence the work reported in this paper.

## Data availability

Data will be made available on request.

## Acknowledgments

This project was supported by the Bundesministerium für Bildung und Forschung (BMBF), Germany, grant number 05P18KFN9 and by the U.S. Department of Energy, Office of Science, Office of Nuclear Physics under Contract No. DE-AC02-06CH11357. Furthermore the authors would like to thank the mechanical workshop at the Institut für Kernphysik (IKP), University of Cologne for the great work in constructing and building the mechanical parts of the new plunger device.

## References

- [1] A. Dewald, S. Harissopulos, P. von Brentano, The differential plunger and the differential decay curve method for the analysis of recoil distance Doppler-shift data, *Z. Phys. A - Atomic Nuclei* 334 (1989) 163–175, [http://dx.doi.org/10.1016/0168-9002\(93\)90944-D](http://dx.doi.org/10.1016/0168-9002(93)90944-D).
- [2] H. Iwasaki, A. Dewald, T. Braunroth, C. Fransen, D. Smalley, A. Lemasson, C. Morse, K. Whitmore, C. Loelius, The triple plunger for exotic beams TRIPLEX for excited-state lifetime measurement studies on rare isotopes, *Nucl. Instrum. Methods Phys. Res. A* 806 (2016) 123–131, <http://dx.doi.org/10.1016/j.nima.2015.09.091>.
- [3] C. Müller-Gatermann, F. von Spee, A. Goasduff, D. Bazzacco, M. Beckers, T. Braunroth, A. Boso, P. Cocconi, G. de Angelis, A. Dewald, C. Fransen, A. Goldkuhle, A. Gottardo, A. Gozzelino, K. Hadynska-Klek, G. Jawroski, P. John, J. Jolie, S. Lenzi, J. Litzinger, R. Menegazzo, D. Mengoni, D. Napoli, F. Recchia, M. Siciliano, D. Testov, S. Thiel, J. Valiente-Dobón, K. Zell, A new dedicated plunger device for the Galileo  $\gamma$ -ray detector array, *Nucl. Instrum. Methods Phys. Res. A* 920 (2019) 95–99, <http://dx.doi.org/10.1016/j.nima.2018.12.077>.
- [4] M. Rejmund, B. Lecornu, A. Navin, C. Schmitt, S. Damoy, O. Delaune, J. Enguerrand, G. Fremont, P. Gangnant, L. Gaudefroy, B. Jacquot, J. Pancin, S. Pullanhiotan, C. Spitaels, Performance of the improved larger acceptance spectrometer: VAMOS++, *Nucl. Instrum. Methods Phys. Res. A* 646 (1) (2011) 184–191, <http://dx.doi.org/10.1016/j.nima.2011.05.007>.
- [5] A. Latina, A. Stefanini, S. Beghini, B. Behera, L. Corradi, G. De Angelis, A. De Rosa, E. Fioretto, A. Gadea, M. Gulmini, G. Inglima, M. La Commara, G. Maron, R. Menegazzo, N. Marginean, G. Montagnoli, D. Napoli, D. Pierroutsakou, G. Pollarolo, M. Romoli, M. Sandoli, F. Scarlassara, S. Szilner, N. Toniolo, M. Trotta, Y. Wu, PRISMA - A magnetic spectrometer for heavy ions at LNL, *Nuclear Phys. A* 734 (2004) E1–E4, <http://dx.doi.org/10.1016/j.nuclphysa.2004.03.005>.
- [6] Q-Motion Miniature Linear Stage Datasheet, URL <https://www.physikinstrumente.com/>.
- [7] CL-3000 Series Confocal Displacement Sensor Catalog, URL <https://www.keyence.com/>.
- [8] M. Beckers, A. Dewald, C. Fransen, L. Kornwebel, F. von Spee, Revisiting the measurement of absolute foil-separation for RDDS measurements and introduction of an optical measurement method, *Nucl. Instrum. Methods (2022)* <http://dx.doi.org/10.1016/j.nima.2022.167416>, in press.

- [9] A. Dewald, O. Möller, P. Petko, Developing the recoil distance Doppler-shift technique towards a versatile tool for lifetime measurements of excited nuclear states, *Prog. Part. Nucl. Phys.* 67 (3) (2012) 786–839, <http://dx.doi.org/10.1016/j.pnpnp.2012.03.003>.
- [10] T. Alexander, A. Bell, A target chamber for recoil-distance lifetime measurements, *Nucl. Instrum. Methods* 81 (1) (1970) 22–26, [http://dx.doi.org/10.1016/0029-554X\(70\)90604-X](http://dx.doi.org/10.1016/0029-554X(70)90604-X).
- [11] M.M. Giles, B.S. Nara Singh, L. Barber, D.M. Cullen, M.J. Mallaburn, M. Beckers, A. Blazhev, T. Braunroth, A. Dewald, C. Fransen, A. Goldkuhle, J. Jolie, F. Mammes, C. Müller-Gatermann, D. Wölk, K.O. Zell, S.M. Lenzi, A. Poves, Probing isospin symmetry in the ( $^{50}\text{Fe}$ ,  $^{50}\text{Mn}$ ,  $^{50}\text{Cr}$ ) isobaric triplet via electromagnetic transition rates, *Phys. Rev. C* 99 (2019) 044317, <http://dx.doi.org/10.1103/PhysRevC.99.044317>.
- [12] K. Arnsfeldt, T. Braunroth, M. Seidlitz, L. Coraggio, P. Reiter, B. Birkenbach, A. Blazhev, A. Dewald, C. Fransen, B. Fu, A. Gargano, H. Hess, R. Hirsch, N. Itaco, S. Lenzi, L. Lewandowski, J. Litzinger, C. Müller-Gatermann, M. Queiser, D. Rosiak, D. Schneiders, B. Siebeck, T. Steinbach, A. Vogt, K. Wolf, K. Zell, Enhanced collectivity along the  $N=Z$  line: Lifetime measurements in  $^{44}\text{Ti}$ ,  $^{48}\text{Cr}$ , and  $^{52}\text{Fe}$ , *Phys. Lett. B* 772 (2017) 599–606, <http://dx.doi.org/10.1016/j.physletb.2017.07.032>.
- [13] R. Ernst, K.-H. Speidel, O. Kenn, U. Nachum, J. Gerber, P. Maier-Komor, N. Benczer-Koller, G. Jakob, G. Kumbartzki, L. Zamick, F. Nowacki, Stringent tests of shell model calculations in  $fp$  shell nuclei  $^{46,48}\text{Ti}$  and  $^{50,52}\text{Cr}$  from measurements of  $g$  factors and  $B(E2)$  values, *Phys. Rev. Lett.* 84 (2000) 416–419, <http://dx.doi.org/10.1103/PhysRevLett.84.416>.
- [14] F. Brandolini, S. Lenzi, D. Napoli, R. Ribas, H. Somacal, C. Ur, D. Bazzacco, J. Cameron, G. de Angelis, M. De Poli, C. Fahlander, A. Gadea, S. Lunardi, G. Martínez-Pinedo, N. Medina, C. Rossi Alvarez, J. Sánchez-Solano, C. Svensson, Precise DSAM lifetime measurements in  $^{48}\text{Cr}$  and  $^{50}\text{Cr}$  as a test of large scale shell model calculations, *Nuclear Phys. A* 642 (3) (1998) 387–406, [http://dx.doi.org/10.1016/S0375-9474\(98\)00543-0](http://dx.doi.org/10.1016/S0375-9474(98)00543-0).
- [15] G. Böhm, A. Dewald, P. Petkov, P. von Brentano, The differential decay curve method for the analysis of Doppler shift timing experiments, *Nucl. Instrum. Methods Phys. Res. A* 329 (1) (1993) 248–261, [http://dx.doi.org/10.1016/0168-9002\(93\)90944-D](http://dx.doi.org/10.1016/0168-9002(93)90944-D).
- [16] B. Brown, W. Rae, The shell-model code NuShellX@MSU, *Nucl. Data Sheets* 120 (2014) 115–118, <http://dx.doi.org/10.1016/j.nds.2014.07.022>.
- [17] A. Poves, J. Sánchez-Solano, E. Caurier, F. Nowacki, Shell model study of the isobaric chains  $A=50$ ,  $A=51$  and  $A=52$ , *Nuclear Phys. A* 694 (1) (2001) 157–198, [http://dx.doi.org/10.1016/S0375-9474\(01\)00967-8](http://dx.doi.org/10.1016/S0375-9474(01)00967-8).
- [18] M. Honma, T. Otsuka, B. Brown, T. Mizusaki, Shell-model description of neutron-rich  $pf$ -shell nuclei with a new effective interaction GXPf 1, *Eur. Phys. J. A* 25 (1) (2005) 499–502, <http://dx.doi.org/10.1140/epjad/i2005-06-032-2>.
- [19] M. Dufour, A.P. Zuker, Realistic collective nuclear Hamiltonian, *Phys. Rev. C* 54 (1996) 1641–1660, <http://dx.doi.org/10.1103/PhysRevC.54.1641>.



#### 4 Publication II:

Revisiting the measurement of absolute foil-separation for RDDS measurements and introduction of an optical measurement method







# Revisiting the measurement of absolute foil-separation for RDDS measurements and introduction of an optical measurement method

M. Beckers\*, A. Dewald, C. Fransen, L. Kornwebel, C.-D. Lakenbrink, F. von Spee

*Institut für Kernphysik der Universität zu Köln, Zùlpicher Str. 77, D-50937 Köln, Germany*

## ARTICLE INFO

### Keywords:

Plunger  
RDDS  
DDCM  
Lifetime measurement  
Transition strengths

## ABSTRACT

Uncertainties in absolute plunger distances are an often overlooked component in measurements with the Recoil Distance Doppler-shift (RDDS) method when the Differential Decay Curve (DDC) method cannot be used for the analysis. It is shown how these uncertainties arise when the capacitance method is used to determine absolute distances and how they influence the obtained lifetime values of a plunger experiment. Furthermore, a new approach to obtain absolute foil separations for plunger measurements using a high precision optical distance probe is introduced, which can reduce these uncertainties by a large margin. The performance of this method is demonstrated by comparisons to the capacitance method as well as to a precise measurement of absolute distances using known lifetimes in  $^{181}\text{Ta}$ .

## 1. Introduction

The Recoil Distance Doppler Shift (RDDS) method is a well established and often used way to measure lifetimes of excited states in atomic nuclei in the picosecond range to extract absolute transition strengths [1]. These are mandatory to compare to different model calculations to enhance the theoretical understanding of the many-body problem a nucleus represents. The RDDS method exploits the decay radiation's Doppler-shift which occurs when the emitting nucleus is in motion. This is used to distinguish, between decay during a defined flight time or after being stopped or slowed down in a degrader foil. The apparatus used for such experiments is the plunger. It is used to vary the flight-time of the nuclei by setting different separations between the target foil, where the nuclei are created or excited and knocked out, and the stopper or degrader foil. The precise knowledge about these separations is therefore crucial for the lifetime determination. When the Differential Decay Curve Method (DDCM) [2] is used to analyze the data, it is sufficient to know relative distances. These can be determined with very high precision in modern plunger devices, for example by using inductive probes. If, however, the DDCM cannot be used, the data have to be analyzed using the Bateman equations of the decay [3], which requires knowledge of the absolute flight-times. Also for differential plunger devices [4], which use more than two foils, absolute distances might be needed, depending on which method is used for the analysis. If distances from between the target and the first degrader foil and distances from between the first degrader foil and the second degrader foil in such a device shall be combined in a single data set, absolute distances are needed [5]. Absolute foil separations

are much harder to measure, since the absolute zero point remains unclear. The standard way to get information about this zero point is an extrapolation using the capacitance method. This method gives absolute distances with uncertainties of around  $5\ \mu\text{m}$  in a standard case, but with the possibility of being significantly larger or also smaller in certain cases. A closer look is taken at these uncertainties in this paper. Depending on the recoil velocity of the nuclei and the lifetimes in question, uncertainties in this order of magnitude can significantly influence the results of a lifetime measurement. Fig. 1 shows the differences of the resulting obtained lifetime values for a hypothetical excited state, when the absolute distances are shifted by  $5\ \mu\text{m}$ . A recoil velocity of  $v/c=1.5\%$  is assumed here, which is a typical value for non-relativistic plunger experiments using normal kinematics. It can be seen that the derived lifetimes vary by more than 10% in this case and that this uncertainty, depending on the overall achievable precision of the experiment, might dominate the uncertainty of the final lifetime. In the idealized case shown in Fig. 1, the systematic deviation of the points from the curve hints clearly at a systematic error. In real cases, however, the statistical fluctuation and possibly larger uncertainties of the data points may obscure these systematic deviations and make it less obvious that a systematic error might be present. Therefore, it is of high interest to minimize this uncertainty by finding new ways to measure the absolute distances directly. In the following, an overview of the capacitance method for absolute plunger distance measurements will be given, with an emphasis on the problems which are immanent and which might easily be overlooked when carrying out a plunger analysis. It will then be shown that a precise and also easy to apply absolute distance measurement can be accomplished by using modern

\* Corresponding author.

E-mail address: [mbeckers@ikp.uni-koeln.de](mailto:mbeckers@ikp.uni-koeln.de) (M. Beckers).

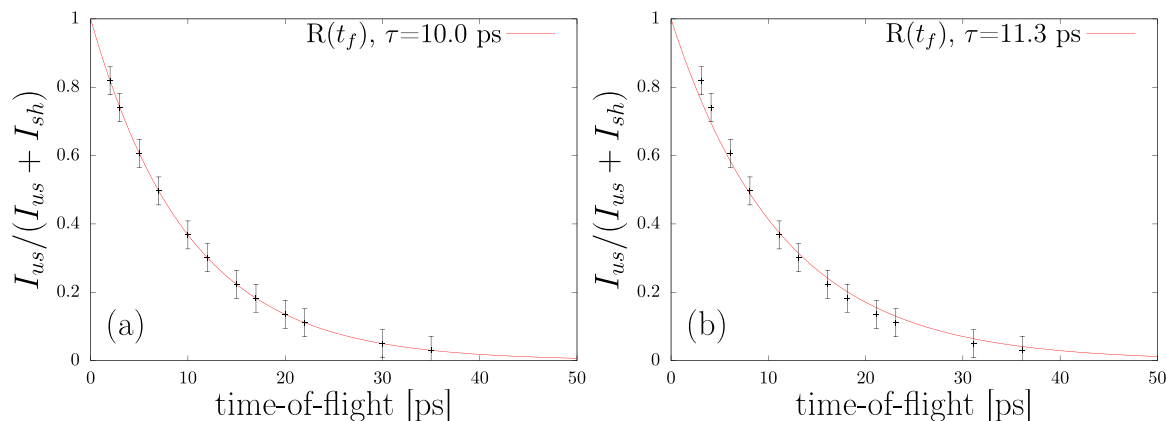


Fig. 1. Decay curves fitted to exemplary data points with correct distances (a) and with a systematic offset of 5  $\mu\text{m}$  (b). The assumed recoil velocity is 1.5%  $c$ , a realistic value for reactions using low energy beams.

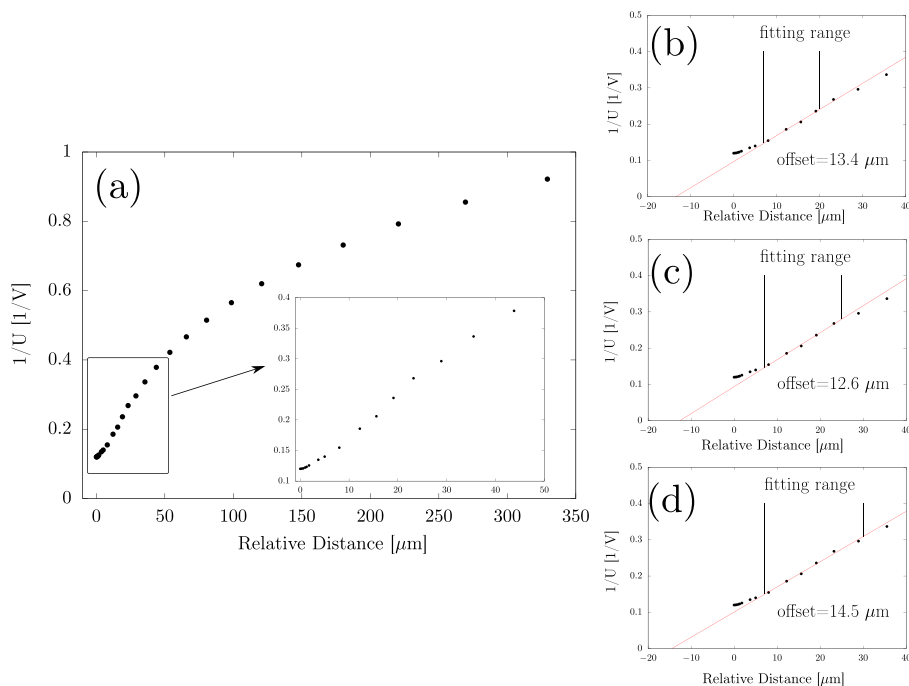
optical sensors, which provide a way to measure directly on the foils themselves, without the risk to damage these very thin and often expensive materials.

## 2. Standard ways to determine absolute plunger foil separations

In most modern day plunger devices the capacitance method, introduced by Alexander and Bell [6], is used to monitor the foil separation during the experiment to be able to correct for changes, for example due to beam-induced thermal effects on the foils. Therefore, the capacitive response between the foils is calibrated using the relative distance measured by the above mentioned probes, e.g. inductive transducers. At the same time, this method can be used to get information about absolute distances, if needed. A pulsed signal is therefore fed to one foil and the induced signal from the other foil is measured, resulting in a voltage  $U$ . This signal resembles the capacitance of the plate capacitor approximately formed by both foils and is inversely proportional to the distance between these foils. The plate capacitor approximation collapses when an electrical contact is formed between the two foils. This happens almost always at some point before the “real” absolute zero distance is reached. Reasons for this are possible roughness or spikes in the foils or an imperfect alignment between the two foils. To determine this absolute minimum, a linear extrapolation of the distance dependence of the inverse voltage signal can be carried out and the y-intercept (distance at  $\frac{1}{U}=0$ ) is assumed to be this minimum distance. In theory this should give high precision knowledge about absolute plunger distances but in practice, there are two main components that introduce uncertainties, both of which affect the plate capacitor approximation. On the one hand, not only the plunger foils but also some stray capacitance of the surrounding holding structure, which cannot be isolated from the foils, add to the measured capacitance. This leads to deviations from the linear distance dependence, in particular for larger separations where the capacitance of the foils is smaller relative to the stray capacitance. On the other hand, under realistic circumstances, for short separations, very often a mechanical contact between non-conducting parts, for example non-removable dust particles on the foils or an oxidation of the surface, happens before the electrical contact and may even prevent reaching electrical contact. This can lead to small deformations of the foils and therefore also to deviations from linearity. A characteristic distance calibration curve from an experiment with the Cologne Coincidence Plunger [1], where both effects can be clearly seen, is shown in Fig. 2. Both problems can be circumvented, but by doing so, new uncertainties are introduced. For the deviations on the small distance part it is the common way to exclude that area from the extrapolation. However, it might not always be clear at which exact point the linear behavior collapses and the choice of the fitting range can influence the extracted absolute zero point. The choice of this lower

boundary of the fitting range has to be made “by eye” as no general rule exists when the deformation of the foils start to break the linearity. This is also true for the larger distances, where it is even harder to decide where the influence of the stray capacitance begins to dominate. In Fig. 2(b)–(d) the effect of including or excluding single data points on the resulting zero point is demonstrated. It can be reduced by a proper treatment of the stray capacitance. An empirical correction constant that estimates the stray capacitance can be introduced, which is then subtracted from the measured voltage. The corrected data points are therefore given by  $\frac{1}{U - c_s}$ , where  $c_s$  is the constant that estimates the stray capacitance. It is obtained via an iteration process: The constant is increased while visually inspecting the behavior of the corrected data points. The plateau for the larger distance data points will begin to disappear while increasing the value of  $c_s$  and finally become linear. The termination condition is, when the slope of the data points starts to increase beyond linearity for large distances. It has to be stressed, however, that for this method the stray capacitance is assumed to be constant i.e. independent of the target-degrader separation, which is not necessarily the case. The final extrapolation, after applying the correction constant for the same data points used in Fig. 2, is shown in Fig. 3. Now a variation of the upper limit of the fitting range between 20  $\mu\text{m}$  and 50  $\mu\text{m}$  only affects the extrapolated distance offset by a maximum of 0.5  $\mu\text{m}$ . Another possibility to account for stray capacitance would be, to dismount the target and stopper foils after the experiment and measure the capacitance of the holding structure at the same distance points, to subtract it from the initial measurement points. Unfortunately, for maximum precision, this would have to be measured separately for every experiment, because the alignment process, carried out before an experiment, influences the capacitance of the holding structure. Furthermore the results of such a measurement still would not give the exact stray capacitance, because also the non-aligned parts of the foils contribute to this value.

Another possible source of uncertainties concerns the alignment of the two foils. Before a distance calibration can be applied in the first place, in most plunger devices, the foils have to be aligned manually. This is mostly done visually and in most cases it is possible to align the foils very accurately with deviations in the range of few  $\mu\text{m}$  over the complete foil surface. In some cases, however, the materials or the general quality of the foil surfaces can lead to worse alignments. This applies in particular for large-area foils with diameters of up to 100 mm, that will be needed in plungers for relativistic radioactive beams, e.g. at the Facility for Antiproton and Ion Research in Europe (FAIR). This does not only affect the zero-offset itself, which increases, but also the quality of the plate capacitor approximation. Lastly, it leads to the problem that the zero-offset determined with the capacitance method does not necessarily reflect the one present at the place the beam particles hit the target.



**Fig. 2.** (a): An example of a distance calibration curve where the inverse of the induced voltage is plotted against the relative distance measurement of the inductive transducer. It is easy to see that the linearity does not hold for large and very small distances. (b)–(d): Linear fits applied to the same data set. The upper limit of the fitting range is varied and the respective extrapolated distance offset is indicated. Note, that the lower limit of the fitting range is held constant, but is still a subjective choice. Variation of the lower limit would therefore also contribute to the variation of the extrapolated value.

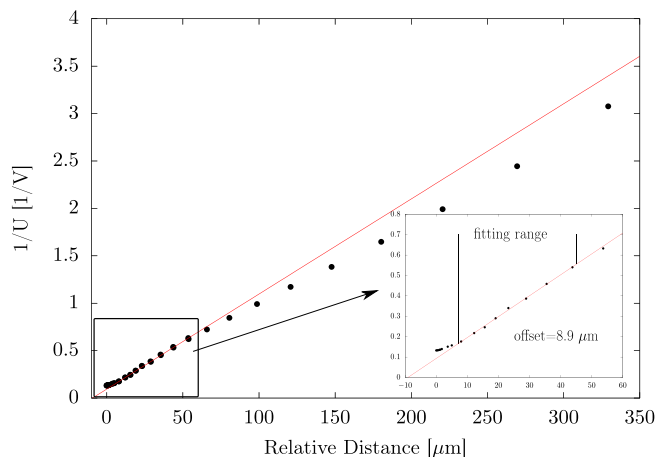
All in all, it is not trivial to extract the uncertainty of the zero-point obtained from this extrapolation. Certainly, the error of the fitting procedure underestimates the real uncertainty by a large margin, because of the assumptions made before the curve-fitting and the systematic uncertainties introduced that way. A reasonably conservative uncertainty estimate can be obtained by extrapolating the data points with and without applying the mentioned correction factor within the same fitting range and use the deviation of the extracted zero points to estimate the error. For the data points shown in Figs. 2 and 3 this results in an uncertainty for the absolute distance of  $4 \mu\text{m}$ , which is a typical value, while relative distances can be obtained with uncertainties  $<0.5 \mu\text{m}$ . Additional uncertainties may also arise from the choice of the lower boundary of the fitting range. In cases, where it is not clear at which point the linear behavior ends for small distances, a variation of the boundary has to be carried out and the variation of the resulting offset has to be taken into account as well.

Another possibility to gain access to absolute foil separations independently from the capacitance method is using well known lifetimes from excited states in reaction products. This is explained in detail in Ref. [1] and can yield very precise results. However, this method can only be used if nuclei with precisely known level lifetimes are populated and therefore it depends heavily on the used reactions. Additionally, these known lifetimes have to be of similar magnitude as the ones targeted by the experiment, since the plunger distances have to be in the region of sensitivity.

To conclude this discussion, the capacitance method is able to deliver absolute distances but it comes with moderate to high uncertainties, which can in the worst case influence the derived lifetimes quite drastically. Furthermore, to obtain correct results with realistic uncertainties, a good knowledge of the method and its common problems is required; it is possible to underestimate these uncertainties or even to derive a wrong zero-offset.

### 3. Optical distance measurements

To solve the problem described above, the best way would be to perform a high precision distance measurement directly on the foil surfaces. The standard very high precision probes used in different plunger



**Fig. 3.** The same data as depicted in Fig. 2 but with a constant modification of the induced voltage to account for holding and stray capacitance. A linear fit is applied to the linear part of the data points to obtain the absolute zero point.

devices, like inductive or opto-mechanical probes, cannot be used for this task, since every contact to the very thin foils leads to deformations and therefore falsifies the results. Only in recent times optical sensors have become commercially available that are able to measure distances with the desired precision ( $\Delta d < 1 \mu\text{m}$ ) and are at the same time small enough to be used with plunger devices without the need to build large and complicated holding structures or introducing the need to remove the plunger from the beam line to conduct the measurement. Good candidates for such measurements are sensors which use the confocal chromatic measurement technique. This enables very high precision and at the same time a relatively small shape of the sensor itself. For this technique, white light with different focal points for each wavelength is emitted through a cascade of lenses. If reflected from a surface at a certain distance, only light where the focal point is close to

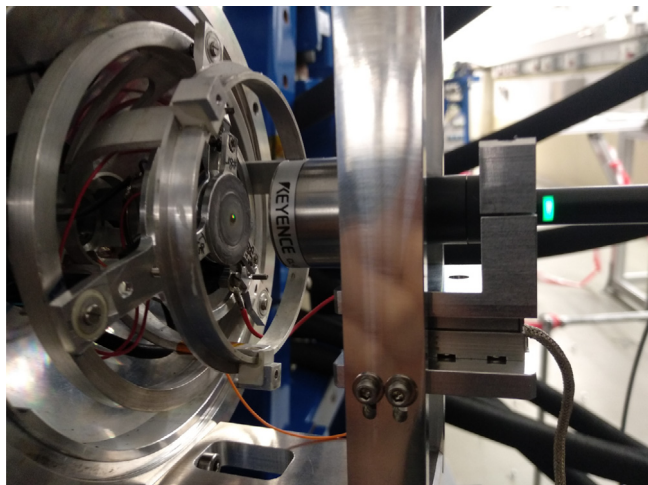


Fig. 4. An optical distance sensor mounted with the dedicated adapter at the Cologne Coincidence Plunger. The optical measurement spot is centered at the beam spot of the target foil. See text for details.

the surface can re-enter the sensor through an aperture. The incoming light is then transmitted through an optical fiber to a spectrometer. From the analysis of the incoming wavelengths, the distance can then be calculated [7]. The most interesting properties for the task at hand are the precision which is for most models well below  $0.5 \mu\text{m}$  as well as the possibility to measure a large diameter of area simultaneously. The later is important to average out the smaller imperfections of the foil surface which might cause the early electrical contact. For this, the KEYENCE CL-3000/L015 displacement sensor has been used as one sensor of the type described above. The precision of the sensor is  $0.25 \mu\text{m}$  and the measured area  $300 \mu\text{m}^2$  [7]. For the absolute foil separation measurement, an adapter for the Cologne Coincidence Plunger has been built. Since the highest precision of these sensors is limited to a small measurement range, it is placed on a precise step motor (*Physik Instrumente Q-521* [8]), which can move the sensor closer to or further away from the foil. The measurement procedure is as follows: Since it is sufficient to obtain one absolute distance as a reference point, from which all other distances can be determined by the precise relative distance measurement, the measurement is performed at the end of the experiment. After some time where the beam-induced foil deformations can recede, the sensor is used to measure as a first reference point the position of the stopper foil. Afterwards the stopper foil is removed and the sensor measures the position of the target foil. Both are measured in the middle of the foils, where the beam hit the target and the recoils entered the stopper foil. Because the beam spot has a certain diameter and the point of entry of the recoils in the stopper can also be broadened by angular straggling, a sensor which can measure a larger area simultaneously is preferred. That way, smaller local surface effects are averaged out and the resulting distance is a very good measure of the average distance traveled by the recoils. The adapter built to connect the sensor to the Cologne Coincidence Plunger allows to adjust the sensor position until the point of measurement coincides with the beam spot, which ensures that deviations in the alignment do not disturb the measurement. The adapter is shown mounted at the plunger in Fig. 4. For every position measurement the step motor holding the sensor automatically moves through the sensitive area of the sensor, which is at a distance of  $14.5 \text{ mm}$  to  $15.5 \text{ mm}$  from the sensor, and 100 data points are taken. From the averages and in combination with the respective motor position which is measured with nanometer precision with an internal optical sensor, the distance between target and stopper foil is calculated. This process is done automatically by software that was written for this purpose and which is now included in the Cologne Plunger Software Package (CPSP). The only other contribution is the

Table 1

Comparison of distance offsets obtained from two measurements with the capacitance method and the optical sensor. The offsets are given with respect to the electrical contact point, which therefore is defined as the origin of the scale. See text for details regarding the different examples.

Example no.	Distance offset capacitance method [ $\mu\text{m}$ ]	Distance offset optical measurement [ $\mu\text{m}$ ]
1	$-4^{+4}_{-7}$	$-2.2(8)$
2	$-40(8)$	$-37(1)$

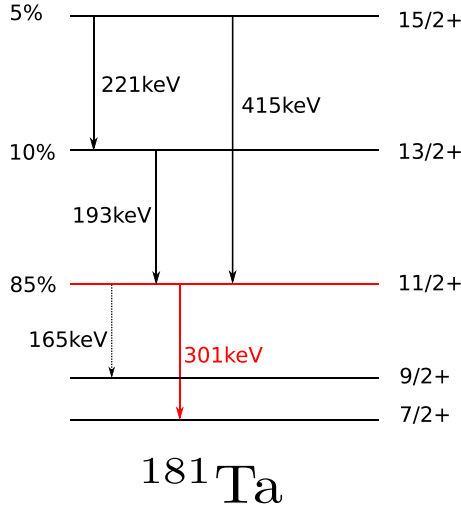
thickness of the stopper foil, since here the measurement can only take place on the backside, i.e. the downstream facing side of the foil. This, however, can be determined with very high precision if it is unknown. One possibility to do this is by conducting a Rutherford Backscattering Spectroscopy (RBS) experiment. RBS is a method to study surface layers of solids by bombarding them with ions in the range of MeV and measuring the energy of the backscattered ions [9]. This gives very precise values including a measure of the roughness at the beam spot. Another possibility is to use two optical sensors of the same type as described above. These can be calibrated in a way that they can measure the thickness of a foil that is placed between them with high precision. The uncertainty of the absolute distance is calculated from the variance of the average positions together with the uncertainty of the stopper foil thickness. Since in many standard experiments metal foils made of tantalum, gold or niobium are used, which can be very well stretched and do exhibit very little overall roughness, these uncertainties are small. In the following it will thus be demonstrated that a distance measurement with the method described above is advantageous in comparison to the capacitance method regarding the precision of the obtained zero-point as well as the simplicity and therefore the prevention of false results.

### 3.1. Proof of principle

The performance of the new method has been tested in comparison to both standard methods of accessing absolute distances: The capacitance method as well as measuring the distance offset with known lifetimes.

For the former, two examples of measurements are presented in Table 1. The first example was taken with very well aligned standard plunger foils. In this case the distance offset is small and both values match very well within their uncertainties. Even though the alignment is very good, the capacitance method results in a rather large uncertainty due to a mechanical contact before the electrical contact point. This is, as explained above, a typical behavior often seen in plunger measurements. In the second example a slight misalignment between the foils was introduced, as can be the consequence of materials with worse overall surface quality or other experimental restraints, which leads to a larger zero-offset. In this case the offsets from both the capacitance measurement and the optical measurement also agree very well within their respective uncertainties. Both examples show that the precision of the zero-offset is largely improved with the optical distance measurement.

Due to the restrictions of the capacitance method discussed above, additionally an independent measurement of absolute distances was carried out by exploiting known lifetimes in  $^{181}\text{Ta}$ . Therefore the RDDS technique was applied to a plunger measurement of that nucleus to sample the decay curve of the first excited  $11/2^+$  state. Excited states in  $^{181}\text{Ta}$  were populated with Coulomb excitation with the reaction  $^{181}\text{Ta}(^{32}\text{S}, ^{32}\text{S})^{181}\text{Ta}^*$  using a  $^{181}\text{Ta}$  foil with an areal density of  $3.3 \frac{\text{mg}}{\text{cm}^2}$  and a beam energy of  $85 \text{ MeV}$  delivered by the Cologne FN Tandem accelerator. A  $^{93}\text{Nb}$  foil was used to stop the recoiling nuclei, which had an average velocity of  $v/c \approx 1.8\%$ . An array of high-purity Ge detectors has been used to detect the  $\gamma$ -radiation of the decaying nuclear states.



**Fig. 5.** Partial level scheme of  $^{181}\text{Ta}$  as has been observed in the experiment. The transition used to obtain the absolute distances is marked in red while all feeding transitions relevant to the decay of the  $11/2^+$  state are marked in solid black lines. The dotted line marks the competing decay of the  $11/2^+$  state, which is not used. To the left the relative initial population of the relevant states is indicated.

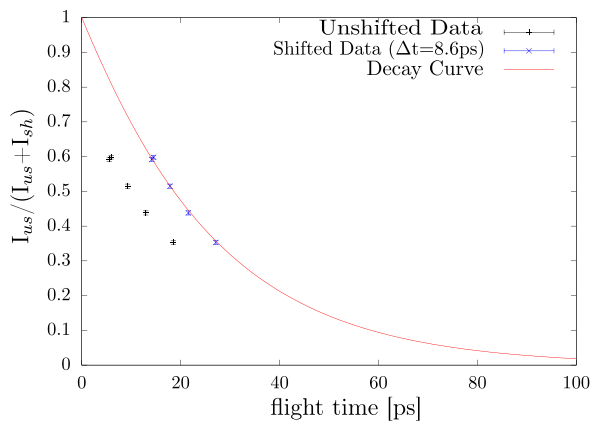
Also an additional array of particle detectors (solar cells) has been placed upstream of the target to detect backscattered  $^{32}\text{S}$  particles. This was used to set a gate on the Coulomb excitation reaction channel. 5 different target-to-stopper separations in the region of sensitivity have been measured.

To obtain absolute distances the precisely known lifetime values from [10] were used to construct the decay curve of the  $11/2^+$  state from the solution of the Bateman equations. The observed feeding pattern and the initial populations of the observed states that have been used to construct the Bateman equations are shown in the level scheme (Fig. 5).

In a RDDS measurement the decay curve  $R(t)$  of a state at a certain plunger distance  $x$  is given by

$$R(x) = \frac{I_{us}(x)}{I_{us}(x) + I_{sh}(x)} \quad (1)$$

where  $I_{us}$  and  $I_{sh}$  are the intensities of the unshifted and the Doppler-shifted components of the decaying transition, respectively. Therefore these intensities have been determined and plotted together with the previously constructed decay curve in the time frame using the relative



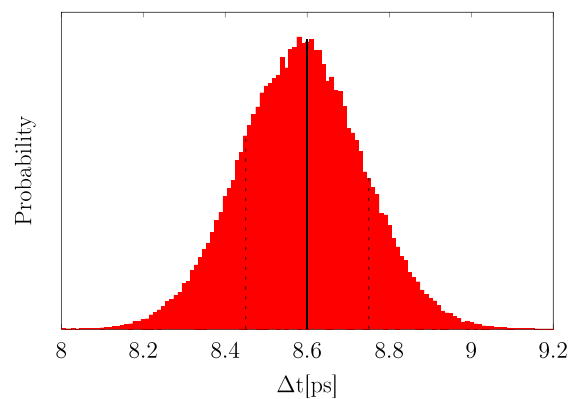
**Fig. 6.** Determination of the zero-offset with known lifetimes in  $^{181}\text{Ta}$ . The shift was obtained by minimizing the least-square cost function. The right panel shows the determination of the uncertainty by a Monte-Carlo type simulation taking into account experimental uncertainties as well as such from the known lifetimes. The  $\sigma$  intervals of the distribution, marked with dashed lines, were taken as the uncertainty.

distances that have been measured during the experiment and the recoil velocity. The zero-offset can be obtained by shifting the experimental data points by a constant time offset to match with the known decay curve. This task was carried out by using a least-square minimization procedure. To obtain the uncertainty of the offset, a Monte-Carlo type simulation was employed, where the uncertainties of the known lifetimes as well as the ones of all experimentally obtained values have been used. Another source of uncertainty for this kind of distance measurement, depending on the type of experiment, is unobserved delayed feeding. In the case considered here, where the levelscheme is very well known and the excited states are populated by Coulomb excitation, which only populates low-spin, low-energy states, these effects were found to be neglectable. This method results in an offset of  $\Delta t = 8.6(2)$  ps which translates to  $\Delta x = 46.4(1.1)$   $\mu\text{m}$ . This process is shown in Fig. 6.

After this measurement the zero-offset was measured with the optical distance sensor, which resulted in  $\Delta x = 47.8(1.0)$   $\mu\text{m}$ . Again both values match within their uncertainties. The precision of both methods in this case is roughly the same. However, it has to be stressed again that the distance determination using known lifetimes is restricted to certain cases, where states with known lifetimes that are also in the region of sensitivity are populated together with the states of interest. For comparison, the offset for this measurement was also calculated with the capacitance method, which yielded a value of  $\Delta x = 54(6)$   $\mu\text{m}$ .

#### 4. Conclusion

It has been shown that the capacitance method as a means to obtain absolute target-stopper separations in plunger devices can introduce uncertainties, which can severely reduce the precision of extracted level lifetimes in non-DDCM plunger measurements, or in the worst case lead to wrong lifetime results. It has also been demonstrated that in order to get precise results with reliable uncertainties from this method good knowledge of the limitations and possible problems is mandatory. The usage of high-precision optical displacement sensors can reduce these uncertainties by a large margin, which is more than sufficient to remove the absolute distance as one of the highest contributors of the resulting level lifetime uncertainty. In addition, this method is easy to use, which is an important factor, especially since nowadays plunger devices often belong to the basic hardware in several nuclear structure physics laboratories and are operated by a wide range of users. It therefore minimizes the risk of obtaining incorrect level lifetimes or underestimating their uncertainties. Furthermore it is not restricted in usage to certain foils or reaction types.



### Declaration of competing interest

The authors declare that they have no known competing financial interests or personal relationships that could have appeared to influence the work reported in this paper.

### Data availability

Data will be made available on request.

### Acknowledgments

This project was supported by the Bundesministerium für Bildung und Forschung (BMBF), grant number 05P18KFN9.

### References

- [1] A. Dewald, O. Möller, P. Petkov, Developing the recoil distance Doppler-shift technique towards a versatile tool for lifetime measurements of excited nuclear states, *Prog. Part. Nucl. Phys.* 67 (3) (2012) 786–839, <http://dx.doi.org/10.1016/j.pnpnp.2012.03.003>.
- [2] G. Böhm, A. Dewald, P. Petkov, P. von Brentano, The differential decay curve method for the analysis of Doppler shift timing experiments, *Nucl. Instrum. Methods Phys. Res. A* 329 (1) (1993) 248–261, [http://dx.doi.org/10.1016/0168-9002\(93\)90944-D](http://dx.doi.org/10.1016/0168-9002(93)90944-D).
- [3] H. Bateman, The solution of a system of differential equations occurring in the theory of radioactive transformations, *Proc. Cambridge Philos. Soc* 15 (5) (1910) 423–427.
- [4] A. Dewald, S. Harissopulos, P. von Brentano, The differential plunger and the differential decay curve method for the analysis of recoil distance Doppler-shift data, *Z. Phys. A - Atomic Nuclei* 334 (1989) 163–175, [http://dx.doi.org/10.1016/0168-9002\(93\)90944-D](http://dx.doi.org/10.1016/0168-9002(93)90944-D).
- [5] M. Beckers, A. Dewald, C. Fransen, K. Arnsward, C. Müller-Gatermann, F. von Spee, Development of the multi-purpose cologne compact differential plunger (CoCoDiff) for the measurement of nuclear level lifetimes with the recoil distance Doppler-shift method, *Nucl. Instrum. Methods* (2022) <http://dx.doi.org/10.1016/j.nima.2022.167416>, in press.
- [6] T. Alexander, A. Bell, A target chamber for recoil-distance lifetime measurements, *Nucl. Instrum. Methods* 81 (1) (1970) 22–26, [http://dx.doi.org/10.1016/0029-554X\(70\)90604-X](http://dx.doi.org/10.1016/0029-554X(70)90604-X).
- [7] CL-3000 series confocal displacement sensor catalog, URL <https://www.keyence.com/>.
- [8] Q-motion miniature linear stage datasheet, URL <https://www.physikinstrumente.com/>.
- [9] S. Rubin, T. Passel, L. Bailey, Chemical analysis of surfaces by nuclear methods, *Anal. Chem.* 29 (5) (1957) 736–743, <http://dx.doi.org/10.1021/ac60125a001>.
- [10] T. Klug, Direkte Lebensdauer messung Coulomb-Angeregter Niveaus in  $^{152}\text{Sm}$ ,  $^{160}\text{Gd}$  und  $^{171}\text{Yb}$  (Ph.D. thesis), Universität zu Köln, 2001, URL <http://kups.ub.uni-koeln.de/id/eprint/537>.




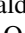
**5 Publication III:**

**Lifetime measurement of excited states in  $^{144}\text{Ce}$ : Enhanced E1 strengths in a candidate for octupole deformation**





## Lifetime measurement of excited states in $^{144}\text{Ce}$ : Enhanced $E1$ strengths in a candidate for octupole deformation

M. Beckers,<sup>\*</sup> C. Müller-Gatermann , A. Blazhev, T. Braunroth, A. Dewald, C. Fransen, A. Goldkuhle ,  
L. Kornweibel, J. Litzinger, F. von Spee, and K.-O. Zell  
*Institut für Kernphysik der Universität zu Köln, Zùlpicher Str. 77, D-50937 Köln, Germany*



(Received 30 March 2020; accepted 1 July 2020; published 28 July 2020)

A lifetime measurement of excited states in  $^{144}\text{Ce}$  using the  $^{142}\text{Ce}(^{18}\text{O}, ^{16}\text{O})$  reaction with a beam energy of 67 MeV and the recoil distance Doppler-shift method was performed at the Cologne FN Tandem accelerator. Lifetimes of the three lowest yrast states in  $^{144}\text{Ce}$  have been measured as well as for the  $3_1^-$  state and an effective lifetime of the  $4_2^+$  state. Reduced  $E2$  transition strengths determined using these results have been compared to predictions from recent shell-model calculations. From the interband transitions reduced  $E1$  strengths could be determined, which are strongly enhanced.

DOI: [10.1103/PhysRevC.102.014324](https://doi.org/10.1103/PhysRevC.102.014324)

### I. INTRODUCTION

The  $^{144}_{58}\text{Ce}_{86}$  nucleus is located on the neutron-rich side of the valley of stability, close to  $N=88$ , a nucleon number that is related to interesting phenomena throughout the nuclear chart. On the one hand a shape phase transition is expected at  $N=88-90$  for nuclei in the Ba-Dy region [1]. Such transitions have been of major interest in nuclear physics research for a long time. Especially, a phase transition from spherical to deformed is expected between  $^{146}\text{Ce}$  and  $^{148}\text{Ce}$ , which was the object of extensive studies in recent work [2]. Knowledge about  $^{144}\text{Ce}$  in the close vicinity would provide helpful information regarding the onset of deformation in that region. On the other hand also the phenomenon of octupole deformation plays an important role in the  $N \approx 88$ ,  $Z \approx 56$  region. At these nucleon numbers nuclei are especially prone to octupole correlations [3]. This is explained with a strong octupole coupling between the  $h_{11/2} \leftrightarrow d_{5/2}$  and the  $i_{13/2} \leftrightarrow f_{7/2}$  single-particle orbitals, respectively [4]. Experimentally, octupole deformation was related to alternating parity bands and low-lying negative-parity band heads. Such bands are reported in several lanthanide nuclei, including  $^{144}\text{Ce}$  [5]. Experimental indications for such a deformation apart from the band structure are enhanced  $E1$  and  $E3$  transition strengths. Direct evidence for octupole deformation was obtained for  $^{144}\text{Ba}$  by measuring  $E3$  transition strengths [6]. For comparison the partial level scheme of  $^{144}\text{Ce}$  is shown together with the ones of  $^{144}\text{Ba}$  and  $^{142}\text{Ba}$  in Fig. 1. These clearly show the typical structure of the supposed octupole bands, which is exhibited in each of these nuclei.

Aside from the  $2_1^+ \rightarrow 0_{gs}^+$  transition, no transition strengths are experimentally known for  $^{144}\text{Ce}$ . To shed some light on the question of octupole deformation it would be most helpful to measure  $E3$  transition strengths in  $^{144}\text{Ce}$ . However, because

up to now no  $E3$  transitions have been observed, the experiment that is presented here aims to get information about the  $B(E1)$  values via transitions connecting positive and negative parity states. While enhanced  $E1$  transition strengths can also be indicators for octupole deformation, lifetime information of negative parity states are essential to deduce  $E3$  transition strengths, for example, if a characteristic  $3_1^- \rightarrow 0_{gs}^+$  transition will be observed in future experiments. Level lifetimes are also very important as model independent input parameters in the analysis of Coulomb excitation experiments, which can deduce  $E3$  matrix elements also for nonobserved transitions. In addition, the  $B(E2)$  values between yrast states provide important insights into the general collective structure of the nucleus, especially by comparing them to theoretical model predictions.

### II. EXPERIMENT

The presented experiment was performed at the Institute for Nuclear Physics at the University of Cologne. Excited states in  $^{144}\text{Ce}$  were populated by the 2n transfer reaction  $^{142}\text{Ce}(^{18}\text{O}, ^{16}\text{O})$ . The beam was delivered by the Cologne FN Tandem Accelerator with a beam energy of 67 MeV. To measure the lifetimes of excited states, the target foil, consisting of  $0.5 \frac{\text{mg}}{\text{cm}^2}$   $^{142}\text{Ce}$  on a  $1.2 \frac{\text{mg}}{\text{cm}^2}$  Ta support layer facing the beam, was mounted in the Cologne Plunger device [9]. At the stopper position a  $4.1 \frac{\text{mg}}{\text{cm}^2}$  Nb foil was installed, which was sufficient to stop the recoiling nuclei with an average velocity of  $v/c = 1.57(1)\%$ . The plunger device is used to set different target-to-stopper distances and to keep them constant by measuring the target-stopper capacitance and compensate for drifts using a piezoelectric device. Emitted  $\gamma$  rays were measured by 11 large volume Germanium detectors with relative efficiencies between 55% and 83%, arranged in two rings, ring 1 (six detectors at  $45^\circ$ ) and ring 2 (five detectors at  $142.3^\circ$ ). Additionally an array of six solar cells, covering the solid angle between  $117^\circ$  and  $167^\circ$ , was used to measure

<sup>\*</sup>mbeckers@ikp.uni-koeln.de

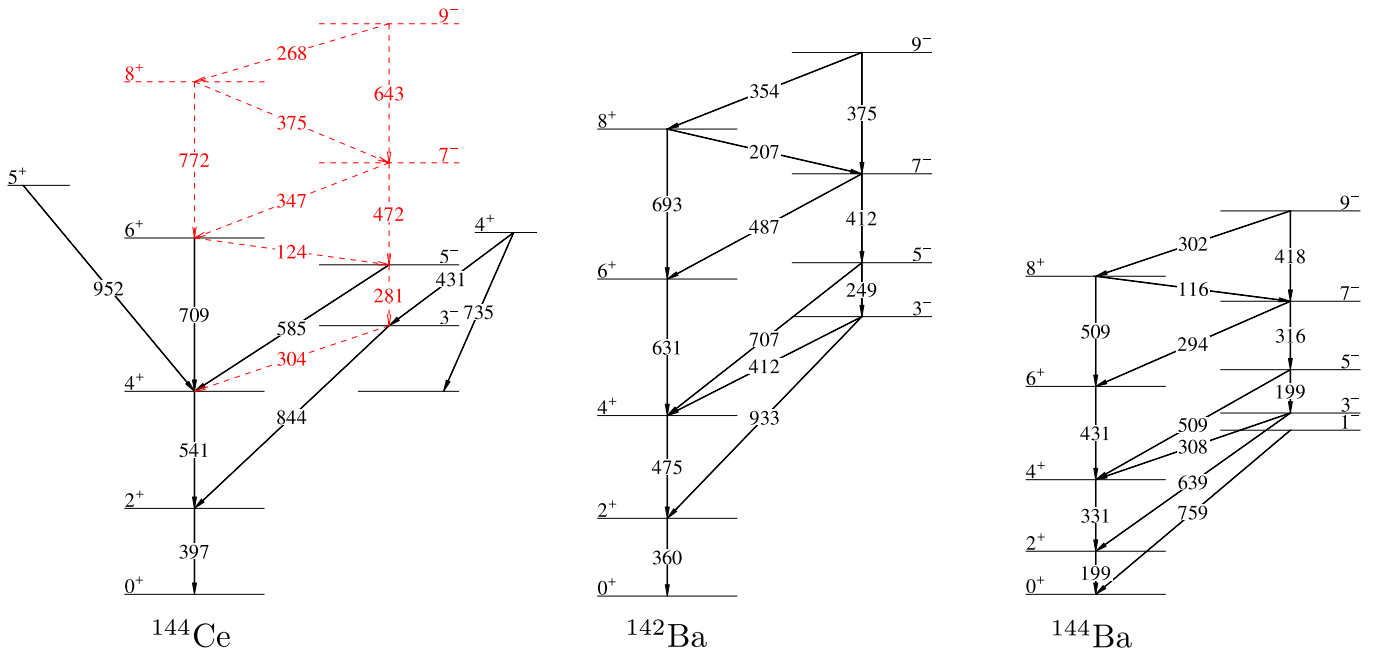


FIG. 1. Partial level schemes of  $^{144}\text{Ce}$ ,  $^{142}\text{Ba}$ , and  $^{144}\text{Ba}$ . Transition energies are given in keV. For  $^{144}\text{Ce}$  the transitions observed in this experiment are shown in black while levels and transitions shown with dashed red lines have been observed in earlier experiments [5,7] and are included to display the mentioned interspacing of positive and negative parity states with the respective interband transitions. Data for  $^{142,144}\text{Ba}$  were taken from [8]. See text for details.

backscattered particles to select the reaction channel using a particle- $\gamma$  coincidence gate. All detector angles are given with respect to the beam axis. During the course of the experiment data for a total of eight different target-to-stopper distances between  $21\ \mu\text{m}$  and  $364\ \mu\text{m}$  were taken. The absolute reaction cross section for the used  $2n$ -transfer reaction could not be obtained, because the decays of  $^{144}\text{Ce}$  are not observable without using a gate on the backscattered particle. Therefore only an effective reaction cross section can be given, i.e., the cross section for the case when the  $^{16}\text{O}$  reaction partner is scattered into the solid angle between  $117^\circ$  and  $167^\circ$  and detected by the solar cells. With an estimated average beam current of about  $6.5 \times 10^9$  pps for a single run the effective cross section for the  $2_1^+ \rightarrow 0_{gs}^+$  transition in  $^{144}\text{Ce}$  was calculated to be about 3 mb. The effective cross section of the  $2n$  transfer in relation to Coulomb excitation, also for the respective  $2_1^+ \rightarrow 0_{gs}^+$  transitions is given by the intensity ratio,

$$\frac{I_{2^+}(2n)/\epsilon(E)}{I_{2^+}(\text{CoulEx})/\epsilon(E)} \approx 0.12,$$

where  $\epsilon(E)$  is the detector efficiency for the respective transition energy. It has to be noted that no angular correlations were taken into account.

### III. LIFETIME ANALYSIS

Spectra for the data analysis were created by employing particle- $\gamma$  coincidence gates to select the nuclear reaction of interest. However, from the spectrum of backscattered particles it was not possible to distinguish between  $^{16}\text{O}$  and  $^{18}\text{O}$ . Therefore also excited states in  $^{142}\text{Ce}$ , populated through Coulomb excitation, are visible in the respective particle-

gated spectra (see Fig. 2). Using  $\gamma$ - $\gamma$  coincidences for this analysis was not possible, because the number of coincident events is far too low, owing to the low cross section of the production reaction.

For the three lowest positive parity yrast states the development of the unshifted and shifted component of the decay is clearly visible for the various plunger distances. Spectra of three different distances (small, medium, long) are shown for these three states in Fig. 3. To determine lifetimes of the  $2_1^+$  and the  $4_1^+$  excited states in  $^{144}\text{Ce}$ , the well-established differential decay curve method (DDCM) for the analysis of recoil distance Doppler-shift (RDDS) measurements in its  $\gamma$ -single implementation was used. A detailed review of this method is given in Ref. [9].

Following the DDCM the lifetime of a given state is obtained via

$$\tau_i(x) = \frac{-R_i(x) + \sum_k b_{ki} \alpha_{ki} R_k(x)}{\frac{d}{dx} R_i(x)} \times \frac{1}{v}, \quad (1)$$

where  $R_i$  and  $R_k$  denote the decay curves of the state of interest ( $i$ ) and the feeding states ( $k$ ), respectively. These can be obtained from the depopulating  $\gamma$  transitions. The velocity of the recoil is denoted as  $v$  and  $x$  is the target-to-degrader separation, while  $\alpha_{ki}$  is a proportionality factor determined by the detector efficiency and the angular distribution of the  $\gamma$  rays and  $b_{ki}$  is the branching ratio. Thus the intensities of the depopulating transitions as well as the ones of all observed populating transitions are needed for the lifetime analysis and a careful investigation of the feeding had to be carried out. In total, two feeding transitions were observed for the  $2_1^+$  state ( $4_1^+ \rightarrow 2_1^+$ ,  $3_1^- \rightarrow 2_1^+$ ) while four such transitions were found for the  $4_1^+$  state ( $6_1^+ \rightarrow 4_1^+$ ,  $5_1^- \rightarrow 4_1^+$ ,  $5_1^+ \rightarrow 4_1^+$ ,  $4_2^+ \rightarrow 4_1^+$ ).

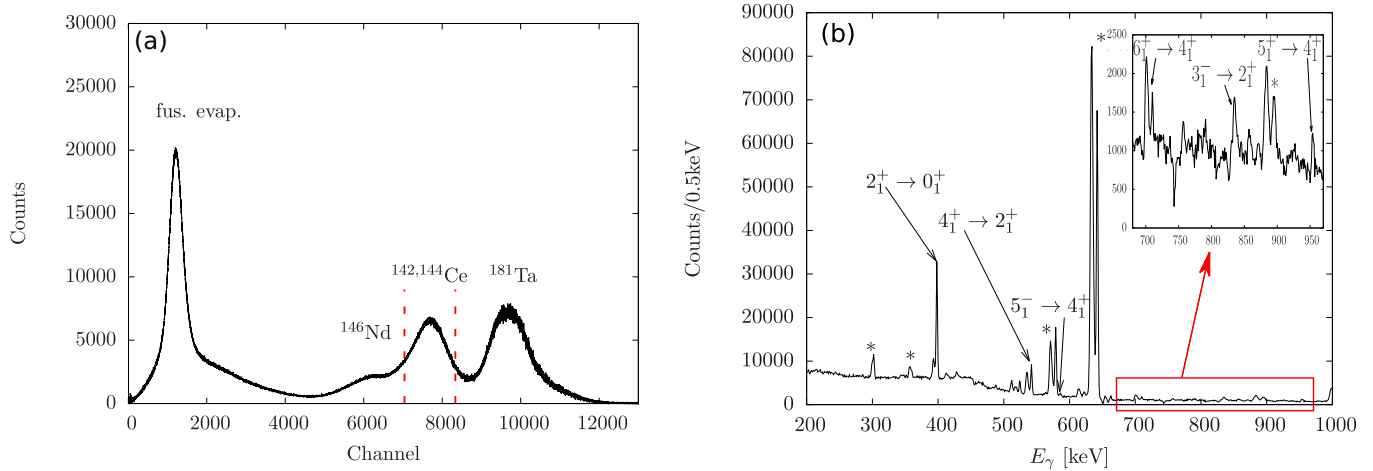


FIG. 2. (a) Particle spectrum measured with solar cells. (b)  $\gamma$ -ray energy spectrum as measured with detectors at backward angles in coincidence to the gate indicated in the particle spectrum (dashed lines). Visible transitions investigated in this paper are marked. Other visible peaks originate from states in the contaminant  $^{142}\text{Ce}$  nucleus and are marked with asterisks.

As can be seen in Fig. 2 the feeding transition  $5_1^- \rightarrow 4_1^+$  is energetically close to a stronger contaminant transition ( $4_1^+ \rightarrow 2_1^+$  in  $^{142}\text{Ce}$ ). Therefore, it is completely overlapped by the flight component of that transition under forward angle detection and thus the spectra of the detectors at a forward angle cannot be used for analyzing the decay of the  $4_1^+$  state. For the feeding transition depopulating the  $5_1^+$  state only the stop component was observed at all distances, which leads to the assumption that the lifetime of this  $5_1^+$  state is long compared to the longest achieved flight time of about 77 ps. A partial level scheme displaying the level feeding observed and taken into account is shown in Fig. 1.

The peak areas of all aforementioned transitions were determined and, after being corrected for detector efficiencies, used to obtain the lifetimes. The  $\tau$  curves resulting of the lifetime determination process together with the intensities

of the shifted and unshifted  $\gamma$ -ray components are shown in Fig. 4. Note that this figure only shows the results for the backward angle detection. For analyzing the decay of the  $2_1^+$  state also the detector ring under forward angle was used and the resulting lifetime is given by the weighted average of both rings as  $\tau(2_1^+) = 55.1(5)\text{ps}$ . The analysis of the  $4_1^+$  state yielded  $\tau(4_1^+) = 9.4^{+0.9}_{-0.4}\text{ps}$ . Here the uncertainties are increased beyond the value given in Fig. 1(b) to account for the low statistics of the transitions feeding the  $4_1^+$  state.

To determine the lifetime of the  $6_1^+$  state the Bateman equation of its decay was used instead of the DDCM. The reason was, that here only few distances are within the region of sensitivity, which diminishes the advantages of the DDCM. No feeding transitions for the  $6_1^+$  state were observed. Because transfer reactions typically lead to the population of only the lowest states in a nucleus, this observation is compatible to the justified assumption that the  $6_1^+$  state is nearly exclusively directly populated. Hence, the Bateman equation for a decay without feeding was used and fitted to the experimentally determined intensity ratios for both detector rings. To determine the uncertainty, a Monte Carlo simulation with  $10^6$  iterations was employed, where uncertainties of the absolute distances, the recoil velocity, and the intensity ratios were taken into account. The given uncertainties correspond to the  $1\sigma$  intervals to both sides of the mean value. This method was used for the analytical analysis of RDDS data before, for example, in Ref. [10], and provides an easy way to incorporate all significant sources of uncertainties. The fit as well as the probability distribution are shown in Fig. 5 exemplary for forward angle detection. The extracted lifetimes for both detector rings in this case show some discrepancies, as for the forward ring the resulting lifetime is  $4.9^{+1.0}_{-0.7}\text{ps}$  while for ring 2 the analysis yields  $7.4^{+1.2}_{-0.9}\text{ps}$ . The spectra were extensively checked for contaminations that could explain such deviations but none have been found. Because no such discrepancies occur for every other state's analysis, other systematic errors related to treatment of the two rings can be excluded. Therefore the discrepancy is very likely caused by the relatively

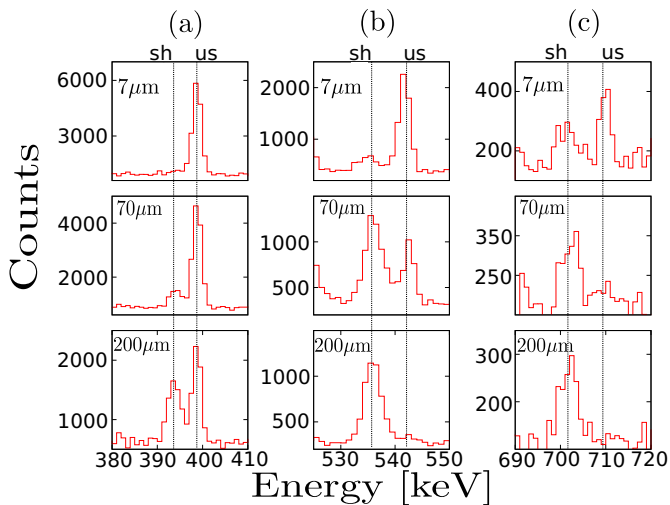


FIG. 3. Spectra of the  $2_1^+ \rightarrow 0_1^+$  (a),  $4_1^+ \rightarrow 2_1^+$  (b), and  $6_1^+ \rightarrow 4_1^+$  (c) decays for three different plunger distances measured under backward angle.

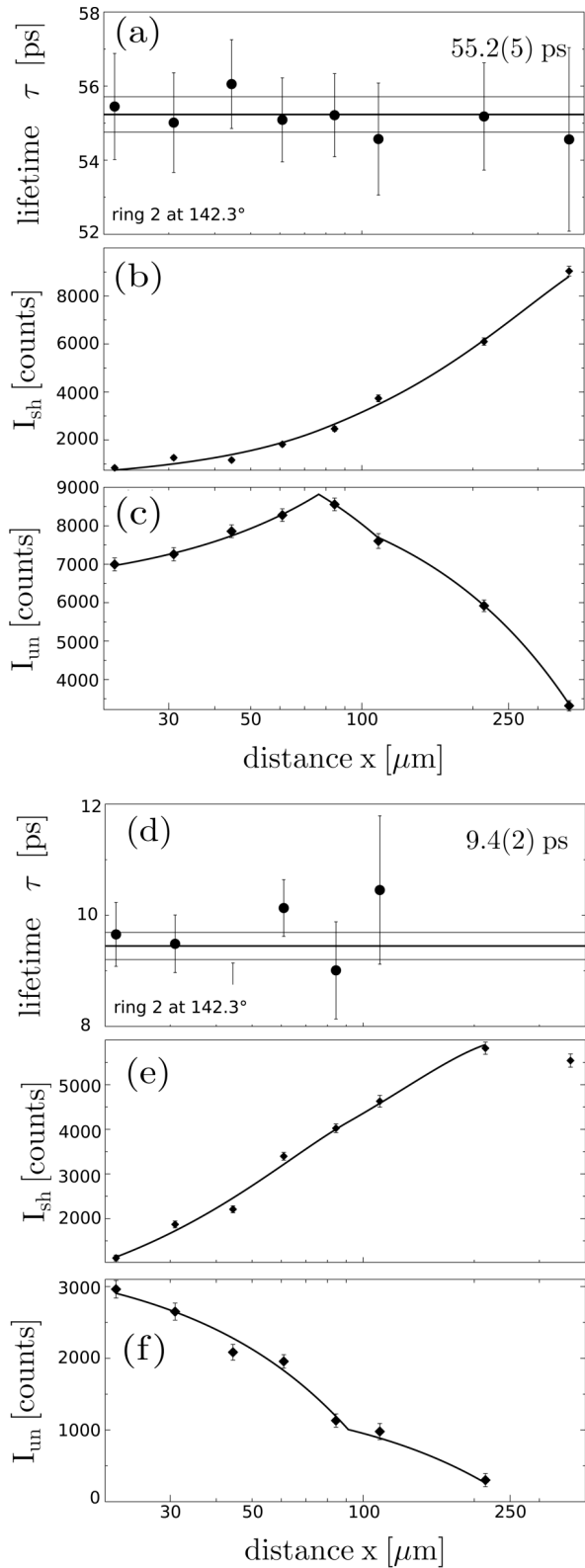


FIG. 4.  $\tau$  curves of the  $2_1^+$  state (a) and of the  $4_1^+$  state (d) together with the respective intensities of the shifted [(b) and (e)] and unshifted [(c) and (f)] components as a function of the target-stopper separation as observed with detectors at backward angles. Uncertainties given here only include statistical uncertainties from the fitting procedure, not from feeding assumptions. Final uncertainties of the lifetimes are given in Table II.

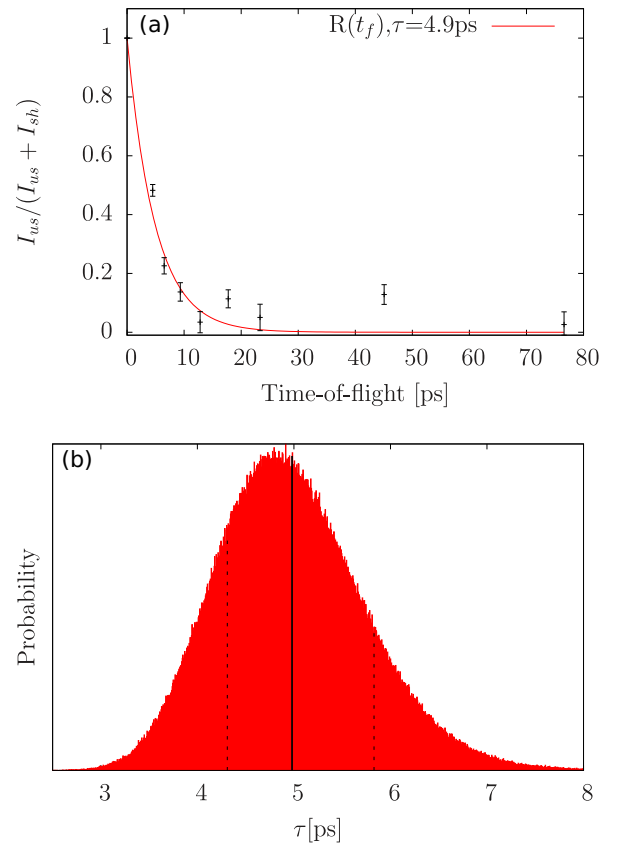


FIG. 5. Decay curve with lifetime fit (a) and probability distribution (b) for the  $6_1^+$  state; decay observed at forward angles.

low statistics for this decay. To account for this, the variance between the two values was used for the calculation of the uncertainty of the weighted mean. This yields a temporary value of  $\tau(6_1^+)_{\text{nofeed}} = 6.2(1.6)\text{ps}$ . To investigate the assumption that the  $6_1^+$  state is exclusively populated directly by the reaction, the effects of possible unobserved feeding have been simulated. A realistic amount of unobserved feeding for a “worst-case scenario” can be extrapolated by looking at the feeding of the lower lying states. Because the population of states in transfer reaction is diminished with rising excitation energy, also the amount of feeding in relation to the direct population of a state is reduced for higher excitation energies. Consequently it is justified to assume that the percentage of unobserved feeding for the  $6_1^+$  state does not exceed the observed feeding of the lower states. It has to be noted that the population of excited states in transfer reactions typically also decreases with level spin. However, the only feeding transitions leading to the population of the  $6_1^+$  state that have been observed in earlier experiments, for example, in Ref. [11], stem from the  $8_1^+$  and the  $7_1^-$  states. According to the relative intensities given in Table I an assumption of 20% feeding for the  $6_1^+$  state should therefore be a sufficiently conservative estimate. For the sake of simplicity the feeding is modeled by a single hypothetical state lying above the  $6_1^+$ . The effective lifetime of that state was chosen to be 100 ps, which proved to be sufficiently long. Longer lifetimes do not lead to distinct changes in the corresponding lifetime value of

TABLE I. Percentages of observed feeding in relation to the total population of the level for the investigated states. In relation to the level excitation energy this value decreases nearly linearly.

State	Energy (keV)	$I_{\text{feed}}/I_{\text{total}}$
$2_1^+$	397.4	59%
$4_1^+$	938.7	34%
$3_1^-$	1242.3	15%
$6_1^+$	1647.8	–
$4_2^+$	1673.9	–

the  $6_1^+$  state. With these assumptions, the determined lifetime value for the  $6_1^+$  state was lowered to  $4.8_{-0.7}^{+0.8}$  ps. The lower limit of this result is thus used to correct the lower limit of the uncertainty for  $\tau(6_1^+)$ . This yields  $\tau(6_1^+) = 6.2_{-2.1}^{+1.6}$  ps. Within these uncertainties the given lifetime still holds, even if a large, but still realistic, amount of unobserved feeding was present.

Furthermore a lifetime for the  $3_1^-$  state was obtained. Here the statistics do not allow the determination of both peak components in every single distance with the precision needed for a lifetime analysis. For this reason the method presented in Ref. [10] for obtaining lifetimes from the summed spectra over all distances was used. Here the solution of the summed decay curve, consisting of the Bateman equations of the single distances  $j$ ,

$$R_{\text{sum}} = \frac{\sum_j I_{\text{un},j}}{\sum_j I_{\text{un},j} + \sum_j I_{\text{sh},j}} = \sum_j n_j R(t_{f,j}), \quad (2)$$

is used, where  $I_{\text{sh}}$  and  $I_{\text{un}}$  are the intensities of the shifted and unshifted components of the decay, respectively,  $t_f$  denotes the corresponding flight time for every distance  $x$ , and  $n_j$  is the respective normalization factor. According to Ref. [11] the  $3_1^-$  state receives most of its feeding via the  $4_2^+$  state with a transition energy of 432 keV. At least an effective lifetime of the feeding state as well as the initial populations of both states are needed for the lifetime determination of the  $3_1^-$ . The  $4_2^+ \rightarrow 3_1^-$  transition is observed in the spectrum but is partly overlapped by the contaminating  $3_1^- \rightarrow 4_1^+$  transition in  $^{142}\text{Ce}$ . This problem could be overcome by using the  $3_1^- \rightarrow 2_1^+$  transition in  $^{142}\text{Ce}$ , of which only the flight component is visible, and the respective branching from Ref. [12] to correct for the intensity of the contamination. After this correction was applied the effective lifetime of the  $4_2^+$  state could be determined from the summed spectra, using the method described above. Because no feeding is visible and only an effective lifetime is needed the Bateman equation without feeding assumptions is used. With  $R_{\text{sum}} = 0.56(7)$ , averaged over both detection rings, an effective lifetime  $\tau_{\text{eff}}(4_2^+) = 27.3_{-6.0}^{+10.9}$  ps is obtained. Graphically this method can be displayed as a  $R(\tau)$  curve which is shown in Fig. 6. Uncertainties are again obtained using a Monte Carlo simulation of the analysis process.

The feeding from the  $4_2^+$  state accounts for 15% of the  $3_1^-$  state's total population, leading to the assumption that direct population accounts for the missing 85%, because no other feeding is visible. According to the feeding percentages of the other states and assuming a first-order dependence of

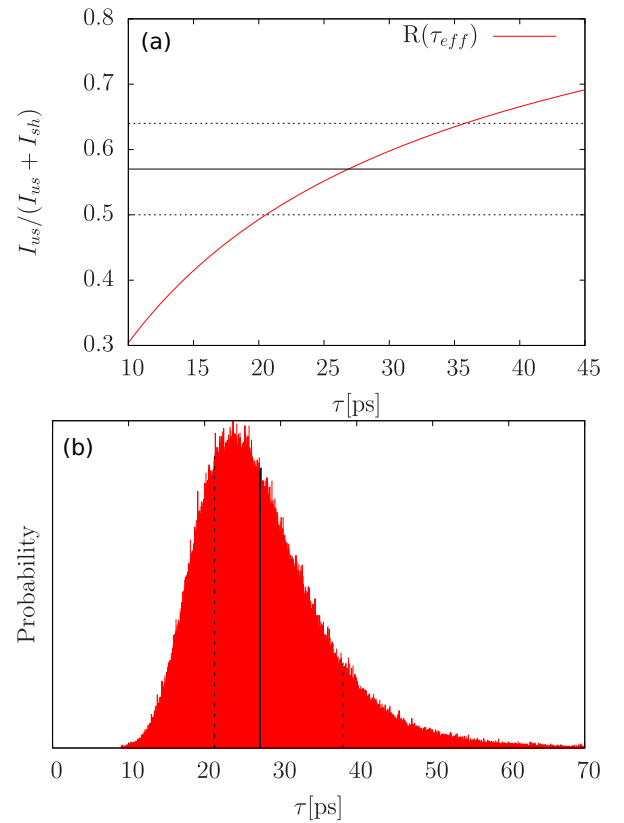


FIG. 6.  $R(\tau)$  curve (a) and probability distribution (b) for the  $4_2^+$  state. See text for details.

the level excitation energy this assumption is realistic. To account for possible unobserved side feeding, additional up to 5% long-lived (100 ps) feeding is assumed for the error calculation via a Monte Carlo simulation. This also accounts for feeding of the  $3_1^-$  state via the  $5_1^-$  state, which could not be observed but can be estimated to be less than 1.5% by using the  $5_1^- \rightarrow 4_1^+$  transition and the known branching from Ref. [11]. With  $R_{\text{sum}} = 0.13(1)$ , again, averaged over both detection rings a lifetime of  $\tau(3_1^-) = 2.5_{-0.5}^{+0.7}$  ps is obtained. The corresponding  $R(\tau)$  curve is shown in Fig. 7. The Monte Carlo simulation to calculate the uncertainties incorporates all mentioned uncertainties of the initial populations as well as

TABLE II. Experimentally obtained lifetime information from this work in comparison to existing values. See text for details.

Decaying State	$E_\gamma$ (keV)	$\tau$ (ps)
$2_1^+$	397.4	55.1(5) 52(3) <sup>a</sup> 42(10) <sup>b</sup>
$4_1^+$	541.3	$9.4_{-0.4}^{+0.9}$
$6_1^+$	709.1	$6.2_{-2.1}^{+1.6}$
$3_1^-$	844.9	$2.5_{-0.5}^{+0.7}$
$4_2^+$	431.6	$27_{-6}^{+11}$ <sup>c</sup>

<sup>a</sup>Moszynski and Mach [13].

<sup>b</sup>Mach *et al.* [14].

<sup>c</sup>Effective lifetime.

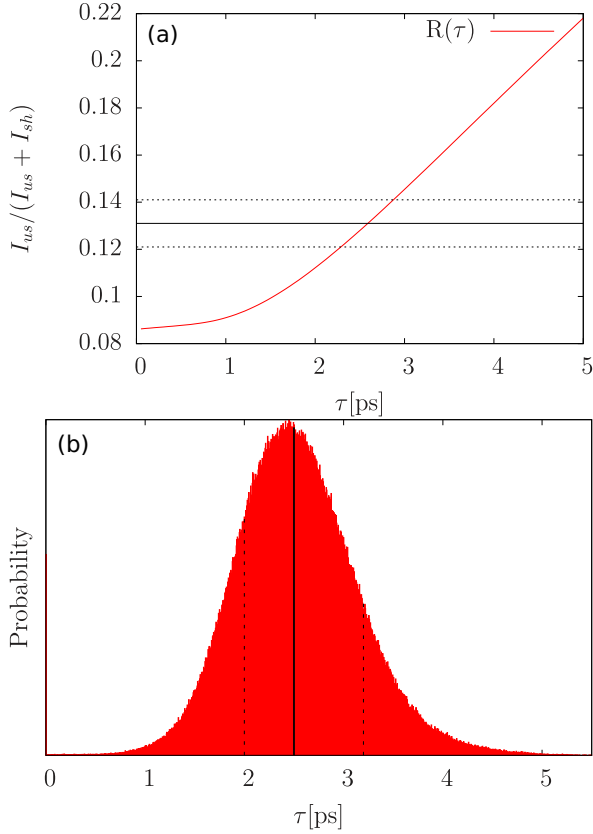


FIG. 7.  $R(\tau)$  curve (a) and probability distribution (b) for the  $3_1^-$  state. See text for details.

the feeding lifetime. All lifetimes resulting from this analysis are summarized in Table II.

#### IV. DISCUSSION OF THE RESULTS

Prior to this experiment lifetime information of excited states in  $^{144}\text{Ce}$  was restricted to the  $2_1^+$  state, where two lifetime measurements from the year 1989 exist [13,14]. Both measurements used timing techniques (slope method and centroid shift, respectively) from which one agrees with the result obtained here within the error bars. The precision of that lifetime, however, is now improved. All other lifetime information is measured for the first time.

The results of this measurement were used to calculate  $B(E2)$  and  $B(E1)$  values, assuming pure transitions. For the  $6_1^+ \rightarrow 4_1^+$  transition Ref. [11] reports a competing transition to the  $5_1^-$  state with a branching of 0.75(6) (to the  $4_1^+$  state) and 0.25(6) (to the  $5_1^-$  state), respectively, which was not observed in this experiment. Nevertheless, the literature branching ratio was used to determine the  $B(E2, 6_1^+ \rightarrow 4_1^+)$  as well as the  $B(E1, 6_1^+ \rightarrow 5_1^-)$  value from the lifetime of the  $6_1^+$  state. For the  $3_1^-$  state additionally to the  $3_1^- \rightarrow 2_1^+$  transition also a transition leading to the  $4_1^+$  state is reported with a branching of 0.07(2) [11]. Also in this case the branching was used to calculate transition strengths for both transitions. The results are shown in Table III.

In Fig. 8 known  $B(E2, 2_1^+ \rightarrow 0_{gs})$  values of the neighboring even-even cerium, barium, and neodymium isotopes

TABLE III. Transition strengths in comparison to shell-model calculations.

Transition	$E\lambda$	$B(E\lambda)(e^\lambda\text{fm}^{2\lambda})$ (expt.)	$B(E\lambda)(e^\lambda\text{fm}^{2\lambda})$ (theor. <sup>a</sup> )
$2_1^+ \rightarrow 0_{gs}^+$	$E2$	$1464^{+13}_{-13}$	1620
$4_1^+ \rightarrow 2_1^+$	$E2$	$1853^{+82}_{-162}$	2355
$6_1^+ \rightarrow 4_1^+$	$E2$	$537^{+289}_{-118}$	2563
$6_1^+ \rightarrow 5_1^-$	$E1$	$(1.3^{+0.7}_{-0.4}) \times 10^{-2}$	—
$3_1^- \rightarrow 4_1^+$	$E1$	$(5.9^{+2.4}_{-1.9}) \times 10^{-4}$	—
$3_1^- \rightarrow 2_1^+$	$E1$	$(3.9^{+1.0}_{-0.8}) \times 10^{-4}$	—

<sup>a</sup>Naidja *et al.* [11].

are shown together with the newly measured one from this work, beginning at the neutron shell closure at  $N=82$ . Up to  $N=88$  the evolution of the  $B(E2)$  values can be well described by a linear function, resembling the description of the neutron-deficient isotopes, as displayed in Ref. [15]. This behavior is expected because the collectivity should grow nearly linearly with increasing numbers of valence nucleons for nuclei near closed shells. The abrupt break of the linear behavior, which occurs in the cerium and neodymium chains for  $N=90$  matches with the above mentioned shape phase transition that is expected between  $N=88$  and  $N=90$  [2]. Also this comparison again points out the similarities of the lanthanide nuclei in this mass region.

In the following the results will be discussed in comparison to recent shell-model calculations, which predict  $B(E2)$  values in the yrast cascade as well as regarding their impact on the discussion about octupole correlations in  $^{144}\text{Ce}$ .

#### A. Comparison with shell-model calculations

Shell-model calculations for  $^{144}\text{Ce}$ , together with  $^{142}\text{Ba}$ , were carried out by Naidja *et al.* in Ref. [11] using the  $r4h - r5i$  model space, which consists of the  $1f_{7/2}$ ,  $0h_{9/2}$ ,  $1f_{5/2}$ ,  $2p_{3/2}$ ,  $1p_{1/2}$ ,  $0i_{13/2}$  orbitals for neutrons and the  $0g_{7/2}$ ,

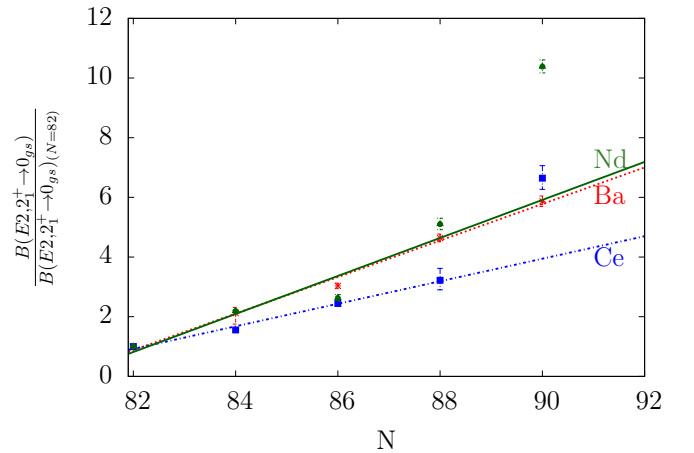


FIG. 8. Systematic of the  $B(E2, 2_1^+ \rightarrow 0_{gs})$  values, normalized to the value for  $N=82$ , for cerium, barium, and neodymium isotopes above the  $N=82$  shell closure. Data for other Ce isotopes taken from Refs. [16–18]. Data of barium and neodymium isotopes adopted from [8]. The lines are drawn to guide the eye.

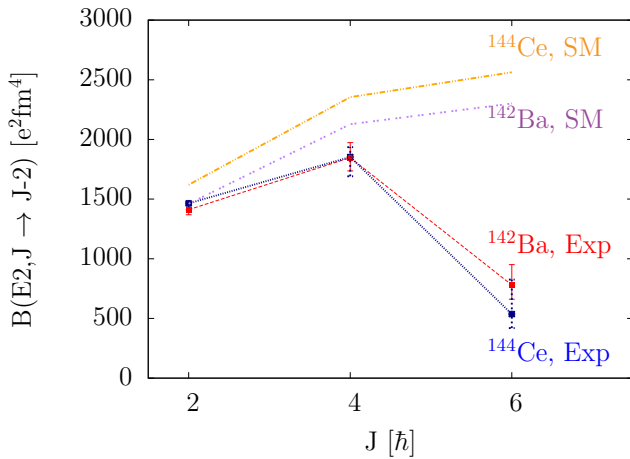


FIG. 9. Comparison of shell-model predictions from Ref. [11] (marked as SM) together with experimentally determined  $B(E2)$  transition strengths of  $^{144}\text{Ce}$  (from this work) and  $^{142}\text{Ba}$  (taken from Refs. [19,21,22]).

$1d_{5/2}$ ,  $1d_{3/2}$ ,  $2s_{1/2}$ ,  $0h_{11/2}$  orbitals for protons and the N3LOP interaction described in Ref. [7]. For  $^{144}\text{Ce}$  the occupation numbers of the  $0h_{11/2}$  proton orbital and the  $0i_{13/2}$  neutron orbital were limited as a necessary truncation. Together with a good reproduction of the level energies of low-lying levels also  $Q_i$  values for the yrast cascade up to the  $6_1^+$  state are given which can be used to deduce the shell-model predictions for the respective  $B(E2)$  values. In Table III and Fig. 9 these predictions are compared to the experimental  $B(E2)$  values. For the  $B(E2)$  values of the  $2_1^+ \rightarrow 0_1^+$  and the  $4_1^+ \rightarrow 2_1^+$  transitions the trend is well reproduced. The slight overestimation may be from the choice of the effective proton and neutron charges of 1.6e and 0.6e, respectively, in the SM calculation. On the other hand, the shell model is not able to reproduce the sharp drop of the  $6_1^+ \rightarrow 4_1^+$  transition strength. For comparison also the  $B(E2)$  values for the same transitions in the neighboring isotope  $^{142}\text{Ba}$  are shown, together with the respective shell-model predictions from Ref. [11]. As can be seen in Fig. 1, the level structure in the yrast and the supposed octupole band of  $^{144}\text{Ce}$  and  $^{142}\text{Ba}$  are very alike. Therefore one could expect the same for the behavior of the  $B(E2)$  values and indeed the experimental values are nearly identical to the ones from  $^{144}\text{Ce}$  including the drop described above. Shell-model predictions are again not able to describe the drop of the  $B(E2, 6_1^+ \rightarrow 4_1^+)$ . However, it has to be mentioned that the pictured  $B(E2)$  value of the  $6_1^+ \rightarrow 4_1^+$  transition in  $^{142}\text{Ba}$  originates from an experiment, analyzed in a thesis [19], from which the same author in a later paper [20] states that it was not possible to analyze the  $6_1^+$  state's decay because of potential contaminations. Nevertheless, the comparison here supports the result of that author's first analysis.

### B. Octupole deformation

The phenomenon of octupole deformation in atomic nuclei was long under research. Recent experimental results, making use of modern ion beam facilities and detector arrays, have again raised interest by directly measuring octupole  $E3$

transition strengths [6,23,24]. Octupole deformation leads to reflection asymmetric nuclear shapes and is mainly indicated by low-lying negative parity bands that alternate with the positive parity yrast bands and fast  $E1$  transitions between these bands. The resulting large intrinsic dipole moments  $D_0$  are explained by the displacement from the center-of-mass of proton and neutron densities in asymmetric nuclei [25]. Characteristic  $E3$  transitions competing with  $E2/E1$  transitions are often too weak to be directly observed but are crucial to determine whether a nucleus exhibits stable octupole deformation or if it behaves like an octupole vibrator. Because this is also the case for  $^{144}\text{Ce}$  this discussion is limited to the measured  $E1$  transition strengths.

The nucleus  $^{144}\text{Ce}$  belongs to the region around  $N \approx 88$ ,  $Z \approx 56$ , where strong octupole deformation is expected and was, in fact, observed in various numbers of experiments. Prominent examples are the aforementioned measurements described in Refs. [6,23] on  $^{144,146}\text{Ba}$  that yielded largely enhanced  $E3$  transition strengths. For cerium isotopes calculations done by Agbemava *et al.* within different covariant density functional frameworks (namely the covariant energy density functionals DD-PC1 [26], NL3\* [27], DD-ME2 [28], PC-PK1 [29], and DD-ME $\delta$  [30]) predict strong octupole deformation for  $N \geq 88$ , whereas weaker octupole deformation is already predicted for  $N = 86$  [31]. Other recent calculations by Xia *et al.* use a quadrupole-octupole collective Hamiltonian (QOCH) with parameters determined based on the PC-PK1 density functional [32]. The resulting deformation energy surfaces show that  $^{144}\text{Ce}$  is expected to be soft on the octupole degree of freedom, but show no finite value of equilibrium octupole deformation. Similar to the calculations by Agbemava *et al.* the latter is predicted for  $^{146}\text{Ce}$  and heavier cerium isotopes. Another aspect worth noting is that the deformation energy surfaces shown in Ref. [32] for  $^{144}\text{Ce}$  and  $^{142}\text{Ba}$  are much alike, as expected from the comparison of the level energies and  $E2$  transition strengths shown in Fig. 9.

On the experimental side, the literature reports the yrast low-lying negative parity band in  $^{144}\text{Ce}$  to be a good candidate for an octupole deformed band [5]. For states with  $J > 5$  it exhibits the typical interspacing of positive and negative parity states together with the positive parity yrast band expected for octupole deformation. To further investigate the case, the experimental observables of choice are the transition strengths between the yrast alternating parity states. These values are significantly enhanced if octupole deformation plays a role. In the case of  $^{144}\text{Ce}$  up to now only  $E1$  transitions between the bands of interest have been observed.  $B(E1)$  transition strengths stronger than  $\approx 10^{-5}$  W.u. are an indicator of reflection asymmetry, i.e., octupole deformation [4]. The values measured in this work for the  $6_1^+ \rightarrow 5_1^-$ ,  $3_1^- \rightarrow 4_1^+$ , and  $3_1^- \rightarrow 2_1^+$  transitions certainly fall into that category. Especially the  $6_1^+ \rightarrow 5_1^-$  transition strength exceeds the typical range for  $E1$  transitions quite drastically. This is best seen when expressed in Weisskopf units, where  $B(E1, 6_1^+ \rightarrow 5_1^-) = (7.2_{-1.9}^{+2.9}) \times 10^{-3}$  W.u. It has to be stressed that this value is extremely close to 0.01 W.u., which is the recommended upper limit for  $E1$  transitions in this mass region as given in Ref. [33]. This value even exceeds  $E1$  strengths in  $^{144}\text{Ba}$ , which is assumed to exhibit much stronger octupole deformation [25].



TABLE IV. Experimental intrinsic dipole moments in comparison with theoretical calculations for the given spin ranges.

$I^\pi (\hbar)$	$D_0(\text{efm})$ (expt.)	$J$ range <sup>theor.</sup>	$D_0(\text{efm})$ (theor.) <sup>a</sup>
$3_1^-$	0.06(1)	0	0.17
$6_1^+$	0.33(9)	5–9	0.20

<sup>a</sup>Butler and Nazarewicz [34].

It is thus an indicator for a very strong collective behavior of this transition.

Furthermore the measured  $B(E1)$  values can be used to calculate the intrinsic dipole transition moment  $D_0$  for the respective transitions between the states with the angular momenta  $I_i$  and  $I_f$  using the formula,

$$D_0^2 = \frac{4\pi}{3} B(E1) \frac{1}{(I_i 010 | I_f 0)^2}, \quad (3)$$

where  $\langle I_i 010 | I_f 0 \rangle$  is the Clebsch-Gordan coefficient. Experimental results for the dipole moments from this work together with theoretical predictions obtained with a shell-correction approach carried out in Ref. [34] are shown in Table IV. To calculate the dipole moment of the  $3_1^-$  state the transition to the  $2_1^+$  state was used. The dipole moment of the  $3_1^-$  state is compared to the predicted value of the ground state, which is the one given for that spin range in Ref. [34], and is somewhat lower than that value. The one of the  $6_1^+$  state is remarkably high but not too far away from the predicted value. In the systematic comparisons shown in Ref. [4] and adapted from there in Ref. [32] it can be seen that similarly high dipole moments in octupole candidates have only been measured in  $^{152}\text{Sm}$  and the much heavier  $^{218-222}\text{Ra}$  and  $^{220-226}\text{Th}$  isotopes.

Concluding this discussion, the newly measured transition strengths and the calculated transition dipole moments provide a strong indication for the octupole character of the negative parity yrast band in  $^{144}\text{Ce}$ . Especially the strong transition between the  $6_1^+$  and the  $5_1^-$  state matches well with the beginning of the interchanging between positive and negative parity states at these spin values, which is typical for octupole deformation. A structural change at this spin could

also possibly explain why the shell-model predictions for this state deviate strongly from the experimental values.

## V. CONCLUSION

In summary, studies of transition strengths between yrast states in  $^{144}\text{Ce}$  have been carried out by measuring lifetimes of the  $2_1^+$ ,  $4_1^+$ ,  $6_1^+$ , and  $3_1^-$  states, the last three were determined for the first time, and a new effective lifetime of the  $4_2^+$  state, using the RDDS method. The newly measured  $B(E2, 2_1^+ \rightarrow 0_{gs}^+)$  value fits very well in the systematics of the surrounding neutron-rich cerium isotopes. Furthermore  $B(E2)$  values in the ground-state band have been compared to existing shell-model calculations, where a good qualitative agreement up to the  $4_1^+ \rightarrow 2_1^+$  transition was found. However, the experimental value for the  $6_1^+ \rightarrow 4_1^+$  deviates strongly from the predictions, hinting at a change in the structure of the  $6_1^+$  state which is not incorporated in the shell model. Lastly, the measured lifetimes were used to get some indications about octupole deformation in  $^{144}\text{Ce}$ , by determining  $B(E1)$  transition strengths as well as intrinsic transition dipole moments and comparing them to calculations assuming such deformations. The resulting very large values for both properties in comparison to similar nuclei yield a strong backing for the hypothesis that the negative parity yrast band exhibits octupole deformation, especially at higher spins.

To provide further knowledge regarding the question if a nonzero static octupole deformation is present in  $^{144}\text{Ce}$ , a measurement of  $E3$  transitions has to be carried out. The best candidate is a  $3_1^- \rightarrow 0_{gs}^+$  transition, that was observed in many nearby nuclei. However, assuming a  $B(E3, 3_1^- \rightarrow 0_{gs}^+)$  value similar to that of other octupole candidates, the expected branching ratio for such a transition would be extremely small. Therefore a measurement employing multistep Coulomb excitation, as described, for example, in Ref. [24], seems to be the most viable method. The lifetimes measured in this work would become extremely useful for such a measurement to restrain the use of free parameters.

## ACKNOWLEDGMENT

This work was supported by the Bundesministerium für Bildung und Forschung (BMBF) under Contract No. 05P18PKFN9.

- [1] J. B. Gupta, *Phys. Rev. C* **87**, 064318 (2013).  
 [2] P. Koseoglou, V. Werner, N. Pietralla, S. Ilieva, T. Nikšić, D. Vretenar, P. Alexa, M. Thürauf, C. Bernards, A. Blanc, A. M. Bruce, R. B. Cakirli, N. Cooper, L. M. Fraile, G. de France, M. Jentschel, J. Jolie, U. Köster, W. Korten, T. Kröll, S. Lalkovski, H. Mach, N. Märginean, P. Mutti, Z. Patel, V. Pazy, Z. Podolyák, P. H. Regan, J.-M. Régis, O. J. Roberts, N. Saed-Samii, G. S. Simpson, T. Soldner, C. A. Ur, W. Urban, D. Wilmsen, and E. Wilson, *Phys. Rev. C* **101**, 014303 (2020).  
 [3] P. A. Butler, *J. Phys. G: Nucl. Part. Phys.* **43**, 073002 (2016).  
 [4] P. A. Butler and W. Nazarewicz, *Rev. Mod. Phys.* **68**, 349 (1996).  
 [5] S. Zhu, Q. Lu, J. Hamilton, A. Ramayya, L. Peker, M. Wang, W. Ma, B. Babu, T. Ginter, J. Kormicki, D. Shi, J. Deng, W. Nazarewicz, J. Rasmussen, M. Stoyer, S. Chu, K. Gregorich, M. Mohar, S. Asztalos, S. Prussin, J. Cole, R. Aryaeinejad, Y. Dardenne, M. Drigert, K. Moody, R. Loughed, J. Wild, N. Johnson, I. Lee, F. McGowan, G. Ter-Akopian, and Y. Oganessian, *Phys. Lett. B* **357**, 273 (1995).  
 [6] B. Bucher, S. Zhu, C. Y. Wu, R. V. F. Janssens, D. Cline, A. B. Hayes, M. Albers, A. D. Ayangeakaa, P. A. Butler, C. M. Campbell, M. P. Carpenter, C. J. Chiara, J. A. Clark, H. L. Crawford, M. Cromaz, H. M. David, C. Dickerson, E. T. Gregor, J. Harker, C. R. Hoffman, B. P. Kay, F. G. Kondev,

- A. Korichi, T. Lauritsen, A. O. Macchiavelli, R. C. Pardo, A. Richard, M. A. Riley, G. Savard, M. Scheck, D. Seweryniak, M. K. Smith, R. Vondrasek, and A. Wiens, *Phys. Rev. Lett.* **116**, 112503 (2016).
- [7] H. Naïdja, F. Nowacki, and B. Bounthong, *Phys. Rev. C* **96**, 034312 (2017).
- [8] ENSDF database as of october 1st, 2019. Version available at <http://www.nndc.bnl.gov/ensarchivals>.
- [9] A. Dewald, O. Möller, and P. Petkov, *Prog. Part. Nucl. Phys.* **67**, 786 (2012).
- [10] J. Litzinger, A. Blazhev, A. Dewald, F. Didierjean, G. Duchêne, C. Fransen, R. Lozeva, K. Sieja, D. Verney, G. de Angelis, D. Bazzacco, B. Birkenbach, S. Bottoni, A. Bracco, T. Braunroth, B. Cederwall, L. Corradi, F. C. L. Crespi, P. Désesquelles, J. Eberth, E. Ellinger, E. Farnea, E. Fioretto, R. Gernhäuser, A. Goasduff, A. Görgen, A. Gottardo, J. Grebosz, M. Hackstein, H. Hess, F. Ibrahim, J. Jolie, A. Jungclaus, K. Kolos, W. Korten, S. Leoni, S. Lunardi, A. Maj, R. Menegazzo, D. Mengoni, C. Michelagnoli, T. Mijatovic, B. Million, O. Möller, V. Modamio, G. Montagnoli, D. Montanari, A. I. Morales, D. R. Napoli, M. Niikura, G. Pollarolo, A. Pullia, B. Quintana, F. Recchia, P. Reiter, D. Rosso, E. Sahin, M. D. Salsac, F. Scarlassara, P.-A. Söderström, A. M. Stefanini, O. Stezowski, S. Szilner, C. Theisen, J. J. Valiente Dobón, V. Vandone, and A. Vogt, *Phys. Rev. C* **92**, 064322 (2015).
- [11] H. Naïdja, F. Nowacki, B. Bounthong, M. Czerwiński, T. Rzaca-Urban, T. Rogiński, W. Urban, J. Wiśniewski, K. Sieja, A. G. Smith, J. F. Smith, G. S. Simpson, I. Ahmad, and J. P. Greene, *Phys. Rev. C* **95**, 064303 (2017).
- [12] T. Johnson, D. Symochko, M. Fadil, and J. Tuli, *Nucl. Data Sheets* **112**, 1949 (2011).
- [13] M. Moszynski and H. Mach, *Nucl. Instrum. Methods A* **277**, 407 (1989).
- [14] H. Mach, R. Gill, and M. Moszynski, *Nucl. Instrum. Methods A* **280**, 49 (1989).
- [15] A. Dewald, *Prog. Part. Nucl. Phys.* **28**, 409 (1992).
- [16] B. Pritychenko, M. Birch, B. Singh, and M. Horoi, *At. Data Nucl. Data Tables* **107**, 1 (2016).
- [17] R. H. Spear, W. J. Vermeer, S. M. Burnett, G. J. Cyapong, and C. S. Lim, *Aust. J. Phys.* **42**, 345 (1989).
- [18] C. Goodin, J. R. Stone, N. J. Stone, A. V. Ramayya, A. V. Daniel, J. H. Hamilton, K. Li, J. K. Hwang, G. M. Ter-Akopian, and J. O. Rasmussen, *Phys. Rev. C* **79**, 034316 (2009).
- [19] G. Mamane, Ph.D. thesis, Weizmann Institute of Science, Rehovot, 1983.
- [20] G. Mamane, E. Cheifetz, E. Dafni, A. Zemel, and J. Wilhelmy, *Nucl. Phys. A* **454**, 213 (1986).
- [21] H. Mach, W. Nazarewicz, D. Kusnezov, M. Moszynski, B. Fogelberg, M. Hellström, L. Spanier, R. L. Gill, R. F. Casten, and A. Wolf, *Phys. Rev. C* **41**, R2469 (1990).
- [22] D. C. Biswas, A. G. Smith, R. M. Wall, D. Patel, G. S. Simpson, D. M. Cullen, J. L. Durell, S. J. Freeman, J. C. Lisle, J. F. Smith, B. J. Varley, T. Yousef, G. Barreau, M. Petit, C. Theisen, E. Bouchez, M. Houry, R. Lucas, B. Cahan, A. Le Coguie, B. J. P. Gall, O. Dorvaux, and N. Schulz, *Phys. Rev. C* **71**, 011301(R) (2005).
- [23] B. Bucher, S. Zhu, C. Y. Wu, R. V. F. Janssens, R. N. Bernard, L. M. Robledo, T. R. Rodríguez, D. Cline, A. B. Hayes, A. D. Ayangeakaa, M. Q. Buckner, C. M. Campbell, M. P. Carpenter, J. A. Clark, H. L. Crawford, H. M. David, C. Dickerson, J. Harker, C. R. Hoffman, B. P. Kay, F. G. Kondev, T. Lauritsen, A. O. Macchiavelli, R. C. Pardo, G. Savard, D. Seweryniak, and R. Vondrasek, *Phys. Rev. Lett.* **118**, 152504 (2017).
- [24] P. A. Butler, L. P. Gaffney, P. Spagnoletti, K. Abrahams, M. Bowry, J. Cederkäll, G. de Angelis, H. De Witte, P. E. Garrett, A. Goldkuhle, C. Henrich, A. Illana, K. Johnston, D. T. Joss, J. M. Keatings, N. A. Kelly, M. Komorowska, J. Konki, T. Kröll, M. Lozano, B. S. Nara Singh, D. O'Donnell, J. Ojala, R. D. Page, L. G. Pedersen, C. Raison, P. Reiter, J. A. Rodriguez, D. Rosiak, S. Rothe, M. Scheck, M. Seidlitz, T. M. Shneidman, B. Siebeck, J. Sinclair, J. F. Smith, M. Stryczyk, P. Van Duppen, S. Vinals, V. Virtanen, N. Warr, K. Wrzosek-Lipska, and M. Zielińska, *Phys. Rev. Lett.* **124**, 042503 (2020).
- [25] W. R. Phillips, I. Ahmad, H. Emling, R. Holzmann, R. V. F. Janssens, T. L. Khoo, and M. W. Drigert, *Phys. Rev. Lett.* **57**, 3257 (1986).
- [26] T. Nikšić, D. Vretenar, and P. Ring, *Phys. Rev. C* **78**, 034318 (2008).
- [27] G. Lalazissis, S. Karatzikos, R. Fission, D. P. Arteaga, A. Afanasjev, and P. Ring, *Phys. Lett. B* **671**, 36 (2009).
- [28] G. A. Lalazissis, T. Nikšić, D. Vretenar, and P. Ring, *Phys. Rev. C* **71**, 024312 (2005).
- [29] P. W. Zhao, Z. P. Li, J. M. Yao, and J. Meng, *Phys. Rev. C* **82**, 054319 (2010).
- [30] X. Roca-Maza, X. Viñas, M. Centelles, P. Ring, and P. Schuck, *Phys. Rev. C* **84**, 054309 (2011).
- [31] S. E. Agbemava, A. V. Afanasjev, and P. Ring, *Phys. Rev. C* **93**, 044304 (2016).
- [32] S. Y. Xia, H. Tao, Y. Lu, Z. P. Li, T. Nikšić, and D. Vretenar, *Phys. Rev. C* **96**, 054303 (2017).
- [33] P. Endt, *At. Data Nucl. Data Tables* **26**, 47 (1981).
- [34] P. Butler and W. Nazarewicz, *Nucl. Phys. A* **533**, 249 (1991).



**6 Publication IV:**

**Lifetime measurement of the  $2_1^+$ ,  $4_1^+$  states in semi-magic  $^{60}\text{Ni}$**





# Lifetime measurement of the $2_1^+$ , $4_1^+$ states in semi-magic $^{60}\text{Ni}$

Marcel Beckers<sup>a</sup> , Claus Müller-Gattermann, Konrad Arnsward, Thomas Braunroth, Alfred Dewald, Christoph Fransen, Alina Goldkuhle, Franziskus von Spee

Institute for Nuclear Physics, University of Cologne, Zùlpicher Str. 77, 50937 Cologne, Germany

Received: 1 February 2023 / Accepted: 13 May 2023

© The Author(s), under exclusive licence to Società Italiana di Fisica and Springer-Verlag GmbH Germany, part of Springer Nature 2023

Communicated by Wolfram Kortén

**Abstract** A  $\gamma$ - $\gamma$  coincidence Recoil Distance Doppler-Shift measurement has been carried out on  $^{60}\text{Ni}$  to re-measure the lifetime of the  $2_1^+$  and  $4_1^+$  states. The new lifetime of the  $2_1^+$  state supports the adopted NNDC value but disagrees with the results of two more recent Doppler-Shift Attenuation Method measurements, which suggested a longer lifetime. The new result for the  $4_1^+$  state's lifetime is significantly shorter than the one recommended in the latest NNDC compilation while also reducing its uncertainty. It therefore resolves an unclear situation, where an unexpected drop in transition strength appeared from  $^{58}\text{Ni}$  to  $^{60}\text{Ni}$ . Both values match very well with recently applied shell model calculations using the GXPF1A interaction.

## 1 Introduction

The chain of semi-magical Ni isotopes has been of interest for nuclear structure studies for a rather long time. Ni isotopes include three double shell-closures at  $^{48}\text{Ni}$  ( $Z = 28$ ,  $N = 20$ ),  $^{56}\text{Ni}$  ( $N = Z = 28$ ) and  $^{78}\text{Ni}$  ( $N = 50$ ) as well as a tentative neutron sub-shell closure at  $^{68}\text{Ni}$  ( $N = 40$ ). A special focus has lately been set on the isotopes leading to and around this sub-shell closure, where Monte-Carlo shell model (MSCM) calculations predict possible shape coexistence and also experimental evidence was found in  $^{68}\text{Ni}$  [1]. Very recently, a measurement on  $^{64}\text{Ni}$  found evidence that features of shape coexistence might be present in this nucleus as well [2].

To gain insights into the structure of nuclei, lifetime measurements of excited states can be utilized to obtain the transition strengths between these states. These serve as important structural indicators and therefore as benchmarks for theoretical approaches like shell-model calculations that aim to describe the nuclei's behavior.

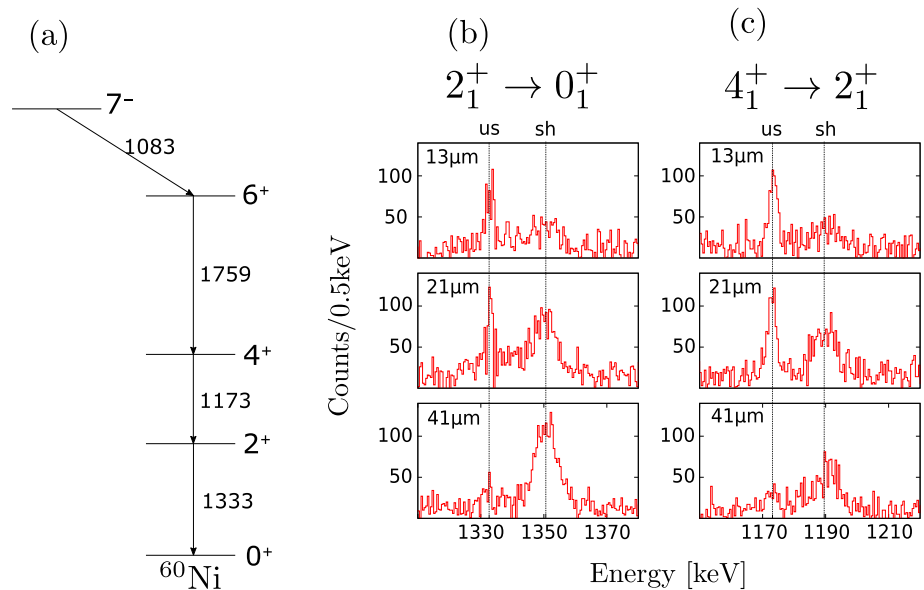
Regarding the Ni isotopic chain, one can find a quite confusing situation around  $^{62}\text{Ni}$ . The region around this nucleus will further be called mid-shell region, referring to the tentative sub-shell closure at  $N = 40$  mentioned above. There are several reports on quadrupole transition strengths for the  $2_1^+ \rightarrow 0_1^+$  and the  $4_1^+ \rightarrow 2_1^+$  transitions in these nuclei that are partly in disagreement with each other.

In detail, there is one data set resulting from a Doppler Shift Attenuation (DSA) measurement by Kenn et al. [3] giving high precision E2 values for  $^{58-62}\text{Ni}$  that mostly disagree with an older compilation by Raman et al. [4]. Especially, for the  $4_1^+ \rightarrow 2_1^+$  transitions the results by Kenn et al. suggest that the transition strength drops from  $A = 58$  towards  $A = 60$ . This behavior would be highly unexpected and could hint at new and interesting structure evolution in these nuclei. Another experiment, reported by Loelius et al. [5], re-measured the lifetime of the  $4_1^+$  state in  $^{58}\text{Ni}$  using the Recoil Distance Doppler-Shift (RDDS) technique. If the lifetime value reported from this measurement is used to calculate the transition strength, the aforementioned drop of the  $B(E2, 4_1^+ \rightarrow 2_1^+)$  values vanishes. However, the available data up to now would then suggest a nearly identical  $B(E2, 4_1^+ \rightarrow 2_1^+)$  for  $^{58,60}\text{Ni}$ , which would be rather uncommon. Loelius et al. report also on results of shell-model calculations for  $B(E2, 4_1^+ \rightarrow 2_1^+)$  values of  $^{56-64}\text{Ni}$ , which show a very good agreement with the newly measured value and suggest that the transition strengths increase further towards mid-shell.

For the  $2_1^+ \rightarrow 0_1^+$  transitions, the different sets of experimentally determined  $B(E2)$  values also pose a problem in the interpretation of the Ni isotopic chain around  $N = 62$ . Following the results of Kenn et al., which are further supported by another measurement by Orce et al. [6], the evolution of the  $B(E2, 2_1^+ \rightarrow 0_1^+)$  values along the isotopic chain would take on a rather symmetric form around mid-shell, which would be expected if the  $N = 40$  sub-shell closure is robust for the Ni isotopes. However, if the value for  $^{60}\text{Ni}$

<sup>a</sup> e-mail: mbeckers@ikp.uni-koeln.de (corresponding author)

**Fig. 1** (a) Partial level scheme of  $^{60}\text{Ni}$ , showing only the transitions used in this analysis and the  $7_1^-$  isomeric feeding state. (b) Spectra of the  $2_1^+$  and the  $4_1^+$  (c) state decays measured with forward angle detectors at different distances. To obtain the spectra, gates on the flight component of the respective direct feeders were used



from the older compilation, that is supported by another more recent Coulomb excitation experiment by Allmond et al. [7] is used, an asymmetric form is exposed, where the transition strength reaches its maximum already at  $N = 60$  and then drops slightly towards mid-shell. This could have implications on the interpretation of the sub-shell closure. To help clarify this confusing situation, a new RDDS measurement on the lifetimes of the  $2_1^+$  and  $4_1^+$  states has been conducted at the Cologne FN tandem accelerator.

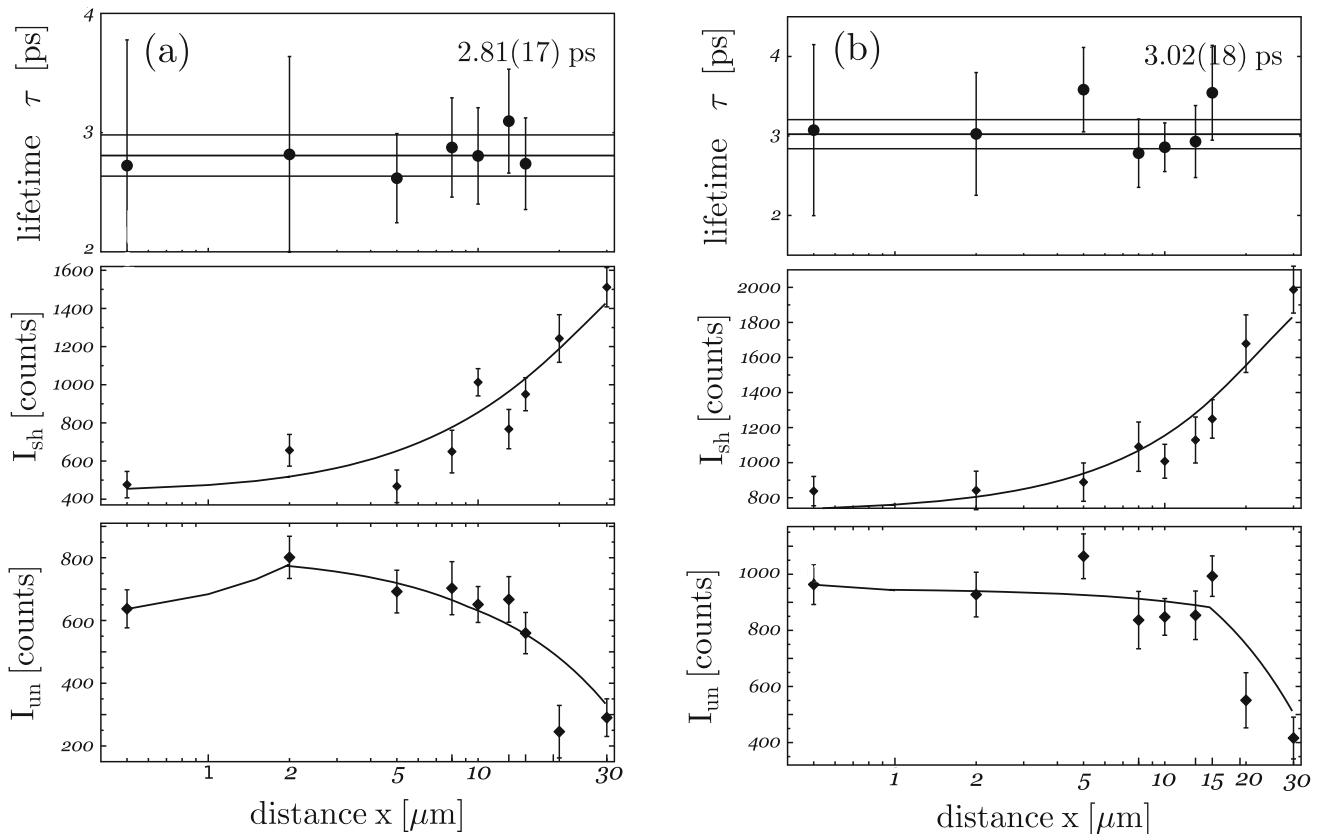
## 2 Experiment

The experiment took place at the Institute for Nuclear Physics of the University of Cologne. The Cologne FN tandem accelerator delivered a beam of  $^{23}\text{Na}$  with an energy of 62 MeV. The reaction took place in the chamber of the Cologne Coincidence Plunger [8], where the beam hit a target of  $0.5 \frac{\text{mg}}{\text{cm}^2}$  natural Ca, sandwiched between a  $2.2 \frac{\text{mg}}{\text{cm}^2}$  Au support foil facing the beam and a  $0.1 \frac{\text{mg}}{\text{cm}^2}$  Au backing, which protects the Ca from oxidation. The  $^{40}\text{Ca}(^{23}\text{Na}, 3p)^{60}\text{Ni}$  reaction produced the nucleus of interest with a recoil velocity of  $\approx 2\%c$ . The recoiling nuclei have been stopped in a  $7.3 \frac{\text{mg}}{\text{cm}^2}$  Ta foil. The Cologne Coincidence Plunger was used to vary the separation between the target and the stopper foil and to keep the distances constant using a feedback system.  $\gamma$  rays emitted from the decaying excited states were measured with eleven large volume Germanium detectors that are arranged in two rings at  $45^\circ$  and  $142.3^\circ$  with respect to the beam axis, respectively. Data was collected using a digital data acquisition (DAQ) system consisting of XIA DGF-4c Rev. F modules. A total of nine different target-to-stopper distances from  $12\mu\text{m}$  to  $41\mu\text{m}$  in absolute values have been measured and the resulting events were sorted in  $\gamma$ - $\gamma$  coincidences after

applying corrections for gain shifts of the Ge detectors and random background subtraction.

## 3 Data Analysis

The  $\gamma$ - $\gamma$  coincidence data have been analyzed using the Differential Decay Curve Method (DDCM) [9]. In the standard implementation of this method, gates on the flight component of the transition feeding the state of interest are used. This way, a fixed decay cascade is selected and no feeding assumptions have to be applied, which enables high precision results that do not depend on any non-observed quantities, such as delayed feeding. Furthermore only relative target-to-stopper distances are needed for this approach, which can be measured with high precision. In addition to the mentioned advantages, in this analysis gates on flight components of feeding transitions were even more important, because in  $^{60}\text{Ni}$  a long-lived ( $\tau \approx 360\text{ps}$  [10]) isomeric  $7_1^-$  state exists, which feeds into the  $6_1^+$  state. Therefore, the majority of the recoiling reaction products are already stopped in the stopper foil before reaching to the states of interest. However, there is sufficient fast feeding to the yrast cascade which avoids the isomer, so that gates on the flight components of the  $6_1^+ \rightarrow 4_1^+$  and the  $4_1^+ \rightarrow 2_1^+$  transitions yield enough statistics for a high precision lifetime experiment. A partial level scheme including only transitions which have been observed in this experiment and are important for the analysis is shown in Fig. 1. Spectra of the  $2_1^+$  and  $4_1^+$  state's decays at three different plunger distances obtained with gates on the flight component of the respective direct feeder are also shown in Fig. 1.



**Fig. 2**  $\tau$ -curves showing the determination of the  $4_1^+$  state’s lifetime for forward (a) and backward (b) angle detectors. In the upper panels the respective  $\tau$ -values are shown while in the middle panels the shifted and in the lower panels the unshifted peak intensities are given. Both

plots are obtained using direct gates on the feeding transition. Note that the lifetimes shown here are for the respective single ring combination only while the final lifetime is given by the weighted average of all detector ring combinations (see text for details)

### 3.1 Lifetime of the $4_1^+$ state

Using the DDCM with gates on the direct feeder, the lifetime of the state of interest is obtained via

$$\tau_i(x) = \frac{I_{us}(x)}{\frac{d}{dx} I_{sh}(x)} \cdot \frac{1}{v} \tag{1}$$

where  $I_{us}$  and  $I_{sh}$  denote the intensities of the unshifted and shifted components of the depopulating transition at distance  $x$ , respectively, and  $v$  is the recoil velocity.

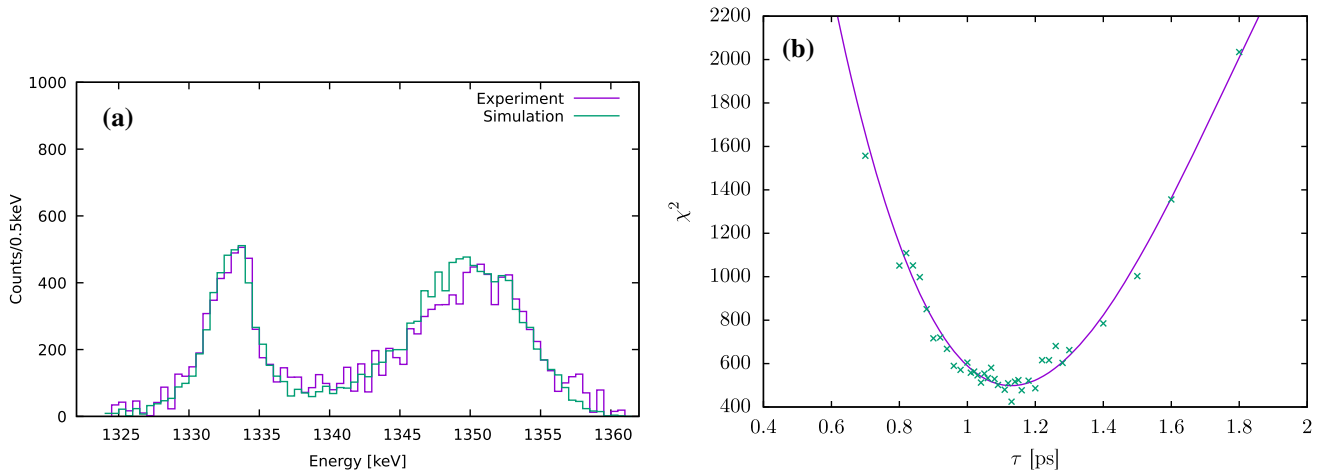
Though no feeding has to be taken into account, much care had to be taken to avoid contaminations within the gates or in the depopulating transitions, because of the high  $\gamma$ -ray line density in the ungated spectra. As a result, not all ring-ring combinations could be used for every state’s analysis.

The intensities of all needed components have been extracted from the spectra and were used to carry out the lifetime analysis. Two examples of resulting  $\tau$  curves for the analysis of the  $4_1^+$  state are shown in Fig. 2. The final result for the  $4_1^+$  state’s lifetime of  $\tau(4_1^+) = 2.9(1)\text{ps}$  is given by the weighted mean over all used ring combinations.

### 3.2 Lifetime of the $2_1^+$ state

Using the DDCM method for the  $2_1^+$  as described above, a lifetime of  $\tau(2_1^+) \approx 0.77\text{ps}$  is derived, which is well within the range of the slowing-down time of the recoils in the stopping foil. Therefore the amount of decays occurring during this slowing-down time can not be neglected and a standard RDDS analysis assuming Gaussian peak shapes is not feasible anymore. The  $2_1^+$  state’s decay was thus analyzed using the *Geant4*-based simulation *PTBG4* [11] which is dedicated to simulate both RDDS and DSAM measurements. The simulation was explicitly adjusted to match the geometry and detector properties of the Cologne Plunger Spectrometer. To fix the feeding for the simulation, the newly analyzed lifetime of the  $4_1^+$  state, which is long enough to neglect the DSA effects, and an effective lifetime of the  $6_1^+$  state were used. The later was determined with a gate from below on both components of the  $2_1^+ \rightarrow 0_1^+$  transition to be 14ps. Despite this relatively long effective feeding time, a gate on the flight component of the  $4_1^+ \rightarrow 2_1^+$  yields an intensity of the  $2_1^+ \rightarrow 0_1^+$  transition of about 22% with respect to a gate





**Fig. 3** (a) Comparison of the experimental spectrum of the  $2_1^+ \rightarrow 0_1^+$  transition and the best fit of the simulation. Shown are summed up spectra with gates from above detected under forward angle. (b)  $\chi^2$  minimization used to determine the lifetime of the  $2_1^+$  state

on both components, meaning there is sufficient fast feeding for the analysis. The gate on the unshifted component of the direct feeder was also used for the comparison with the simulated spectra, where the same gating condition was applied.

The lifetime analysis for the  $2_1^+$  state was performed by minimizing the reduced  $\chi^2$  given by

$$\chi^2 = \sum_N \left( \frac{n_{exp} - n_{sim}}{\Delta n_{exp}} \right)^2, \tag{2}$$

where  $n_{exp}$  and  $n_{sim}$  denote the contents of a single bin from the experimental and the simulated spectra, respectively and  $N$  is the total number of bins taken into account. The lifetime assumption fed into the simulation is varied in steps from 0.01ps to 0.2ps while getting further away from the minimum. The statistical uncertainty is obtained using the  $\chi^2 + 1$ . Because of the delayed feeding issue mentioned above, the experimental statistics in the gated spectra is low and the summed up spectra over all distances have been used to compare to the simulation. The resulting best fit together with the  $\chi^2$  minimization is shown in Fig. 3 for forward detection angles. The same procedure was also applied for backward angle detection. Taking into account the the variance of both values as a measure of systematic uncertainty a final lifetime of  $\tau(2_1^+) = 1.07(7)$ ps is derived.

The results of the lifetime analysis are summarized and compared to results from other measurements in Table 1.

### 4 Discussion

The lifetime of the  $2_1^+$  in  $^{60}\text{Ni}$  state obtained in this measurement matches very well with the adopted value of the

**Table 1** Lifetimes and B(E2) values determined in this work in comparison with older values

Level	$\tau$ [ps]	B(E2)( $J^+ \rightarrow (J - 2)^+$ ) [ $\text{e}^2\text{fm}^4$ ]
$2_1^+$	1.07(7) <sup>(a)</sup>	182(12) <sup>(a)</sup>
	1.31(3) <sup>(b)</sup>	149(3) <sup>(b)</sup>
	1.04(2) <sup>(c)</sup>	187(4) <sup>(c)</sup>
	$1.30^{+0.30}_{-0.20}$ <sup>(d)</sup>	$150^{+27}_{-28}$ <sup>(d)</sup>
	–	182(7) <sup>(e)</sup>
$4_1^+$	2.9(1) <sup>(a)</sup>	$127^{+5}_{-4}$ <sup>(a)</sup>
	4.8(1.5) <sup>(b)</sup>	$77^{+35}_{-18}$ <sup>(b)</sup>

<sup>a</sup>This work

<sup>b</sup>Kenn et al. [3]

<sup>c</sup>Raman et al. [4]

<sup>d</sup>Orce et al. [6]

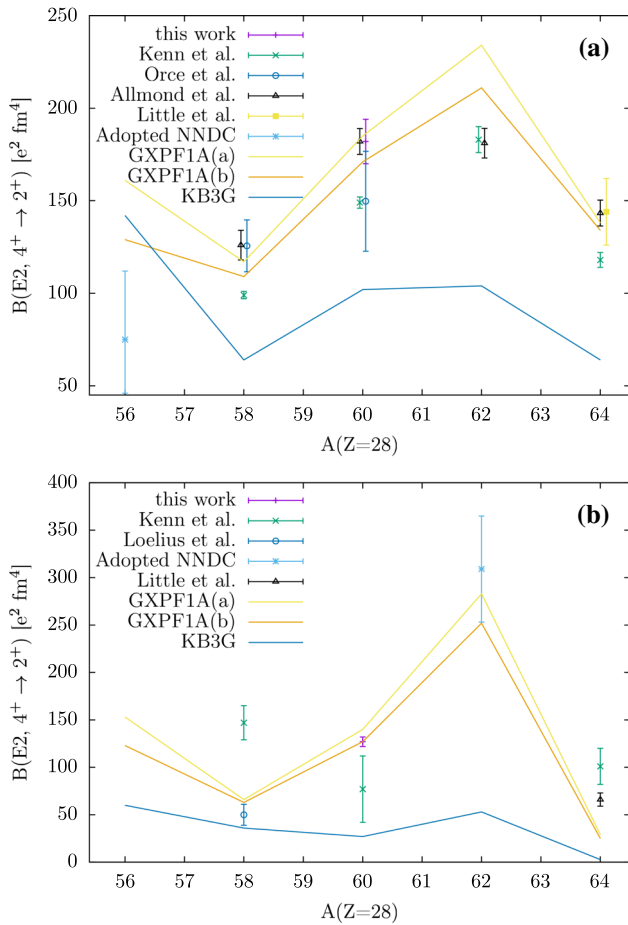
<sup>e</sup>Allmond et al. [7] (calculated from B(E2)( $0_1^+ \rightarrow 2_1^+$ ))

older compilation by Raman et al. The longer lifetime values given by Kenn et al. and Orce et al. can not be reproduced. For the  $4_1^+$  state the obtained lifetime value also differs from the one reported in Ref. [3] while also reducing the uncertainty significantly.

From the newly measured lifetimes, E2 transition strengths have been calculated, which are presented in Table 1. The transition strength determined from the  $2_1^+$  state’s lifetime resulting from this work matches exactly with the one obtained by Allmond et al. from a Coulomb excitation experiment [7].

#### 4.1 Overview of the Ni systematics around A = 62

An overview of the known E2 transition strengths of the Ni isotopes around the mid-shell (A = 62) is given in Fig. 4 for the  $2_1^+ \rightarrow 0_1^+$  and the  $4_1^+ \rightarrow 2_1^+$  transitions. For the former,



**Fig. 4** Comparison of experimentally determined transition strengths for the  $2_1^+$  (a) and the  $4_1^+$  (b) state's decays and different Shell-Model predictions from Ref. [5] for the Ni isotopic chain around the mid-shell. See text for details regarding the different calculations

one can see an increase in B(E2) values from A = 58 to A = 60. This is the expected behavior, because the valence space should reach its maximum the mid-shell if both the shell closure at N = Z = 28 and the subshell closure at N = 40 are robust. However, using the value obtained in this work for A = 60 and the ones for A = 62 from Ref. [3], which also agrees with the one reported by Allmond et al. [7], the transition strength is more or less constant or even decreasing from A = 60 to A = 62. This leads to an asymmetry around the supposed mid-shell at A = 62 since with the increase of the mass number towards A = 64 there is a distinct drop in the B(E2) values. A similar behavior has been mentioned also in Ref. [7] and has been compared to the behavior of the Sn isotopes near to N = Z = 50, shown in Ref. [12]. It might hint at the possibility, that N = 40 is not a good subshell closure in Ni. The robustness of the N = 40 subshell closure has indeed been of high interest in recent studies, especially regarding the phenomenon of shape-coexistence around this neutron number. There have been many reports

of features, that suggest shape-coexistence starting around N = 40 and above in Ni and neighboring nuclei [13]. In a recent study, it was shown that also  $^{64}\text{Ni}$  exhibits shape-coexistence by measuring several  $0^+$  and  $2^+$  states with high excitation energies [14]. Furthermore, there have been high precision mass measurements of nuclei around N = 40 that searched for typical signs of a shell closure and which could not come up with clear indicators [15].

For the  $4_1^+ \rightarrow 2_1^+$  transitions the former anomalous trend that has been present in the data of Ref. [3] disappears when the data point taken from the newer measurement from Loelius et al. [5] is used together with the new value from this work. The data from Ref. [3] suggested a decrease in B(E2) values from A = 58 towards A = 60. This has been rejected by the more recent measurement in A = 58. Combining this with the newly measured value for  $^{60}\text{Ni}$  from this work, an increase in B(E2) from A = 58 to A = 60 can instead be reported, which is consistent with the expected systematic behavior. As opposed to the  $B(E2, 2_1^+ \rightarrow 0_1^+)$  transition strengths, the evolution of transition strengths for the  $4_1^+ \rightarrow 2_1^+$  transitions shows no asymmetry towards mid-shell and above.

#### 4.2 Comparison to Shell-Model Calculations

A recent shell-model calculation for the Ni isotopes around A = 62 has been carried out by Loelius et al. [5], using the GXPF1A [16] and the KB3G [17] interactions to obtain B(E2) values. The results are also shown in Fig. 4. There, the transition strengths labeled as GXPF1A(a) have been calculated with effective boson charges of  $e_p = 1.5, e_n = 0.5$  while for the ones labeled as GXPF1A(b)  $e_p = 1.12, e_n = 0.67$  were used. The values shown for KB3G were also obtained using the standard values of  $e_p = 1.5, e_n = 0.5$ . For A = 60, the newly obtained  $2_1^+ \rightarrow 0_1^+$  transition strength is best described by the “standard” parameter set of GXPF1A(a). Both GXPF1A calculations predict a strong maximum for A = 62, which is not reproduced by the latest experimental results. The KB3G interaction was not able to reproduce the experimental values for all Ni isotopes in that region. However, it predicts a near constant B(E2) for A = 60, A = 62, which is closer to the trend of the experimental values than the expressed peak for A = 62 in the GXPF1A calculations. The failure of the shell-model calculations to reproduce the experimentally observed behavior around the supposed mid-shell could also be accounted for by the aforementioned possibility, that the N = 40 subshell closure might not be very robust. In fact, to describe the more neutron-rich Ni isotopes, which exhibit features of shape-coexistence, it was shown that untruncated Monte-Carlo shell model (MCSM) calculations are needed (for example in Refs. [14, 18]). If the asymmetry is therefore indeed a result of these characteristics, it might even be expected that the calculations shown here are not able to reproduce the exact behavior.

The predicted  $B(E2, 4_1^+ \rightarrow 2_1^+)$  is very similar for both GXPF1A calculations and matches very well with the new experimental value. Here also the overall description of the isotopic chain is very well reproduced when the most recent experimental values are used as a reference. The KB3G calculation is again not able to reproduce the experimental results.

## 5 Conclusion

The lifetimes of the  $2_1^+$  and the  $4_1^+$  states in  $^{60}\text{Ni}$  have been re-measured in a  $\gamma$ - $\gamma$  coincidence RDDS experiment with the intention to clarify the confusing situation introduced by partly contradicting existing data. The results for the  $2_1^+$  state support the older values from the Raman et al. compilation as well as the more recent Coulomb-excitation measurement by Allmond et al. while not supporting the longer lifetime values from the DSAM measurements of Kenn et al. and Orce et al. For the  $4_1^+$  state a high-precision measurement was done for the first time, reducing the uncertainty of its lifetime significantly while also disagreeing with the lifetimes values from the earlier DSAM measurement by Kenn et al.

The newly measured lifetimes match well with GXPF1A shell-model predictions. Especially, the unexpected decrease in the  $4_1^+ \rightarrow 2_1^+$  transition strength as a function of the mass number reported previously for the  $^{58}\text{Ni}$  and  $^{60}\text{Ni}$  pair is neither supported by the data reported here together with the latest measurement in  $^{58}\text{Ni}$  nor the discussed shell model calculations. The lack of a maximum for  $A = 62$  in the behavior of the  $2_1^+ \rightarrow 0_1^+$  transition strengths around mid-shell seems to be verified and can not be described by the standard shell-model calculations. Here, further work, possibly including large-scale Monte-Carlo shell model calculations, might be helpful.

Likewise, a re-measurement of  $4_1^+$  lifetimes in  $^{62}\text{Ni}$  might be interesting to confirm that the evolution of  $B(E2)$  values is in this case indeed symmetric since the uncertainty is rather large for this value.

**Acknowledgements** This work was supported by the German Research Foundation (DFG) under grant no. FR 3276/2-1 and DE 1516/5-1.

**Data Availability Statement** This manuscript has no associated data or the data will not be deposited. [Author's Comment: The datasets generated during and/or analysed during the current study are available from the corresponding author on reasonable request.]

## References

1. S. Suchyta, S.N. Liddick, Y. Tsunoda, T. Otsuka, M.B. Bennett, A. Chemey, M. Honma, N. Larson, C.J. Prokop, S.J. Quinn, N. Shimizu, A. Simon, A. Spyrou, V. Tripathi, Y. Utsuno, J.M. Von Moss, Phys. Rev. C **89**, 021301 (2014). <https://doi.org/10.1103/PhysRevC.89.021301>
2. D. Little, A.D. Ayangeakaa, R.V.F. Janssens, S. Zhu, Y. Tsunoda, T. Otsuka, B.A. Brown, M.P. Carpenter, A. Gade, D. Rhodes, C.R. Hoffman, F.G. Kondev, T. Lauritsen, D. Seweryniak, J. Wu, J. Henderson, C.Y. Wu, P. Chowdhury, P.C. Bender, A.M. Forney, W.B. Walters, Phys. Rev. C **106**, 044313 (2022). <https://doi.org/10.1103/PhysRevC.106.044313>
3. O. Kenn, K.H. Speidel, R. Ernst, J. Gerber, P. Maier-Komor, F. Nowacki, Phys. Rev. C **63**, 064306 (2001). <https://doi.org/10.1103/PhysRevC.63.064306>
4. S. Raman, C. Nestor, P. Tikkanen, At. Data Nucl. Data Tables **78**(1), 1 (2001). <https://doi.org/10.1006/adnd.2001.0858>
5. C. Loelius, H. Iwasaki, B.A. Brown, M. Honma, V.M. Bader, T. Baugher, D. Bazin, J.S. Berryman, T. Braunroth, C.M. Campbell, A. Dewald, A. Gade, N. Kobayashi, C. Langer, I.Y. Lee, A. Lemasson, E. Lunderberg, C. Morse, F. Recchia, D. Smalley, S.R. Stroberg, R. Wadsworth, C. Walz, D. Weisshaar, A. Westerberg, K. Whitmore, K. Wimmer, Phys. Rev. C **94**, 024340 (2016). <https://doi.org/10.1103/PhysRevC.94.024340>
6. J.N. Orce, B. Crider, S. Mukhopadhyay, E. Peters, E. Elhami, M. Scheck, B. Singh, M.T. McEllistrem, S.W. Yates, Phys. Rev. C **77**, 064301 (2008). <https://doi.org/10.1103/PhysRevC.77.064301>
7. J.M. Allmond, B.A. Brown, A.E. Stuchbery, A. Galindo-Uribarri, E. Padilla-Rodal, D.C. Radford, J.C. Batchelder, M.E. Howard, J.F. Liang, B. Manning, R.L. Varner, C.H. Yu, Phys. Rev. C **90**, 034309 (2014). <https://doi.org/10.1103/PhysRevC.90.034309>
8. A. Dewald, O. Möller, P. Petkov, Prog. Part. Nucl. Phys. **67**(3), 786 (2012). <https://doi.org/10.1016/j.pnpnp.2012.03.003>
9. G. Böhm, A. Dewald, P. Petkov, P. von Brentano, Nucl. Instrum. Methods Phys. Res. Sect. A Accel. Spectrom. Detect. Assoc. Equip. **329**(1), 248 (1993). [https://doi.org/10.1016/0168-9002\(93\)90944-D](https://doi.org/10.1016/0168-9002(93)90944-D)
10. F. Kearns, L.P. Ekstrom, G.D. Jones, T.P. Morrison, O.M. Mustaffa, H.G. Price, D.N. Simister, P.J. Twin, R. Wadsworth, N.J. Ward, J. Phys. G Nucl. Phys. **6**(9), 1131 (1980). <https://doi.org/10.1088/0305-4616/6/9/010>
11. T. Braunroth, Private Communication (2020)
12. V.M. Bader, A. Gade, D. Weisshaar, B.A. Brown, T. Baugher, D. Bazin, J.S. Berryman, A. Ekström, M. Hjorth-Jensen, S.R. Stroberg, W.B. Walters, K. Wimmer, R. Winkler, Phys. Rev. C **88**, 051301 (2013). <https://doi.org/10.1103/PhysRevC.88.051301>
13. A. Gade, S.N. Liddick, J. Phys. G Nucl. Part. Phys. **43**(2), 024001 (2016). <https://doi.org/10.1088/0954-3899/43/2/024001>
14. N.Mărginean, D. Little, Y. Tsunoda, S. Leoni, R.V.F. Janssens, B. Fornal, T. Otsuka, C. Michelagnoli, L. Stan, F.C.L. Crespi, C. Costache, R. Lica, M. Sferrazza, A. Turturica, A.D. Ayangeakaa, K. Auranen, M. Barani, P.C. Bender, S. Bottoni, M. Boromiza, A. Bracco, S. Călinescu, C.M. Campbell, M.P. Carpenter, P. Chowdhury, M. Ciemala, N. Cieplicka-Orynczak, D. Cline, C. Clisu, H.L. Crawford, I.E. Dinescu, J. Dudouet, D. Filipescu, N. Florea, A.M. Forney, S. Fracassetti, A. Gade, I. Gheorghe, A.B. Hayes, I. Harca, J. Henderson, A. Ionescu, L.W. Iskra, M. Jentschel, F. Kandzia, Y.H. Kim, F.G. Kondev, G. Korschinek, U. Köster, Krishichayan, M. Krzysiek, T. Lauritsen, J. Li, R. Mărginean, E.A. Maugeri, C. Mihai, R.E. Mihai, A. Mitsu, P. Mutti, A. Negret, C.R. Niță, A. Olăcel, A. Oprea, S. Pascu, C. Petrone, C. Porzio, D. Rhodes, D. Seweryniak, D. Schumann, C. Sotty, S.M. Stolze, R. Șuvăilă, S. Toma, S. Ujenuic, W.B. Walters, C.Y. Wu, J. Wu, S. Zhu, S. Ziliani, Phys. Rev. Lett. **125**, 102502 (2020). <https://doi.org/10.1103/PhysRevLett.125.102502>
15. C. Guénaut, G. Audi, D. Beck, K. Blaum, G. Bollen, P. Delahaye, F. Herfurth, A. Kellerbauer, H.J. Kluge, J. Libert, D. Lunney, S. Schwarz, L. Schweikhard, C. Yazidjian, Phys. Rev. C **75**, 044303 (2007). <https://doi.org/10.1103/PhysRevC.75.044303>

16. M. Honma, T. Otsuka, B. Brown, T. Mizusaki, *Eur. Phys. J. A* **25**, 499 (2005). <https://doi.org/10.1140/epjad/i2005-06-032-2>
17. A. Poves, J. Sánchez-Solano, E. Caurier, F. Nowacki, *Nucl. Phys. A* **694**(1), 157 (2001). [https://doi.org/10.1016/S0375-9474\(01\)00967-8](https://doi.org/10.1016/S0375-9474(01)00967-8)
18. Y. Tsunoda, T. Otsuka, N. Shimizu, M. Honma, Y. Utsuno, *Phys. Rev. C* **89**, 031301 (2014). <https://doi.org/10.1103/PhysRevC.89.031301>

Springer Nature or its licensor (e.g. a society or other partner) holds exclusive rights to this article under a publishing agreement with the author(s) or other rightsholder(s); author self-archiving of the accepted manuscript version of this article is solely governed by the terms of such publishing agreement and applicable law.



---

## 7 Summary and Outlook

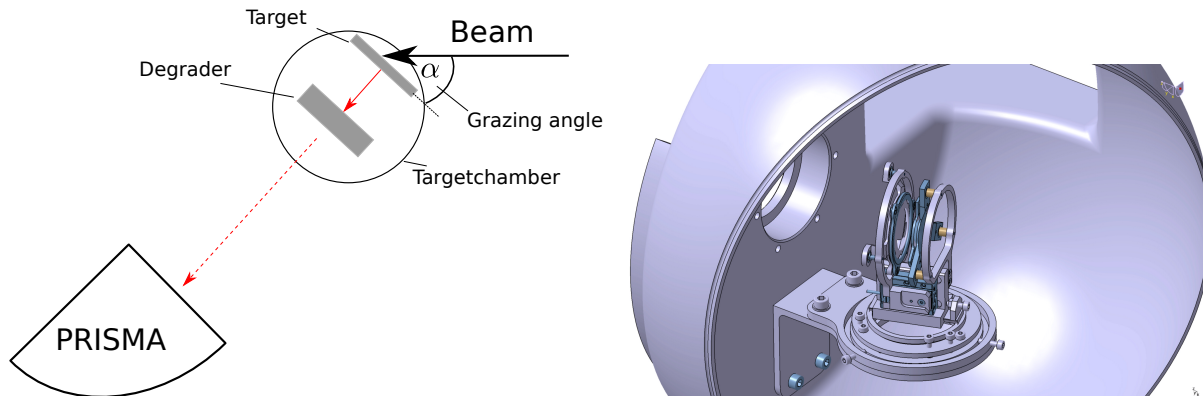
In the following, a brief conclusion and an outlook on further developments and future prospects of the work presented in chapters 3-6 will be given. The aim of this thesis was the development and commissioning of a new (three-foil) plunger and of auxiliary techniques as well as the analysis of lifetime measurements of two nuclei in different regions of the nuclear chart. The different topics led to three publications and one manuscript that has been submitted for publication.

### 7.1 Development of the CoCoDiff plunger

The CoCoDiff three-foil plunger has been newly designed, built, tested and commissioned during this thesis. The first experiment using the CoCoDiff plunger has been the measurement of lifetimes of the first two excited states in  $^{50}\text{Cr}$  at the Cologne FN Tandem Accelerator. For this experiment, a new dedicated target chamber for the CoCoDiff plunger was built. The result for the  $2_1^+$  state's lifetimes agrees very well with the literature values, proving the concept of the new plunger device as well as of the proposed method of analysis. The new value for the lifetime of the  $4_1^+$  state helps to decide between two different groups of literature values that do not agree with each other by clearly favoring the literature that suggests a shorter lifetime value. After this successful measurement, the plunger could be reported to be operational. However, some revisions have been proposed to improve the handling of the device, e.g. a different way to mount the stopper foil, which have been implemented after the commissioning run.

To be able to use the advantages of the new plunger to the full extend, also a new version of the Cologne plunger software has been developed prior to the commissioning experiment. The main focus was put on the remodeling of the motor control. As described in chapter 1.2, the previous version of the software was initially written for the Cologne Coincidence Plunger which has not only a motor but also an additional piezo stack as well as an inductive distance probe. Both of those have been omitted in the compact plunger design for the sake of reducing the size and amount of material to reduce  $\gamma$ -ray absorption. Therefore, the motor is now not only used to set the desired distance but also to read out the distance and keep it constant with the help of a feedback system. This means that the precision with which the motor is controlled had to be increased, which was realized with the new software bundle by changing from an open-loop approach to a closed-loop approach and by changing large parts of the software routines relating to the feedback system and the distance calibration. The latter could be improved quite drastically by a more precise way to reach the desired positions, which also improves the determination of absolute distances with the capacitance method. The new software can also be used for the GALILEO plunger, which existed prior to this work but was still using the non-optimized software of the Cologne Coincidence Plunger.

The CoCoDiff plunger will be used in an upcoming campaign at the LNL together with the AGATA detector array [77] and the PRISMA magnetic spectrometer [78] [79] [80]. For this

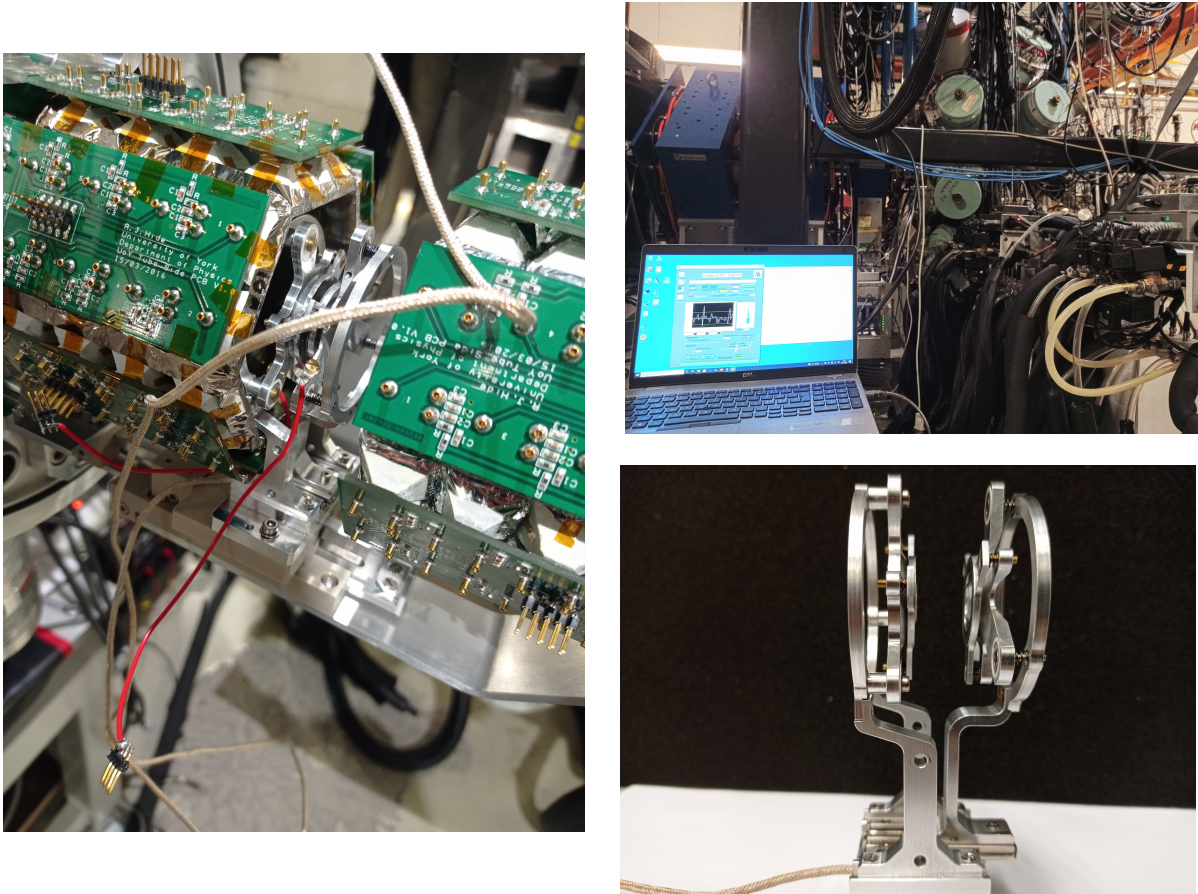


**Figure 16:** Left: Schematic drawing of the set-up of the CoCoDiff two-foil plunger version at the PRISMA magnetic spectrometer under a certain grazing angle  $\alpha$  for multi-nucleon transfer reactions. Right: CAD drawing of the CoCoDiff two-foil plunger version in the target chamber for PRISMA with a dedicated rotatable holding structure.

campaign, some adaptations were made to the plunger. For more flexibility, it was made possible to also use it as a regular two-foil plunger. For experiments using PRISMA, the plunger (together with PRISMA) is usually rotated by the grazing angle of the reaction with respect to the beam axis to maximize the amount of recoils that can enter the PRISMA magnet (see Fig. 16). To keep the angle constant during the experiment, the target has to be fixed and the degrader has to be movable. Moreover, the diameter of the degrader foil was increased to maximize the acceptance angle with which the plunger can be used. At the time of writing, several experiments using the new plunger device have been proposed by different working groups and have been accepted for the upcoming experimental campaign.

### 7.1.1 Further developments of plunger devices and plunger software package

After the successful commissioning of the CoCoDiff plunger, other dedicated two-foil plunger devices based on the same design have been developed in collaborations with the Physics Department of the University of Jyväskylä, Finland (JYFL) and Argonne National Laboratory, USA (ANL). The Advanced Plunger-Particle detector Array (APPA) is designed to be used at JYFL. It fits inside the JYtube particle detector array in a dedicated target chamber and can be used with the JUROGAM3 [81] detector array and either the MARA [82] or RITU [83] recoil separators. A commissioning experiment has successfully been carried out and a complete campaign with the new plunger is planned. The integrated Cologne Argonne Plunger Setup (iCAPS) can be mounted inside the MICROBALL detector and can be used with the germanium arrays GRETINA [84] or Gammasphere [85] together with the recoil separators FMA [86] or AGFA [87], located at the ATLAS facility at ANL. A commissioning experiment for iCAPS was done by measuring lifetimes in  $^{110}\text{Sn}$  using the reaction  $^{12}\text{C}(^{106}\text{Cd}, ^{110}\text{Sn})^8\text{Be}$ . GRETINA was used for the detection of  $\gamma$ -rays while MICROBALL surrounded the plunger to detect the 2  $\alpha$  particles from the decay of the  $^8\text{Be}$  reaction product as a trigger for GRETINA. Since the successful commissioning, several further experiments using the iCAPS plunger have been carried



**Figure 17:** Left: The compact APPA plunger inside the JYTube particle detector at JYFL. Upper right: Newly developed compact plunger software running with the APPA plunger with JYTube and the JUROGAM  $\gamma$ -detector array. Lower right: The compact iCAPS plunger.

out successfully. For both devices a new stand-alone version of the plunger software package has been developed based on the CoCoDiff software and the closed-loop approach. This package has been delivered to JYFL and ANL and has been used successfully in the commissioning experiments for both new plunger devices and a following plunger campaign at the ANL. Since the new software version together with the respective compact plunger is used at different laboratories by different collaborators, a comprehensive manual for the usage of the software and the general set-up of a compact plunger measurement has been written and is given in the appendix of this work.

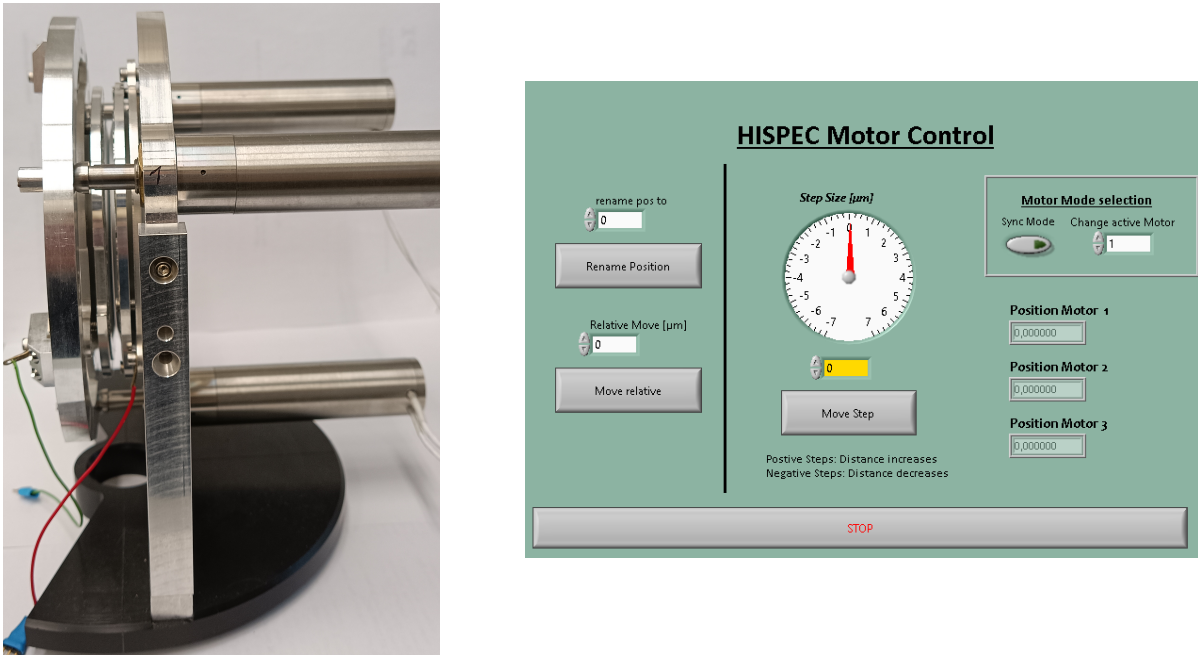
### Cologne Coincidence Plunger

For the Cologne Coincidence Plunger, a complete working software package using the open-loop motor control exists and has been in use for many years. However, in the recent time, problems with the motor of the plunger became obvious, which required changes in the software. It has been observed that over time the traveled distance for a selected number of step cycles decreased massively, probably due to abrasion effects. This effect became more severe until the motor could not be moved with step sizes  $< 5\mu\text{m}$ . To overcome this, for the Cologne Coincidence Plunger the



motor control was also changed to a closed-loop approach, based on the new compact plunger software. The applied voltage is automatically adjusted to keep the travel distance constant and abrasion effects are therefore countered without the need for the user to interfere. As an additional bonus, the closed-loop motor movement allows for a much faster distance calibration process and helps to increase the precision in the calibration since the calibration points can be reached more precisely.

### HISPEC Plunger



**Figure 18:** View of the HISPEC plunger device (left) and the front panel of the dedicated motor control software with the possibility to move all three piezo motors simultaneously or separately for the alignment of the foils.

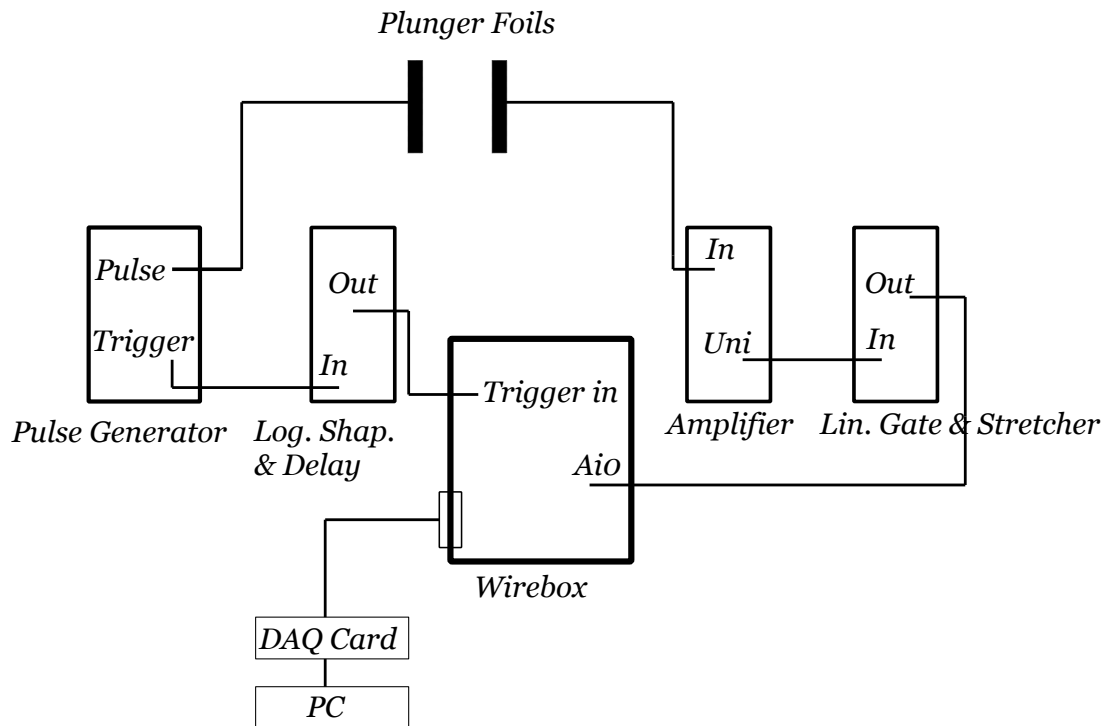
A new plunger device for the use at the HIgh-resolution in-flight SPECTroscopy (HISPEC) and DEcay SPECTroscopy (DESPEC) branches of the upcoming Facility for Antiproton and Ion Research (FAIR) had been developed and built prior to this work. However, no software did exist to run experiments with the new device.

The HISPEC plunger was especially designed for the use at FAIR. Due to the large diameter of the future radioactive beam at FAIR, the foils need to have a much larger diameter (about 10 cm) than in other plunger devices. At the same time, the plunger has to be able to maintain the same precision as other plungers. To follow these requirements, a design was chosen, where three precise step motors of the type used in the Cologne Coincidence Plunger are used to move the target foil (see Fig. 18). The software controlling the movement of the plunger had to ensure that all three motors move simultaneously. Therefore, the step size of all three motors has to be precisely identical and the usage of the closed-loop approach to control the motors becomes even more important. With the open-loop approach, the design of the plunger could not work without further sensors that monitor the movement of each motor independently. At the same

time, the three-motor setup can be used to align the plunger foils very precisely, for which each motor has to be able to move independently.

A new software has therefore been written on the basis of the compact plunger software, where the user can lock and unlock the movement of certain motors. After the alignment process, all motors are automatically locked together and move simultaneously for the rest of the experiment, thus keeping the parallel alignment untouched while moving.

### 7.1.2 Work in progress and future developments



**Figure 19:** Plunger control circuit using several NIM modules for pulse processing.

Since the CoCoDiff plunger is designed to be multi-purpose and it is planned to be used at different laboratories, it is of interest to also realize a compact solution for the plunger control system to simplify the transport of the device. One measure that has been applied is the exchange of PCI data acquisition (DAQ) cards for USB DAQ cards, making it possible to use a laptop for the plunger control system instead of a desktop PC. In the current version, the largest footprint of the complete system stems from the use of external (NIM) modules for the feedback system. They are used to apply the voltage signal to one foil and to process the induced voltage signal on the other foil (see Fig. 19). All in all four NIM modules are needed for the operation. To further reduce the footprint, a new way to measure the capacity has been implemented, based on the method explained in Ref. [88]. Briefly summarized, the pulsed voltage signal is being replaced by a high-frequency alternating voltage in the form of a sine wave. In an A/C circuit

a capacitor acts as an impedance, meaning the amplitude of the A/C voltage measured over a resistor behind the second foil if the signal  $U$  is fed to the first foil is given by

$$U_{out} \propto U_{in} \frac{1}{\omega C} \quad (21)$$

and is therefore still proportional to the distance between the foils. The A/C voltage behind the second foil can be directly fed into the DAQ card without the need for an amplifier and other modules needed for timing and pulse shaping purposes. Since the DAQ card can also deliver a simple A/C sine voltage to the first foil, no more NIM modules are needed.

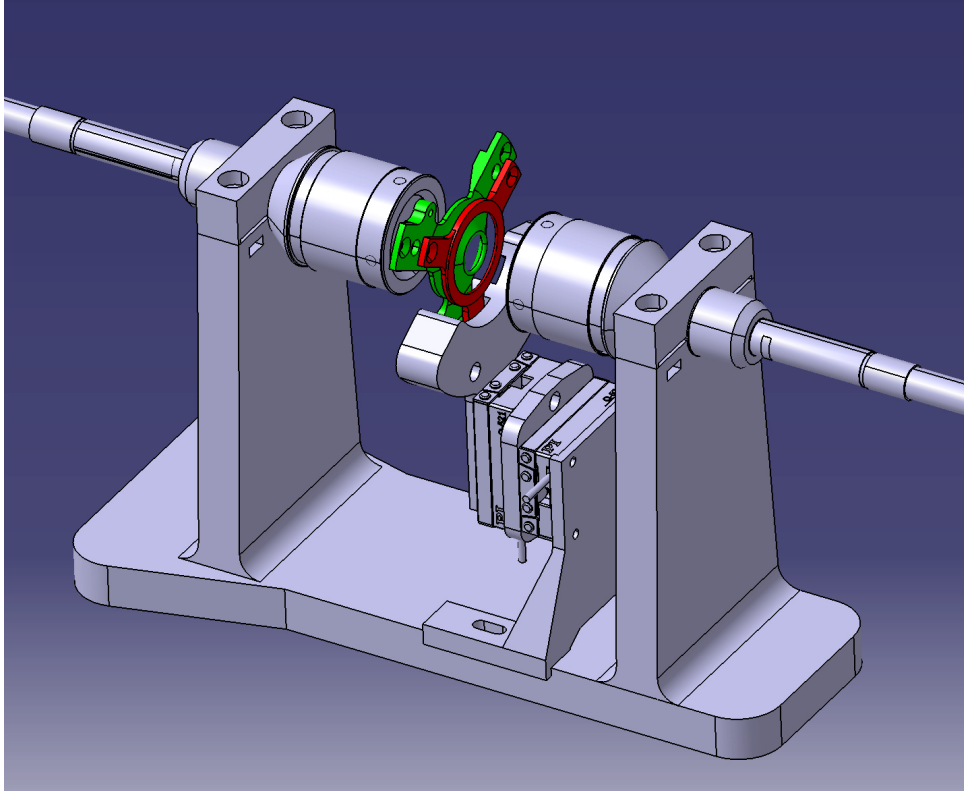
A software version applying these principles has been developed and first tests show that it results in a precision that is comparable to the version using the NIM modules. However, the A/C signal delivered by the DAQ card can be assumed to be less stable than the pulsed signal of a specialized pulser NIM module. Therefore, the current version of the software integrates the amplitude over several sine cycles for a single step in the feedback system. It might also be appropriate to simultaneously measure the delivered signal and compare it to the resulting signal at the second foil to correct for deviations in the incoming signal. This feature will be implemented in the future.

## 7.2 Optical plunger foil distance measurement method

A new method has been proposed to precisely measure the absolute plunger foil separations directly with a modern optical sensor. It has been tested and compared to the capacitance method, which is well established but prone to systematic uncertainties, as well as against a distance measurement using known lifetimes in  $^{181}\text{Ta}$  in a Coulomb excitation experiment. The results show, that the new method produces very precise measurements.

The new optical method has since been established for Cologne plunger measurements and has been used in several experiments with the Cologne Coincidence plunger where absolute distances were needed (e.g. for the measurement reported on in Ref. [89]).

An additional use case for the optical sensor that is used in the distance measurement is the very precise measurement of plunger foil thicknesses. For this, a second sensor is needed which has recently, at the time of writing, been obtained. Using the technique described by the manufacturer [90] a set-up for this type of measurement is currently being developed. The plunger foil will be fixed on two connected piezo motors. These can be used to move the foil in x- and y-direction between the two sensors to get a mapping of the complete surface of the foil. A drawing of a prototype is shown in Fig. 20. Since the foil thickness is usually measured as an average over the complete surface of the foil (e.g. by weighing or energy loss measurements), inhomogeneities in the foil can lead to incorrect assumptions for the thickness at the beam spot and therefore to wrong parameters in the planning of an experiment. For rolled foils, these inhomogeneities are typically in the order of 10% and can mostly be neglected. However, if material is evaporated onto a backing foil to form a target, the inhomogeneities can become much larger in certain cases and have to be taken into account. With the mapping of the complete surface, a precise value will be obtained for the beam spot as well as a measure of the



**Figure 20:** Prototype for a thickness measurement station for plunger foils. The foils can be moved in 2 dimensions by two precise piezo motors to map the complete foil surface.

surface roughness. At the time of writing, there are still some precision elements missing for the completion of the set-up, which are needed to adjust the two sensors with respect to each other. This adjustment has to be done with a very high precision to ensure correct thickness measurements.

### 7.3 Lifetime measurement in $^{144}\text{Ce}$

A RDDS measurement on  $^{144}\text{Ce}$  has been conducted at the Cologne FN Tandem accelerator, using the 2n-transfer reaction  $^{142}\text{Ce}(^{18}\text{O},^{16}\text{O})^{144}\text{Ce}$ . The lifetimes of the  $4_1^+$ ,  $6_1^+$  and  $3_1^-$  states have been measured for the first time as well as the effective lifetime of the  $4_2^+$  state. Additionally, the previously measured lifetime of the  $2_1^+$  state could be confirmed with a well reduced uncertainty.  $^{144}\text{Ce}$  is predicted to be on the edge of a region of octupole deformed nuclei with a level scheme that suggests octupole correlations for this nucleus as well. Therefore the extraction of  $B(E1)$  values from the newly measured lifetimes has been of great interest and indeed, using known branching ratios, three E1 transition strengths could be obtained. Especially, the  $6_1^+ \rightarrow 5_1^-$  transition with around  $1.3 \times 10^{-2} e \text{ fm}^2$  is strongly enhanced. At the same time, the E2 transition strength from the same state ( $6_1^+ \rightarrow 4_1^+$ ) is much lower than predicted by shell model calculations that do not include octupole deformation. As also the  $R(I)$  values, defined in Eqs. 18,19 roughly double from  $I=4$  to  $I=6$ , one can conclude that it is

possible that a significant change in the nuclear structure happens around  $I=6$ . However, also the other E1 transition strengths, which are in the range of  $10^{-4}\text{efm}^2$  while being significantly lower than the one from the  $6_1^+ \rightarrow 5_1^+$  transition, are still enhanced and can be interpreted as indications for octupole correlations. The mentioned  $R(I)$  value can only be calculated up to  $I=7$  due to missing information about higher-lying states, but gives no indications of stable octupole deformations. It is therefore most likely that  $^{144}\text{Ce}$  acts as an octupole vibrator with a degree of freedom in  $\beta_3$ .

For decisive evidence, however, a CoulEx measurement using a very high efficiency  $\gamma$ -spectrometer to search for the  $3_1^- \rightarrow 0_1^+$  transition is needed to determine the branching ratio between this transition and the  $3_1^- \rightarrow 2_1^+$  transition. With this, the E3 transition strengths could be calculated from the newly measured lifetime of the  $3_1^-$  state.

#### 7.4 Lifetime measurement in $^{60}\text{Ni}$

In a measurement on  $^{60}\text{Ni}$  it was possible to shed light on an unclear situation of contradicting experimental results. The experiment used the DDCM and  $\gamma$ - $\gamma$  coincidences to measure the lifetimes of the two lowest yrast states with very high precision. That way, for both states literature values that suggested considerably longer lifetimes could be rejected. In the case of the  $2_1^+$  state, a recent CoulEx measurement could be confirmed independently, further increasing the trust also in the newly measured lifetime of the  $4_1^+$  state. The resulting transition strengths match very well with shell-model predictions and resolve an unexpected systematic behavior that occurred using older literature values. They are very important for the question of the robustness of the  $N=40$  subshell closure and for the question of possible shape-coexistence in the Ni isotopes starting around  $N=40$ . The lifetime analysis of the  $2_1^+$  state was also used to benchmark the handling of DSA effects with the PTBG4 simulation toolkit. Since it was possible to re-create the experimental spectra with good precision and the resulting value for the lifetime shows a good agreement with the latest literature value, the toolkit can be reported to be viable to analyze RDDS experiments suffering from DSA effects at the Cologne plunger setup, for which the toolkit is optimized.

## References

- [1] E.A. McCutchan. In: *Nucl. Data Sheet* 126 (151 2015). URL: <https://www.nndc.bnl.gov/ensdf/>.
- [2] P J Nolan and J F Sharpey-Schafer. “The measurement of the lifetimes of excited nuclear states”. In: *Reports on Progress in Physics* 42.1 (1979), p. 1. DOI: 10.1088/0034-4885/42/1/001. URL: <https://dx.doi.org/10.1088/0034-4885/42/1/001>.
- [3] A. Dewald, O. Möller, and P. Petkov. “Developing the Recoil Distance Doppler-Shift technique towards a versatile tool for lifetime measurements of excited nuclear states”. In: *Progress in Particle and Nuclear Physics* 67.3 (2012), pp. 786–839. ISSN: 0146-6410. DOI: <https://doi.org/10.1016/j.ppnp.2012.03.003>.
- [4] M.J. Taylor, D.M. Cullen, A.J. Smith, A. McFarlane, V. Twist, G.A. Alharshan, M.G. Procter, T. Braunroth, A. Dewald, E. Ellinger, C. Fransen, P.A. Butler, M. Scheck, D.T. Joss, B. Saygi, C.G. McPeake, T. Grahn, P.T. Greenlees, U. Jakobsson, P. Jones, R. Julin, S. Juutinen, S. Ketelhut, M. Leino, P. Nieminen, J. Pakarinen, P. Peura, P. Rahkila, P. Ruotsalainen, M. Sandzelius, J. Sarén, C. Scholey, J. Sorri, S. Stolze, and J. Uusitalo. “A new differentially pumped plunger device to measure excited-state lifetimes in proton emitting nuclei”. In: *Nuclear Instruments and Methods in Physics Research Section A: Accelerators, Spectrometers, Detectors and Associated Equipment* 707 (2013), pp. 143–148. ISSN: 0168-9002. DOI: <https://doi.org/10.1016/j.nima.2012.12.120>. URL: <https://www.sciencedirect.com/science/article/pii/S0168900213000028>.
- [5] H. Iwasaki, A. Dewald, T. Braunroth, C. Fransen, D. Smalley, A. Lemasson, C. Morse, K. Whitmore, and C. Loelius. “The TRIPLE PLunger for EXotic beams TRIPLEX for excited-state lifetime measurement studies on rare isotopes”. In: *Nuclear Instruments and Methods in Physics Research Section A: Accelerators, Spectrometers, Detectors and Associated Equipment* 806 (2016), pp. 123–131. ISSN: 0168-9002. DOI: <https://doi.org/10.1016/j.nima.2015.09.091>. URL: <https://www.sciencedirect.com/science/article/pii/S0168900215011626>.
- [6] D.G. Sarantites, P.-F. Hua, M. Devlin, L.G. Sobotka, J. Elson, J.T. Hood, D.R. LaFosse, J.E. Sarantites, and M.R. Maier. “‘The microball’ Design, instrumentation and response characteristics of a  $4\pi$ -multidetector exit channel-selection device for spectroscopic and reaction mechanism studies with Gammasphere”. In: *Nuclear Instruments and Methods in Physics Research Section A: Accelerators, Spectrometers, Detectors and Associated Equipment* 381.2 (1996), pp. 418–432. ISSN: 0168-9002. DOI: [https://doi.org/10.1016/S0168-9002\(96\)00785-1](https://doi.org/10.1016/S0168-9002(96)00785-1). URL: <https://www.sciencedirect.com/science/article/pii/S0168900296007851>.
- [7] A. Dewald, S. Harissopoulos, and P. von Brentano. “The Differential Plunger and the Differential Decay Curve Method for the Analysis of Recoil Distance Doppler-Shift Data”. In: *Z.Physik A - Atomic Nuclei* 334 (1989), pp. 163–175. DOI: [https://doi.org/10.1016/0168-9002\(93\)90944-D](https://doi.org/10.1016/0168-9002(93)90944-D).

- [8] T. Braunroth. *Private Communication*.
- [9] B. Bucher, S. Zhu, C. Y. Wu, R. V. F. Janssens, D. Cline, A. B. Hayes, M. Albers, A. D. Ayangeakaa, P. A. Butler, C. M. Campbell, M. P. Carpenter, C. J. Chiara, J. A. Clark, H. L. Crawford, M. Cromaz, H. M. David, C. Dickerson, E. T. Gregor, J. Harker, C. R. Hoffman, B. P. Kay, F. G. Kondev, A. Korichi, T. Lauritsen, A. O. Macchiavelli, R. C. Pardo, A. Richard, M. A. Riley, G. Savard, M. Scheck, D. Seweryniak, M. K. Smith, R. Vondrasek, and A. Wiens. “Direct Evidence of Octupole Deformation in Neutron-Rich  $^{144}\text{Ba}$ ”. In: *Phys. Rev. Lett.* 116 (11 2016), p. 112503. DOI: 10.1103/PhysRevLett.116.112503. URL: <https://link.aps.org/doi/10.1103/PhysRevLett.116.112503>.
- [10] A. deShalit and H. Feshbach. *Theoretical Nuclear Physics, Volume I: Nuclear Structure*. John Wiley & Sons, 1974.
- [11] J. M. Blatt and V. F. Weisskopf. *Theoretical Nuclear Physics*. Springer-Verlag, 1979.
- [12] H. Bateman. “Solution of a system of differential equations in the theory of radioactive transformations”. In: *Proc. Cambridge Phil. Soc.* 15 (1910), pp. 423–427.
- [13] Peter L. Bonate. “A Brief Introduction to Monte Carlo Simulation”. In: *Clinical Pharmacokinetics* 40 (1 2001), pp. 15–22. DOI: 10.2165/00003088-200140010-00002. URL: <https://doi.org/10.2165/00003088-200140010-00002>.
- [14] M. Beckers, C. Müller-Gatermann, A. Blazhev, T. Braunroth, A. Dewald, C. Fransen, A. Goldkuhle, L. Kornwibel, J. Litzinger, F. von Spee, and K.-O. Zell. “Lifetime measurement of excited states in  $^{144}\text{Ce}$ : Enhanced  $E1$  strengths in a candidate for octupole deformation”. In: *Phys. Rev. C* 102 (1 2020), p. 014324. DOI: 10.1103/PhysRevC.102.014324. URL: <https://link.aps.org/doi/10.1103/PhysRevC.102.014324>.
- [15] G. Böhm, A. Dewald, P. Petkov, and P. von Brentano. “The differential decay curve method for the analysis of Doppler shift timing experiments”. In: *Nuclear Instruments and Methods in Physics Research Section A: Accelerators, Spectrometers, Detectors and Associated Equipment* 329.1 (1993), pp. 248–261. ISSN: 0168-9002. DOI: [https://doi.org/10.1016/0168-9002\(93\)90944-D](https://doi.org/10.1016/0168-9002(93)90944-D).
- [16] M. Beckers, A. Dewald, C. Fransen, K. Arnsward, C. Müller-Gatermann, and F. von Spee. “Development of the multi-purpose Cologne Compact Differential Plunger (CoCoD-iff) for the measurement of nuclear level lifetimes with the Recoil Distance Doppler-shift method”. In: *Nuclear Instruments and Methods in Physics Research Section A: Accelerators, Spectrometers, Detectors and Associated Equipment* 1042 (2022), p. 167418. ISSN: 0168-9002. DOI: <https://doi.org/10.1016/j.nima.2022.167418>. URL: <https://www.sciencedirect.com/science/article/pii/S0168900222007100>.
- [17] M.M. Giles, D.M. Cullen, L. Barber, B.S. Nara Singh, M.J. Taylor, A.J. Smith, A. McFarlane, C. Read, T. Grahn, H. Badran, P.T. Greenlees, R. Julin, J. Pakarinen, J. Partanen, P. Rahkila, P. Ruotsalainen, M. Sandzelius, J. Sarén, J. Sorri, S.V. Szewc, J. Uusitalo, J. Heery, E. Parr, P. Papadakis, and R.D. Herzberg. “TPEN: A Triple-foil differential

- Plunger for lifetime measurements of excited states in Exotic Nuclei”. In: *Nuclear Instruments and Methods in Physics Research Section A: Accelerators, Spectrometers, Detectors and Associated Equipment* 923 (2019), pp. 139–146. ISSN: 0168-9002. DOI: <https://doi.org/10.1016/j.nima.2019.01.089>. URL: <https://www.sciencedirect.com/science/article/pii/S0168900219301597>.
- [18] T.K. Alexander and A. Bell. “A target chamber for Recoil-Distance lifetime measurements”. In: *Nuclear Instruments and Methods* 81.1 (1970), pp. 22–26. ISSN: 0029-554X. DOI: [https://doi.org/10.1016/0029-554X\(70\)90604-X](https://doi.org/10.1016/0029-554X(70)90604-X).
- [19] L.C. Northcliffe and R.F. Schilling. “Range and stopping-power tables for heavy ions”. In: *Atomic Data and Nuclear Data Tables* 7.3 (1970), pp. 233–463. ISSN: 0092-640X. DOI: [https://doi.org/10.1016/S0092-640X\(70\)80016-X](https://doi.org/10.1016/S0092-640X(70)80016-X). URL: <https://www.sciencedirect.com/science/article/pii/S0092640X7080016X>.
- [20] S. Agostinelli et al. “Geant4—a simulation toolkit”. In: *Nuclear Instruments and Methods in Physics Research Section A: Accelerators, Spectrometers, Detectors and Associated Equipment* 506.3 (2003), pp. 250–303. ISSN: 0168-9002. DOI: [https://doi.org/10.1016/S0168-9002\(03\)01368-8](https://doi.org/10.1016/S0168-9002(03)01368-8). URL: <https://www.sciencedirect.com/science/article/pii/S0168900203013688>.
- [21] J. Allison, K. Amako, J. Apostolakis, H. Araujo, P. Arce Dubois, M. Asai, G. Barrand, R. Capra, S. Chauvie, R. Chytracsek, G.A.P. Cirrone, G. Cooperman, G. Cosmo, G. Cuttone, G.G. Daquino, M. Donszelmann, M. Dressel, G. Folger, F. Foppiano, J. Generowicz, V. Grichine, S. Guatelli, P. Gumplinger, A. Heikkinen, I. Hrivnacova, A. Howard, S. Incerti, V. Ivanchenko, T. Johnson, F. Jones, T. Koi, R. Kokoulin, M. Kossov, H. Kurashige, V. Lara, S. Larsson, F. Lei, O. Link, F. Longo, M. Maire, A. Mantero, B. Mascialino, I. McLaren, P. Mendez Lorenzo, K. Minamimoto, K. Murakami, P. Nieminen, L. Pandola, S. Parlati, L. Peralta, J. Perl, A. Pfeiffer, M.G. Pia, A. Ribon, P. Rodrigues, G. Russo, S. Sadilov, G. Santin, T. Sasaki, D. Smith, N. Starkov, S. Tanaka, E. Tcherniaev, B. Tome, A. Trindade, P. Truscott, L. Urban, M. Verderi, A. Walkden, J.P. Wellisch, D.C. Williams, D. Wright, and H. Yoshida. “Geant4 developments and applications”. In: *IEEE Transactions on Nuclear Science* 53.1 (2006), pp. 270–278. DOI: 10.1109/TNS.2006.869826.
- [22] J. Allison, K. Amako, J. Apostolakis, P. Arce, M. Asai, T. Aso, E. Bagli, A. Bagulya, S. Banerjee, G. Barrand, B.R. Beck, A.G. Bogdanov, D. Brandt, J.M.C. Brown, H. Burkhardt, Ph. Canal, D. Cano-Ott, S. Chauvie, K. Cho, G.A.P. Cirrone, G. Cooperman, M.A. Cortés-Giraldo, G. Cosmo, G. Cuttone, G. Depaola, L. Desorgher, X. Dong, A. Dotti, V.D. Elvira, G. Folger, Z. Francis, A. Galoyan, L. Garnier, M. Gayer, K.L. Genser, V.M. Grichine, S. Guatelli, P. Guèye, P. Gumplinger, A.S. Howard, I. Hřivnáčová, S. Hwang, S. Incerti, A. Ivanchenko, V.N. Ivanchenko, F.W. Jones, S.Y. Jun, P. Kaitaniemi, N. Karakatsanis, M. Karamitros, M. Kelsey, A. Kimura, T. Koi, H. Kurashige, A. Lechner, S.B. Lee, F. Longo, M. Maire, D. Mancusi, A. Mantero, E. Mendoza, B. Morgan, K. Murakami, T. Nikitina, L. Pandola, P. Paprocki, J. Perl, I. Petrović, M.G. Pia, W. Pokorski, J.M. Quesada, M. Raine, M.A. Reis, A. Ribon, A. Ristić Fira, F. Romano, G. Russo, G. Santin, T. Sasaki,



- D. Sawkey, J.I. Shin, I.I. Strakovsky, A. Taborda, S. Tanaka, B. Tomé, T. Toshito, H.N. Tran, P.R. Truscott, L. Urban, V. Uzhinsky, J.M. Verbeke, M. Verderi, B.L. Wendt, H. Wenzel, D.H. Wright, D.M. Wright, T. Yamashita, J. Yarba, and H. Yoshida. “Recent developments in Geant4”. In: *Nuclear Instruments and Methods in Physics Research Section A: Accelerators, Spectrometers, Detectors and Associated Equipment* 835 (2016), pp. 186–225. ISSN: 0168-9002. DOI: <https://doi.org/10.1016/j.nima.2016.06.125>. URL: <https://www.sciencedirect.com/science/article/pii/S0168900216306957>.
- [23] James F. Ziegler, M.D. Ziegler, and J.P. Biersack. “SRIM – The stopping and range of ions in matter (2010)”. In: *Nuclear Instruments and Methods in Physics Research Section B: Beam Interactions with Materials and Atoms* 268.11 (2010). 19th International Conference on Ion Beam Analysis, pp. 1818–1823. ISSN: 0168-583X. DOI: <https://doi.org/10.1016/j.nimb.2010.02.091>. URL: <https://www.sciencedirect.com/science/article/pii/S0168583X10001862>.
- [24] J. M. Allmond, B. A. Brown, A. E. Stuchbery, A. Galindo-Uribarri, E. Padilla-Rodal, D. C. Radford, J. C. Batchelder, M. E. Howard, J. F. Liang, B. Manning, R. L. Varner, and C.-H. Yu. “High-precision B(E2) measurements of semi-magic  $^{58,60,62,64}\text{Ni}$  by Coulomb excitation”. In: *Phys. Rev. C* 90 (3 2014), p. 034309. DOI: 10.1103/PhysRevC.90.034309. URL: <https://link.aps.org/doi/10.1103/PhysRevC.90.034309>.
- [25] J. Henderson, P. Ruotsalainen, D. G. Jenkins, C. Scholey, K. Auranen, P. J. Davies, T. Grahn, P. T. Greenlees, T. W. Henry, A. Herzan, U. Jakobsson, P. Joshi, R. Julin, S. Juuntinen, J. Konkiand M. Leino, G. Lotay, A. J. Nichols, A. Obertelli, J. Pakarinen, J. Partanen, P. Peura, P. Rahkila, M. Sandzelius, J. Saren, J. Sorri, S. Stolze, J. Uusitalo, and R. Wadsworth. “Enhancing the sensitivity of recoil-beta tagging”. In: *Journal of Instrumentation* 8 (2013), pp. 4–25. DOI: <https://doi.org/10.1088/1748-0221/8/04/P04025>. URL: <https://iopscience.iop.org/article/10.1088/1748-0221/8/04/P04025>.
- [26] C. Müller-Gatermann, F. von Spee, A. Goasduff, D. Bazzacco, M. Beckers, T. Braunroth, A. Boso, P. Cocconi, G. de Angelis, A. Dewald, C. Fransen, A. Goldkuhle, A. Gottardo, A. Gozzelino, K. Hadynska-Klek, G. Jawroski, P.R. John, J. Jolie, S.M. Lenzi, J. Litzinger, R. Menegazzo, D. Mengoni, D.R. Napoli, F. Recchia, M. Siciliano, D. Testov, S. Thiel, J.J. Valiente-Dobón, and K.O. Zell. “A new dedicated plunger device for the GALILEO  $\gamma$ -ray detector array”. In: *Nuclear Instruments and Methods in Physics Research Section A: Accelerators, Spectrometers, Detectors and Associated Equipment* 920 (2019), pp. 95–99. ISSN: 0168-9002. DOI: <https://doi.org/10.1016/j.nima.2018.12.077>. URL: <https://www.sciencedirect.com/science/article/pii/S0168900218318916>.
- [27] *Q-Motion Miniature Linear Stage Datasheet*. 2020. URL: <https://www.physikinstrumente.com/>.
- [28] *PZ205E User Manual E-861 NEXACT ® Controller*. 2010. URL: <https://www.physikinstrumente.de/>.
- [29] T. Mayer-Kuckuck. *Kernphysik, 6. Auflage*. Teubner Studienbücher, 1994.

- [30] K. Bethge, G. Walter, and B. Wiedemann. *Kernphysik, 3. Auflage*. Springer-Verlag, 2008.
- [31] T. Glasmacher. “Coulomb Excitation at intermediate Energies”. In: *Annual Review of Nuclear and Particle Science* 48.1 (1998), pp. 1–31. DOI: 10.1146/annurev.nucl.48.1.1. eprint: <https://doi.org/10.1146/annurev.nucl.48.1.1>. URL: <https://doi.org/10.1146/annurev.nucl.48.1.1>.
- [32] A. Chester, G. C. Ball, R. Caballero-Folch, D. S. Cross, S. Cruz, T. Domingo, T. E. Drake, A. B. Garnsworthy, G. Hackman, S. Hallam, J. Henderson, R. Henderson, W. Korten, R. Krücken, M. Moukaddam, B. Olaizola, P. Ruotsalainen, J. Smallcombe, K. Starosta, C. E. Svensson, J. Williams, and K. Wimmer. “Recoil distance method lifetime measurement of the  $2_1^+$  state in  $^{94}\text{Sr}$  and implications for the structure of neutron-rich Sr isotopes”. In: *Phys. Rev. C* 96 (1 2017), p. 011302. DOI: 10.1103/PhysRevC.96.011302. URL: <https://link.aps.org/doi/10.1103/PhysRevC.96.011302>.
- [33] E. Caurier, G. Martínez-Pinedo, F. Nowacki, A. Poves, and A. P. Zuker. “The shell model as a unified view of nuclear structure”. In: *Rev. Mod. Phys.* 77 (2 2005), pp. 427–488. DOI: 10.1103/RevModPhys.77.427. URL: <https://link.aps.org/doi/10.1103/RevModPhys.77.427>.
- [34] R. F. Casten. *Nuclear Structure from a Simple Perspective*. Oxford Science Publications, 2000.
- [35] M. Goeppert-Mayer. “On Closed Shells in Nuclei”. In: *United States Atomic Energy Commission Technical Report* (1948). URL: <https://www.osti.gov/biblio/4424422>.
- [36] Maria Goeppert-Mayer. “On Closed Shells in Nuclei. II”. In: *Phys. Rev.* 75 (12 1949), pp. 1969–1970. DOI: 10.1103/PhysRev.75.1969. URL: <https://link.aps.org/doi/10.1103/PhysRev.75.1969>.
- [37] Otto Haxel, J. Hans D. Jensen, and Hans E. Suess. “On the “Magic Numbers” in Nuclear Structure”. In: *Phys. Rev.* 75 (11 1949), pp. 1766–1766. DOI: 10.1103/PhysRev.75.1766.2. URL: <https://link.aps.org/doi/10.1103/PhysRev.75.1766.2>.
- [38] A. Bohr. “The Coupling of Nuclear Surface Oscillations to the Motion of Individual Nucleons”. In: *K. Dansk. Vidensk. Mat.-Fys. Meddr.* 26 (14 1952).
- [39] A. Bohr and B. Mottelson. “Collective and Individual-Particle Aspects of Nuclear Structure”. In: *K. Dansk. Vidensk. Mat.-Fys. Meddr.* 27 (16 1953), pp. 1–174. URL: <https://cds.cern.ch/record/213298/files/p1.pdf>.
- [40] P A Butler. “Octupole collectivity in nuclei”. In: *Journal of Physics G: Nuclear and Particle Physics* 43.7 (2016), p. 073002. DOI: 10.1088/0954-3899/43/7/073002. URL: <https://dx.doi.org/10.1088/0954-3899/43/7/073002>.
- [41] Roger D. Woods and David S. Saxon. “Diffuse Surface Optical Model for Nucleon-Nuclei Scattering”. In: *Phys. Rev.* 95 (2 1954), pp. 577–578. DOI: 10.1103/PhysRev.95.577. URL: <https://link.aps.org/doi/10.1103/PhysRev.95.577>.
- [42] K. S. Krane. *Introductory Nuclear Physics*. John Wiley & Sons, 1988.

- [43] L. Coraggio and N. Itaco. “Perturbative Approach to Effective Shell-Model Hamiltonians and Operators”. In: *Front. Phys* 8 (345 2020). DOI: <https://doi.org/10.3389/fphy.2020.00345>.
- [44] M. Honma, T. Otsuka, B. A. Brown, and T. Mizusaki. “Effective interaction for pf-shell nuclei”. In: *Phys. Rev. C* 65 (6 2002), p. 061301. DOI: [10.1103/PhysRevC.65.061301](https://doi.org/10.1103/PhysRevC.65.061301). URL: <https://link.aps.org/doi/10.1103/PhysRevC.65.061301>.
- [45] Morten Hjorth-Jensen, Thomas T.S. Kuo, and Eivind Osnes. “Realistic effective interactions for nuclear systems”. In: *Physics Reports* 261.3 (1995), pp. 125–270. ISSN: 0370-1573. DOI: [https://doi.org/10.1016/0370-1573\(95\)00012-6](https://doi.org/10.1016/0370-1573(95)00012-6). URL: <https://www.sciencedirect.com/science/article/pii/0370157395000126>.
- [46] M. Honma, T. Otsuka, B. A. Brown, and T. Mizusaki. “Shell-model description of neutron-rich pf-shell nuclei with a new effective interaction GXPF1”. In: *The European Physical Journal A - Hadrons and Nuclei* 25 (1 2005), pp. 499–502. DOI: [10.1140/epjad/i2005-06-032-2](https://doi.org/10.1140/epjad/i2005-06-032-2).
- [47] M. Honma, T. Otsuka, and T. Mizusaki. “Shell-model description of neutron-rich Ca isotopes”. In: *RIKEN Accel. Prog. Rep.* 41 (2008), p. 32.
- [48] A. Poves, J. Sánchez-Solano, E. Caurier, and F. Nowacki. “Shell model study of the isobaric chains  $A=50$ ,  $A=51$  and  $A=52$ ”. In: *Nuclear Physics A* 694.1 (2001), pp. 157–198. ISSN: 0375-9474. DOI: [https://doi.org/10.1016/S0375-9474\(01\)00967-8](https://doi.org/10.1016/S0375-9474(01)00967-8). URL: <https://www.sciencedirect.com/science/article/pii/S0375947401009678>.
- [49] H. Naïdja, F. Nowacki, and B. Bounthong. “Shell-model investigation of spectroscopic properties and collectivity in the nuclei beyond  $^{132}\text{Sn}$ ”. In: *Phys. Rev. C* 96 (3 2017), p. 034312. DOI: [10.1103/PhysRevC.96.034312](https://doi.org/10.1103/PhysRevC.96.034312). URL: <https://link.aps.org/doi/10.1103/PhysRevC.96.034312>.
- [50] D. R. Entem and R. Machleidt. “Accurate charge-dependent nucleon-nucleon potential at fourth order of chiral perturbation theory”. In: *Phys. Rev. C* 68 (4 2003), p. 041001. DOI: [10.1103/PhysRevC.68.041001](https://doi.org/10.1103/PhysRevC.68.041001). URL: <https://link.aps.org/doi/10.1103/PhysRevC.68.041001>.
- [51] Bruce R. Barrett, Petr Navrátil, and James P. Vary. “Ab initio no core shell model”. In: *Progress in Particle and Nuclear Physics* 69 (2013), pp. 131–181. ISSN: 0146-6410. DOI: <https://doi.org/10.1016/j.ppnp.2012.10.003>. URL: <https://www.sciencedirect.com/science/article/pii/S0146641012001184>.
- [52] T. Otsuka, M. Honma, T. Mizusaki, N. Shimizu, and Y. Utsuno. “Monte Carlo shell model for atomic nuclei”. In: *Progress in Particle and Nuclear Physics* 47.1 (2001), pp. 319–400. ISSN: 0146-6410. DOI: [https://doi.org/10.1016/S0146-6410\(01\)00157-0](https://doi.org/10.1016/S0146-6410(01)00157-0). URL: <https://www.sciencedirect.com/science/article/pii/S0146641001001570>.

## REFERENCES

---

- [53] Noritaka Shimizu, Yusuke Tsunoda, Yutaka Utsuno, and Takaharu Otsuka. “Variational approach with the superposition of the symmetry-restored quasiparticle vacua for nuclear shell-model calculations”. In: *Phys. Rev. C* 103 (1 2021), p. 014312. DOI: 10.1103/PhysRevC.103.014312. URL: <https://link.aps.org/doi/10.1103/PhysRevC.103.014312>.
- [54] F. S. Stephens, Frank Asaro, and I. Perlman. “Radiations from 1 — States in Even-Even Nuclei”. In: *Phys. Rev.* 100 (5 1955), pp. 1543–1545. DOI: 10.1103/PhysRev.100.1543. URL: <https://link.aps.org/doi/10.1103/PhysRev.100.1543>.
- [55] Kiuck Lee and D. R. Inglis. “Stability of Pear-Shaped Nuclear Deformations”. In: *Phys. Rev.* 108 (3 1957), pp. 774–778. DOI: 10.1103/PhysRev.108.774. URL: <https://link.aps.org/doi/10.1103/PhysRev.108.774>.
- [56] L. P. Gaffney, P. A. Butler, M. Scheck, A. B. Hayes, F. Wenander, M. Albers, B. Bastin, C. Bauer, A. Blazhev, S. Bönig, N. Bree, J. Cederkäll, T. Chupp, D. Cline, T. E. Cocolios, T. Davinson, H. De Witte, J. Diriken, T. Grahn, A. Herzan, M. Huysse, D. G. Jenkins, D. T. Joss, N. Kesteloot, J. Konki, M. Kowalczyk, Th. Kröll, E. Kwan, R. Lutter, K. Moschner, P. Napiorkowski, J. Pakarinen, M. Pfeiffer, D. Radeck, P. Reiter, K. Reynders, S. V. Rigby, L. M. Robledo, M. Rudigier, S. Sambhi, M. Seidlitz, B. Siebeck, T. Stora, P. Thoele, P. Van Duppen, M. J. Vermeulen, M. von Schmid, D. Voulot, N. Warr, K. Wimmer, K. Wrzosek-Lipska, C. Y. Wu, and M. Zielinska. “Studies of pear-shaped nuclei using accelerated radioactive beams”. In: *Nature* 497.7448 (2013), pp. 199–204. ISSN: 1476-4687. DOI: 10.1038/nature12073. URL: <https://doi.org/10.1038/nature12073>.
- [57] G. de Angelis, A. Gadea, E. Farnea, R. Isocrate, P. Petkov, N. Marginean, D.R. Napoli, A. Dewald, M. Bellato, A. Bracco, F. Camera, D. Curien, M. De Poli, E. Fioretto, A. Fitzler, S. Kasemann, N. Kintz, T. Klug, S. Lenzi, S. Lunardi, R. Menegazzo, P. Pavan, J.L. Pedroza, V. Pucknell, C. Ring, J. Sampson, and R. Wyss. “Coherent proton–neutron contribution to octupole correlations in the neutron-deficient 114Xe nucleus”. In: *Physics Letters B* 535.1 (2002), pp. 93–102. ISSN: 0370-2693. DOI: [https://doi.org/10.1016/S0370-2693\(02\)01728-8](https://doi.org/10.1016/S0370-2693(02)01728-8). URL: <https://www.sciencedirect.com/science/article/pii/S0370269302017288>.
- [58] *The Colourful Nuclide Chart*. URL: <https://people.physics.anu.edu.au/~ecs103/chart/>.
- [59] I Ahmad and P A Butler. “Octupole Shapes in Nuclei”. In: *Annual Review of Nuclear and Particle Science* 43.1 (1993), pp. 71–116. DOI: 10.1146/annurev.ns.43.120193.000443. eprint: <https://doi.org/10.1146/annurev.ns.43.120193.000443>. URL: <https://doi.org/10.1146/annurev.ns.43.120193.000443>.
- [60] J.F.C. Cocks, D. Hawcroft, N. Amzal, P.A. Butler, K.J. Cann, P.T. Greenlees, G.D. Jones, S. Asztalos, R.M. Clark, M.A. Deleplanque, R.M. Diamond, P. Fallon, I.Y. Lee, A.O. Macchiavelli, R.W. MacLeod, F.S. Stephens, P. Jones, R. Julin, R. Broda, B. Fornal, J.F. Smith, T. Lauritsen, P. Bhattacharyya, and C.T. Zhang. “Spectroscopy of Rn, Ra and

- Th isotopes using multi-nucleon transfer reactions”. In: *Nuclear Physics A* 645.1 (1999), pp. 61–91. ISSN: 0375-9474. DOI: [https://doi.org/10.1016/S0375-9474\(98\)00586-7](https://doi.org/10.1016/S0375-9474(98)00586-7). URL: <https://www.sciencedirect.com/science/article/pii/S0375947498005867>.
- [61] G. L. Zimba, J. F. Sharpey-Schafer, P. Jones, S. P. Bvumbi, L. P. Masiteng, S. N. T. Majola, T. S. Dinoko, E. A. Lawrie, J. J. Lawrie, D. Negi, P. Papka, D. Roux, O. Shirinda, J. E. Easton, and N. A. Khumalo. “Octupole correlations in  $N = 88$   $^{154}\text{Dy}$ : Octupole vibration versus stable deformation”. In: *Phys. Rev. C* 94 (5 2016), p. 054303. DOI: 10.1103/PhysRevC.94.054303. URL: <https://link.aps.org/doi/10.1103/PhysRevC.94.054303>.
- [62] A. A. Sonzogni. In: *Nucl. Data Sheet* 93 (599 2001). URL: <https://www.nndc.bnl.gov/ensdf/>.
- [63] T. D. Johnson, D. Symochko, M. Fadil, and J. K. Tuli. In: *Nucl. Data Sheet* 112 (1949 2011). URL: <https://www.nndc.bnl.gov/ensdf/>.
- [64] S. K. Basu and A. A. Sonzogni. In: *Nucl. Data Sheet* 114 (435 2013). URL: <https://www.nndc.bnl.gov/ensdf/>.
- [65] H. Naïdja, F. Nowacki, B. Bounthong, M. Czerwiński, T. Rząca-Urban, T. Rogiński, W. Urban, J. Wiśniewski, K. Sieja, A. G. Smith, J. F. Smith, G. S. Simpson, I. Ahmad, and J. P. Greene. “New excitations in  $^{142}\text{Ba}$  and  $^{144}\text{Ce}$ : Evolution of  $\gamma$  bands in the  $N = 86$  isotones”. In: *Phys. Rev. C* 95 (6 2017), p. 064303. DOI: 10.1103/PhysRevC.95.064303. URL: <https://link.aps.org/doi/10.1103/PhysRevC.95.064303>.
- [66] P.A. Butler and W. Nazarewicz. “Intrinsic dipole moments in reflection-asymmetric nuclei”. In: *Nuclear Physics A* 533.2 (1991), pp. 249–268. ISSN: 0375-9474. DOI: [https://doi.org/10.1016/0375-9474\(91\)90489-S](https://doi.org/10.1016/0375-9474(91)90489-S). URL: <https://www.sciencedirect.com/science/article/pii/037594749190489S>.
- [67] P. A. Butler. “Pear-shaped atomic nuclei”. In: *Proceedings of the Royal Society A: Mathematical, Physical and Engineering Sciences* 476.2239 (2020), p. 20200202. DOI: 10.1098/rspa.2020.0202. eprint: <https://royalsocietypublishing.org/doi/pdf/10.1098/rspa.2020.0202>. URL: <https://royalsocietypublishing.org/doi/abs/10.1098/rspa.2020.0202>.
- [68] A. D. Sakharov. “Violation of CP Invariance, C asymmetry, and baryon asymmetry of the universe”. In: *Prisma Zh. Eksp. Teor. Fiz.* 5 (1967), pp. 32–35. DOI: 10.1070/PU1991v034n05ABEH002497.
- [69] L. I. Schiff. “Measurability of Nuclear Electric Dipole Moments”. In: *Phys. Rev.* 132 (5 1963), pp. 2194–2200. DOI: 10.1103/PhysRev.132.2194. URL: <https://link.aps.org/doi/10.1103/PhysRev.132.2194>.
- [70] T. E. Chupp, P. Fierlinger, M. J. Ramsey-Musolf, and J. T. Singh. “Electric dipole moments of atoms, molecules, nuclei, and particles”. In: *Rev. Mod. Phys.* 91 (1 2019), p. 015001. DOI: 10.1103/RevModPhys.91.015001. URL: <https://link.aps.org/doi/10.1103/RevModPhys.91.015001>.

- [71] P. A. Butler, L. P. Gaffney, P. Spagnoletti, J. Konki, M. Scheck, J. F. Smith, K. Abrahams, M. Bowry, J. Cederkäll, T. Chupp, G. de Angelis, H. De Witte, P. E. Garrett, A. Goldkuhle, C. Henrich, A. Illana, K. Johnston, D. T. Joss, J. M. Keatings, N. A. Kelly, M. Komorowska, T. Kröll, M. Lozano, B. S. Nara Singh, D. O'Donnell, J. Ojala, R. D. Page, L. G. Pedersen, C. Raison, P. Reiter, J. A. Rodriguez, D. Rosiak, S. Rothe, T. M. Shneidman, B. Siebeck, M. Seidlitz, J. Sinclair, M. Stryjczyk, P. Van Duppen, S. Vinals, V. Virtanen, N. Warr, K. Wrzosek-Lipska, and M. Zielinska. “The observation of vibrating pear-shapes in radon nuclei”. In: *Nature Communications* 10.2473 (2019). DOI: <https://doi.org/10.1038/s41467-019-10494-5>. URL: <https://www.nature.com/articles/s41467-019-10494-5>.
- [72] K. Nomura, R. Rodríguez-Guzmán, L. M. Robledo, J. E. García-Ramos, and N. C. Hernández. “Evolution of octupole deformation and collectivity in neutron-rich lanthanides”. In: *Phys. Rev. C* 104 (4 2021), p. 044324. DOI: 10.1103/PhysRevC.104.044324. URL: <https://link.aps.org/doi/10.1103/PhysRevC.104.044324>.
- [73] B. Bucher, S. Zhu, C. Y. Wu, R. V. F. Janssens, R. N. Bernard, L. M. Robledo, T. R. Rodríguez, D. Cline, A. B. Hayes, A. D. Ayangeakaa, M. Q. Buckner, C. M. Campbell, M. P. Carpenter, J. A. Clark, H. L. Crawford, H. M. David, C. Dickerson, J. Harker, C. R. Hoffman, B. P. Kay, F. G. Kondev, T. Lauritsen, A. O. Macchiavelli, R. C. Pardo, G. Savard, D. Seweryniak, and R. Vondrasek. “Direct Evidence for Octupole Deformation in  $^{146}\text{Ba}$  and the Origin of Large  $E1$  Moment Variations in Reflection-Asymmetric Nuclei”. In: *Phys. Rev. Lett.* 118 (15 2017), p. 152504. DOI: 10.1103/PhysRevLett.118.152504. URL: <https://link.aps.org/doi/10.1103/PhysRevLett.118.152504>.
- [74] S. Goriely, S. Hilaire, M. Girod, and S. Péru. “First Gogny-Hartree-Fock-Bogoliubov Nuclear Mass Model”. In: *Phys. Rev. Lett.* 102 (24 2009), p. 242501. DOI: 10.1103/PhysRevLett.102.242501. URL: <https://link.aps.org/doi/10.1103/PhysRevLett.102.242501>.
- [75] M. Beckers, A. Dewald, C. Fransen, L. Kornwebel, C.-D. Lakenbrink, and F. von Spee. “Revisiting the measurement of absolute foil-separation for RDDS measurements and introduction of an optical measurement method”. In: *Nuclear Instruments and Methods in Physics Research Section A: Accelerators, Spectrometers, Detectors and Associated Equipment* 1042 (2022), p. 167416. ISSN: 0168-9002. DOI: <https://doi.org/10.1016/j.nima.2022.167416>. URL: <https://www.sciencedirect.com/science/article/pii/S0168900222007082>.
- [76] M. Beckers, C. Müller-Gatermann, K. Arnsward, T. Braunroth, D. Dewald, C. Fransen, and A. Goldkuhle. “Lifetime measurement of the  $2_1^+, 4_1^+$  states in semi-magic  $^{60}\text{Ni}$ ”. In: *The European Physical Journal A* 59 (129 2023). DOI: 10.1140/epja/s10050-023-01031-6.
- [77] S. Akkoyun et al. “AGATA — Advanced GAMMA Tracking Array”. In: *Nuclear Instruments and Methods in Physics Research Section A: Accelerators, Spectrometers, Detectors and Associated Equipment* 668 (2012), pp. 26–58. ISSN: 0168-9002. DOI: <https://doi.org/10.1016/j.nima.2011.11.081>. URL: <https://www.sciencedirect.com/science/article/pii/S0168900211021516>.

- [78] D. Montanari, E. Farnea, S. Leoni, G. Pollarolo, L. Corradi, G. Benzoni, A. Gadea, E. Fioretto, A. Latina, G. Montagnoli, F. Scarlassara, A.M. Stefanini, and S. Szilner. “Response function of the magnetic spectrometer PRISMA”. In: *The European Physical Journal A* 47.4 (2010). DOI: <https://doi.org/10.1140/epja/i2011-11004-9>. URL: <https://www.sciencedirect.com/science/article/pii/S0168900205013501>.
- [79] S. Beghini, L. Corradi, E. Fioretto, A. Gadea, A. Latina, G. Montagnoli, F. Scarlassara, A.M. Stefanini, S. Szilner, M. Trotta, and A.M. Vinodkumar. “The focal plane detector of the magnetic spectrometer PRISMA”. In: *Nuclear Instruments and Methods in Physics Research Section A: Accelerators, Spectrometers, Detectors and Associated Equipment* 551.2 (2005), pp. 364–374. ISSN: 0168-9002. DOI: <https://doi.org/10.1016/j.nima.2005.06.058>. URL: <https://www.sciencedirect.com/science/article/pii/S0168900205013501>.
- [80] G. Montagnoli, A.M. Stefanini, M. Trotta, S. Beghini, M. Bettini, F. Scarlassara, V. Schiavon, L. Corradi, B.R. Behera, E. Fioretto, A. Gadea, A. Latina, S. Szilner, L. Donà, M. Rigato, N.A. Kondratiev, A. Yu. Chizhov, G. Kniajeva, E.M. Kozulin, I.V. Pokrovskiy, V.M. Voskressensky, and D. Ackermann. “The large-area micro-channel plate entrance detector of the heavy-ion magnetic spectrometer PRISMA”. In: *Nuclear Instruments and Methods in Physics Research Section A: Accelerators, Spectrometers, Detectors and Associated Equipment* 547.2 (2005), pp. 455–463. ISSN: 0168-9002. DOI: <https://doi.org/10.1016/j.nima.2005.03.158>. URL: <https://www.sciencedirect.com/science/article/pii/S0168900205009241>.
- [81] J. Pakarinen, J. Ojala, P. Ruotsalainen, H. Tann, H. Badran, T. Calverley, J. Hilton, T. Grahn, P.T. Greenlees, M. Hytönen, A. Illana, A. Kauppinen, M. Luoma, P. Papadakis, J. Partanen, K. Porras, M. Puskala, P. Rahkila, K. Ranttila, J. Saren, M. Sandzelius, S. Szvec, J. Tuunanen, J. Uusitalo, and G. Zimba. “The JUROGAM 3 spectrometer”. In: *The European Physical Journal A* 56.149 (2020). DOI: <https://doi.org/10.1140/epja/s10050-020-00144-6>. URL: <https://link.springer.com/article/10.1140/epja/s10050-020-00144-6>.
- [82] J. Sarén, J. Uusitalo, M. Leino, P.T. Greenlees, U. Jakobsson, P. Jones, R. Julin, S. Juutinen, S. Ketelhut, M. Nyman, P. Peura, P. Rahkila, C. Scholey, and J. Sorri. “The new vacuum-mode recoil separator MARA at JYFL”. In: *Nuclear Instruments and Methods in Physics Research Section B: Beam Interactions with Materials and Atoms* 266.19 (2008). Proceedings of the XVth International Conference on Electromagnetic Isotope Separators and Techniques Related to their Applications, pp. 4196–4200. ISSN: 0168-583X. DOI: <https://doi.org/10.1016/j.nimb.2008.05.027>. URL: <https://www.sciencedirect.com/science/article/pii/S0168583X08007040>.
- [83] M. Leino, J. Äystö, T. Enqvist, P. Heikkinen, A. Jokinen, M. Nurmi, A. Ostrowski, W.H. Trzaska, J. Uusitalo, K. Eskola, P. Armbruster, and V. Ninov. “Gas-filled recoil separator for studies of heavy elements”. In: *Nuclear Instruments and Methods in Physics Research Section B: Beam Interactions with Materials and Atoms* 99.1 (1995). Application

- of Accelerators in Research and Industry '94, pp. 653–656. ISSN: 0168-583X. DOI: [https://doi.org/10.1016/0168-583X\(94\)00573-7](https://doi.org/10.1016/0168-583X(94)00573-7). URL: <https://www.sciencedirect.com/science/article/pii/0168583X94005737>.
- [84] S. Paschalis, I.Y. Lee, A.O. Macchiavelli, C.M. Campbell, M. Cromaz, S. Gros, J. Pavan, J. Qian, R.M. Clark, H.L. Crawford, D. Doering, P. Fallon, C. Lionberger, T. Loew, M. Petri, T. Stezelberger, S. Zimmermann, D.C. Radford, K. Lagergren, D. Weisshaar, R. Winkler, T. Glasmacher, J.T. Anderson, and C.W. Beausang. “The performance of the Gamma-Ray Energy Tracking In-beam Nuclear Array GRETINA”. In: *Nuclear Instruments and Methods in Physics Research Section A: Accelerators, Spectrometers, Detectors and Associated Equipment* 709 (2013), pp. 44–55. ISSN: 0168-9002. DOI: <https://doi.org/10.1016/j.nima.2013.01.009>. URL: <https://www.sciencedirect.com/science/article/pii/S0168900213000508>.
- [85] I-Yang Lee. “The GAMMASPHERE”. In: *Nuclear Physics A* 520 (1990). Nuclear Structure in the Nineties, pp. c641–c655. ISSN: 0375-9474. DOI: [https://doi.org/10.1016/0375-9474\(90\)91181-P](https://doi.org/10.1016/0375-9474(90)91181-P). URL: <https://www.sciencedirect.com/science/article/pii/037594749091181P>.
- [86] Cary N. Davids and James D. Larson. “The Argonne fragment mass analyzer”. In: *Nuclear Instruments and Methods in Physics Research Section B: Beam Interactions with Materials and Atoms* 40-41 (1989), pp. 1224–1228. ISSN: 0168-583X. DOI: [https://doi.org/10.1016/0168-583X\(89\)90624-1](https://doi.org/10.1016/0168-583X(89)90624-1). URL: <https://www.sciencedirect.com/science/article/pii/0168583X89906241>.
- [87] Back, B. B. “The AGFA and AIRIS separators at ATLAS”. In: *EPJ Web Conf.* 163 (2017), p. 00003. DOI: [10.1051/epjconf/201716300003](https://doi.org/10.1051/epjconf/201716300003). URL: <https://doi.org/10.1051/epjconf/201716300003>.
- [88] A. Chester, G.C. Ball, N. Bernier, D.S. Cross, T. Domingo, T.E. Drake, L.J. Evitts, F.H. Garcia, A.B. Garnsworthy, G. Hackman, S. Hallam, J. Henderson, R. Henderson, R. Krücken, E. MacConnachie, M. Moukaddam, E. Padilla-Rodal, O. Paetkau, J.L. Pore, U. Rizwan, P. Ruotsalainen, J. Shoults, J. Smallcombe, J.K. Smith, K. Starosta, C.E. Svensson, K. Van Wieren, J. Williams, and M. Williams. “Recoil distance method lifetime measurements at TRIUMF-ISAC using the TIGRESS Integrated Plunger”. In: *Nuclear Instruments and Methods in Physics Research Section A: Accelerators, Spectrometers, Detectors and Associated Equipment* 882 (2018), pp. 69–83. ISSN: 0168-9002. DOI: <https://doi.org/10.1016/j.nima.2017.11.029>. URL: <https://www.sciencedirect.com/science/article/pii/S0168900217312275>.
- [89] A. Esmaylzadeh, A. Blazhev, K. Nomura, J. Jolie, M. Beckers, C. Fransen, R.-B. Gerst, A. Harter, V. Karayonchev, L. Knafla, M. Ley, and F. von Spee. “Investigation of  $\gamma$  softness: Lifetime measurements in  $^{104,106}\text{Ru}$ ”. In: *Phys. Rev. C* 106 (6 2022), p. 064323. DOI: [10.1103/PhysRevC.106.064323](https://doi.org/10.1103/PhysRevC.106.064323). URL: <https://link.aps.org/doi/10.1103/PhysRevC.106.064323>.



## REFERENCES

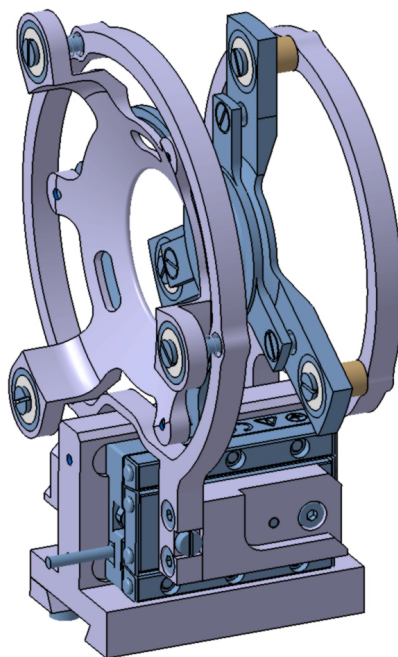
---

- [90] *CL-3000 Series Confocal Displacement Sensor Catalog*. 2019. URL: <https://www.keyence.com/>.

## Appendix

Manual for the Cologne Plunger Software Package and the Set-Up of a Compact Plunger measurement

# Setting up a Compact Plunger Measurement with the Cologne Plunger Software Package (CPSP) for Windows



**A Manual**

Marcel Beckers  
mbeckers@ikp.uni-koeln.de

# 1 Introduction and general remarks

A software package, needed to carry out several tasks related to the operation of a plunger, has been developed by the Cologne plunger group over several years. Its official name was Plunger Feedback Control for Linux (PFCL) and it was (and still is) used in different laboratories all over the world. It consists of different programs, designed to handle the following tasks: Moving the motor that changes the foil distance (*Motor*), reading out the induced voltage signal in the foil (*MCA*), creating sample points for a distance calibration (*CalPoints*), obtaining a distance calibration (*DistCal*), investigate the distance calibration curve (*Spline*) and finally the core task of setting distances during the experiment with the motor and keeping them constant using a feedback system and a piezo crystal (*Feedback*).

The need for a remade software package came up due to two main reasons: First, the fact, that National Instruments, the manufacturer of the DAQ equipment used for the plunger control decided to drop Linux support for their future releases. Second, the advent of the so-called compact plungers built in Cologne, e.g. GALILEO plunger, APPA, iCAPS and the three-foil plunger CoCoDiff [1], which do not use any kind of additional distance measurement probe and also omit the piezo used for the feedback system due to spacial restrictions. Since the motor has to take over the duties previously performed by these devices (measuring the relative distance and controlling the distance during the measurement), the precision of the motor control had to be greatly increased by using a closed-loop system (instead of an open-loop one, like in the older version of the plunger software). For someone being used to the older version of the software, the main differences are that one can now set exact step widths in  $\mu\text{m}$  in the *Motor* program (instead of an abstract "velocity" value) as well as choose precisely the step width for the *Feedback* program. Another difference can be seen in the *DistCal* program, where the measurement points are now reached in a more direct and precise way, which eliminates most of the noise that was often found in the distance calibration curves, especially at close distances. This manual is meant as a short guideline how to install the new software package for windows and how to set up a measurement with one of the new compact plungers as well as a short reference for the usage of the different programs. It does not claim to be complete in any way. For details about the plunger method itself and the physical background of choosing the right parameters for a measurement the reader is referred to the review paper [2].

## 2 Getting ready

### 2.1 Installing the Software

An executable installer has been built to install the software package. To ensure a smooth procedure it is recommended using a designated plunger control PC with a fresh install of Windows 10 where no other NI DAQ related software is installed. It is also recommended,

to name the user of the PC "plunger", to ensure the consistency of all file/folder paths, although that is not a strict prerequisite (s. below). You will need some kind of a DAQ card from National Instruments to make the software work, either a USB type or PCI type one. For this manual it is assumed, that you have the complete install directory available, including the installer and the additional directories. Before starting the install procedure, make sure the DAQ card is connected and powered up. Then:

- run the *installer.exe* and keep every setting at default. You will have to restart the PC afterwards, make sure that the DAQ cards remains connected to the system during that.

- As the system restarts, the installer will prompt you to import configurations. Leave everything on default and move through the steps.

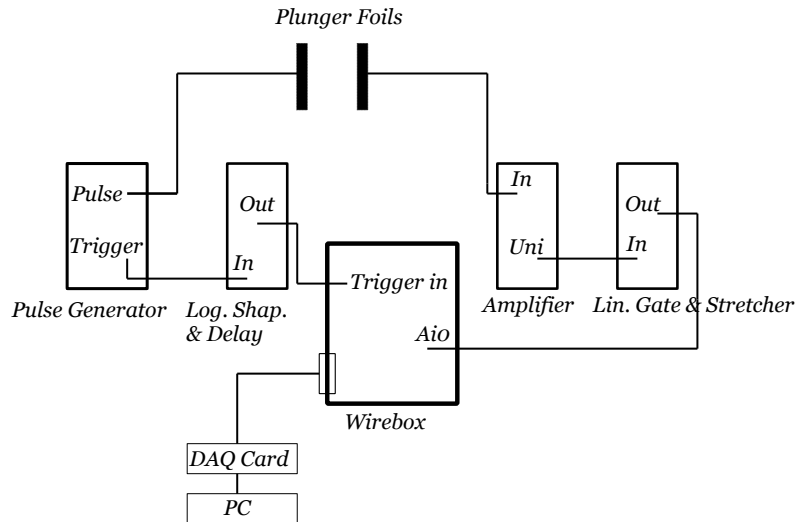
- Some necessary sub-VIs can not be installed with the installer. Also the configuration file *plunger.ini* does not come with the installer. To get everything working correctly, you have to copy all folders in the install directory to C:\Users\plunger\Documents. Leave the directory structure untouched.

IMPORTANT: If your Windows user is not named "plunger", you have to create that path manually, even if this user does not exist. To be able to write in that directory (which is necessary for most programs), you have to run all programs as a administrator in that case, because the active user will have no rights to write there.

- After these steps, the executable of the programs can be found at C:\Users\username\Program files\plunger. For convenience you can create shortcuts on your desktop and, if the user is not named plunger, set them to be always executed as administrator.

## 2.2 Setting up the DAQ and Motor

After you have everything installed, you have to make sure that the names of the connected devices match those expected by the programs. First, you have to connect the motor controller to the PC. This has to be done using the serial port of the motor controller and a serial-to-USB adapter. Then, open up the *plunger.ini* configuration file, found at C:\Users\plunger\Documents \\_plunger with a text editor. Search for the line called "motor\_port" in the section [exp\_single]. Then open up "NIMax" (which has been installed with the installer) and search for the menu point "Devices" at the left. There you can find all the devices currently connected to your PC. Find out, which of these is the motor controller (e.g. by disconnecting all devices except for one). The name of the devices should be something like ASRL::4(COM4). Make sure that the number (in this case 4) is the same as in the configuration file (changing it in the configuration file if necessary). Do the same for "daqcard\_port" (which should be named e.g. Dev1). Now everything should be set up and ready to go.



### 2.3 Wiring the signals

To be able to measure the voltage signal for the capacitance method you need to have the following NIM modules ready:

- Model PB-5 Pulse Generator from BNC (or similar)
- Logic Shaper and Delay unit e.g. CANBERRA
- Spectroscopic amplifier module (e.g. ORTEC 572A)
- Linear Gate and Stretcher unit (e.g. CANBERRA 1454)

Additionally you will need the above mentioned NI DAQ card and a so-called wirebox to

feed analog signals into the DAQ card. Pulser(Pulse) → Degraded Foil

Pulser (Trigger) → Logic Shaper and Delay → Trigger input on wirebox

Target Foil → Amplifier → Linear Gate and Stretcher →

input ai0 on wirebox

Make sure to check on a scope that the pulse from the Logic Shaper and Delay output is correctly aligned with the signal from the Linear Gate and Stretcher. The pulse has to come in during the stretched signal. If not you can move the pulse around with the delay unit and/or enlarge the stretched signal with the stretcher. If everything is set up correctly you should be able to see an output voltage using the *MCA* program. If the voltage is (close to) zero the pulse will likely be outside the stretched signal, if the voltage is very unstable (jumping between 0 and some non-zero value) the pulse will likely be at the edge of the stretched signal.

## 3 Setting up a plunger measurement

It is assumed, that the software is correctly installed and the wiring is correct. It is also assumed, that the foils are already in place on the holding structure.

### 3.1 Finding the electrical contact point

Start the Programs *Motor* and *MCA*. You should be able to read out the induced voltage in *MCA* while changing the distance with the program *Motor*. Start moving the foils together (voltage should increase<sup>1</sup>). Check optically how close you are while doing this and adjust the step width accordingly to avoid damaging the foils. At some point the induced voltage will jump to 10V, which is the maximum output of the stretcher module and indicates a short circuit. This is your electrical contact point. After you moved out of contact again (voltage is no longer 10V), it is suggested that you adjust the pre-contact voltage using the amplifier module to a value of  $\approx 7-8$  V. Thus, you will have a large voltage range for the movement.

### 3.2 Parallel Alignment

At first, the two foils have to be aligned. The alignment is done with the 3 screws and springs at the target holder and controlled optically. The way it is normally done, is by getting to a very short distance and watch through the slit between the foils while slowly moving the foils further together. To see this properly, a counter-light should be used. One can normally see very well at which part of the slit the light starts to vanish first, i.e. where the foils touch first. If the foils are aligned, this should be from the middle of the slit and almost at the same time for the complete slit. This has to be checked from both directions (left-right, up-down). To adjust, use the spring and screws at the three holding points of the cone to change the orientation slightly. Make sure to not damage the foils e.g. by moving to a safe distance where they can not touch while working with the screws. You might also want to check frequently if the optical contact point matches with the electrical contact point (more or less, deviations of some  $\mu\text{m}$  in both directions can appear, due to non conducting layers on the foils (e.g. oxide-layers) or invisible spikes in the foil which lead to earlier contact). Keep in mind, that aligning the foils will increase the pre-contact voltage. It might thus be possible that the voltage signal exceeds the 10 V cutoff before the electrical contact. In this case, you have to lower the amplification on the amplifier module. Keep adjusting the alignment until you are satisfied.

### 3.3 Distance Calibration

After the foils are aligned, you have to perform a distance calibration. To prepare for this, determine again the electrical contact point (which will have changed during the alignment process). Use the option in the *Motor* program to "rename position to" zero, so that the motor reading is equal to the relative distance from the contact point. You should again adjust the pre-contact voltage to a value of  $\approx 7-8$  V using the amplifier module. Don't change the amplification after the distance calibration! Then, create a file with relative

---

<sup>1</sup>If the foil separation is really large ( $>1\text{mm}$ ), the voltage read out will be mostly electronic noise. You should then decrease the separation while ensuring optically that you are not getting into close contact until the voltage starts to increase.

distance points, you want to sample at, using *CalPoints*. Here you can enter the name of the experiment, which will create a folder for that experiment. Finally, run *DistCal* to conduct the distance calibration. Enter a voltage higher than the one just before the contact point as a limit and set the precision to e.g. 0.1. After the distance calibration, you should inspect the calibration curve. You can start with opening the *Spline* program, which automatically loads the last curve and displays it. You should also do a short extrapolation of the linear part, to extract the absolute zero point. The offset between this and the last point before the electrical contact is the smallest achievable plunger distance. If you need smaller distances, go back to the alignment process and try to get a better alignment. However, it finally depends on the material and the quality of the foils, what the smallest achievable distance will be, due to spikes or oxide layers etc. You might also check for removable particles on the foils, e.g. dust.

### **3.4 Starting the measurement**

After you are satisfied with the distance calibration, start the *Feedback* program. It loads the latest calibration file from the current experiment directory. You can now start setting the desired first distance and start measuring. The tolerance setting has to be adjusted respective to the distance which is being measured. Since for large distances the induced voltage gets smaller, the percentage of electronic noise becomes larger and the tolerance has to be increased. If you want to measure at very small distances like 1  $\mu\text{m}$  with respect to the electrical contact, consider this to be one of the first distances, because it might be that it can not be reached anymore after some time due to thermal deformations.

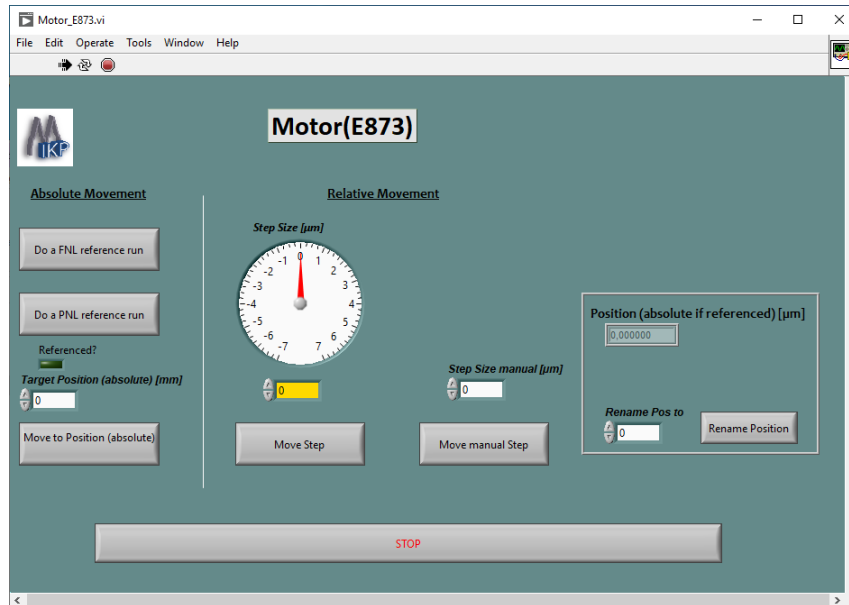
### **3.5 Changing the distance**

To change the distance during an experiment it is important to first stop the experiment's data acquisition. Afterwards, start a new plunger run in the *Feedback* program. Then turn off the feedback (green light button), specify the new distance and drive manually to that distance using the motor controls at the bottom. Then, turn the feedback back on and start a new plunger run again. That way, you have a single plunger run that contains the motion of the motor and otherwise clean runs that only contain one distance each.



## 4 Appendix - Programs of the Cologne Plunger Software Package (CPSP)

### 4.1 Motor



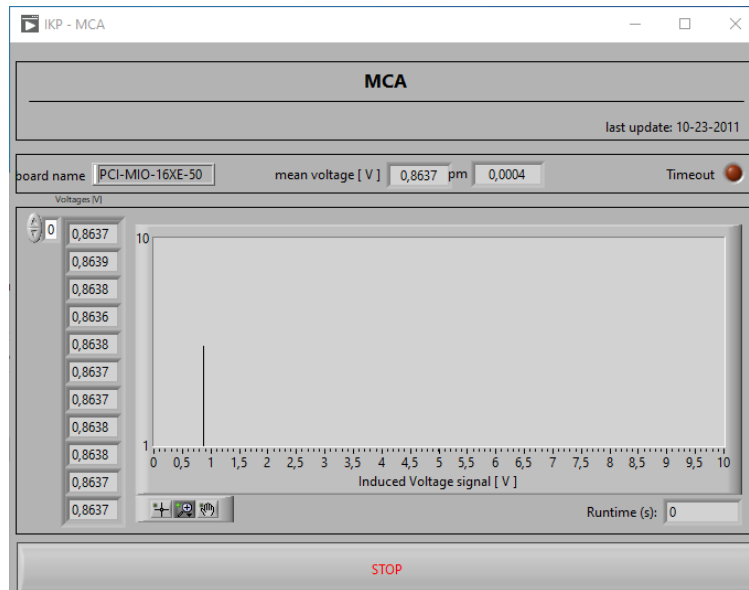
The *Motor* program is used to send movement commands to the motor controller and eventually to the motor itself. It uses a closed-loop approach, which means, that the controller receives a command to move a step in physical units and handles the adjustment of the voltage given to the motor internally, by checking the motion of the motor with the internal optical distance measurement.

It is possible to calibrate the motor for absolute movement (left side of the program interface). For this, the motor has to be able to travel the complete travel range, which is in general not possible when it is used in a plunger. After this, the position readout of the motor is equal to the "real" position of the motor.

For a plunger measurement, relative movement is normally what we want to use (right side of the interface). There one has the possibility to send the desired step size to the motor, either by using the "wheel" for step sizes from  $-7$  to  $7 \mu\text{m}$  or by entering a manual step size, e.g. if larger distances need to be traveled. ATTENTION: Larger steps can obviously damage the target and degrader, if the separation is too small. Also, make sure that the motor moves in the direction you expect it to before moving larger steps. If you disassembled the plunger lately or changed the motor direction in the *plunger.ini*, the directions of "+" and "-" might have changed. In the standard configuration "-" decreases the separation between the foils while "+" increases it.

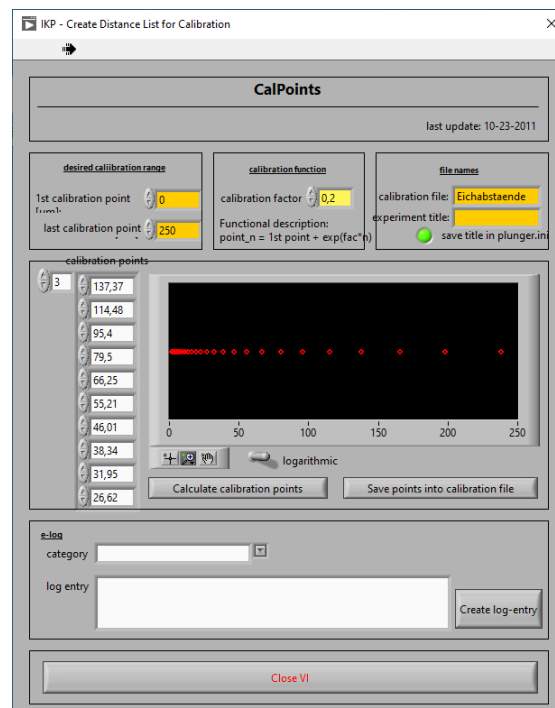
Finally, it is also possible to set the position readout to a certain value (only in relative mode). This does not lead to a movement but just renames the position.

## 4.2 Voltage Readout (MCA)



The *MCA* program reads the induced voltage from the input specified in *plunger.ini* (default: ai0). The measurement is triggered by the external trigger connected via the trigger input, therefore it only works if said trigger is present and the signals are correctly tuned (see above). The voltage is displayed numerically and at the same time is written into a histogram together with the last measurements to help judging if the signal is stable.

## 4.3 CalPoints

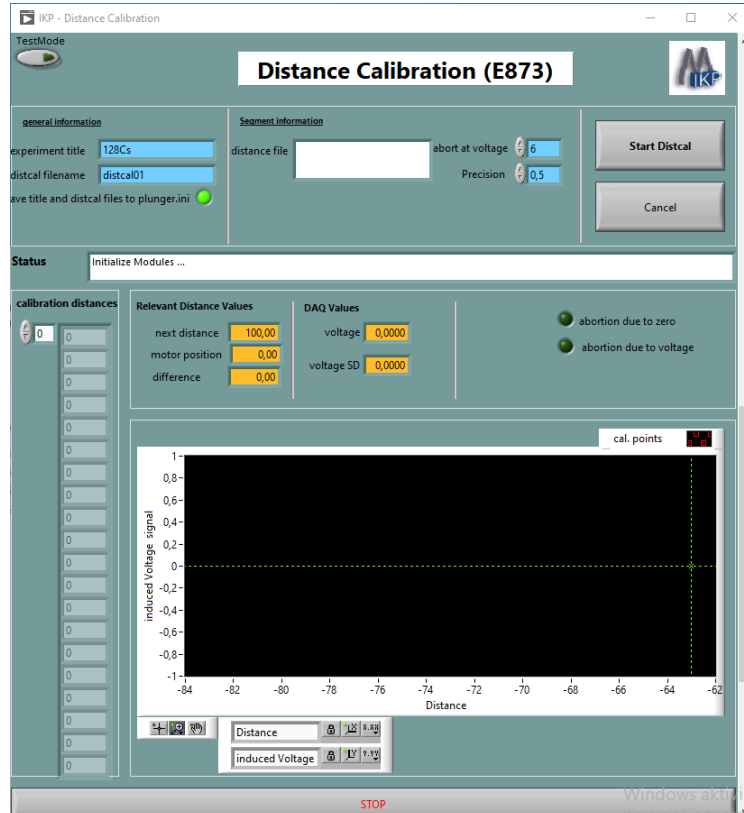


*CalPoints* is used to create a file with distance points, which can be used by the *DistCal* program to determine at which points it conducts its measurement. Since the change in voltage becomes larger at small distances and at the same time these small distances are more important for the determination of the absolute zero point, the function

$$Point_n = Point_1 + e^{k*n} \quad (1)$$

where  $k$  can be chosen by the user to determine how many points will be created, is used to ensure that the spacing between points gets smaller closer to the zero point. More points are generally better, so a value around 0.15 or smaller is recommended, especially as the new version of the *DistCal* program works quite fast compared to older versions. Also, the first and the last point that should be used for the calibration have to be specified. Note that these points correspond to the reading of the motor. Therefore, if you have set the motor reading to zero at the electrical contact point, the first point to use for the calibration should always be 0. Lastly, the user can enter the name of the experiment here, which creates a folder with that name and uses this folder in the following steps of the set-up in the other programs of the CPSP. The path to the folder will be written to the *plunger.ini* configuration file.

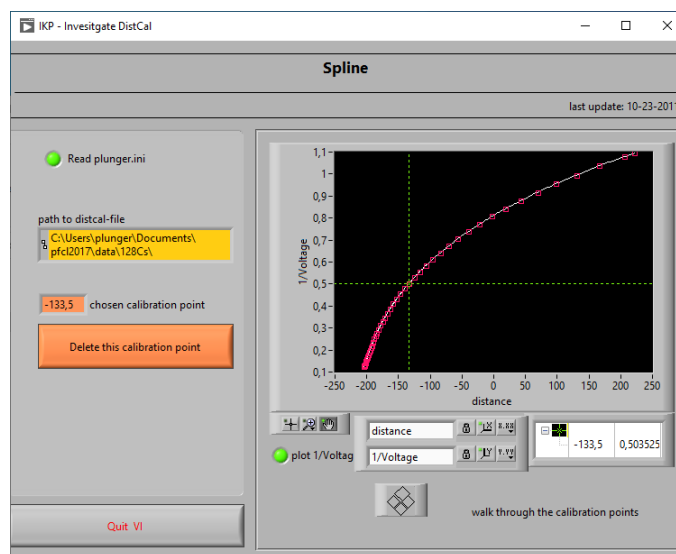
#### 4.4 DistCal



*DistCal* performs the calibration between (relative) distance and induced voltage.

Therefore it drives the motor to the calibration points specified in *CalPoints*, measures the respective voltage and writes these values to a file. It automatically aborts the measurement if the voltage is larger than the maximum as specified by the user or if the closest calibration point is reached. The result of the measurement is plotted "live" while it is being conducted. The file with the calibration points is automatically loaded from the experiment directory specified in *CalPoints*. If another file should be used, the experiment path can be reset manually in *plunger.ini*. The user has to specify the name of the resulting file with the calibration values and the abortion voltage. After the calibration is finished, *DistCal* writes the path of the created file to *plunger.ini*, for the *Spline* and *Feedback* programs to read from.

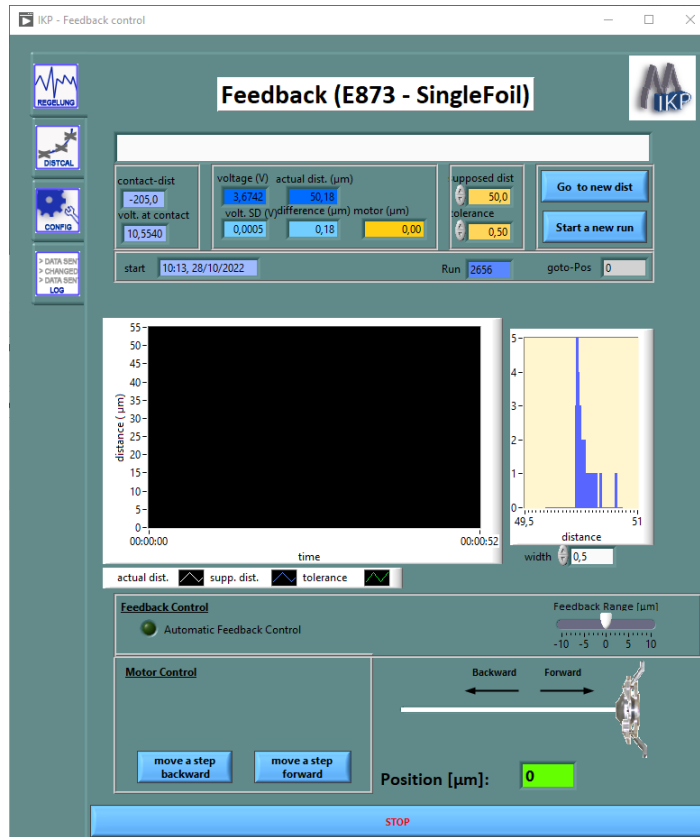
#### 4.5 Calibration Curve Investigator (Spline)



*Spline* is used to look in detail at the calibration curve created by *DistCal*. It automatically loads the last file created in the experiment directory. To estimate the absolute zero point by extrapolation it is best to plot the values by  $1/U$ . One can also use *Spline* to remove certain points from the calibration file. If changes have been made, *Spline* asks the user if they should be changed when the program is closed. Otherwise the original status of the calibration file is restored. *Spline* keeps a copy of the original file, too, with an added label of the date and time it was saved.

#### 4.6 Feedback

*Feedback* is the core program of the CPSP. It is used during the measurement to keep the distance constant. It automatically reads the last *DistCal* file from the current experimental directory. Under the tab "DistCal" one can check the calibration file. At the start of the experiment, one has to enable the "expert mode" by clicking the respective button under the "Config" tab to be able to specify the feedback and motor step widths. By



default, both are set to 0. The desired distance can be chosen at the top of the GUI. This will not change the actual distance, however, but only set the distance for the feedback system. To change the distance, one has to move the motor manually using the buttons at the bottom left. To start the feedback system, one has to press the green button next to "automatic feedback control". The user can also specify the tolerance, which is displayed in the plot around the desired distance. The plot also shows the continuously measured distance, calculated from the induced voltage using the calibration file. The displayed feedback range limits the feedback system to a travel distance of  $10\mu\text{m}$  in each direction to protect the foils in the case of unforeseeable events like a breakdown of the induced voltage. In the case of a contact, e.g., the motor The feedback range can be reset by the user by manually pulling the marker back to 0. This will not cause a movement of the foils. In case the limit is reached in any direction, the feedback system will automatically be turned off and an error message will be prompted to the user. If the user made sure that no voltage breakdown etc. has occurred, the range can be reset and the feedback system can be turned on again. The feedback step width can also be chosen by the user and should always be chosen to be equal or smaller than half of the tolerance.

## References

- [1] M. Beckers, A. Dewald, C. Fransen, K. Arnsward, C. Müller-Gatermann, and F. von Spee. Development of the multi-purpose Cologne Compact Differential Plunger

(CoCoDiff) for the measurement of nuclear level lifetimes with the Recoil Distance Doppler-shift method. *Nuclear Instruments and Methods in Physics Research Section A: Accelerators, Spectrometers, Detectors and Associated Equipment*, 1042:167418, 2022.

- [2] A. Dewald, O. Möller, and P. Petkov. Developing the Recoil Distance Doppler-Shift technique towards a versatile tool for lifetime measurements of excited nuclear states. *Progress in Particle and Nuclear Physics*, 67(3):786 – 839, 2012.

## List of Publications

- [1] L. Barber, D.M. Cullen, M.M. Giles, B.S. Nara Singh, M.J. Mallaburn, M. Beckers, A. Blazhev, T. Braunroth, A. Dewald, C. Fransen, A. Goldkuhle, J. Jolie, F. Mammes, C. Müller-Gatermann, D. Wölk, and K.O. Zell. “Performing the differential decay curve method on  $\gamma$ -ray transitions with unresolved Doppler-shifted components”. In: *Nuclear Instruments and Methods in Physics Research Section A: Accelerators, Spectrometers, Detectors and Associated Equipment* 950 (2020), p. 162965. ISSN: 0168-9002. DOI: <https://doi.org/10.1016/j.nima.2019.162965>. URL: <https://www.sciencedirect.com/science/article/pii/S0168900219313567>.
- [2] M. Ciemala, S. Ziliani, F. Crespi, S. Leoni, B. Fornal, A. Maj, P. Bednarczyk, G. Benzoni, A. Bracco, C. Boiano, S. Bottoni, S. Brambilla, M. Bast, M. Beckers, T. Braunroth, F. Camera, N. Cieplicka-Oryńczak, E. Clément, O. Dorvaux, S. Erturk, G. de France, C. Fransen, A. Goldkuhle, J. Grebosz, M.N. Harakeh, L.W. Iskra, B. Jacquot, A. Karpov, M. Kicińska-Habior, Y. Kim, M. Kmiecik, A. Lemasson, S.M. Lenzi, M. Lewitowicz, H. Li, I. Matea, K. Mazurek, C. Michelagnoli, M. Matejska-Minda, B. Million, C. Müller-Gatermann, V. Nanal, P. Napiorkowski, D.R. Napoli, R. Palit, M. Rejmund, Ch. Schmitt, M. Stanoiu, I. Stefan, E. Vardaci, B. Wasilewska, O. Wieland, M. Zielińska, and M. Ziebliński. “Short-range Lifetime Measurements for Deep-inelastic Reaction Products: the  $^{190}\text{Tl}$  Test Case”. In: *Acta Physica Polonia B* 51 (2020), p. 699. DOI: 10.5506/APhysPo1B.51.699.
- [3] M. Ciemala, S. Ziliani, F. Crespi, S. Leoni, B. Fornal, A. Maj, P. Bednarczyk, G. Benzoni, A. Bracco, C. Boiano, S. Bottoni, S. Brambilla, M. Bast, M. Beckers, T. Braunroth, F. Camera, N. Cieplicka-Oryńczak, E. Clément, O. Dorvaux, S. Erturk, G. De France, A. Goldkuhle, J. Grebosz, M.N. Harakeh, L.W. Iskra, B. Jacquot, A. Karpov, M. Kicińska-Habior, Y. Kim, M. Kmiecik, A. Lemasson, H. Li, I. Matea, K. Mazurek, C. Michelagnoli, B. Million, C. Müller-Gatermann, P. Napiorkowski, V. Nanal, M. Matejska-Minda, M. Rejmund, B. Sowicki, Ch. Schmitt, M. Stanoiu, I. Stefan, B. Wasilewska, M. Zielińska, and M. Ziebliński. “Determination of Lifetimes of Excited States in Neutron-rich  $^{20}\text{O}$  Isotope from Experiment with the AGATA+PARIS+VAMOS Setup”. In: *Acta Physica Polonia B* 50 (2019), p. 615. DOI: 10.5506/APhysPo1B.50.615.
- [4] M. Ciemala, S. Ziliani, F. C. L. Crespi, S. Leoni, B. Fornal, A. Maj, P. Bednarczyk, G. Benzoni, A. Bracco, C. Boiano, S. Bottoni, S. Brambilla, M. Bast, M. Beckers, T. Braunroth, F. Camera, E. Clément, S. Coelli, O. Dorvaux, S. Erturk, G. de France, C. Fransen, A. Goldkuhle, J. Grebosz, M. N. Harakeh, L. W. Iskra, B. Jacquot, A. Karpov, M. Kicińska Habior, Y. Kim, M. Kmiecik, A. Lemasson, S. M. Lenzi, M. Lewitowicz, H. Li, I. Matea, K. Mazurek, C. Michelagnoli, M. Matejska-Minda, B.

- Million, C. Müller-Gatermann, V. Nanal, P. Napiorkowski, D. R. Napoli, R. Palit, M. Rejmund, Ch. Schmitt, M. Stanoiu, I. Stefan, E. Vardaci, B. Wasilewska, O. Wieland, M. Zieblinski, D. Barrientos, B. Birkenbach, A. J. Boston, B. Cederwall, L. Charles, J. Collado, D. M. Cullen, P. Désesquelles, C. Domingo-Pardo, J. Dudouet, J. Eberth, V. González, J. Goupil, L. J. Harkness-Brennan, H. Hess, D. S. Judson, A. Jungclaus, W. Korten, M. Labiche, A. Lefevre, R. Menegazzo, D. Mengoni, J. Nyberg, R. M. Perez-Vidal, Zs. Podolyak, A. Pullia, F. Recchia, P. Reiter, F. Saillant, M. D. Salsac, E. Sanchis, O. Stezowski, Ch. Theisen, J. J. Valiente-Dobón, J. D. Holt, J. Menéndez, A. Schwenk, and J. Simonis. “Testing ab initio nuclear structure in neutron-rich nuclei: Lifetime measurements of second  $2^+$  state in  $^{16}\text{C}$  and  $^{20}\text{O}$ ”. In: *Phys. Rev. C* 101 (2 2020), p. 021303. DOI: 10.1103/PhysRevC.101.021303. URL: <https://link.aps.org/doi/10.1103/PhysRevC.101.021303>.
- [5] M. Droste, A. Blazhev, P. Reiter, K. Arnsward, M. Beckers, C. Fransen, R. Hetzenegger, R. Hirsch, L. Kaya, L. Knafla, L. Lewandowski, C. Müller-Gatermann, P. Petkov, D. Rosiak, M. Seidlitz, B. Siebeck, A. Vogt, N. Warr, and K. Wolf. “Lifetime measurements in the ground-state band in  $^{104}\text{Pd}$ ”. In: *Phys. Rev. C* 106 (2 2022), p. 024329. DOI: 10.1103/PhysRevC.106.024329. URL: <https://link.aps.org/doi/10.1103/PhysRevC.106.024329>.
- [6] A. Esmaylzadeh, V. Karayonchev, G. Häfner, J. Jolie, M. Beckers, A. Blazhev, A. Dewald, C. Fransen, A. Goldkuhle, L. Knafla, and C. Müller-Gatermann. “Triaxiality in the mid-shell nucleus  $^{112}\text{Pd}$ ”. In: *Phys. Rev. C* 103 (5 2021), p. 054324. DOI: 10.1103/PhysRevC.103.054324. URL: <https://link.aps.org/doi/10.1103/PhysRevC.103.054324>.
- [7] A. Esmaylzadeh, V. Karayonchev, K. Nomura, J. Jolie, M. Beckers, A. Blazhev, A. Dewald, C. Fransen, R.-B. Gerst, G. Häfner, A. Harter, L. Knafla, M. Ley, L. M. Robledo, R. Rodríguez-Guzmán, and M. Rudigier. “Lifetime measurements to investigate  $\gamma$  softness and shape coexistence in  $^{102}\text{Mo}$ ”. In: *Phys. Rev. C* 104 (6 2021), p. 064314. DOI: 10.1103/PhysRevC.104.064314. URL: <https://link.aps.org/doi/10.1103/PhysRevC.104.064314>.
- [8] M. M. Giles, B. S. Nara Singh, L. Barber, D. M. Cullen, M. J. Mallaburn, M. Beckers, A. Blazhev, T. Braunroth, A. Dewald, C. Fransen, A. Goldkuhle, J. Jolie, F. Mammes, C. Müller-Gatermann, D. Wölk, K. O. Zell, S. M. Lenzi, and A. Poves. “Probing isospin symmetry in the ( $^{50}\text{Fe}$ ,  $^{50}\text{Mn}$ ,  $^{50}\text{Cr}$ ) isobaric triplet via electromagnetic transition rates”. In: *Phys. Rev. C* 99 (4 2019), p. 044317. DOI: 10.1103/PhysRevC.99.044317. URL: <https://link.aps.org/doi/10.1103/PhysRevC.99.044317>.
- [9] A. Goldkuhle, A. Blazhev, C. Fransen, A. Dewald, M. Beckers, B. Birkenbach, T. Braunroth, E. Clément, J. Dudouet, J. Eberth, H. Hess, B. Jacquot, J. Jolie, Y.-H. Kim, A. Lemasson, S. M. Lenzi, H. J. Li, J. Litzinger, C. Michelagnoli, C. Müller-



- Gatermann, B. S. Nara Singh, R. M. Pérez-Vidal, D. Ralet, P. Reiter, A. Vogt, N. Warr, and K. O. Zell. “Lifetime measurements of excited states in neutron-rich  $^{53}\text{Ti}$ : Benchmarking effective shell-model interactions”. In: *Phys. Rev. C* 102 (5 2020), p. 054334. DOI: 10.1103/PhysRevC.102.054334. URL: <https://link.aps.org/doi/10.1103/PhysRevC.102.054334>.
- [10] A. Goldkuhle, C. Fransen, A. Blazhev, M. Beckers, B. Birkenbach, T. Braunroth, E. Clément, A. Dewald, J. Dudouet, J. Eberth, H. Hess, B. Jacquot, J. Jolie, Y.-H. Kim, A. Lemasson, S. M. Lenzi, H. J. Li, J. Litzinger, C. Michelagnoli, C. Müller-Gatermann, B. S. Nara Singh, R. M. Pérez-Vidal, D. Ralet, P. Reiter, A. Vogt, N. Warr, K. O. Zell, D. Barrientos, C. Barthe-Dejean, G. Benzoni, A. J. Boston, H. C. Boston, P. Bourgault, I. Burrows, J. Cacitti, B. Cederwall, M. Ciemala, D. M. Cullen, G. De France, C. Domingo-Pardo, J.-L. Foucher, G. Fremont, A. Gadea, P. Gangnant, V. González, J. Goupil, C. Henrich, C. Houarner, M. Jean, D. S. Judson, A. Korichi, W. Korten, M. Labiche, A. Lefevre, L. Legeard, F. Legrue, S. Leoni, J. Ljungvall, A. Maj, C. Maugeais, L. Ménager, N. Ménard, R. Menegazzo, D. Mengoni, B. Million, H. Munoz, D. R. Napoli, A. Navin, J. Nyberg, M. Ozille, Zs. Podolyak, A. Pullia, B. Raine, F. Recchia, J. Ropert, F. Saillant, M. D. Salsac, E. Sanchis, C. Schmitt, J. Simpson, C. Spitaels, O. Stezowski, Ch. Theisen, M. Toulemonde, M. Tripon, J.-J. Valiente Dobón, G. Voltolini. “Lifetime measurements in  $^{52,54}\text{Ti}$  to study shell evolution toward  $N = 32$ ”. In: *Phys. Rev. C* 100 (5 2019), p. 054317. DOI: 10.1103/PhysRevC.100.054317. URL: <https://link.aps.org/doi/10.1103/PhysRevC.100.054317>.
- [11] A. Goldkuhle, C. Fransen, A. Dewald, K. Arnsward, M. Bast, M. Beckers, A. Blazhev, T. Braunroth, G. Hackenberg, G. Häfner, J. Litzinger, C. Müller-Gatermann, F. von Spee, N. Warr, D. Werner, and K. O. Zell. “Lifetime measurement of excited states in  $^{46}\text{Ti}$ ”. In: *The European Physical Journal A* 55.53 (5 2019), p. 054317. DOI: <https://doi.org/10.1140/epja/i2019-12722-6>. URL: <https://link.aps.org/doi/10.1103/PhysRevC.100.054317>.
- [12] D. Kalaydjieva, D. Kocheva, G. Rainovski, V. Karayonchev, J. Jolie, N. Pietralla, M. Beckers, A. Blazhev, A. Dewald, M. Djongolov, A. Esmaylzadeh, C. Fransen, K. A. Gladnishki, A. Goldkuhle, C. Henrich, I. Himm, K. E. Ide, P. R. John, R. Kern, J. Kleemann, Th. Kröll, C. Müller-Gatermann, M. Scheck, P. Spagnoletti, M. Stoyanova, K. Stoychev, V. Werner, A. Yaneva, S. S. Dimitrova, G. De Gregorio, H. Naïdja, and A. Gargano. “Microscopic structure of the one-phonon  $2^+$  states of  $^{208}\text{Po}$ ”. In: *Phys. Rev. C* 104 (2 2021), p. 024311. DOI: 10.1103/PhysRevC.104.024311. URL: <https://link.aps.org/doi/10.1103/PhysRevC.104.024311>.
- [13] D. Kocheva, G. Rainovski, J. Jolie, N. Pietralla, A. Blazhev, R. Altenkirch, S. Ansari, A. Astier, M. Bast, M. Beckers, Th. Braunroth, M. Cappellazzo, A. De-

- wald, F. Diel, M. Djongolov, C. Fransen, K. Gladnishki, A. Goldkuhle, A. Hennig, V. Karayonchev, J. M. Keatings, E. Kluge, Th. Kröll, J. Litzinger, K. Moschner, C. Müller-Gatermann, P. Petkov, M. Scheck, Ph. Scholz, T. Schmidt, P. Spagnoletti, C. Stahl, R. Stegmann, A. Stolz, A. Vogt, N. Warr, V. Werner, D. Wölk, J. C. Zamora, K. O. Zell, V. Yu. Ponomarev, and P. Van Isacker. “Low collectivity of the  $2_1^+$  state of  $^{212}\text{Po}$ ”. In: *Phys. Rev. C* 96 (4 2017), p. 044305. DOI: 10.1103/PhysRevC.96.044305. URL: <https://link.aps.org/doi/10.1103/PhysRevC.96.044305>.
- [14] D. Kocheva, G. Rainovski, J. Jolie, N. Pietralla, A. Blazhev, A. Astier, R. Altenkirch, M. Bast, M. Beckers, S. Ansari, Th. Braunroth, M. Cappellazzo, M.L. Cortés, A. Dewald, F. Diel, M. Djongolov, C. Fransen, K. Gladnishki, A. Goldkuhle, A. Hennig, V. Karayonchev, J.M. Keatings, E. Kluge, Th. Kröll, J. Litzinger, K. Moschner, C. Müller-Gatermann, P. Petkov, M. Rudigier, M. Scheck, P. Spagnoletti, Ph. Scholz, T. Schmidt, M. Spieker, C. Stahl, R. Stegmann, A. Stolz, A. Vogt, M. Stoyanova, P. Thöle, N. Warr, V. Werner, W. Witt, D. Wölk, J.C. Zamora, K.O. Zell, P. Van Isacker, and V.Yu. Ponomarev. “Low collectivity of the first  $2+$  states of  $^{212,210}\text{Po}$ ”. In: *Journal of Physics: Conference Series* 1023.1 (5 2018), p. 012019. DOI: 10.1088/1742-6596/1023/1/012019. URL: <https://dx.doi.org/10.1088/1742-6596/1023/1/012019>.
- [15] D. Kocheva, A. Yaneva, D. Kalaydjieva, G. Rainovski, J. Jolie, N. Pietralla, M. Beckers, A. Blazhev, L. Bussmann, M. Cappellazzo, A. Dewald, F. Diel, M. Djongolov, F. Dunkel, A. Esmaylzadeh, B. Falk, C. Fransen, J. Garbe, L. Gerhard, R.-B. Gerst, K. A. Gladnishki, A. Goldkuhle, G. Hackenberg, C. Henrich, I. Homm, K. Ide, V. Karayonchev, R. Kern, J. Kleeman, L. Knafla, L. Kornwebel, Th. Kröll, M. Ley, C. Müller-Gatermann, M. Scheck, T. Schmidt, P. Spagnoletti, M. Stoyanova, and V. Werner. “Lifetime measurements of the low-lying excited states of  $^{208}\text{Po}$ ”. In: *Journal of Physics: Conference Series* 1555.1 (5 2020), p. 012020. DOI: 10.1088/1742-6596/1555/1/012020. URL: <https://dx.doi.org/10.1088/1742-6596/1555/1/012020>.
- [16] C. Müller-Gatermann, A. Dewald, C. Fransen, K. Auranen, H. Badran, M. Beckers, A. Blazhev, T. Braunroth, D. M. Cullen, G. Fruet, A. Goldkuhle, T. Grahn, P. T. Greenlees, U. Jakobsson, D. Jenkins, J. Jolie, R. Julin, S. Juutinen, J. Konki, M. Leino, J. Litzinger, K. Nomura, J. Pakarinen, P. Peura, M. G. Procter, P. Rahkila, P. Ruotsalainen, M. Sandzelius, J. Sarén, C. Scholey, J. Sorri, S. Stolze, M. J. Taylor, J. Uusitalo, and K. O. Zell. “Shape coexistence in  $^{178}\text{Hg}$ ”. In: *Phys. Rev. C* 99 (5 2019), p. 054325. DOI: 10.1103/PhysRevC.99.054325. URL: <https://link.aps.org/doi/10.1103/PhysRevC.99.054325>.
- [17] C. Müller-Gatermann, A. Dewald, C. Fransen, M. Beckers, A. Blazhev, T. Braunroth, A. Goldkuhle, J. Jolie, L. Kornwebel, W. Reviol, F. von Spee, and K. O. Zell.

- “Evolution of collectivity in  $^{118}\text{Xe}$ ”. In: *Phys. Rev. C* 102 (6 2020), p. 064318. DOI: 10.1103/PhysRevC.102.064318. URL: <https://link.aps.org/doi/10.1103/PhysRevC.102.064318>.
- [18] C. Müller-Gatermann, F. von Spee, A. Goasduff, D. Bazzacco, M. Beckers, T. Braunroth, A. Boso, P. Cocconi, G. de Angelis, A. Dewald, C. Fransen, A. Goldkuhle, A. Gottardo, A. Gozzelino, K. Hadyńska-Klek, G. Jawroski, P.R. John, J. Jolie, S.M. Lenzi, J. Litzinger, R. Menegazzo, D. Mengoni, D.R. Napoli, F. Recchia, M. Siciliano, D. Testov, S. Thiel, J.J. Valiente-Dobón, and K.O. Zell. “A new dedicated plunger device for the GALILEO  $\gamma$ -ray detector array”. In: *Nuclear Instruments and Methods in Physics Research Section A: Accelerators, Spectrometers, Detectors and Associated Equipment* 920 (5 2019), pp. 95–99. ISSN: 0168-9002. DOI: <https://doi.org/10.1016/j.nima.2018.12.077>. URL: <https://www.sciencedirect.com/science/article/pii/S0168900218318916>.
- [19] M. Stoyanova, G. Rainovski, J. Jolie, N. Pietralla, A. Blazhev, M. Beckers, A. Dewald, M. Djongolov, A. Esmaylzadeh, C. Fransen, L. M. Gerhard, K. A. Gladnishki, S. Herb, P. R. John, V. Karayonchev, J. M. Keatings, R. Kern, L. Knafla, D. Kocheva, L. Kornwebel, Th. Kröll, M. Ley, K. M. Mashtakov, C. Müller-Gatermann, J.-M. Régis, M. Scheck, K. Schomacker, J. Sinclair, P. Spagnoletti, C. Sürder, N. Warr, V. Werner, and J. Wiederhold. “Lifetimes of the  $4_1^+$  states of  $^{206}\text{Po}$  and  $^{204}\text{Po}$ : A study of the transition from noncollective seniority-like mode to collectivity”. In: *Phys. Rev. C* 100 (6 2019), p. 064304. DOI: 10.1103/PhysRevC.100.064304. URL: <https://link.aps.org/doi/10.1103/PhysRevC.100.064304>.
- [20] M. Beckers, A. Dewald, C. Fransen, K. Arnsward, C. Müller-Gatermann, and F. von Spee. “Development of the multi-purpose Cologne Compact Differential Plunger (CoCoDiff) for the measurement of nuclear level lifetimes with the Recoil Distance Doppler-shift method”. In: *Nuclear Instruments and Methods in Physics Research Section A: Accelerators, Spectrometers, Detectors and Associated Equipment* 1042 (5 2022), p. 167418. ISSN: 0168-9002. DOI: <https://doi.org/10.1016/j.nima.2022.167418>. URL: <https://www.sciencedirect.com/science/article/pii/S0168900222007100>.
- [21] M. Beckers, A. Dewald, C. Fransen, L. Kornwebel, C.-D. Lakenbrink, and F. von Spee. “Revisiting the measurement of absolute foil-separation for RDDS measurements and introduction of an optical measurement method”. In: *Nuclear Instruments and Methods in Physics Research Section A: Accelerators, Spectrometers, Detectors and Associated Equipment* 1042 (5 2022), p. 167416. ISSN: 0168-9002. DOI: <https://doi.org/10.1016/j.nima.2022.167416>. URL: <https://www.sciencedirect.com/science/article/pii/S0168900222007082>.

- [22] M. Beckers, C. Müller-Gatermann, A. Blazhev, T. Braunroth, A. Dewald, C. Fransen, A. Goldkuhle, L. Kornwebel, J. Litzinger, F. von Spee, and K.-O. Zell. “Lifetime measurement of excited states in  $^{144}\text{Ce}$ : Enhanced  $E1$  strengths in a candidate for octupole deformation”. In: *Phys. Rev. C* 102 (1 2020), p. 014324. DOI: 10.1103/PhysRevC.102.014324. URL: <https://link.aps.org/doi/10.1103/PhysRevC.102.014324>.
- [23] M. Trichkova, M. Beckers, K. Gladnishki, A. Dewald, A. Blazhev, C. Müller-Gatermann, C. Fransen, J. Jolie, D. Kalaydjieva, G. Rainovski, and K.-O. Zell. “Lifetimes and electromagnetic transition strength in  $^{124}\text{Ba}$ ”. In: *EPJ Web Conf.* 194 (5 2018), p. 03004. DOI: 10.1051/epjconf/201819403004. URL: <https://doi.org/10.1051/epjconf/201819403004>.
- [24] S. Ziliani, M. Ciemala, F. C. L. Crespi, S. Leoni, B. Fornal, T. Suzuki, T. Otsuka, A. Maj, P. Bednarczyk, G. Benzoni, A. Bracco, C. Boiano, S. Bottoni, S. Brambilla, M. Bast, M. Beckers, T. Braunroth, F. Camera, E. Clément, S. Coelli, O. Dorvaux, S. Erturk, G. de France, C. Fransen, A. Goldkuhle, M. N. Harakeh, L. W. Iskra, B. Jacquot, A. Karpov, M. Kicińska-Habior, Y. Kim, M. Kmiecik, A. Lemasson, S. M. Lenzi, M. Lewitowicz, H. Li, I. Matea, K. Mazurek, C. Michelagnoli, M. Matejska-Minda, B. Million, C. Müller-Gatermann, V. Nanal, P. Napiorkowski, D. R. Napoli, R. Palit, M. Rejmund, Ch. Schmitt, M. Stanoiu, I. Stefan, E. Vardaci, B. Wasilewska, O. Wieland. “Complete set of bound negative-parity states in the neutron-rich nucleus  $^{18}\text{N}$ ”. In: *Phys. Rev. C* 104 (4 2021), p. L041301. DOI: 10.1103/PhysRevC.104.L041301. URL: <https://link.aps.org/doi/10.1103/PhysRevC.104.L041301>.
- [25] S. Ziliani, M. Ciemala, F.C.L. Crespi, S. Leoni, B. Fornal, A. Maj, P. Bednarczyk, G. Benzoni, A. Bracco, C. Boiano, S. Bottoni, S. Brambilla, M. Bast, M. Beckers, T. Braunroth, F. Camera, N. Cieplicka-Oryńczak, E. Clément, S. Coelli, O. Dorvaux, S. Erturk, G. de France, C. Fransen, A. Goldkuhle, J. Grebosz, M.N. Harakeh, L.W. Iskra, B. Jacquot, A. Karpov, M. Kicińska-Habior, Y. Kim, M. Kmiecik, A. Lemasson, S.M. Lenzi, M. Lewitowicz, H. Li, I. Matea, K. Mazurek, C. Michelagnoli, M. Matejska-Minda, B. Million, C. Müller-Gatermann, V. Nanal, P. Napiorkowski, D.R. Napoli, R. Palit, M. Rejmund, Ch. Schmitt, M. Stanoiu, I. Stefan, E. Vardaci, B. Wasilewska, O. Wieland, M. Ziebliński, and M. Zielińska. “Spectroscopy of Neutron-rich Nitrogen Isotopes with AGATA+PARIS+VAMOS”. In: *Acta Physica Polonia B* 51 (4 2020), p. 709. DOI: 10.5506/APhysPolB.51.709. URL: <https://link.aps.org/doi/10.1103/PhysRevC.104.L041301>.

## List of Figures

1	Schematic representation of a plunger measurement . . . . .	5
2	Monte-Carlo type simulation example . . . . .	6
3	Differential Plunger Method schematics . . . . .	7
4	DSA influence visualization . . . . .	10
5	Cologne Coincidence Plunger . . . . .	11
6	Model of a NEXACT® module . . . . .	13
7	Representation of the open-loop and closed-loop operation modes . . . . .	14
8	Cologne plunger spectrometer . . . . .	15
9	Schematic drawing of different reaction types . . . . .	16
10	Example of a solar cell spectrum . . . . .	18
11	Energy levels of the shell model . . . . .	20
12	Regions of octupole deformation . . . . .	23
13	Octupole nuclear potentials and example of octupole deformed level scheme . . . . .	24
14	Plot of $R(I)$ for different nuclei . . . . .	25
15	Potential energy surfaces for nuclei in the $Z \approx 56$ , $N \approx 88$ region . . . . .	27
16	Schematics of CoCoDiff@PRISMA . . . . .	75
17	Pictures of different compact plungers . . . . .	76
18	HISPEC plunger . . . . .	77
19	Plunger control circuit . . . . .	78
20	Thickness measurement station . . . . .	80

## Danksagung

Zuerst möchte ich mich bei Alfred Dewald bedanken für die Vergabe des spannenden Themas und der Möglichkeit daran mit großer Freiheit zu arbeiten. Durch Dich bin ich als ehemaliger Lehramtsstudent überhaupt erst in die Welt der Experimentalphysik eingetaucht und dort hängengeblieben. Dazu haben vor Allem die spannenden Themen, die ich schon seit meiner Bachelorarbeit in Deiner Gruppe bearbeiten durfte und Deine immer interessierte Betreuung beigetragen. Du hast mir immer die Möglichkeit gegeben an eigenen Ideen zu arbeiten aber auch immer dein großes Fachwissen zur Unterstützung zur Verfügung gestellt.

Bei Prof. Dr. Andreas Zilges bedanke ich mich für die Bereitschaft die Zweitkorrektur dieser Arbeit zu übernehmen und bei Prof. Dr. Andreas Schadschneider für die Leitung der Prüfungskommission.

Besonderer Dank gebührt auch Christoph Fransen, für die unermüdliche Hilfsbereitschaft. Du hattest trotz deines immensen Arbeitspensums im IKP immer ein offenes Ohr für Fragen und Probleme. Ohne deinen Einsatz für die Detektoren und den Beschleuniger wäre wahrscheinlich keins der Experimente in dieser Arbeit möglich gewesen.

Weiterer Dank geht raus an die "alte" (Alina, Claus) und "neue" (Caspar, Franziskus, Lisa) Besetzung des Büro 225 und die restliche Plungergruppe für die Unterstützung und die lustige Zeit.

Besonders bedanken möchte ich mich dabei nochmal bei Claus Müller-Gatermann, der zu jeder Tages- und/oder Nachtzeit für jegliche Fragen zur Verfügung stand (auch nachdem er das IKP verlassen hat) und mich auch in die Kunst der Lebensdauerauswertung eingeführt hat.

Weiterer Dank gebührt Stefan Thiel und seinem Team in der Feinmechanikwerkstatt, die meine Ideen immer sehr professionell und schnell verwirklicht haben. Dringende Umbauarbeiten, und davon gab es einige, wurden unter großem Einsatz auch oft spontan dazwischen geschoben.

Last, but not least, bedanke ich mich natürlich auch bei meinem privaten Umfeld für die (moralische) Unterstützung während der ganzen Zeit und viele schöne Ablenkungen.

## Erklärung zur Dissertation gemäß der Promotionsordnung vom 12. März 2020

Hiermit versichere ich an Eides statt, dass ich die vorliegende Dissertation selbstständig und ohne die Benutzung anderer als der angegebenen Hilfsmittel und Literatur angefertigt habe. Alle Stellen, die wörtlich oder sinngemäß aus veröffentlichten und nicht veröffentlichten Werken dem Wortlaut oder dem Sinn nach entnommen wurden, sind als solche kenntlich gemacht. Ich versichere an Eides statt, dass diese Dissertation noch keiner anderen Fakultät oder Universität zur Prüfung vorgelegen hat; dass sie - abgesehen von unten angegebenen Teilpublikationen und eingebundenen Artikeln und Manuskripten - noch nicht veröffentlicht worden ist sowie, dass ich eine Veröffentlichung der Dissertation vor Abschluss der Promotion nicht ohne Genehmigung des Promotionsausschusses vornehmen werde. Die Bestimmungen dieser Ordnung sind mir bekannt. Darüber hinaus erkläre ich hiermit, dass ich die Ordnung zur Sicherung guter wissenschaftlicher Praxis und zum Umgang mit wissenschaftlichem Fehlverhalten der Universität zu Köln gelesen und sie bei der Durchführung der Dissertation zugrundeliegenden Arbeiten und der schriftlich verfassten Dissertation beachtet habe und verpflichte mich hiermit, die dort genannten Vorgaben bei allen wissenschaftlichen Tätigkeiten zu beachten und umzusetzen. Ich versichere, dass die eingereichte elektronische Fassung der eingereichten Druckfassung vollständig entspricht.

Köln, 13.02.2023



(Marcel Beckers)

Teilpublikationen:

- M. Beckers *et al.* "Lifetime measurement of excited states in  $^{144}\text{Ce}$ : Enhanced E1 strengths in a candidate for octupole deformation", *Phys. Rev. C* 102, 014324 (2020).
- M. Beckers *et al.* "Development of the multi-purpose Cologne Compact Differential Plunger (CoCoDiff) for the measurement of nuclear level lifetimes with the Recoil Distance Doppler-shift method", *Nucl. Inst. Meth. A* 1042, 167418 (2022).
- M. Beckers *et al.* "Revisiting the measurement of absolute foil-separation for RDDS measurements and introduction of an optical measurement method", *Nucl. Inst. Meth. A* 1042, 167416 (2022).
- M. Beckers *et al.* "Lifetime Measurement of the  $2_1^+$ ,  $4_1^+$  States in semi-magic  $^{60}\text{Ni}$ ", *Eur. Phys. J. A* 59 129 (2023).

Die Dissertation beinhaltet die Gewinnung und Analyse von Primärdaten. Diese Daten sind auf den Servern des Instituts für Kernphysik gesichert und zugänglich.